SUPRAMOLECULAR MODIFICATION OF ISONIAZID: AN *IN VITRO* AND *IN SILICO* ANALYSIS OF COMBINATION DRUG EFFICACY AGAINST MYCOBACTERIA SPECIES

by

ITUMELENG BRIDGETTE SETSHEDI

submitted in accordance with the requirements for

the degree of

DOCTOR OF PHILOSOPHY

in

PHD – LIFE SCIENCES

at the

UNIVERSITY OF SOUTH AFRICA

SUPERVISOR: DR PN KAYOKA

CO-SUPERVISOR: DR MG SMITH

Submitted: (12 October 2023)

DECLARATION

Name: Itumeleng Bridgette Setshedi

Student number: 45951012

Degree: 90012 PhD – Life Sciences

Exact wording of the title of the thesis as appearing on the electronic copy submitted for examination:

Supramolecular modification of isoniazid: an *in vitro* and *in silico* analysis of combination

efficacy against mycobacteria species

I declare that the above thesis is my own work and that all the sources that I have used or quoted have been indicated and acknowledged by means of complete references.

I further declare that I submitted the thesis to originality checking software and that it falls within the accepted requirements for originality.

I further declare that I have not previously submitted this work, or part of it, for examination at Unisa for another qualification or at any other higher education institution.

12 October 2023

SIGNATURE   DATE

ABSTRACT

Tuberculosis was for the longest of time a leading infectious killer instigated by a single pathogen until the emergence of SARS-CoV-2. The disease continues to be a major global health problem causing high rates of morbidity and mortality. Unfortunately, both the estimated disease incidence and mortality related to tuberculosis infections have been reported to be on the rise as treatment of the disease has been neglected due to a shift in attention to address the COVID-19 global pandemic. The remnants thereof still pose a direct negative impact on tuberculosis diagnosis and treatment, resulting in the partial reversal of any progress that had been made in the quest to end tuberculosis prior to the global COVID-19 pandemic. It is presumed that the challenges around tuberculosis treatment and misdiagnosis are as a result of the continuous ability of the pathogen to evade the host's immune system and development of resistance against tuberculosis drugs. However, diagnosis seems to be the weakest link contributing to delayed treatment thereof.

If detected early, tuberculosis can be cured. However, if tuberculosis is not detected, it definitely cannot be treated; and, if it cannot be treated, it certainly cannot be eradicated. In addition, there is also an emergence of nontuberculous mycobacteria which are caused by mycobacteria species other than those belonging to the *Mycobacterium tuberculosis* complex. Some of these organisms cause pulmonary infections indistinguishable to those caused by *M. tuberculosis* infections, presenting with pulmonary and extrapulmonary tuberculosis-like diseases. The prevalence of these diseases has steadily gained traction in recent years, reported and isolated from clinical isolates around the world. Yet, these mycobacteria are not targeted when screening for tuberculosis in clinical isolates. This is a public health problem as nontuberculous mycobacteria are generally resistant to the tuberculosis treatment regimen used in screening assays and if not screened, they can easily be misdiagnosed as *Mycobacterium tuberculosis.* If there are no obvious ways in which these organisms can be distinguished during diagnosis, it would be beneficial if drugs that are designed could target both *Mycobacterium tuberculosis* and nontuberculous mycobacteria as nontuberculous mycobacteria are not susceptible to first- and second-line tuberculosis treatment regimens.

The aim of this study was to design and synthesise isoniazid derivatives that are effective against clinically infectious *Mycobacterium tuberculosis* as well as nontuberculous mycobacteria isolates. To achieve this, methods such as the one-pot reflux method were

employed for the synthesis of the isoniazid derivative. Crystallographic data were collected using the Bruker APEX II CCD area detector diffractometer. Data were reduced and corrected using the SAINT-Plus software and the SADABS software, respectively. Diagrams were generated using WinGX and PLATON software. To test for the efficacy of the derivatives against mycobacteria of choice (*M. tuberculosis* $H_{37}R_a$, *M. bovis* BCG, *M. smegmatis*, *M. avium* and *M. fortuitum*) in comparison to the efficacy of isoniazid and that of rifampicin, a number of disciplines with varying techniques were employed and these include microbiology, where minimum inhibitory concentration experiments were conducted, and cell biology where cell viability was assessed using real-time cell analysis techniques and flow cytometry analysis conducted using the xCELLigence RTCA system and the BD FACSArai™ III cell sorter, respectively. The potential safety of these compounds was also assessed on RAW 264.7 murine macrophage cells where methods such as the MTT assay and real-time cell analysis assay as well as flow cytometry assay (Muse® Cell Analyzer) were employed to conduct cell viability assessment. Lastly, molecular docking and modelling experiments were conducted to determine the target protein and binding of the ligands thereof (protein-ligand binding).

Unit cells were collected for all nineteen synthesised derivatives, where nine have been previously synthesised and ten were found to be novel. Of the ten, six were refined successfully and five of those published in peer-reviewed journals. All derivatives were screened against mycobacteria of choice and only a few were found to have inhibitory effects against some of the mycobacteria with some noteworthy concentrations varying between 0.25 µg/mL and 11.36 µg/mL as single compounds, and 0.09 µg/mL and 0.59µg/mL for combination drug treatments. Isoniazid was comparable against single and combination derivatives with concentrations ranging between 3.9 µg/mL and 22.73 µg/mL, and rifampicin gave competitive results at concentrations ranging between 0.16 µg/mL and 15.65 µg/mL against single and derivatives. In most cases, the derivatives were observed to cause direct apoptotic effects on mycobacterial cells at competitive percentages of between 59% and 90%, thus better than the apoptosis percentage induced by isoniazid and rifampicin of less than 10%. Nonetheless, the related apoptosis results were in accordance with RTCA and flow cytometry results that saw most derivatives posing less toxicity against murine macrophage cells and the ability of the said cells to recover as compared to when exposed to isoniazid and rifampicin. The molecular modelling results also saw a few molecules and combinations possessing exceptional binding abilities with the catalase-peroxidase enzyme with no degree

of displacement and good drug residence time, thus suggestive of some derivatives being effective mycobacteria inhibitors targeting the catalase-peroxidase enzyme with docking scores ranging from -4.879 kcal/mol, -5.390 kcal/mol, to -6.065 kcal/mol.

DEDICATION

I dedicate this thesis to my entire family, for this would have not been possible without their undying support and roles played by each and every single one of them. The support availed to me on demand has earned us a "Doctor of Philosophy" degree.

ACKNOWLEDGEMENTS

SCOPE AND SYNOPSIS OF THE THESIS

1 **Research Problem:** Tuberculosis and drug resistance. (**Chapter 1:** Section 1.2 & 1.2)

2 **ResearchGap:** Mycobacteria tuberculosis or Nontuberculous mycobacteria infections? Drug resistance & Misdiagnosis (**Chapter 1:** Section 1.3 & Problem ststement)

3 **Proposed solution:** Design drugs effective against both MTB & NTM (**Chapter 1:** Objectives & **Chapter 2**)

4 **Approach:** Drug design, synthesis (**Chapter 2**)

5 **Application:** Screening for efficacy against Mycobacteria species of choice. (**Chapter 3**) - Determine safety and assess for toxicity (**Chapter 4**)

6 **Comfirm drug efficancy:** Drug modelling and sumulation *in silico*. (**Chapter 5**)

STRUCTURE OF THE THESIS

Chapter 1: General introduction and literature review

This chapter provides the general background, thus introducing the focus area of this research. It then delves into the history, pathogenesis, diagnosis and treatment of *Mycobacterium tuberculosis*. The research gap is identified and the problem statement is formulated, followed by the aim, objectives and hypothesis of the research.

Chapter 2: The design and synthesis of isonicotinic acid hydrazide derivatives

This chapter focuses on the design and synthesis of novel isonicotinic acid hydrazide (isoniazid) derivatives, followed by the supramolecular modification and co-crystallisation of isoniazid derivatives and crystal structure refinement.

The chapter is structured as follows:

- Background
- Materials and methods
- Results and discussion
- Conclusion

Chapter 3: Target identification and validation

The chapter provides an introductory background on multidisciplinary principles involved in drug discovery, particularly those employed to achieve the aims of this study. It then provides a detailed background on the research gap ("organisms of interest") as highlighted in the problem statement provided in Chapter 1. The aim of this chapter is to validate the drug target ("organism") and efficacy of the synthesised isoniazid derivatives achieved through conducting a series of minimum inhibitory concentration and microbial cell viability assays. In addition, the individual and synergistic effects of the designed isoniazid derivatives on mycobacteria of choice are determined.

The chapter is structured as follows:

- Background
- Materials and methods: Experimental procedure
- Results and discussion
- Conclusion

Chapter 4: Drug safety/cytotoxicity screening

The aim of this chapter is to determine the safety of the synthesised derivatives. It provides introductory principles of drug discovery and safety techniques employed in this study to gain a general understanding of the effects of the synthesised isoniazid derivatives on a biological system.

The chapter is structured as follows:

- Introduction
- Materials and methods
- Results and discussion
- Conclusion

Chapter 5: Molecular docking and dynamic studies

This chapter focuses on the simulation of compound activity against mycobacteria isolates based on the results of the minimum inhibitory concentration and microbial cell viability assays obtained in Chapter 3.

The chapter is structured as follows:

- Introduction
- Materials and methods
- Results and discussion
- Conclusion

Chapter 6: General discussion

This chapter provides a summarised discussion of the results from Chapter 2 through to Chapter 5.

Chapter 7: General conclusion and future perspectives

This chapter provides a detailed general conclusion based on the results obtained and described in previous chapters. The conclusion links the experimental work, results, objectives and hypothesis. Future perspectives and prospective projects are outlined with details drawn from the results, and the challenges encountered throughout the research period, as well as the identified unanswered research questions.

CONTENTS

LIST OF FIGURES

nohydrazide 0.5 hydrate $C_{10}H_{13}N_3O \cdot 0.5H_2O$ – **IBS017**. **(b)** The crystal morphology of IBS017 as observed under a light microscope.

Chapter 3: Target identification and validation

Chapter 4: Drug safety/cytotoxicity screening

Chapter 5: Molecular docking and dynamic studies

LIST OF TABLES

LIST OF SCHEMES

LIST OF ABBREVIATIONS

Chemicals, reagents and media	
ADC	albumin dextrose catalase
AO	auramine O
CO_2	carbon dioxide
DMEM	Dulbecco's Modified Eagle Medium
DMSO	dimethyl sulfoxide
EMB	ethambutol
FBS	foetal bovine serum
FIT-C	fluorescein isothiocyanate
HCl	hydrochloric acid
INH	isonicotinic acid hydrazide (isoniazid)
INT	2-[4-iodophenyl]-3-[4-dinitrophenyl]-5-phenyltetrazoliumchloride
INTF	INT reduced to iodonitrotetrazolium formazan
M 7H9	Middlebrook 7H9
MTT	3-[4,5-dimethylthiazol-2-yl]-2,5 diphenyl tetrazolium bromide
OADC	oleic acid albumin dextrose catalase
Pen/Strep	penicillin-streptomycin
PI	propidium iodide

PZA	pyrazinamide
RIF	rifampicin
ZN	Ziehl-Neelsen stain

Instruments and assays

BD FACS	Becton Dickinson Fluorescence-Activated Cell Sorter
CT	computed tomography
FM	fluorescence microscopy
FTIR	Fourier transform infrared spectroscopy
PCR	polymerase chain reaction
RTCA	real-time cell analysis assay
RT-PCR	real-time polymerase chain reaction
SC-XRD	single crystal X-ray diffraction

Microorganisms

AIDS	acquired immunodeficiency syndrome
BCG	bacillus Calmette-Guérin
COVID-19	coronavirus disease 2019
EPTB	extrapulmonary tuberculosis
HIV	human immunodeficiency virus
MAC	*Mycobacterium avium* complex
MDR-TB	multidrug-resistant tuberculosis
MOTT	mycobacteria other than tuberculosis
MTBC	*Mycobacterium tuberculosis* complex
NTM	nontuberculous mycobacteria
PTB	pulmonary tuberculosis
RR-TB	rifampicin-resistant tuberculosis
TB	tuberculosis
TDR-TB	total drug-resistant tuberculosis
XDR-TB	extensively drug-resistant tuberculosis

Organisations	
FDA	Food and Drug Administration
NHLS	National Health Laboratory Services
UNAIDS	United Nations Programme on HIV/AIDS
WHO	World Health Organization

Sundry abbreviations	
API	active pharmaceutical ingredient
ATCC	American Type Culture Collection
CCDC	Cambridge Crystallography Data Centre
CDC	Centers for Disease Control and Prevention
CR1 and CR3	complement receptor type 1 and type 3
CSD	Cambridge Structural Database
CSF	cerebrospinal fluid
DNA	deoxyribonucleic acid
FSC-H	forward scatter height
MIC	minimum inhibitory concentration
NADH	reduced nicotinamide adenine dinucleotide
NCTC	National Collection of Type Culture
Rab5	Rabaptin-5
RNA	ribonucleic acid
SSC-H	side scatter – height
STI	sexually transmitted infections

Units of measurements	
%	percentage
±	plus-minus sign
°	degrees
°C	degrees Celsius
µg/mL	microgram per millilitre
µL	microlitre

Å	angstrom
cells/mL	cells per millilitre
EC_{50}	half-maximal effective concentration
g	gram
g/L	gram per litre
g/mol	gram per mole
h	hour
Hz	hertz
kcal/mol	kilocalories per mole
L	litre
LC_{50}	lethal concentration 50 is the amount of substance that will kill 50% of the cells
mg	milligram
mg/m^3	milligram per cubic metre
Min	Minute
mg/L	Milligram per litter
mL	millilitre
mmol	millimolar
nm	nanometre
ppm	parts per million
U/mL	unit per millilitre

CHAPTER 1
General introduction and literature review

1.1. General introduction

Mycobacteria are aerobic acid-fast bacilli (rods) slow-growing microorganisms found in nature (Rogall, Flohr & Böttger, 1990). *Mycobacterium tuberculosis* complex (MTBC) comprises species that cause tuberculosis, namely *M. africanum, M. bovis, M. tuberculosis, M. canettii, M. caprae, M. microti, M. mungi, M. pinnipedii,* the dassie bacillus*, M. orygis* and *M. suricattae*. These organisms are pathogenic mycobacteria of medical importance (Daniel, 2006). Tuberculosis (TB) is a disease that has beleaguered humankind for millions of years throughout history and for some time was known to have killed more people than any other microbial pathogen. Irrespective of the outstanding history of scientific achievements in therapeutics and microbiology, TB continues to pose a threat to mankind decades later (WHO, 2021a) with the emergence of drug-resistant strains difficult to control, even in countries with the most highly developed health-care systems (Mukherjee *et al.*, 2004; World Health Organization (WHO, 2018).

There are other nontuberculous mycobacteria (NTM) capable of infecting humans presenting with symptoms clinically similar to those caused by tuberculosis. These infections are often mistaken for tuberculosis. These mycobacteria make up the bulk of the species within the genus *Mycobacterium* and are known to be important opportunistic pathogens of humans, animals, poultry, and fish mainly found in the environment. *Mycobacterium avium, M. intracellulare, M. kansasii, M. xenopi, M. marinum, M. malmoense and M. simiae* are the slow growing NTM known to infect humans (Koh, 2017). There are also rapidly growing environmental opportunistic mycobacteria known to infect humans, and those include *M. abscessus*, *M. chelonae*, *M. smegmatis* and *M. fortuitum*. It is, however, important to note that rapidly growing NTM still grow at a relatively slower rate in comparison to several other bacteria (Falkinham, 2009).

The development of resistance among antimycobacterial drugs has been reported by different researchers. Isonicotinic acid hydrazide, commonly known as isoniazid (INH) was introduced as an anit-TB drug in 1951 and was used mainly to treat active and latent infections. Over time, mycobacteria have developed resistance due to various genetic mutations between

codons 138 and 328. With the most common one being the Ser315Thr mutation, which produces a modified catalase-peroxidase enzyme incapable of activating INH (Shehzad *et al*., 2013). Rifampicin (RIF), which was later used in conjunction with isoniazid is believed to interfere with RNA synthesis by inhibiting bacteria DNA-dependent RNA polymerase. Resistance towards this drug is due to a mutation observed in the distinct 81-base-pair (bp) (27-codon), which is the central region of the gene that is known to encode for the beta (β)-subunit of RNA polymerase (Shehzad *et al.*, 2013). Pyrazinamide (PZA) was also later added as a vital first-line drug regimen for its sterilising effects on semi-dormant tubercle bacilli. However, the mechanism of resistance against PZA is unknown. It is known that PZA-resistant isolates carry a mutation either in the structural gene or in the putative promoter region of the gene, as observed in about 72-97% of all PZA-resistant clinically isolated specimens (Shehzad *et al*., 2013).

Ethambutol (EMB), also part of the first-line drug regimen against TB, is a bacteriostatic agent that inhibits three arabinosyltransferase enzymes, namely embA, embB and embC, which are actively involved in cell wall biosynthesis, but unfortunately it has no effect on non-replicating bacilli. Resistance is due to the over-production of arabinosyltransferase enzyme which results from random spontaneous genetic mutation. This enzyme overwhelms the inhibitory effects of EMB. The mutation is observed in codon 306 in embB of about 70-90% of EMB-resistant strains (Zhao *et al.*, 2015).

Besides the challenges with the current TB treatment, drug developers are also faced with the task of developing drugs that can be active against multidrug-resistant TB (MDR-TB), extensively drug-resistant TB (XDR-TB), totally drug-resistant strains, as well as nontuberculous mycobacteria (NTM) that are totally resistant to the commonly used TB treatment regimens (Maitra *et al*., 2015). There is a need to develop drugs which will not only be active against the resistant strains, but also with fewer side effects which are effective at lower concentrations. Therefore, developing new drugs either by identifying novel constituents, or by modifying the already existing anti-TB drugs is a task of global interest, and might ultimately lead to the effective control of TB in the future.

1.2. Literature review

1.2.1. Mycobacteria species

The *Mycobacterium tuberculosis* complex (MTBC) is a group of genetically related pathogens causing tuberculosis in humans and animals. The members of this complex share about 99% genetic similarity with each other at nucleotide level. They do, however, differ in terms of their host preference, geographic distributions as well as pathogenicity (Clarke *et al.*, 2016). This complex was initially known to comprise of four *Mycobacterium* species, namely *M. tuberculosis* (*sensu strictu*) commonly known to cause infections in both primates and humans; *M. africanum* was reported to infect humans, but was only isolated in Africa; *M. microti*, which was less frequently isolated and is the main causative agent of tuberculosis in voles, but was identified in immunocompromised individuals in 1998; and lastly, *M. bovis* which is known to infect cattle. However, *M. bovis* has since adapted and can cause disease in other animals, as well as humans (Cousins *et al.*, 2003).

Two more strains, namely *M. canettii* and *M. caprae* were identified. *Mycobacterium canettii* was first isolated from a Somali born patient and was later isolated from a Swiss patient reported to have been exposed in Africa; and *M. caprae* was a strain predominantly isolated from Spanish goats (Cousins *et al.*, 2003). Other species have been added to MTBC, which now comprises of 11 species. These added species are *M. pinnipedii*, *M. mungi,* the dassie bacillus*, M. orygis*, *M. suricattae* as well as the Chimpanzee bacillus which are all reported to cause TB in a range of animals (Van Ingen *et al.*, 2012a; Thapa *et al.*, 2017).

There is scientific evidence which indicates that all MTBC species share commonality in origin. Nonetheless, the diverse ecological, biological and clinical characteristics suggest that MTBC follows different evolutionary paths; this is supported by phylogenetic studies which bring forth developmental progression information (BañUls *et al.*, 2015). These phylogenetic data have shown that there are six major lineages linked to different regions within the globe respectively. *Mycobacterium tuberculosis* Lineage 1 was linked from the Philippines to East Africa, within the Indian Ocean region; lineage 2 to East Asia; lineage 3 to both Central Asia and East Africa; lineage 4 to Africa, America and Ethiopia; lineage 5 was linked to West Africa 1; whereas lineage 6 was linked to West Africa 2 (BañUls *et al*., 2015), as presented in **Figure 1.1** below which is a global phylogeny representation of the six human-adapted MTBC isolates (Gagneux, 2012).
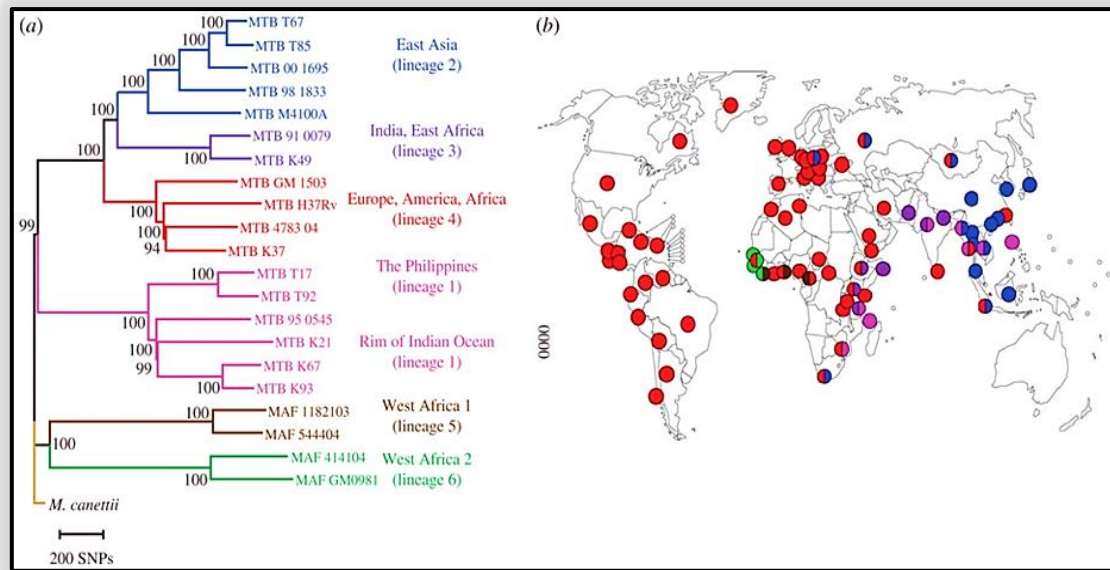
Figure 1.1(a) Global phylogeography representation of MTBC based on 22 whole-genome sequences and the corresponding colour dots in **Figure 1.1 (b)** which indicate the global epidemiological abundance and geographic location (Gagneux, 2012).

Lineages 5 and 6, generally referred to as *M. africanum,* are considered to be the most basal strains occuring exclusively in West Africa, thus suggestive of them giving rise to later strains (Gagneux, 2012). However, recent genome-based research by Orgeur and Brosch (2018) suggests that MTBC most probably emerged from a single clonal group in a pool of recombinogenic mycobacterial strains that bear a resemblance to the rare *M. canettii* strains which were isolated primarily from patients connected to the geographic region around the Horn of Africa.

If one was to accept the assumption made by Gagneux (2012), namely that the evolutionary scenario for the origin and global spread of human TB being the "Out-of-Africa migrations", then a more pressing question would be, "why then did *M. africanum* lineages remain in West Africa despite centuries of cross-Atlantic slave trade and modern human migration Out-of-Africa-Back-to-Africa"? In addition to that, Africa seems to be the only region on the globe to habour all six human-adpated MTBC lineages (Gagneux, 2012). This list now includes the most recently discovered lineage 7 linked to Ethiopia (BañUls *et al*., 2015) as shown in Figure 1.2 below. Lineages 1, 2, 3, 4, 5 and 6 are presented in Figure 1.1 above whereas lineage 7 is presented in Figure 1.2 below, which is a representation of genome-wide MTB complex and a representation of the above mentioned animal strains, with those in the

green ellipse being a representation of the 'modern' lineages, while all the others are termed 'ancestral' lineages. This figure represents two other individualised lineages of *M. africanum* (lineages 5 and 6) and the ancestral position of *M. canettii* (BañUls *et al*., 2015).
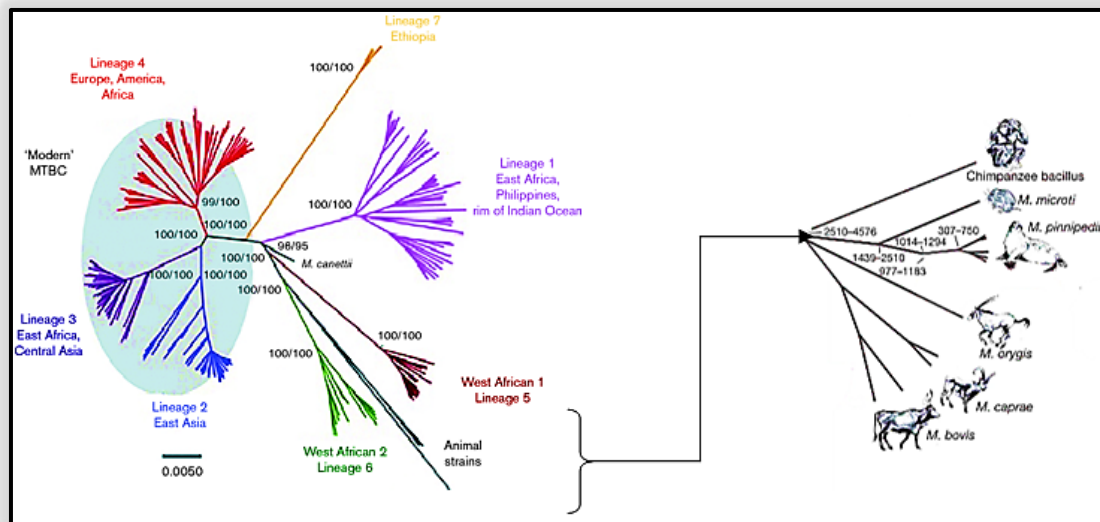
Figure 1.2. Phylogeny of MTB complex based on genome-wide studies (BañUls *et al.,* 2015) and the expansion of animal strain diversity (Bos *et al*., 2014).

1.2.2. Tuberculosis statistical data

Tuberculosis is an infectious disease caused by bacterial species belonging to the MTBC. Ranking above human immunodeficiency virus (HIV) and acquired immunodeficiency syndrome (AIDS), tuberculosis was the world's ninth leading cause of death (WHO, 2017). After the COVID-19 pandemic, TB is still a global cause for concern, causing high rates of morbidity and mortality in most parts of the world, with South-East Asia (45%), Africa (25%) as well as Western Pacific regions (17%) being the highest contributors of reported TB incidence (WHO, 2021b). According to the WHO Global Tuberculosis Report (2021b), 10 million people developed active TB globally in 2019 as compared to the nine million recorded in 2013 (WHO, 2012). The rate of incident cases seems to have remained constant between 2015 and 2016 with a staggering 10.4 million recorded TB infections worldwide (WHO, 2016; WHO, 2017). These statistics show a global increase in the recorded TB incidence, as well as TB-related mortality between 2013 and 2016. However, the statistical data are not in agreement with the conclusions formally made in the WHO (2017) report, which stated that global TB mortality rates have declined by an estimated 3% per annum and that the incidence rate has fallen by about 2% per annum.

Recent reports on mortality due to TB among HIV-negative people is stated to be approximately 1.2 million (WHO, 2021a) showing that there has not been much improvement in meeting TB eradication targets. Statistics also show that there were 374 000 deaths among those living with HIV in 2017 (WHO, 2017) and a notable decrease in deaths attributed to TB-HIV syndemic of approximately 208 000 recorded deaths in 2019 (WHO, 2021a). Nonetheless, reports do state that these statistics needed to have improved by at least 4-5% per annum if the 2020 milestone of 35% reduction in TB set by the World Health Organization's "End TB Strategy" (WHO, 2018) was to be met. This clearly did not happen by 2020; consequently, the deadline was moved from 2020 to 2030 by the leadership of the United Nations (WHO, 2021a; Zhang *et al.*, 2023). This has resulted in the conclusion drawn in the 2021c WHO report, stating that "despite some success stories in other countries where less than one age standardised mortality rate and less than ten deaths per 100,000 populations have been observed (Zhang *et al*., 2023), the global TB targets are mostly off-track requiring some noteworthy improvements if the targets are to be met".

The South African statistics revealed that tuberculosis was responsible for over 33 000 morbidity cases in 2015 (ANA Reporter, 2017). However, recent reports show a major increase in the incidence of TB within the country, with the WHO estimation of the incidence standing at 360 000 cases of active TB in South Africa for 2019, which can be unpacked to 615 per 100 000 population. Of those, an estimated 58 000 people died as a result of contracting multidrug-resistant TB (MDR-TB) or rifampicin-resistant TB (RR-TB (Kanabus, 2021). Taking these statistics into account, it is unclear why WHO (2021a) classified South Africa as part of the 2019 TB eradication success stories at country level among other high TB burden countries such as Ethiopia, Kenya, Myanmar and Namibia. It is nonetheless safe to state that South Africa is far from being on the other side of this scourge as it still makes up one of the top 30 countries in the WHO's global list of high-burden countries for TB, MDR-TB and HIV-associated TB infections (WHO, 2021a).

Such statistics are rather unexpected in this era as some deaths caused by TB are preventable through efficient treatment. In addressing this matter, a 2012 – 2016 Southern African National TB Strategic Plan was developed (TBFacts.org, 2010) and launched on 01 December 2011 (UNAIDS, 2011). This strategy has been amended over time and continues to be adapted with the aim to reduce the number of new TB infections and deaths. This was

to be achieved by implementing measures such as rapid testing and initiation of treatment, whilst reducing the stigma related to TB and eliminating any preventable TB-related deaths (Churchyard *et al*., 2014). The mandate remains the same as the South African Government is still using its 2016 National Strategic Plan in addressing TB, HIV and STIs for 2017-2023 (National Department of Health, South Africa, 2016).

1.2.3. Pathogenesis

Mycobacterium tuberculosis is an obligate aerobe bacillus, which is commonly contracted mainly by inhalation of airborne MTB (Guirado *et al.*, 2013). However, TB can be contracted through other unconventional ways that include accidental injection of the skin by syringe prick or scratching of a broken spittoon glass mostly during sample examination or post-mortem examination of men or animals. The infection remains mainly localised and in some cases is cured. As a result, pathogenesis in this instance will be limited to TB disease progressing by inhalation. Once inhaled, MTB travels to the lungs where it settles in the aerated areas of the upper lobes of the lungs. The bacteria mainly invade phagocytic cells called macrophages found in the lungs where its active replication takes place and causes cell death (Guirado *et al.*, 2013). However, it is an intracellular pathogen well adapted to the human immune defence system and can sustain its viability with ease within the host (Madacki *et al.*, 2019). The success of the pathogen's survival within the host is attributed to the pathogen's armaments attained throughout decades of delicate interaction with the host's immune system (Brosch, 2018).

There are two different types of clinical manifestation of TB, namely, the pulmonary TB (PTB), commonly seen in MTB cases, and extrapulmonary TB (EPTB) seen in up to one-third of MTB cases as well as in TB cases (Lee, 2015; WHO, FAO & WOAH, 2017). Pulmonary TB is the most commonly diagnosed TB, whereas EPTB on the other hand is TB that has spread beyond the lungs, involving organs other than the lungs (e.g., joints and bones, skin, abdomen, genitourinary tract, pleura, lymph nodes or meninges) and is less reported unless diagnosed correctly (Lee, 2015; WHO, FAO & WOAH, 2017).

Mycobacterium tuberculosis is reported to gain entry into macrophages and survive in phagosomes by entering a receptor-mediated pathway which involves the integrin family CR1 and CR3 complement receptors as well as the mannose receptors (Figure 1.3).

Mycobacterium tuberculosis resides within the host phagosomes where it modifies the maturation of the phagosomal compartment to enhance its intracellular survival. As a result, the aberrant expression of rabaptin-5 (Rab5) found on the surface of the phagosome containing MTB causes maturation arrest of these infected cells at the early endosomal stage, thus ultimately inhibiting phagolysosomal fusion (Meena & Rajni, 2010).

It has long been speculated that MTB infections result in different cytokine secretion responses or different downstream activation leading to the different survival mechanisms as shown in Figure 1.3. In an attempt to gain an understanding of those downstream survival tactics, Vergne, Gilleron and Nigou (2015) tried to further unpack the complicated processes in which MTB manipulates the endocytic pathway as well as the phagocyte functions and its responses. *Mycobacterium tuberculosis* has multifunctional virulence; however, its major reliance is on its ability to infest and manipulate the phagocytic cells in the lungs. In summary, mannose-capped lipoarabinomannan (ManLAM) which is a macro amphiphilic lipoglycan found at the surface of the MTB cell envelope plays a key role in phagocyte function manipulation. This in turn reproduces other noticeable properties of MTB in phagocytic cells which include the inhibition of pro-inflammatory cytokine production, inhibition of phagosome maturation, inhibition of macrophage apoptosis, and the inhibition of autophagy (Vergne *et al*., 2015).
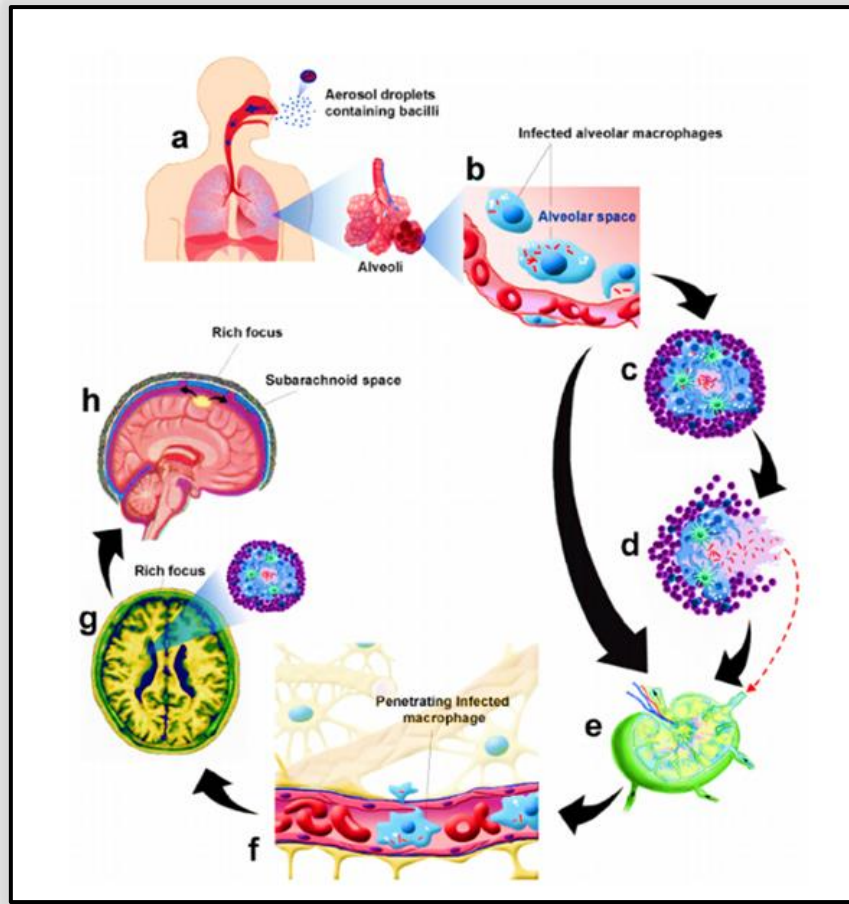
Figure 1.3. Pathogenesis of MTB and postulation of the formation of "Rich foci": (a) Transmission of MTB aerosol; (b) phagocytosis of MTB by alveolar macrophages; (c) granuloma formation in the lung; (d) escape of MTB from the granuloma; (e) filtering of MTB into a regional lymph node from a "leaked granuloma"; (f) MTB accessing the CNS during blood circulation; and (g) bacilli seed to the meninges or the brain parenchyma (Faksri *et al.,* 2012).

1.2.4. Diagnosis

Rapid and accurate diagnosis of TB is vital in TB control. However, the unfortunate overstretched clinical and laboratory services mainly in large sub-Saharan cities pose a challenge for both clinical staff and patients to adhere to correct diagnostic procedures (Van Cleeff *et al.*, 2005). It is important to note that diagnostic procedures for TB-like respiratory infections caused by NTM are very different, complicated and challenging as compared to those for TB caused by the MTB complex (Ryu *et al.*, 2016) and these are detailed in Chapter 3 to follow. For the reason that the majority of countries only carry out diagnosis for TB under the assumption that it is only caused by MTB complex organisms, this section focuses on those general diagnostic procedures conducted for the diagnosis of TB.

1.2.4.1. Stained smears and culture isolation

In humans, sputum specimens are often collected for routine microscopic analysis and detection of the TB bacilli using the Ziehl-Neelsen (ZN) method for smear microscopy which is by far the cheapest and easiest method (Van Cleeff *et al.*, 2005). Although widely used, the ZN smear examination method has proven to be less sensitive (30-60%) compared to the culture-based method (Schmid *et al.*, 2014). The sensitivity proportion can however be increased to 60-78% by the use of fluorescence microscopy (FM) (Van Cleeff *et al.*, 2005) where smears are stained with the auramine O (AO) fluorescent acid-fast stain (Small *et al.*, 1993). Therefore, a combination of both the ZN and the AO method can increase sensitivity and efficiency during screening and testing (Laifangbam *et al.*, 2009). After microscopic examination, acid-fast bacillus (AFB)-positive specimens are inoculated onto Löwenstein-Jensen slant medium and incubated at 37 °C with 5 to 10% carbon dioxide (CO_2) for at least six weeks (Small *et al.*, 1993).

The use of liquid culture media in TB screening has become somewhat of a gold standard technique employed by many clinical laboratories due to its shortened turnaround time and improved sensitivity in detecting mycobacteria. These include the radiometric BACTEC 460Tb system (Becton Dickinson Microbiology Systems, Sparks, MD, USA), The BACTEC MGIT 960 system (Becton Dickinson, Heidelberg, Germany) as well as the Septi-Check AFB system (Becton Dickinson). The BACTEC MGIT 960 system is the most common and preferred of them all due to its fully automated, nonradiometric and non-invasive features (Sun *et al.*, 2009). Even so, the radiometric BACTEC 460 instrument was found to be more sensitive than the BACTEC MGIT 960 (Tortoli *et al.*, 1999).

1.2.4.2. Biopsy, body fluid examination and CT scan of the chest

Tissue biopsy samples, body fluid examination, and computed tomography (CT) scans of the chest are classified as TB infection suggestive tests, which means that they cannot be used to confirm TB infections alone but can support positive results by providing visualised supportive data of disease progression. Due to the low sensitivity of the AFB smear test and the extended duration for MTB culture growth, a diagnosis of EPTB usually depends on histological evidence. Histopathological diagnosis of EPTB is confirmed by the identification

of the presence of granulomas, classification and demonstration of AFB. More often than not, tissue biopsy yields positive culture results compared to fluid aspiration. However, the selection of the diagnostic procedure depends on the organ involved in EPTB. Other methods of interest such as needle biopsy, excision and endoscopy among others have been employed to ascertain the diagnosis (Lee, 2015).

Body fluid retrieval is invasive and is sometimes inaccessible, such as pleural peritoneal and pericardial fluids (Lee, 2015). During EPTB infection, inflammation causes blood cells to seep into spaces within the body, thus changing the colour of the fluid which can appear yellowish. Examination of the cerebrospinal fluid (CSF) of infected individuals presents with leucocytosis (10 x 10^3 to 1 000 x 10^3 cells/mL; with lymphocytes being the highest in percentage), raised protein (0.5 - 3.0 g/L), and CSF plasma glucose of <50%. Adenosine deaminase (ADA) activity is often measured and is a highly preferred biomarker when body fluid is used for EPTB diagnosis (Lee, 2015). A typical X-ray scan is not very detailed, and it can be difficult to make a positive diagnosis from a routine X-ray scan (Vorster *et al*., 2015). A computed tomography (CT) scan or computed axial tomography (CAT) scan captures numerous pictures to build a detailed chest profile which can then be used in support to other tests to confirm infection (Hughes & Osman, 2014). Computed tomography (CT) scanning is useful in the assessment of all three phases of TB empyema, being: 1) the exudative phase which mainly shows the uncomplicated initial effusion; 2) the fibrinopurulent phase which shows the thickened visceral as well as the split pleura; and 3) the organising phase where loculated pleural fluid collects with thickened pleural peel and calcification of extrapleural fat (Vorster *et al.*, 2015).

1.2.4.3. Nucleic acid amplification test

The nucleic acid amplification test, also commonly known as the polymerase chain reaction (PCR) test is a technique frequently employed in molecular biology. It is a powerful tool, but availability and accessibility are limited to the most financially fortunate due to the costs involved. Even so, it is of great use as it offers the benefit of rapid diagnosis that allows early detection. Early detection is of major importance for the successful treatment of life-threatening diseases such as TB meningitis. It is also a very effective technique to employ due to its increased sensitivity as it can detect as few as 10 mycobacteria, rendering it ideal for the diagnosis of paucibacillary diseases such as EPTB (Lee, 2015). This technique

identifies MTB with isoniazid and rifampicin resistance associated with specific mutations in the *rpoB* gene through an automated real-time (RT)-PCR technique (Hughes & Osman, 2014).

1.2.4.4. Immunological test

The tuberculin skin test (TST) and interferon-gamma (IFN-γ) releasing assay (IGRA) are employed as supportive tests. The tuberculin skin test is, however, not reliable in the diagnosis of active TB as the interpretation can easily be complicated by cross-reactivity with previous bacillus Calmette-Guérin (BCG) vaccination or latent TB infections. The tuberculin skin test can also be influenced by several other factors such as HIV infections, recent viral or bacterial infections as well as vaccination with live virus, which can reduce the test's sensitivity. Similar to TST, IGRA is unable to distinguish between latent infection and active pulmonary TB or EPTB. A negative result can lead to infections being overlooked in the patient. The aforementioned methods are not highly recommended in countries where TB is prevalent (Lee, 2015).

1.2.5. Vaccination

The bacillus Calmette-Guérin (BCG) vaccine is an attenuated strain of *M. bovis* (cattle isolate). The vaccine is not 100% efficacious; however, it has been the most commonly used TB vaccine worldwide in the quest to prevent human-related TB infections. An effective vaccine is one which is required to protect infants and anyone at risk under the age of 16 years (Loxton *et al*., 2017) and (TBFacts.org, 2010). The vaccine is relatively inexpensive, safe to use and readily available, thus estimated to being administered to approximately 80% of all newborn children and infants in countries where it is part of the national childhood immunisation programme (TBFacts.org, 2010).

In South Africa, the BCG vaccine manufactured by the Serum Institute of India (BCG Danish SSI) is administered at birth as a single intradermal injection. The efficacy of this vaccine against TB meningitis was reported to range between 64 and 86%. However, severe cases of TB meningitis among vaccinated children have been observed where 75% of those who recovered showed neurological impairment (Loxton *et al*., 2017). Just like MTB, the BCG vaccine strain is phagocytosed by the host's macrophages where it is retained in the phagosomes. Mycobacterial antigens enter the major histocompatibility complex class II

(MHC-II) pathway preferentially prompting CD4^{+} T-cell response which is important in disease control. It is thought that the restricted MHC-I CD8^{+} T cells also play an important role in the immune response to MTB infection. However, these cells are further only weakly induced by BCG (Loxton *et al*., 2017).

The recombinant BCG (rBCG) vaccine VPM1002 was developed to elicit MHC-I related immune response, thus rendering it an effective yet safer option than the conventional BCG vaccine (Loxton *et al*., 2017). In VPM1002, the urease C encoding gene (*ureC*) is replaced by the *hly* gene encoding listeriolysin O (LLO) from *Listeria monocytogenes*. Listeriolysin then agitates the phagosome, in so doing antigen translocation is enabled in the cytoplasm authorising efficient presentation to CD8^{+} T-cells. The VPM1002 vaccine candidate has been shown to have further benefits such as expanding CD4^{+} central memory T cells, increasing T helper 1 (TH1) and TH17 cells at a more significant level than the conventional BCG vaccine, as well as effectively inducing the production of CD8 (Loxton *et al*., 2017).

1.3. Nontuberculous mycobacteria

Other notable infections of late are caused by nontuberculous mycobacteria (NTM). These represent over 150 species of mycobacteria other than tuberculosis (MOTT) (Varghese *et al*., 2013). Nontuberculous mycobacteria are typically non-motile aerobic organisms with a thick firm cell wall (Alqurashi *et al*., 2019). In recent years, several species within this group have been isolated from clinical cases. Some of those noteworthy NTM causing pulmonary and/or extrapulmonary infections and their respective total number of isolates were reported by Al-Ghafli and Al-Hajoj (2017) as follows: *M. avium* complex (79), *M. fortuitum* (90), *M. abscessus* (55) and *M. kansasii* (14), among others.

Up until recently, *M. smegmatis* was not known to cause infections in humans. However, reposts by Varghese *et al*. (2013) suggest that *M. smegmatis* was identified in five clinical specimens collected from Saudi Arabian humans suffering from pulmonary infections (Al-Ghafli & Al-Hajoj, 2017). With most, if not all, of the above mentioned NTM capable of causing either pulmonary and/or extrapulmonary infections in humans, does the term "nontuberculous mycobacteria" still apply? The increase of such infections is worrisome, especially given that these organisms are found to flourish in natural human habitats and artificially built systems such as shower systems as well as medical devices (Al-Ghafli & Al-

Hajoj, 2017). Most importantly, the manifestation of diseases caused by NTM results in a significant medical burden in humans, often observed amongst the aged and frail (Donohue, 2018).

1.3.1. Is the problem *Mycobacterium tuberculosis* or nontuberculous mycobacteria

In light of the journey humans have had to travel in company of the antagonistic MTB over the past decades, reports of pulmonary and extrapulmonary diseases associated with NTM are of paramount concern. In the literature, the number of NTM species is catalogued to range between 125 and 150 to over 175 (Narasimham *et al*., 2013; Ratnatunga *et al*., 2020; Varghese *et al.*, 2013), with 42 being interconnected with disease in humans (Narasimham *et al*., 2013). The world has seen an increase in the prevalence of NTM infections in recent years accounting for incidence cases ranging from 2.4 cases/100 000 in the early 1980s to about 15.2 cases/100 000 population in 2013 in the United States of America (USA) alone. In general, the prevalence was also found to be slightly higher in the elderly and in women *et al* (Saboe, Sari & Febrianora, 2020).

Isolation of NTM is proving to be more common than *M. tuberculosis* in Canada and the USA. This is a phenomenon not only limited to the aforementioned countries, but the trend has also been observed in other countries around the globe such as the United Kingdom, Saudi Arabia, Germany, Denmark, South Korea, Europe, Brazil, Taiwan and the Middle East (Ratnatunga *et al*., 2020). It is unfortunate that NTM prevalence is not notifiable in the majority of countries with the lowest developmental indices. This has resulted in limited and inaccurate epidemiological data. Based on the reported data, it is evident that the most common NTM pathogens responsible for causing diseases belong to the *Mycobacterium avium* complex, even though the prevalence differs in terms of gender, age and geographic region (Ratnatunga *et al*., 2020).

1.4. Treatment and control

The aims of TB treatment are to cure infected patients, decrease transmission of TB, prevent the development of acquired drug resistance, prevent relapse, and to prevent TB related mortality (TBFacts.org, 2010). However, as urgent as finding efficacious treatment is, the emergence of MTB drug-resistant strains has played a major role in hindering and delaying TB disease control (Janin, 2007). Rifampicin, isoniazid, pyrazinamide and ethambutol are

commonly used to treat TB as first-line drugs, given for administration over a 6-month period while sensitivity is being monitored (Janin, 2007). During the first two months of treatment, patients are given isoniazid, rifampicin, pyrazinamide and ethambutol to administer for seven days a week as a fixed dose combination. At the end of the second month, the patient is then put on isoniazid and rifampicin in fixed dose combinations given for seven days a week over a period of four months. If found to have a positive TB smear with no clinical improvement, then that is classified as drug-resistant tuberculosis (Blumberg *et al.*, 2003).

1.4.1. Resistance

There has been a strong emergence of drug-resistant MTB strains in the past few decades. These were classified as either multidrug-resistant or extensively drug-resistant TB. However, incurable TB (i.e., totally drug-resistant (TDR)–TB) is becoming regularly referenced due to the increased observation of patients presenting with TB strains that do not respond to either MDR-TB or XDR-TB treatment. Tuberculosis strains classified as MDR-TB are those resistant to the two most potent first-line anti-tuberculosis drugs, namely isoniazid and rifampicin. The strains classified as XDR-TB are resistant to either isoniazid or rifampicin as well as any of the fluoroquinolones and at least one of three second-line anti-tuberculosis injectable drugs such as capreomycin, kanamycin and amikacin (Caminero *et al.*, 2010). Totally drug-resistant TB strains have been emerging at a fast rate rendering the strains virtually incurable as there are strains resistant to all first-line and all second-line drugs (Jang *et al.*, 2017). The literature has shown that isolates mainly from India and Iran have been reported; however, it is clear that this is a problem soon to be faced by all countries confronted with the TB pandemic (Jang *et al.*, 2017). Most healthcare providers tend to TB without carrying out drug susceptibility tests, which then results in the administration of wrong and inadequate treatment, thus resulting in further development of resistance to several other anti-TB drugs (WHO, FAO & WOAH, *et al.,* 2017).

1.5. Problem statement

It is estimated that approximately a third of the world's population has latent TB (Zhang *et al.*, 2011). Tuberculosis is among the biggest contributors of disease-related mortality in the world and a leading associated killer of HIV-positive people accounting for about 35% of deaths worldwide (WHO, 2018). Despite the success of the drug combination treatment for *M. tuberculosis* in the world's most developed countries, Africa is unfortunately experiencing

a continued scourge of this disease in its most disadvantaged communities (Zhang *et al.*, 2011). In South Africa, TB remains a daunting challenge flagged high as a leading cause of disease-related mortality, being second to COVID-19 after 2020 (WHO, 2021a; Yogan Pillay, 2017), where nearly one in every 615 per 100 000 population is infected with TB (Kanabus, 2021). These statistics are alarming as they are three times higher than the rest of Africa and six times higher than any other country in the world (Yogan Pillay, 2017). Even though the WHO (2021a) report flags improvement in South African statistics, their statistical data show an increase in TB incidences attributed to factors such as high influx of foreign nationals, thus placing a huge demand on the public health system and its capacity in delivering appropriate health services to the population. Lack of reporting by infected and affected individuals, as well as incorrect diagnosis are among the factors contributing to the increase in the incidence of TB.

Indeed, tuberculosis continues to be a constant source of human suffering, showing a failure on multiple levels in the prevention and treatment of this disease. This failure is epitomised by the emergence of more virulent and drug-resistant TB strains that have been on the rise over many years, during which the bacterium has developed mechanisms to resist the effectiveness of currently used drugs (Kana *et al.*, 2014). Resistance usually occurs as a result of incorrect prescription by the medical practitioner, medication being administered for a period that is too short to be effective, overuse of antibiotics, as well as patient noncompliance, amongst other reasons (CDC, 2016). Additionally, there is rather a poor understanding of host-pathogen interaction that has resulted in the lack of target identification for host-adjunctive therapy as well as misdiagnosis, thus resulting in wrong treatment (Kana *et al.*, 2014).

Worldwide statistics of tuberculosis cases showed that Asia and Africa accounted for the highest number of new TB infection cases recorded for the year 2015, with Asia displaying a staggering 61% and Africa presenting with 26% of new cases. South Africa and Nigeria are reported to be amongst four other non-African countries contributing to 60% of new TB cases yearly (WHO, 2018). Current statistics show that Southeast Asia and Africa are still the leading contributors to the incidence of TB, as reported by Kock *et al* (2021), while 2015 statistics of global cases of new multidrug-resistant TB (MDR-TB) infections was revealed to be around 480 000. A fairly impressive reduction of about 19% was recorded for several

Southern Africa countries, with South Africa being a success story among those (WHO, 2021a).

Non-compliance is the primary cause of the emergence of drug resistance in South African patients. This non-compliance is usually attributed to socio-economic status that results in patients not being able to afford treatment or are unable to access treatment. This has a direct impact and contributes to the sluggish improvement in TB treatment. Socio-economic factors such as unemployment and overcrowding are the main contributing factors to the slow decline in TB infections. Other leading contributing factors include poor management and failure to retain TB patients on the multidrug treatment regimen for prolonged periods. Amongst other reasons, rapid influx of migrants, late detection, staff shortage and long waiting periods for treatment are also of major concern. Therefore, new drugs designed to be effective within a shorter period and with a higher potency against MDR-TB and XDR-TB strains with the added benefit of ease of administration are urgently required.

It is also important to recognise that nontuberculous mycobacteria are widespread in the human environment and thus readily available. This means that NTM infections in humans could be overlooked and misdiagnosed as active TB. Nontuberculous mycobacteria are not susceptible to TB treatment, yet are capable of causing similar clinical diseases, i.e., pulmonary TB and extrapulmonary TB. Thus, based on the statistics outlined in Chapter 3 to follow, there is a high possibility that the circulating MDR-TB and XDR-TB strains are in fact NTM strains. This too highlights the importance of finding new drugs that could be active against drug-resistant strains, whether it be those belonging to the MTBC or NTM group of mycobacteria.

Many studies have shown that many more NTM are responsible for pulmonary infections in humans (Al-Ghafli & Al-Hajoj, 2017; Hu *et al.*, 2019; Lee *et al.*, 2011). It is therefore important that appropriate steps are taken to identify species responsible for causing infections in humans. The challenge is that most countries do not take further steps to identify NTM as these infections are generally not communicable in nature due to the fact that their infections are not contagious (Donohue, 2018). However, due to the aforementioned challenges, even if not the reported; NTM should still be screened during diagnosis in suspected tuberculosis cases. This poses the question "does our health system acknowledge this burden and the rise in such NTM infections"? Are further steps taken to investigate NTM

infections or are they oblivious to the idea that it is not only MTB that is responsible for such pulmonary infections in humans? It cannot be that South Africa and Africa as a whole is immune to this phenomenon. Could it be that some if not most patients diagnosed with MDR, XDR and totally drug-resistant TB are actually infected with NTM (Hu *et al.*, 2019)? Such questions and all of the above-mentioned challenges highlight and support the importance of this study.

1.6. Aim and objectives

The overall aim of the study was to design isoniazid crystal and co-crystal derivatives and to assess their antimycobacterial activity and synergistic capabilities against mycobacteria species of choice.

The abovementioned aim was achieved through the following specific objectives:
- To design novel isoniazid derivatives.
- To co-crystallise isoniazid derivatives with a salicylic acid in order to enhance drug performance.
- To confirm and/or elucidate the crystal structures of the derivatives using single-crystal X-Ray diffraction (XRD) methods.
- To conduct antimycobacterial susceptibility tests of isoniazid derivatives and co-crystals.
- To determine the biological impact of the isoniazid derivatives on murine macrophage cells through cytotoxicity, real-time cell analysis and flow cytometry analysis.
- To determine the mode of action and confirm targets of isoniazid derivatives by employing computer-based drug docking (*in silico*) experiments.

1.7. Hypothesis

Modifying the NH_2 group of the hydrazide moiety of INH may yield derivatives presenting with an enhanced antimycobacterial inhibitory activity especially when tested in synergy.

1.8. Ethical consideration

Ethical clearance to conduct this study was granted by the University of South Africa's College of Agriculture and Environmental Science ethics committee – ethics reference number 2018/CAES/160.

1.9. Funding

CHAPTER 2

The design and synthesis of isonicotinic acid hydrazide derivatives

2.1.   Isonicotinic acid hydrazide [isoniazid]

Isonicotinic acid hydrazide, commonly known as "isoniazid" (4-pyridinecarboxylic acid hydrazide; isonicotinic hydrazide (INH)) [accession number: DB00951 (APRD01055, EXPT01940)] (Scholar, 2007), is an antibacterial drug available as 100 mg – 300 mg tablets meant only for oral administration. It has been used as front-line chemotherapeutic treatment for tuberculosis, progressing from the introduction of streptomycin in 1946, to the combination of streptomycin, para-aminosalicylic acid (PAS) and isoniazid (INH), which was embraced by the western world in 1995 (Janin, 2007). This drug is used in the treatment of pulmonary and extrapulmonary TB infections caused specifically by *M. tuberculosis*, *M. bovis* and *M. kansasii* (Isoniazid, 2008; Mahmoud *et al*., 2017). However, administration of this wonder drug is associated with peripheral neuropathy and hepatotoxicity. To ensure that a patient does not experience such adverse side effects of neurotoxicity, INH is customarily co-administered with pyridoxine (vitamin B6) (Scholar, 2007).
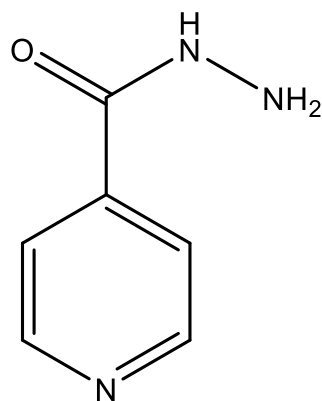
Figure 2.1. Chemical structure of isoniazid - ACD/ChemSketch freeware (PubChem, 2018).

Isoniazid has a simple chemical structure as shown in Figure 2.1 above, featuring a pyridine ring and a hydrazine group attached at the *para* position to the pyridine nitrogen. It is manufactured through a 7 h synthesis reaction under reflux as shown in Scheme 2.1 below, being a representative of a chemical reaction between hydrazine hydrate and the 4-cyanopyridine in an aqueous alkaline solvent-system at 100 °C. The subsequent crystallisation is accomplished in ethanol with a compound yield of roughly 62% (Fernandes

et al., 2017). The white or colourless crystalline powder has the molecular formula $C_6H_7N_3O$, a molecular weight of 137.14 g/mol, a melting point of 171.4 °C, and a polarity, LogP of - 0.64 (Fernandes *et al*., 2017).
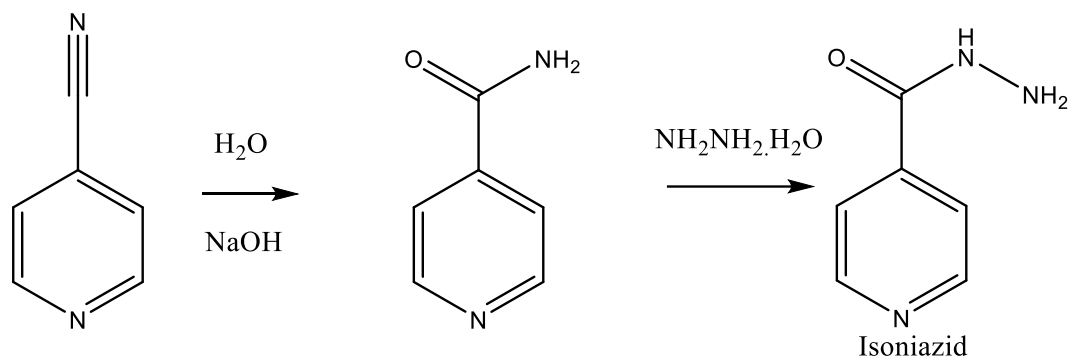
Scheme 2.1. Diagram depicting the synthesis of isoniazid – ACD/ChemSketch freeware (Fernandes *et al*., 2017).

2.2. Structure, design, and modification

For years, mycobacterial infections have been managed with drugs ranging from natural products (such as *Coleus scutellarioides* leaf extracts, Bergenin secondary metabolites, immunomodulators like allicin, piperine, curcumin among others as well as phytocompounds such as flavonoids, terpenoids and alkaloids) that possess antimicrobial properties (Gautam *et al*., 2023); to semi-synthetic derivatives that have been modified time and again. However, over time these strategies have failed due to the emergence of resistant mycobacteria, thus creating a vicious cycle of the continuous, yet necessary, optimisation and identification of novel antimycobacterial classes (Cully, 2014). These investigations in turn resulted in the increased knowledge around structural based antimicrobial activity that creates a movement channelled towards innovative re-evaluation of known antimicrobials that might have been overlooked due to their reduced potency (Cully, 2014).

With that in mind, novel anti-TB drugs can be developed using several approaches. One of those approaches which has attracted the interest of the pharmaceutical industry is known as the covalent modification of active pharmaceutical ingredients (APIs), which is the synthesis of new analogues or modification of old drugs/existing compounds. The aim of this approach is to produce a drug whose mode of action is known and understood, with enhanced activity that will allow the decrease of toxicity while yielding results within a shorter period and most importantly be more effective against MDR-TB and XDR-TB (Hu *et al*., 2017). This in

essence cannot be guaranteed for isoniazid in particular, due to its reported complex mechanism of action against mycobacteria. In the quest to overcome the resistance of MTB against INH, a combination of INH and INH-derivatives with different moieties have been explored and are continuous investigation. Modification of the isoniazid NH$_2$ group of the hydrazide moiety is achieved through a condensation reaction between isoniazid and molecules containing ketone or aldehyde functional groups, thus replacing the two H atoms with different functional groups. The reaction involves the nucleophilic attack on the carbonyl group by the amine nitrogen to form an unstable carbinolamine moiety, followed by acid catalysed dehydration. This resulting INH derivative is referred to as "modified isoniazid" (Smith Forbes & Lemmerer, *et al.,* 2015). This kind of modification of this NH$_2$ group within the isoniazid molecule, as depicted in Scheme 2.2 below, has been shown to render the drug more effective against resistant strains of TB (Hearn & Cynamon, 2004; Suarez *et al.*, 2009) by assisting in the evasion of the N-arylaminoacetyl transferases (NATs), enzymes capable of reducing the efficacy of INH in particular by acetylating the NH$_2$ position thus ultimately preventing its reaction with reduced nicotinamide adenine dinucleotide (NADH) (Vishweshwar *et al.*, 2006; Smith *et al.*, 2015).
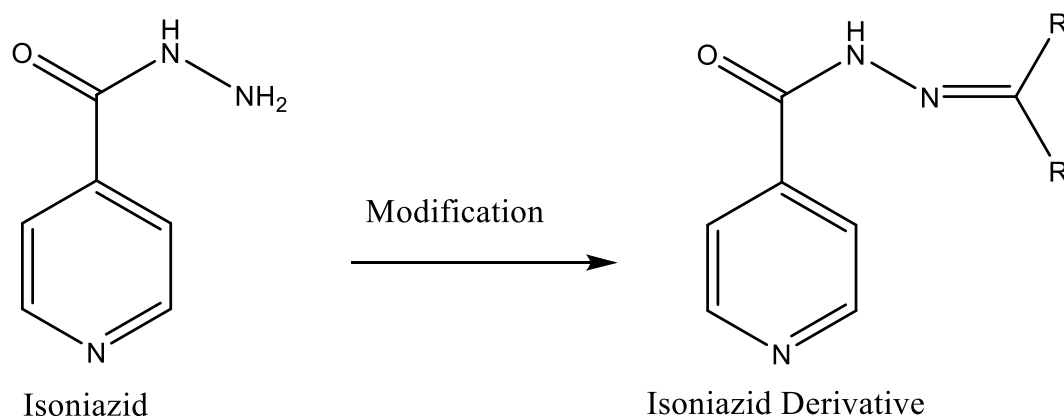
Scheme 2.2. A representation of the covalent modification of isoniazid to form a modified isoniazid derivative (Martins *et al.*, 2014).

2.2.1. Crystal and co-crystal design

Crystal engineering is a rapidly expanding field of research first introduced in 1955 by Pepinsky and later trialled by Schmidt in the framework of organic solid-state photochemical reaction, as reviewed by Vishweshwar *et al*. (2006). Crystal engineering is one aspect within the chemistry field that has drastically evolved into an archetype for the supramolecular synthesis of new composites. Crystals are usually synthesised by the process of slow

evaporation of a solvent. It is desirable to crystallise isoniazid derivatives since this allows the structure to be unambiguously determined using single-crystal XRD diffractometry (Smith, Forbes & Lemmerer, 2015). Crystals are modified forms of APIs to mainly assist against drug resistance; however, in most cases they demonstrate low solubility. In such an instance, it is more suitable to use a multicomponent form such as a co-crystal (applicable for more neutral APIs) or a salt (applicable for ionisable APIs) as these tend to be more soluble than the crystal form of an API (Aitipamula *et al*., 2012).

According to the United States Food and Drug Administration (FDA), co-crystals are defined as crystalline material found in solid form composed of two or more molecules stacked in a lattice pattern within the same crystal (Aitipamula *et al*., 2012). Co-crystallisation is a process used to derive co-crystals where two compounds are linked together by crystal co-formers and can be used as an isolating or a purifying agent of an API. Co-crystals offer endless opportunities to modifying the physical properties of an API without altering its covalent bonds. It is for these reasons that the pharmaceutical industry is extremely attracted to pharmaceutical co-crystallised bioactive compounds (Smith Forbes & Lemmerer, 2015; Vishweshwar *et al.*, 2006). If the co-crystallisation of an API is designed in a way that the entire molecule can be consumed, it must have what is considered to be a "generally regarded as safe (GRAS)" status. It is ideally preferred as in most cases it results in a more soluble compound. However, the API can be discarded at a later stage prior to formulation (Vishweshwar *et al*., 2006).

This chapter focuses on the design and synthesis of both known and novel drug agents which may potentially advance human health by inhibiting the growth of mycobacteria species as well as treating infections caused by those organisms in singular or in combination form.

2.3.   Materials and methods

2.3.1. Synthesis of INH crystal and co-crystal derivatives

The covalent modification and supramolecular synthesis of isoniazid with a ketone and most modifiers occurs via an acid-catalysed condensation reaction. Modification generally happens after exposure to heat and increased pressure under reflux for extended periods of time as INH does not readily react with its modifier under ambient conditions. Crystals of different shapes, sizes and colour may form after exposure to the atmosphere depending on the

concentration and nature of the crystal solution at times ranging between a few minutes to three days or more.

To carry out the above synthetic crystal modification and co-crystallisation, all chemicals used were AR-grade solvents procured from Sigma-Aldrich (South Africa) and no modifications or adjustments were done prior to experimental usage. All solvents used for the purpose of this experiment are listed in Table 2.1 below. In this experiment, very small quantities of solvent were required (roughly 3 mL) making it impractical to set up the reflux apparatus, especially since synthesis of multiple crystals was done simultaneously.

As a result, for INH modification and co-crystallisation to be achieved, a general method for the one-pot synthesis of modified isoniazid crystals and co-crystals was adopted (Smith *et al*., 2015). Equal moles of isoniazid, ketone modifier and co-former were placed into a glass screw-top rubber-sealed dram vial presented in Figure 2.4 (a) below. The solids were then dissolved in respective AR-grade solvents, and thereafter refluxed at a specific temperature in a closed air-tight dram vial for a certain number of hours/days. Note that the vials were only closed after reaching the desired temperature to avoid pressure build-up. For the same reason, it was important to ensure that the vials were not filled to more than the halfway mark to allow for the expansion of the solution and/or vapour. The vials were also covered with a flat bottom round laboratory dish to maintain a constant optimum temperature for the duration of the reflux period as well as a safety measure should the pressure in the vial become too high causing the sealed vial to burst. The vials where then left to stand at room temperature to cool off. The vials were never opened while hot, since the sudden release of pressure would cause the hot liquids to vaporise and shoot out of the vial, causing loss of solvent and potential burns to the experimenter. Once cool, the vials were then opened slightly to allow slow evaporation. In order to yield larger quantities where larger volumes of solvent were used, a 50 mL Schott bottle was used as presented in Figure 2.4 (b) below. Conditions of INH modification for each sample were different and are all detailed in Table 2.1 below.
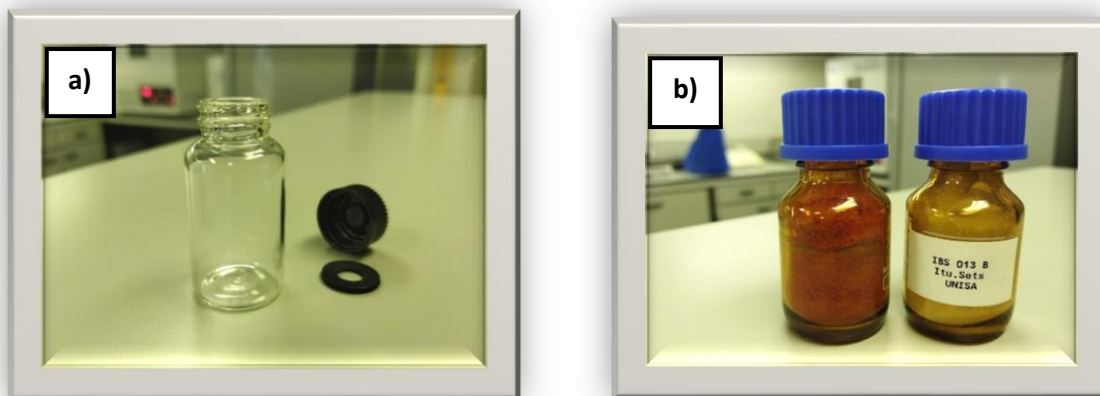
Figure 2.2. (a) The 14 mL glass screw cap rubber lined dram vial excellent for refluxing as the rubber prevents loss of solvent at high temperatures; and **(b)** Schott bottles proved to be as tightly sealed and served the same purpose where larger yields were required (Images captured by the author of this thesis).

The above method was adjusted for the synthesis of sample IBS017 - (E)-N′-(butan-2-ylidene)isonicotinohydrazide 0.5 hydrate $C_{10}H_{13}N_3O \cdot 0.5H_2O$ (Setshedi, Lemmerer & Smith, 2021). Isoniazid modification was achieved by using the Retsch Mixer Mill MM 200 shaker (Verder Scientific, South Africa). A 25 mL stainless steel grinding jar containing 2 x 7 mm stainless steel grinding balls was used. Approximately 1.0 g of INH was weighed out and mixed with 55.0 mL of 2-butanone AR-grade solvent. Once homogeneous, the mixture was transferred into the stainless-steel jar and sealed tightly. The tightly sealed jar was then screwed back onto the mixer mill where it was subsequently shaken for 30 min at 25 Hz. Once reacted, the mixture was transferred into a 50 mL amber Schott bottle, left semi-open to allow slow evaporation at room temperature as described by Setshedi *et al*. (2021). All the reagents used and conditions applied for the synthesis of each INH derivative are documented in Table 2.1 below.

2.3.2. Crystal data and X-ray structure analysis

For each of the crystals presented in the results, many attempts were made to co-crystallise the final product. In order to select crystals for XRD analysis, a light microscope was used to examine the morphology of the crystals. Every sample was examined to determine whether the morphology of the final product was different to that of the starting materials. This presents a useful, quick and cost-effective method for screening where a co-crystal has

formed in comparison to more conventional methods of screening such as running Fourier Transform Infrared Spectroscopy (FTIR).

Crystal data were collected using the Bruker APEX II CCD area detector diffractometer with graphite monochromated Mo-K_a radiation (50 kV, 30 mA) (Bruker SA (Pty) Ltd, Sandton, South Africa). The sample was cooled to 173 K with an Oxford Cryostream 700 (Oxford Cryosystems Ltd, Long Hanborough, UK). The collection method involved ω-scans of width 0.5°. Data were reduced by using the SAINT-Plus software, version 6.02.6, while empirical absorption correction was processed using the SADABS software (SAINT-Plus and SADABS, Bruker AXS Inc., Madison, Wisconsin, USA). Publication material and diagrams were generated using WinGX (Farrugia, 1999) and SHELX (Sheldrick, 2007) and PLATON (Spek, 2009). Hydrogen atoms were geometrically positioned while permitted to ride on their individual parental atoms with d(C—H) = 0.95 Å and Uiso(H) = 1.2 Ueq(C) (Setshedi Lemmerer & Smith, 2021). All asymmetric unit diagrams in this thesis were generated from the XRD data using ORTEP-3 (Farrugia, 1999). Packing diagrams were generated from the XRD data using Mercury software v2022.1.0.

Table 2.1. Reagents and conditions for synthesis of isoniazid crystal derivatives.

Sample number	Mass of INH (MW – 137.1 g/mol)	Mass of modifier	Mass of salicylic acid (MW = 138.1 g/mol)	Catalyst	Solvent	Reflux conditions	Crystallisation	Known /Novel
IBS001	0.23 g (1.68 mmol)	Benzophenone (0.31 g, MW: 182.22 g/mol, 1.70 mmol)	-	- 10% p-toluenesulphonic acid: (0.06 g, MW: 190.22 g/mol)	3 mL – (1:1) 1,2-dichloroethane:1,1,1-trichloroethane	Closed vial, at 110 ℃, for 96 h [4 days]	Slow evaporation at room temperature	Known
IBS002	0.20 g (1.46 mmol)	Benzophenone (0.27 g, MW: 182.2 g/mol, 1.48 mmol)	0.20 g (1.45 mmol)	-	3 mL – methanol	Closed vial, at 110 ℃, for 96 h [4 days]	Slow evaporation at room temperature	Known
IBS003	0.22 g (1.60 mmol)	4-methylbenzophenone	-	10% p-toluenesulphonic acid (0.06 g, MW: 190.22 g/mol)	3 mL – (2:1) Ethanol:Acetonitrile	Closed vial, at 110 ℃, for 96 h [4 days]	Slow evaporation at room temperature	Known

IBS004	0.22 g (1.60 mmol)	4-methylbenzophenone	0.22 g (1.59 mmol)	-	3 mL – methanol	Closed vial, at 90 ℃, for 24 h [1 day]	Slow evaporation at room temperature	Known
IBS005	0.20 g (1.46 mmol)	4,4-dimethylbenzophenone (1.31 g, MW: 210.28 g/mol, 6.67 mmol)	-	1 drop 5M HCL (followed by workup with sodium carbonate to remove the acid later)	3 mL – methanol	Closed vial, at 60 ℃, for 96 h [4 days]	Slow evaporation at room temperature	Novel
IBS006	0.20 g (1.46 mmol)	4,4-dimethylbenzophenone (0.31 g, MW: 210.28 g/mol, 1.47 mmol)	0.20 g (1.45 mmol)	-	3 mL – methanol	Closed vial, at 90 ℃, for 24 h [1 day]	Slow evaporation at room temperature	Known
IBS007	0.21 g (1.53 mmol)	2,2-dihydroxybenzophenone (0.33 g, MW: 214.2 g/mol, 1.51 mmol)	-	4-hydroxybenzoic acid (0.21 g, MW: 138.1 g/mol, 1.52 mmol)	3 mL – methanol	Closed vial, at 90 ℃, for 24 h [1 day]	Slow evaporation at room temperature	Novel
IBS008	0.21 g (1.53 mmol)	2,2-dihydroxybenzophenone (0.33 g, MW: 214.2 g/mol)	021 g (1.52 mmol)	5% nickel nitrate (0.02 g, MW: 290.8 g/mol, 0.069 mmol)	Acetonitrile	Closed vial, at 90 ℃, for 96 h [4 days]	Slow evaporation at room temperature	Known

IBS009	0.22 g (1.60 mmol)	4-aminobenzophenone (0.32 g, MW: 197.2 g/mol, 1.62 mmol)	-	10% p-toluene-sulphonic acid (0.03 g, MW: 190.2 g/mol, 0.16 mmol)	3 mL – methanol	Closed vial, at 110 ℃, for 96 h [4 days]	Slow evaporation at room temperature	Novel
IBS010	0.21 g (1.53 mmol)	4-aminobenzophenone (0.30 g, MW: 197.2 g/mol)	0.21 g	5% nickel nitrate (0.20 g, MW: 290.8 g/mol)	3 mL – methanol	Closed vial, at 60 ℃, for 24 h [1 day]	Slow evaporation at room temperature	Known
IBS011	0.22 g (1.60 mmol)	4(dimethylamino) benzophenone (0.36 g, MW: 225.3 g/mol)	-	10% p-toluenesulphonic acid (0.03 g, MW: 190.2 g/mol)	3 mL – methanol	Closed vial, at 110 ℃, for 96 h [4 days]	Slow evaporation at room temperature	Known
IBS012	0.22 g (1.60 mmol)	4-(dimethylamino) benzophenone (0.36 g, MW: 225.3 g/mol)	0.22g (1.59 mmol)	-	3 mL – methanol	Closed vial, at 90 ℃, for 24 h [1 day]	Slow evaporation at room temperature	Known
IBS013	0.22 g (1.60 mmol)	3 mL of acetone (this sample was modified with acetone)	-	-	-	Closed vial, at 60 ℃, for 24 h [1 day]	Slow evaporation at room temperature	Known
IBS014	0.32 g (2.33 mmol)	3 mL of acetone (this sample was modified	0.23 g (1.66	-	-	Closed vial, at 60 ℃, for	Slow evaporation at	Known

	with acetone)	mmol)				24 h [1 day]	room temperature	
IBS015	0.22 g (1.60 mmol)	3 mL of benzaldehyde (this sample was modified with benzaldehyde)	-	-	-	Closed vial, at 60 °C, for 24 h [1 day]	Slow evaporation at room temperature	Novel
IBS016	0.23 g (1.67 mmol)	-	0.23 g (1.66 mmol)	-	3 mL – benzaldehyde	Closed vial, at 60 °C, for 24 h [1 day]	Slow evaporation at room temperature	Novel
IBS017	0.22 g (1.60 mmol)	3 mL of 2-butanone (this sample was modified with 2-butanone)	-	-	-	Closed vial, at 60 °C, for 24 h [1 day]	Slow evaporation at room temperature	Novel
IBS018	0.22 g (1.60 mmol)	3 mL of 2-butanone (this sample was modified with acetone)	0.22 g (1.59 mmol)	-	-	Closed vial, at 60 °C, for 24 h [1 day]	Slow evaporation at room temperature	Novel
IBS019	1.04 g (7.55 mmol)	3-benzoylpropionic acid (1.36 g, MW: 178.18 g/mol, 7.63 mmol)	-	-	10 mL – methanol	Closed vial, at 25 °C, for 72 h [3 days]	Slow evaporation at room temperature	Novel
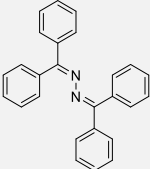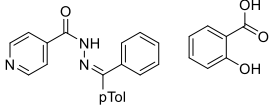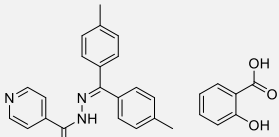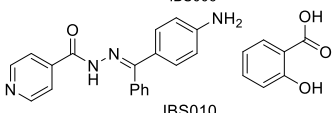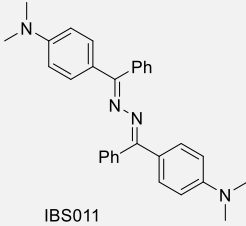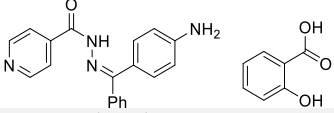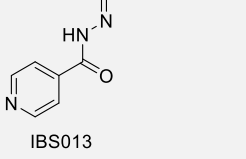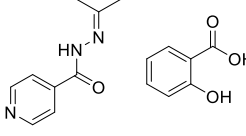
2.4. Results and discussion

In this study, salicylic acid was used as a co-former in the synthesis of INH co-crystal derivatives. Salicylic acid is known to enhance the rectal absorption of various drugs. It is also reported to have anti-inflammatory properties, to act as antacid, and to act as a mild antibiotic (Tamai & Tsuji, 1996). It is for these reasons that this compound was selected to be used as a co-former during the co-crystallisation of isoniazid derivatives as it could hypothetically result in quicker time in which the drug acts due to the increased influx of the drug into the cells as well as enhanced activity in treating side effects and other symptoms caused by treatment regimen and disease progression.

An API crystallisation and co-crystallisation is a process that can yield one-, two- and three-dimensional (1D, 2D and 3D) hydrogen-bonded networks (Smith, Forbes and Lemmerer, 2015). A 1D chain consists of a ribbon in the packing of the molecule where all molecules are connected by a single hydrogen bond. In a 1D tape, the ribbon has two hydrogen bonds joining successive molecules. A 2D pattern represents packing in a plane, whereas a 3D pattern represents a network along all three axes of the crystal (Burrows, 2004). This can be observed in Table 2.1 above, where crystal and co-crystal synthesis of INH derivatives yielded several known and novel crystal and co-crystal compounds.

By means of unit cells obtained using the Bruker APEX II CCD area detector diffractometer, structures of the known crystals were confirmed using data provided from the Cambridge Crystallographic Data Centre (CCDC) via the Cambridge Structural Database (CSD) website. Out of the nineteen (19) synthesised crystals and co-crystals, nine (9) compounds were found to be known, some being the same as the unmodified starting material or as the modified duplicate sample (modified but not a co-crystal). The details of some of those are stated in Table 2.2 below. The remaining ten (10) compounds were found to be novel. Of the 10, five are published and their crystallographic data are presented in Table 2.3. below. Of the five unpublished novel compounds, one has been resolved and is in preparation for publication. Its crystallographic data are presented in Table 2.4 below. The remaining four unpublished novel compounds are undergoing full XRD analysis.

Table 2.2. List of previously published crystallised compounds reproduced in this study.

Sample #	Modifiers	Structure	CSD Reference Code	Reference
IBS001 IBS002	Benzophenone		LIMXIR	(Smith & Lemmerer, 2018)
IBS004	4-methylbenzophenone		YUJRAY	(Smith *et al.*, 2015)
IBS006	4,4-dimethylbenzophenone		YUJJOE	(Smith *et al.*, 2015)
IBS010	4-aminobenzophenone		YUJNAU	(Smith *et al.*, 2015)
IBS011	4-(dimethylamine)benzophenone		LIMYAK	(Smith & Lemmerer, 2018)
IBS012	-		YJKAR	(Smith *et al.*, 2015)
IBS013	-		*ROFCIZ01*	(Lemmerer, 2012)
IBS014	-		LATLAV	(Lemmerer, 2012)

\- No modifier was used.

Table 2.3. Crystallographic data of published novel compounds produced in the study.

Sample name	IBS007	IBS017	IBS015	IBS018	IBS019
Formula	$C_{19}H_{15}N_3O_3$	$(C_{10}H13N_3O)\cdot(0.5H_2O)$	$C_{20}H_{20}N_3O_5$	$(C_{10}H_{13}N_3O)\cdot(C_7H_6O_3)$	$C_{16}H_{15}N_3O_3$
M_r	333.34	400.48	382.39	329.35	297.31
temperature/K	173	173	173	173	173
wavelength/ Å	0.71073	0.71073	071073	0.71073	0.71073
crystal size/mm^3	$0.36 \times 0.25 \times 0.20$	$0.91 \times 0.79 \times 0.14$	0.42 x0.27 x 0.028	$0.43 \times 0.34 \times 0.31$	$0.62 \times 0.25 \times 0.23$
Space group	*C2/c*	*Aba2*	*Pbca*	P2$_1$/n	P2$_1$/c
crystal system	monoclinic	orthorhombic	orthorhombic	monoclinic	monoclinic
a/Å	20.6917(6)	19.9676(19)	8.2775(5)	7.4038(9)	9.4957(3)
b/Å	10.1392(3)	8.4674(7)	12.6054(9)	30.448(3)	18.2275(5)
c/Å	16.9544(5)	12.4082(10)	35.082(2)	7.6744(8)	9.0896(3)
α/deg	90	90	90	90	90
β/deg	115.739(1)	90	90	112.013(3)	114.372(1)
γ/deg	90	90	90	90	90
V/Å3	3204.07(17)	2097.9(3)	3660.5(4)	1603.9(3)	1433.05(15)
Z	8	8	8	4sets	4
ρ (calcd)/Mg/m^{-3}	1.382	1.268	1.388	1.364	1.378
μ (mm^{-1})	0.10	0.09	0.101	0.10	0.10
F(000)	1392	888	1608	696.33	624.0
θ range for data collection/deg	2.185 – 27.995	2.91 – 28.31	2.721 – 25.498	2.68 – 28.27	2.235 – 27.994
reflections collected	23999	58009	27619	77005	20811
No. of unique data [R(int)]	3872, 0.037	2526, 0.040	3398	3868, 0.034	3446, 0.072
No. of data with I ≥ 2σ(I)	3440	2474	2421	3459	3009
final R (I > 2σ(I))	R1=0.0375, wR2=0.0997	R1=0.0299, wR2=0.0849	R1=0.0891, wR2=0.2528	R1=0.0492, wR2=0.1384	R1=0.038, wR2=0.098
final wR2 (all data)	0.1009	0.0849	0.2904	0.1384	0.1011
CCDC deposition number	2167402	2086756	02904	2081948	2120068
Citation	(Setshedi *et al.*, 2022)	(Setshedi *et al.*, 2021)	(Setshedi *et al.*, 2023)	(Setshedi & Smith, 2021)	(Setshedi & Smith, 2022)

2.4.1. Crystals and co-crystals

It is important to note that in crystallography, structure description is precise and direct. Therefore, most of this section will be reported as found in the articles published by the author of this thesis and referenced accordingly. Full articles can be accessed in the Annexure Section at the end of the thesis for cross-reference purposes.

For many years, the drug isoniazid, a synthetic derivative of nicotinic acid (PubChem, 2018) has been used as the backbone of the first-line anti-tuberculosis (TB) drug regimen. However, over time, bacterial strains targeted by this drug have gained progressive resistance, thus leading to the crucial need to derive novel anti-TB drugs (Setshedi & Smith, 2021). There are various ways in which novel anti-TB drugs can be developed. However, one method that stands out is by making modifications to functional groups in the existing drugs so that they can no longer be deactivated by mycobacteria (Hu *et al.*, 2017). Co-crystallisation has also been found to be an effective way of improving the bioavailability of isoniazid derivatives. Therefore, the compounds being reported in this section are covalent and supramolecular modifications of isoniazid designed, produced, and published from this study.

2.4.1.1. Crystal structure of IBS007
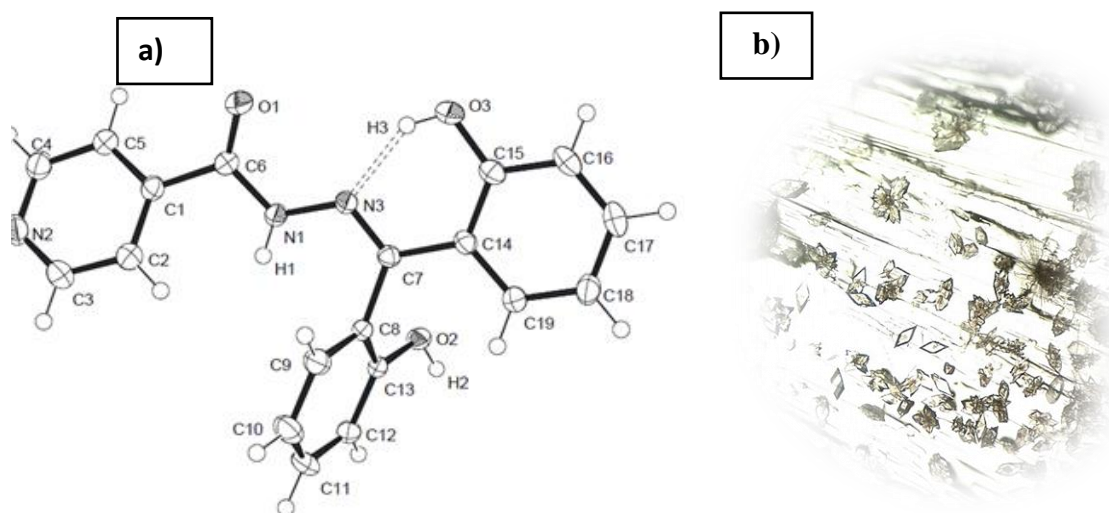
Figure 2.3.1. **(a)** The asymmetric unit of the crystal: N′-[bis(2-hydroxyphenyl)methylidene]pyridine-4-carbohydrazide, $C_{19}H_{15}N_3O_3$ – IBS007; and **(b)** the crystal morphology of IBS007 as observed under a light microscope.
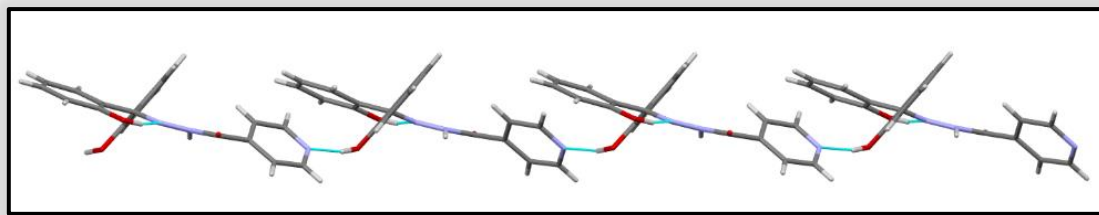
Figure 2.3.1. (c) The 1D chain structure of IBS007 showing that each molecule is connected via a single hydrogen bond.
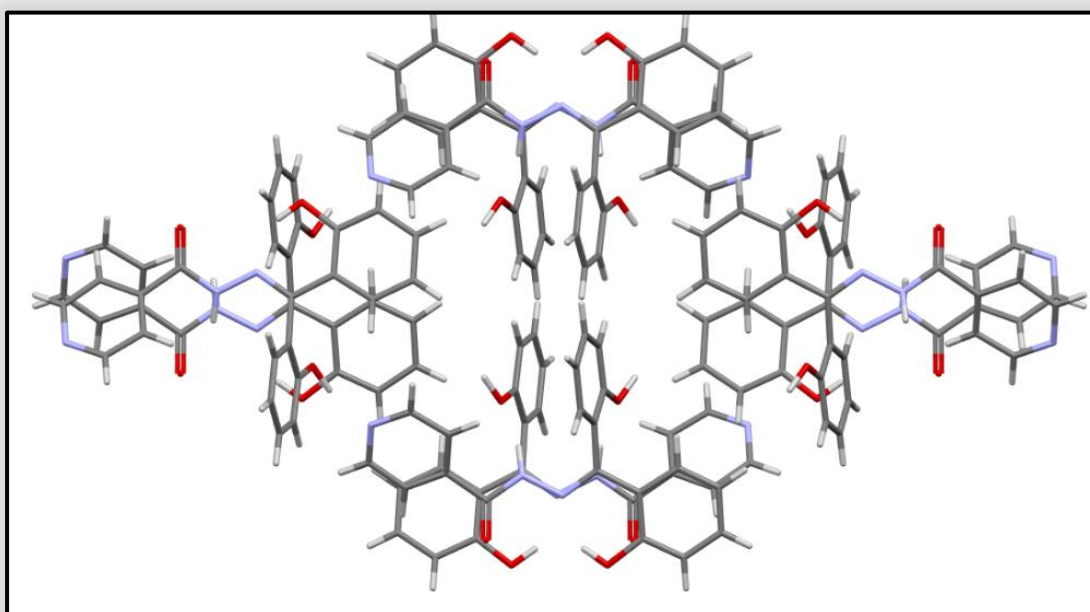
Figure 2.3.1. (d) Packing of IBS007 viewed along the b-axis.

The structure of the crystal shown in Figures 2.3.1 (a) – (d) above, has been described in Setshedi & Smith (2021) and is adapted below.

The crystal structure of isoniazid modified with 2,2′-dihydroxybenzophenone is presented in Figure 2.3.1 (a) where the compound crystallised in the monoclinic C2/c space group and the asymmetric unit contains one molecule. There is one hydroxyl group on each of the benzophenone rings. As expected for hydrogen bonding (Motherwell and Clegg, 1978), one of the hydroxyl groups forms a six-membered intramolecular hydrogen bonded ring with the hydrazide nitrogen atom (N_3) and is not involved in any intermolecular interactions. The other hydroxyl group is hydrogen bonded to the pyridyl nitrogen atom of an adjacent molecule via the robust O–H… N pyridine heterosynthon. Its oxygen atom acts as an

acceptor to the amide hydrogen atom donor (H1). The packing of the crystal forms one-dimensional chains as shown in Figure 2.3.1 (c) with a two-one screw axis. These hydrogen bonding patterns form two rings, namely an $R_4^4(18)$ ring involving four molecules, and an $R_4^4(14)$ ring involving three molecules. The packing along the b-axis is shown in Figure 2.3.1 (d).

2.4.1.2. Crystal structure of IBS015
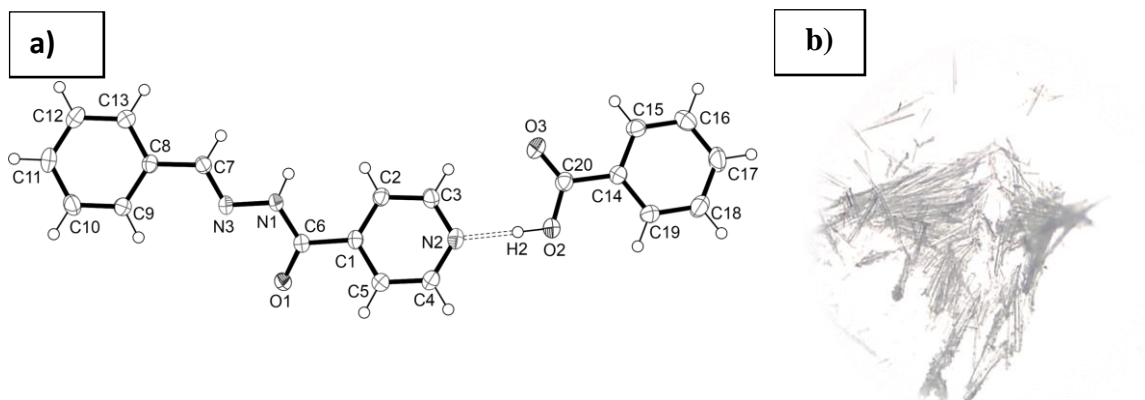
Figure 2.3.2. (a) The asymmetric unit of the co-crystal *N*'-benzylidenepyridine-4 carbohydrazide and benzoic acid – IBS015; and **(b)** the crystal morphology of IBS015 as observed under a light microscope.
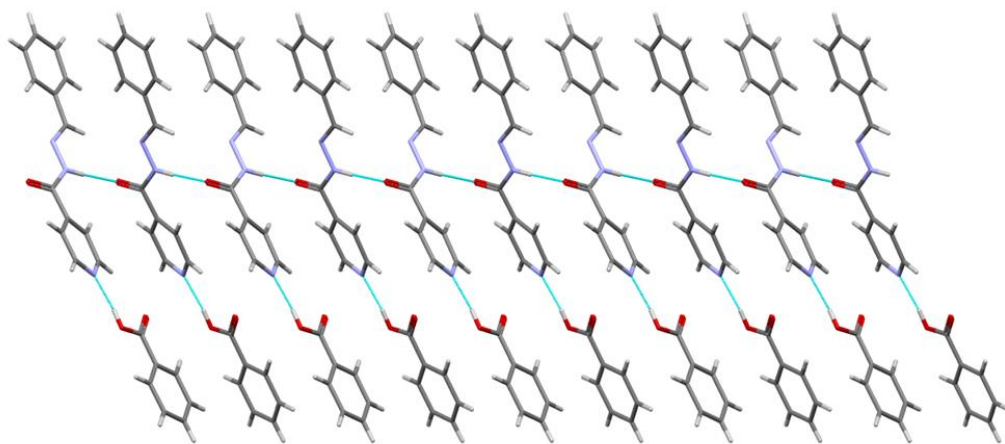
Figure 2.3.2. (c) Packing of IBS015 showing the hydrogen bonding along the a-axis.

The structure of the crystal, shown in Figures 2.3.2 (a) – (d) above, has been described in Setshedi *et al.* (2023) and is adapted below.

The asymmetric unit contains one molecule of benzoic acid N'-benzylidenepyridine-4-carbohydrazide and one molecule of benzoic acid. This molecule crystallises in the *Pbca* space group. Each carbohydrazide moiety is hydrogen bonded by an O_2—$H_2a\cdots N_2$ hydrogen bond to a benzoic acid molecule to form a co-crystal. This co-crystal is formed through a robust carboxylic acid $\cdots$ pyridine heterosynthon. Each carbohydrazide moiety is also hydrogen bonded via its N1–H donor to the carbonyl oxygen (O1) acceptor of an adjacent carbohydrazide moiety. These hydrogen bonding interactions within the packing form a one-dimensional (1D) chain along the *a*-axis (as shown in Figure 2.3.2 (b)).
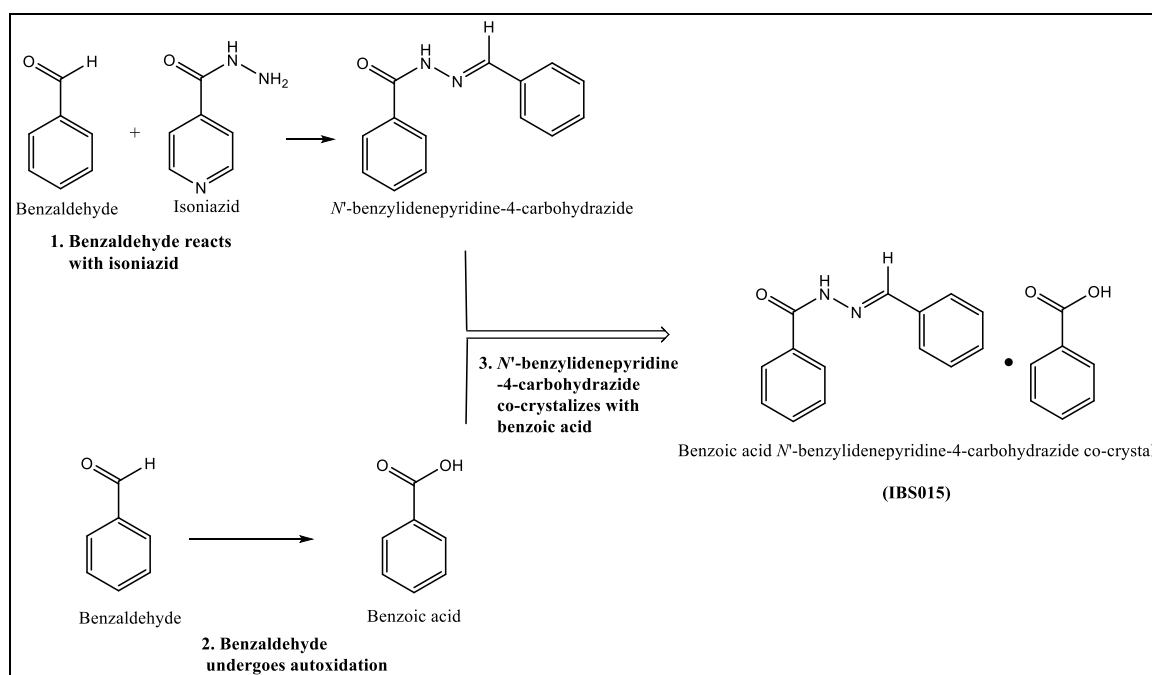
Scheme 2.3. The schematic representation showing the formation of IBS015.

Benzaldehyde is known to undergo autoxidation resulting in the formation of benzoic acid. The formation of benzoic acid occurs when benzaldehyde is exposed to air at room temperature (293 K) where the rate of the reaction is increased by the presence of a catalyst. However, this phenomenon can occur spontaneously without a catalyst over a prolonged period of time (Sankar *et al.*, 2014). The synthesis of this co-crystal was interesting as there were three separate processes that took place within the reaction mixture to create final product (as shown in Scheme 2.3 above). Firstly, benzaldehyde reacted with isoniazid to form N'-benzylidenepyridine-4-carbohydrazide. Secondly, excess benzaldehyde spontaneously autoxidised to form benzoic acid as described above (no benzoic acid was added to the

reaction mixture). Lastly, the carbohydrazide moiety co-crystallised with the benzoic acid to form the product, IBS015 as shown in the asymmetric unit diagram in Figure 2.3.2 (a) above.

2.4.1.3.   Crystal structure of IBS017
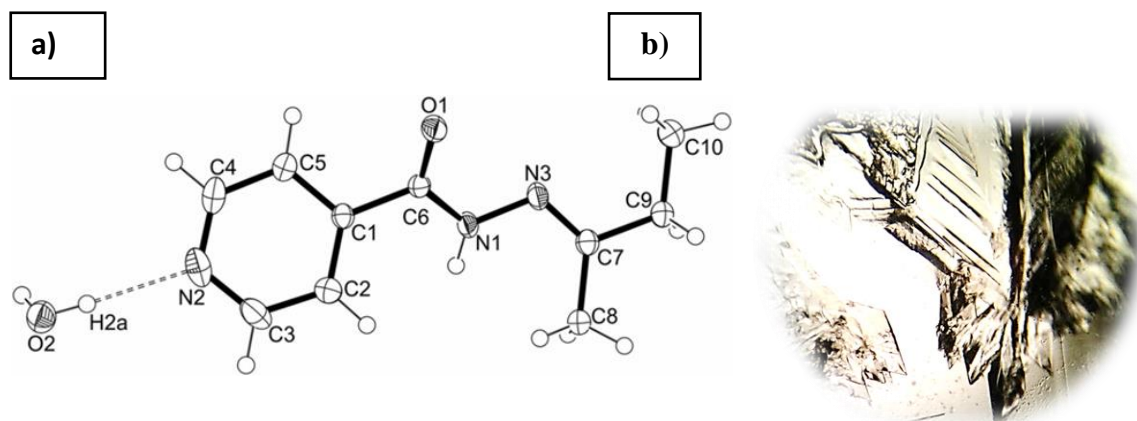
Figure 2.3.3. (a) The asymmetric unit of the crystal: (E)-N′-(butan-2-ylidene)isonicotinohydrazide 0.5 hydrate $C_{10}H_{13}N_3O \cdot 0.5H_2O$ – IBS017; and **(b)** the crystal morphology of IBS017 as observed under a light microscope.
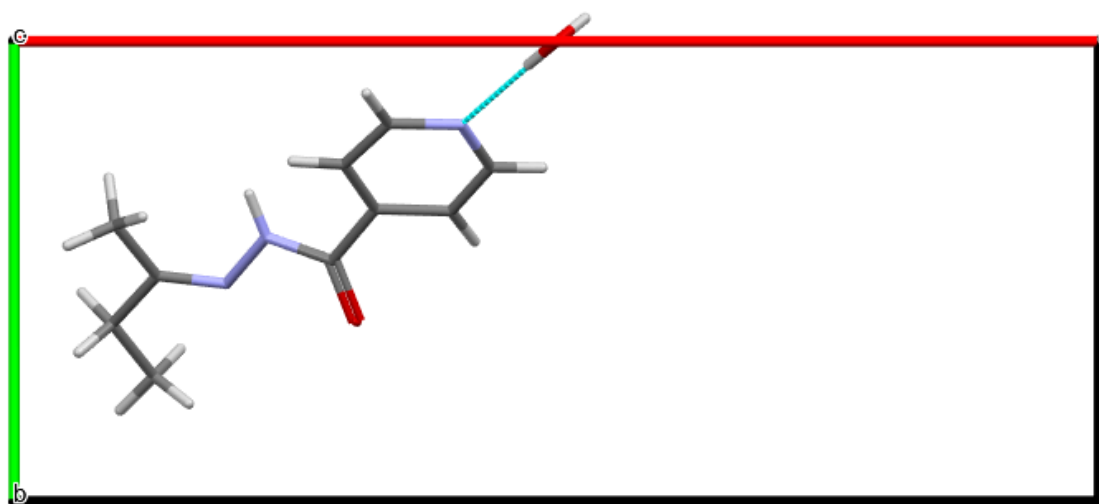
Figure 2.3.3. (c) Unit cells showing the hemihydrate where only half a water molecule is within the unit cell.
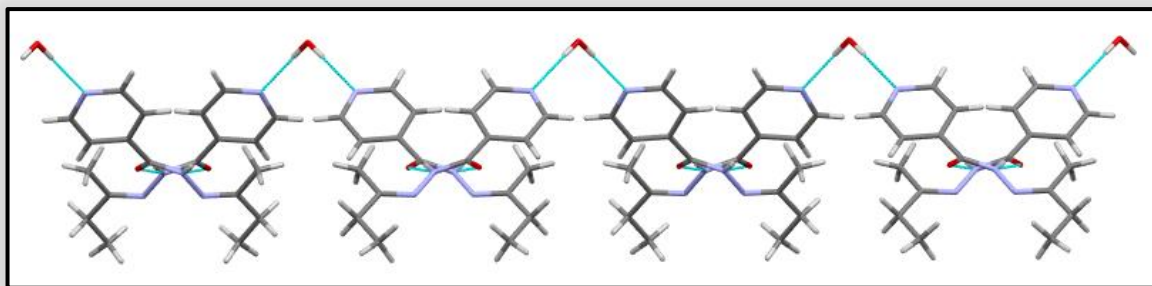
Figure 2.3.3. **(d)** Packing diagram of IBS017 along the b-axis, showing that the crystal structure is stabilised by water molecules connecting pairs of isoniazid derivatives.

The structure of the crystal, shown in Figure 2.3.3 above, has been described in Setshedi & Smith (2021) and is adapted below. The crystal structure being reported in Figure 2.3.3 (a) – (d) represents a covalent modification of isoniazid. The compound crystallises in the orthorhombic Aba2 space group. The asymmetric unit shown in the figure is a hemihydrate, containing one organic target molecule and half a water molecule represented in Figure 2.3.3 (c) where it is shown that half of the water molecule lies outside of the unit cell. The water sits in a special position in the unit cell, with a twofold rotation axis passing through the oxygen atom of the water molecule.

The crystal packing contains bilayers of (E)-N′-(butan-2-ylidene)isonicotinohydrazide alternating with layers of water molecules shown in Figure 2.3.3 (d). Each carbohydrazide moiety is hydrogen bonded by a O2–H2a···N2 hydrogen bond to a water molecule to form the hemihydrate. Each carbohydrazide moiety is also hydrogen bonded via its N1–H donor to the carbonyl oxygen (O1) acceptor of an adjacent carbohydrazide moiety. The water present in the crystal is generated as a by-product of the Schiff base reaction between isoniazid and butanone and is not added to the reaction mixture shown in Scheme 2.4 below.
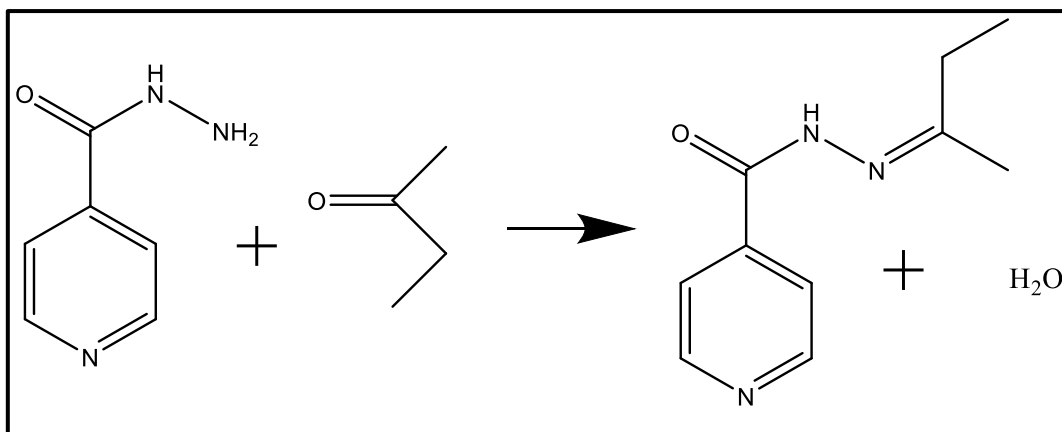
Scheme 2.4: The production of water as a by-product of the reaction of isoniazid with butanone. The resulting crystal is a hydrate where the water molecule is required to stabilise the crystal structure.

2.4.1.4.   The crystal structure of IBS018
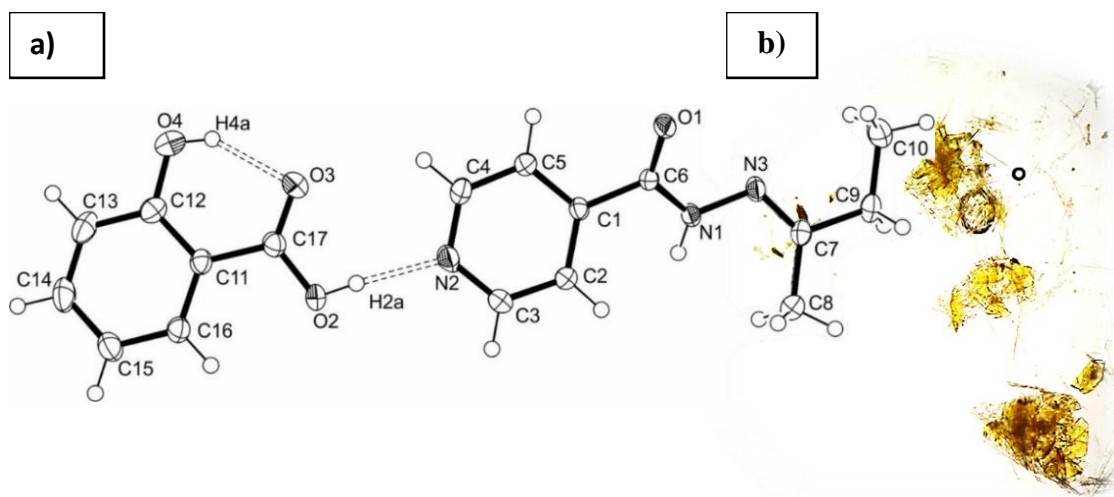
Figure 2.3.4. (a) The asymmetric unit of the co-crystal: 2-hydroxybenzoic acid – N′-(butan-2-ylidene)pyridine-4-carbohydrazide, $C_{10}H_{13}N_3O \cdot C_7H_6O_3$ – IBS018 (Setshedi & Smith, 2021); and **(b)** the crystal morphology of IBS018 as observed under a light microscope.
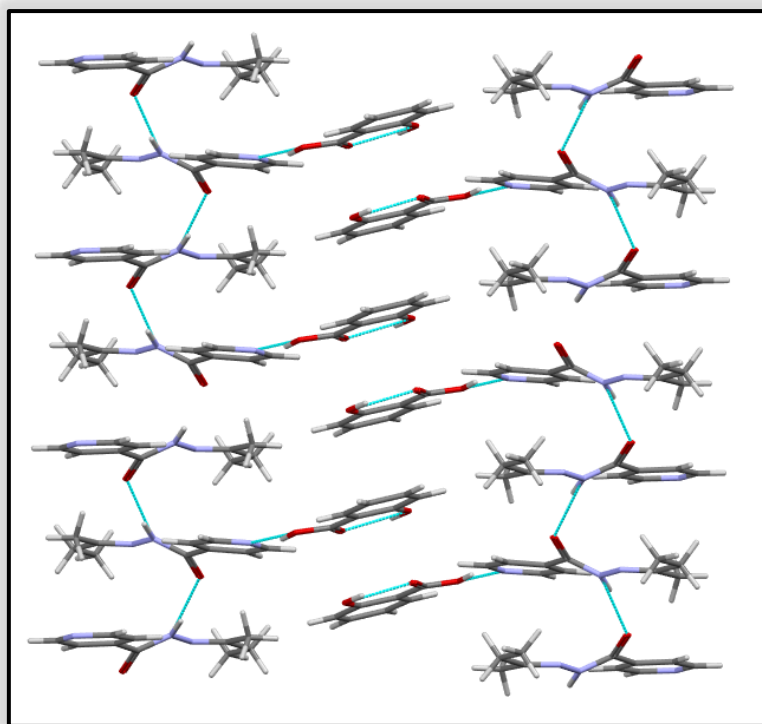
Figure 2.3.4. (c) Packing diagram of IBS018 viewed along the c-axis.

The structure of the crystal, shown in Figure 2.3.4 (a) and (b) above, has been described in Setshedi & Smith (2021) and is adapted below.

The asymmetric unit of this crystal contains one molecule of N′-(butan-2-ylidene)pyridine-4-carbohydrazide and one molecule of 2-hydroxybenzoic acid (salicylic acid). Each carbohydrazide moiety is hydrogen bonded by a O2—H2a···N2 hydrogen bond to a salicylic acid molecule to form a co-crystal. As is expected from similar co-crystals reported in the literature (Aakeröy et al., 2006), this co-crystal is formed through a robust carboxylic acid ··· pyridine heterosynthon. The phenol group on the salicylic acid molecule forms an expected intramolecular S(6) hydrogen bond between the H4a donor and the O3 acceptor.

An S(6) hydrogen bond pattern is a six-membered intramolecular ring within the molecule. Each carbohydrazide moiety is also hydrogen bonded via its N1–H donor to the carbonyl oxygen (O1) acceptor of an adjacent carbohydrazide moiety (not shown in the figure). These hydrogen bonding interactions within the packing form a one-dimensional (1D) chain along the *a*-axis. The plane of the salicylic acid is slightly offset from the plane of the pyridine ring by an acute angle of 22°. However, the pyridine rings of the carbohydrazide moiety as well as

41

the benzene rings of salicylic acid lie parallel to each other respectively, and the packing is thus stabilised by π-stacking of these rings along the *a*-axis.

2.4.1.5.   Crystal structure of IBS019
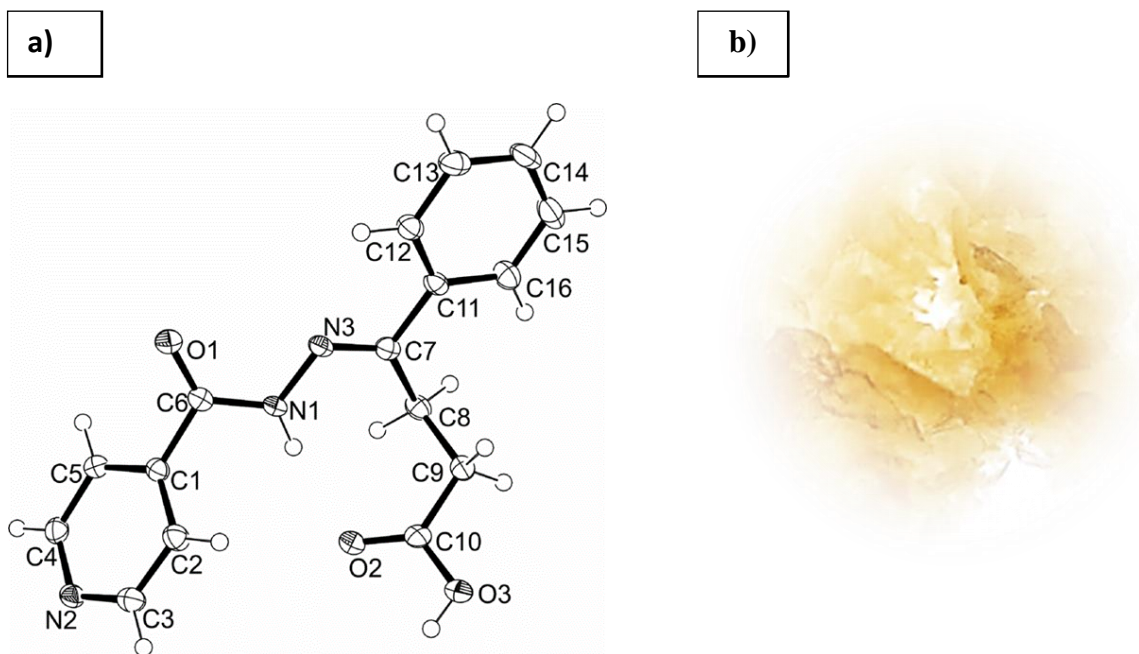
Figure 2.3.5. (a) The asymmetric unit of the crystal: 4-phenyl-4-[2-(pyridine-4-carbonyl) hydrazinyli dene]butanoic acid, C16H15N3O3 – IBS019; and **(b)** the crystal morphology of IBS015 as observed under a light microscope.
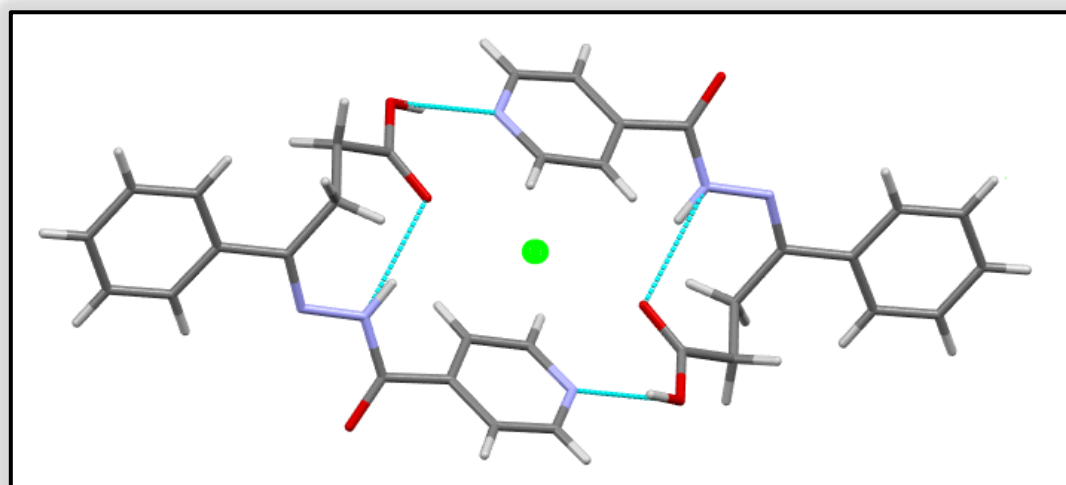
Figure 2.3.5. (c) The symmetrical dimer of IBS 019 showing the inversion centre.
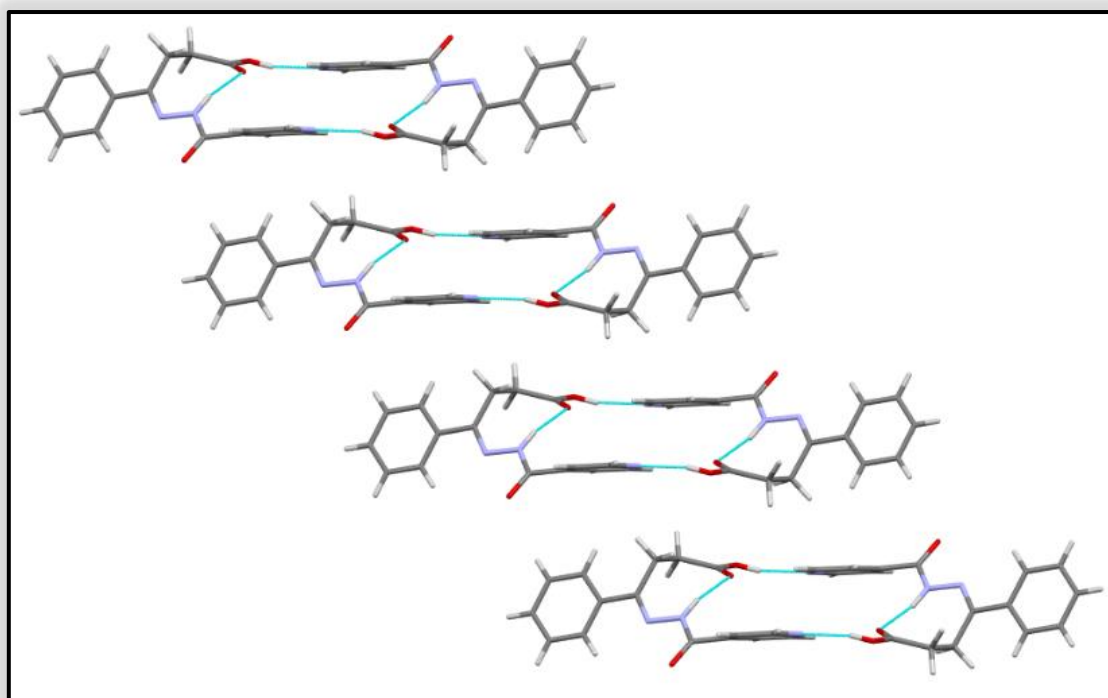
Figure 2.3.5. (d) Representation of dimer stacking within the crystal.

The structure of the crystal, shown in Figure 2.3.5 (a) above, has been described in Setshedi & Smith (2021) and is adapted below. The crystal structure represents a covalent modification of isoniazid derivative. The asymmetric unit shown in the figure contains one molecule of 4-phenyl-4-[2-(pyridine-4-carbonyl)hydrazinylidene]butanoic acid. There is an intramolecular hydrogen bond between the O2 oxygen and the H1 donor atom, forming an $S_1^1(8)$ ring in graph set notation (Bernstein *et al.*, 1995). Every molecule is bonded to an adjacent molecule which is flipped over, thus forming a symmetrical dimer with an inversion centre between the two molecules as presented in Figure 2.3.5 (b). This results in each molecule being hydrogen bonded to its neighbour twice via COOH···N heterosynthons, namely O3–H3A···N2, as shown in Figure 2.3.5 (c). The COOH···N heterosynthons are as expected in the literature (Aakeröy *et al*., 2006). The bonding between the two adjacent molecules is further stabilised by a weak C–H···O interaction between H3 and O2.

Table 2.4. Crystallographic data of novel unpublished compounds produced in this study.

Sample name	IBS 016
formula	$C_{20}H_{20}N_3O_5$
M_R	382.39
temperature/K	173
wavelength/ Å	071073
crystal size/mm^3	0.42 x 0.27 x 0.028
Space group	*Pbca*
crystal system	Orthorhombic
a/Å	8.2775(5)
b/Å	12.6054(9)
c/Å	35.082(2)
α/deg	90
β/deg	90
γ/deg	90
V/Å3	3660.5(4)
Z	8
ρ (calcd)/Mg/m^{-3}	1.388
μ	0.101
F(000)	1608
θ range for data collection/deg	2.721 – 25.498
reflections collected	27619
No. of unique data [R(int)]	3398
No. of data with I ≥ 2σ(I)	2421
final R (I > 2σ(I))	R1=0.0891, wR2=0.2528
final wR2 (all data)	0.2904
CCDC deposition number	2251424

2.4.1.6. Crystal structure of IBS016
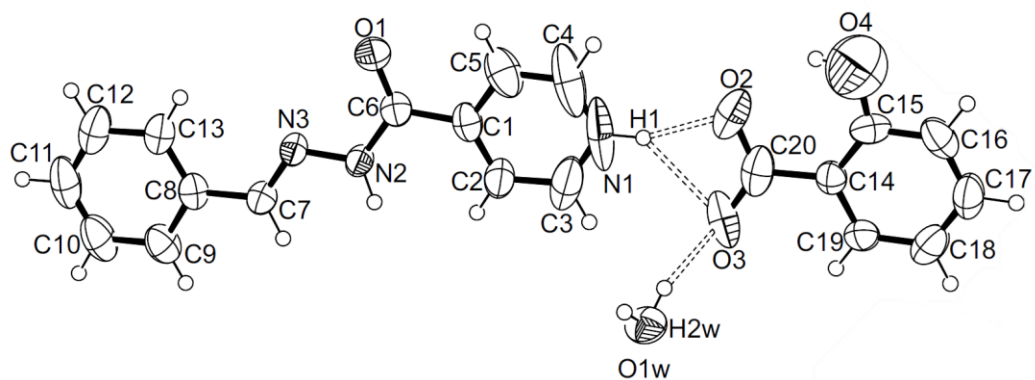
Figure 2.3.6. (a) The asymmetric unit of (E)-4-(2-benzylidenehydrazine-1-carbonyl)pyridin-1-ium 2-hydroxybenzoate hydrate - IBS016.
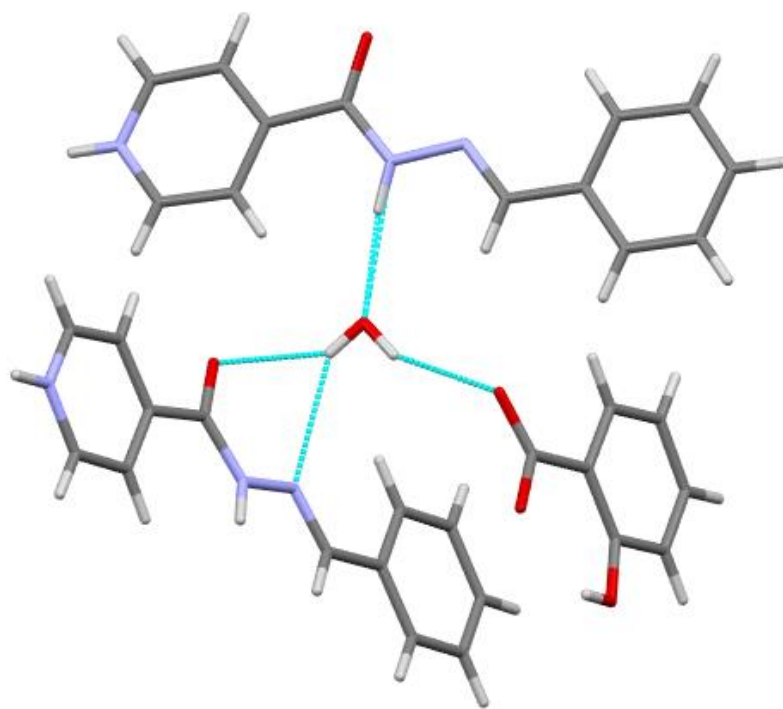
Figure 2.3.6. (b) IBS016 showing the stabilisation of the crystal by the water molecule.
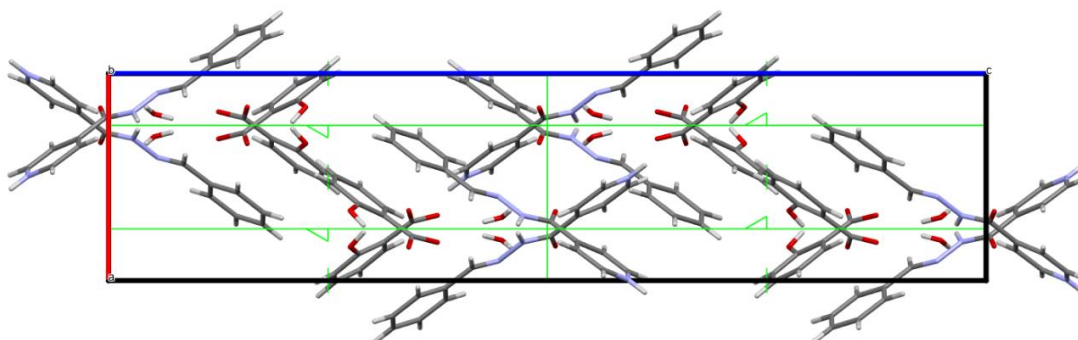
Figure 2.3.6. (c) Packing diagram of IBS016 showing the anticlockwise twofold screw rotation along the b-axis.

During XRD structure determination, it was not possible to pick a good crystal. After repeated collection attempts with different crystals, several of the ellipsoids were larger than the acceptable sizes for publication. There were reattempts to remake the crystal; however, all subsequent XRD structures still had poor R1 values. The crystals were very thin as shown in Figure 2.3.6 (b) which could have been one of the causes resulting in poor diffraction. Even though the crystal structure of IBS016 was not publishable, the structure was unambiguously determined as shown in Figure 2.3.6 (a) and is useful for the purpose of this study.

The crystal structure of the hydrated salt (*E*)-4-(2-benzylidenehydrazine-1-carbonyl)pyridin-1-ium 2-hydroxybenzoate hydrate is presented in Figure 2.3.6 (a). The compound crystallised in the monoclinic *Pbca* space group and the asymmetric unit contains one molecule of (*E*)-4-(2-benzylidenehydrazine-1-carbonyl)pyridin-1-ium, one molecule of 2-hydroxybenzoate and one molecule of water. In the asymmetric unit, the H1 atom of the carbohydrazide moiety is bonded via bifurcated hydrogen bonds to the two oxygen atoms of the carboxylate functional group of the co-former. It is interesting that the O3 oxygen on the co-former is also bifurcated and hydrogen bonded to both H1 as described above as well as to the H2 atom on the water molecule. Each water molecule in the unit cell is connected to two carbohydrazide moieties. The first carbohydrazide moiety is hydrogen bonded to the water through the N2—H2···O1 hydrogen bond. The second carbohydrazide moiety has a bifurcated hydrogen bond between H1 on the water molecule and O1 and N3 on the moiety. Furthermore, the second hydrogen atom on the water molecule, H2, is bonded to the O3 atom on the 2-hydroxybenzoate molecule. The salt is therefore stabilised by the water molecule in the crystal as shown in Figure 2.3.6 (b). The packing of IBS016 contains an anticlockwise twofold screw rotation

along the b-axis, resulting in a three-dimensional (3D) network in the crystal structure, as shown in Figure 2.3.6 (c).

2.5.   Conclusion

The aim of this chapter was to design and synthesise known and novel crystal and co-crystal isoniazid derivatives as well as confirming the structures and elucidating where necessary. The goal of modifying isoniazid was to create derivatives that may enhance activity against drug-resistant TB organisms. However, crystallisation and co-crystallisation often yield unpredictable products. As a result, modification of isoniazid was targeted at the site where isoniazid is deactivated by the organism to produce products that possess more desirable physical properties than the non-co-crystallised analogues. Some known and novel derivatives were reproduced using methods found in literature and some new methods were designed for the project. These derivatives were used in subsequent chapters where biological assays were conducted to study their synergistic and biological properties as well as to test for cytotoxicity against murine RAW 264.7 macrophage cells.

CHAPTER 3
Target identification and validation

3.1.1. Drug discovery

Drug discovery is a continuous process conducted to develop new drugs designed to address unmet medical needs applied across multiple therapeutics, mainly conducted by pharmaceutical industries, academic institutions and research institutes (Sinha & Vohora, 2018). Often, at research and academic institutes, the process is limited to the first phase and does not proceed further. This is where a target is identified and validated, then followed by preclinical research where compound screening assays are developed and used to conduct high throughput compound screening for the identification of active pharmaceutical ingredients (APIs) (Pandey, s.a.). Once an API is identified as a prospective drug candidate, the process is narrowed down leading to the commencement of preclinical research whose results lead to drug development, a complex and lengthy process that encompasses several steps, namely: clinical development, FDA review and lastly, post-marketing monitoring (Sinha & Vohora, 2018).

The preclinical research phase of new drugs begins with *in vitro* assays followed by *in vivo* experiments. This requires an understanding of the basic nature of life in molecular terms which involves the investigation of chemical progressions that transpire in living organisms. This process is fundamentally referred to as biochemistry (Wilson, 2010). Molecular biology is a discipline that seeks to understand cellular processes at a genetic level, whereas biochemistry is a discipline that looks into exploiting available techniques in order to comprehend such processes. These two disciplines complement each other in that they provide endless opportunities in addressing issues around processes involved in drug development and discovery as well as the nature of viral, bacterial and fungal diseases, among many other recorded applications (Wilson & Walker, 2010).

3.1.2. Disciplines involved in drug discovery

It is impossible to carry out an investigation around diseases related to microorganisms without tapping into microbiology as a discipline. Microbiology is important as it is the study of all living organisms that are too small to be seen with the naked eye. These organisms include viruses, protozoa, fungi and bacteria, to name a few, and are collectively known as

'microbes' (Microbiology Society, 2003). The focus of this study is on mycobacteria species including nontuberculous mycobacteria (NTM) organisms which belong to the genus *Mycobacterium.* This is solely because NTM are slowly gaining traction as opportunistic human pathogens causing minor to severe pulmonary and extrapulmonary infections in humans (Ratnatunga *et al*., 2020), as well as the fact that some of these NTM bacteria possess resistance to leading drugs used to treat MTB. Should there be a breakthrough on such NTM, the results could hypothetically be of great importance in understanding MTB resistance, drug development thereof as well as the development of treatment for all mycobacteria within the *Mycobacterium* genus.

As this study focuses on drug design and drug modification, employing only microbiology techniques will not suffice. When studying drug development while employing the molecular biology approach, and not only that of physical and analytical chemistry, cell biology is also of paramount importance as it gives a glimpse of the effects of the drugs on both the organism of interest as well as help draw a picture that will allow the determination of the safety or level of toxicity of the drugs on the target host. Cell biology makes up a small but direct experimental approach of systems biology that uses complex murine or human cell systems to assist in the prediction and interpretation of biological gene target responses to tested drugs (Butcher *et al*., 2004).

The purpose of this chapter was to combine all the aforementioned disciplines to validate the drug target, activity, effects and impact of the designed isoniazid derivatives on mycobacteria of choice in individual form as well as in combination for assessment of possible synergism.

3.1.3. Nontuberculous mycobacteria

Nontuberculous mycobacteria (NTM) are organisms of ubiquitous distribution found around human habitats. For many years it was thought that infections of these opportunistic organisms were from the environment due to the lack of evidence supporting human-to-human transmission. Very much understandably so as these slow-growing and rapidly growing mycobacteria can be found in habitats shared with both animals and humans, appearing in larger quantities within natural water systems and in biofilm form within drinking water supply systems (Falkinham, 2009). They can also be found in soil and dust

and are readily aerosolised due to their hydrophobic nature attributed to their lipid-rich outer membrane (Jeon, 2018).

The term NTM is broadly used to classify approximately 186 recognised distinctive mycobacteria species, most of which pose no direct harm to human health (Donohue, 2018). Some NTM species are pathogenic to humans with a high potential of causing dermal infections, as well as severe pulmonary and non-pulmonary diseases (Hu *et al.*, 2019). These organisms, like their aggressively known counterpart MTB, can cause clinically indistinguishable infections to those of TB, thus are in turn misdiagnosed as multidrug-resistant MTB (Hu *et al.*, 2019). Table 3.1 below is a representation of the most common NTM isolated from humans reported to cause pulmonary and or extrapulmonary infections.

Table 3.1. Environmentally abundant opportunistic mycobacteria commonly known to infect humans (Falkinham, 2009).

Classification	Species
Slow-growing mycobacteria (colony formation ≥7 days)	*M. avium* *M. marinum* *M. xenopi* *M. kansasii* *M. simiae* *M. malmoense* *M. intracellulare*
Rapidly growing mycobacteria (colony formation 3 – 7 days)	*M. chelonae* *M. abscessus* *M. fortuitum* *M. smegmatis*

In addition to those tabulated in Table 3.1 above, several other NTM have been reported to cause pulmonary infections in humans, and these include *M. szulgai*, *M. triviale*, *M. nonchromogenicum*, *M. gilvum*, *M. scrofulaceum*, *M. porcinum*, *M. gastri*, *M. phlei*, *M. gordonae*, *M. diernhoferi*, *M. vaccae*, *M. ulcerans* (Hu *et al.*, 2019), *M. terrae* (Lee *et al.*, 2011), *M. lentiflavum*, *M. flavescens*, *M. asiaticum*, *M. riyadhense* and *M. celatum* (Al-Ghafli

& Al-Hajoj, 2017). It is therefore of major concern that health practices in most countries do not generally investigate TB infections to the extent of excluding NTM as causative agents, especially since infections by these drug-resistant organisms are easily misdiagnosed for multidrug-resistant tuberculosis (MDR-TB) and extensively drug-resistant tuberculosis (XDR-TB) infections (Hu *et al*., 2019), thus resulting in treatment complexities (Ryu *et al*., 2016).

Identification and diagnosis of NTMs is more complicated, difficult, and costly as compared to that of TB. Proper identification of NTM species requires the integration of radiographic, microbiological, and clinical data. These would most likely focus on lung biopsy, mainly transbronchial accompanied by a positive culture or other related radiographic findings such as stainable acid-fast bacilli (Ryu *et al*., 2016). Treatment of NTM is very challenging due to their virulence and broad-spectrum resistance, which means they also require lengthy specialised treatment (Ryu *et al.*, 2016). Therefore, in order to facilitate appropriate treatment for pulmonary diseases associated with NTM infections, it is very important focus attention on the clinical characteristics of those infections for proper diagnosis. In addition to that, treatment of chronic lung infections caused by NTM requires expert management and multiple antimycobacterial drugs administered over longer periods of time (Hu *et al*., 2019).

Treatment is generally lengthy, most likely attributed to the high natural antibiotic resistance observed in NTMs which ultimately leads to drug-related toxicity and noncompliance (Van Ingen *et al*., 2012a). There is a considerable variation in pathogenicity and resistance from one NTM organism to another. As a result, different treatment regimens are administered of which most are recommended as a susceptibility-based treatment (Daley *et al*., 2020). For example, in a study by Adjemian *et al*. (2014), patients who were infected with *M. avium* complex (MAC) received oral antibiotic treatment of azithromycin in combination with rifampicin and ethambutol, whereas patients infected with *M. abscessus* received oral antibiotic treatment of clarithromycin. Often amikacin, imipenem/cilastatin, cefoxitin, tigecycline, meropenem and linezolid are the commonly prescribed intravenous antibiotics for treating patients with *Mycobacterium avium* complex (MAC) and *M. abscessus*. This gives a glimpse of how easily an infection with NTM can be misdiagnosed as an XDR-TB or MDR-TB infection when treated blindly based on the assumption that the patient is suffering from tuberculosis.

3.2. Experimental procedures

3.2.1. Safety

Some parts of the study could not be conducted on clinical isolates, due to the restrictions of access to the collaborative institutional Biosafety Level 3 (BSL-3) laboratory at the National Health Laboratory Services (NHLS, University of Pretoria, Pretoria, South Africa) during the peak of COVID-19 lock-down within the country and a year after the effects. Instead of halting the project with no indication of how long the lockdown was going to last, and the unexpected consequences thereof, alternative measures had to be put in place. As a result, *M. smegmatis*, *M. bovis* bacillus Calmette-Guérin (BCG) and avirulent *M. tuberculosis* (MTB) $H_{37}R_a$ were sourced and used as clinical isolate representative strains, with *M. smegmatis* serving as a model bacterium.

Since no clinically infectious isolates were used in this study, a standard Biosafety Level 2 (BSL-2) microbiology laboratory was used, and the practices thereof were applied. These include the standard use of pipetting devices, prohibition of smoking, drinking and eating in the laboratory space. Standard personal protective equipment requirements for laboratories, such as laboratory coat, and gloves were met (CDC, 2021). Although face protection is not mandatory, such was used as mycobacteria organisms can be aerosolised and exposure should be avoided as opportunistic infections by these bacteria have been reported (Singh & Reyrat, 2009). All Petri-dish cultures were sealed in plastic during incubation and storage. All broth flask lids were sealed with parafilm® (Amcor, USA; supplied by Glassworld, Maraisburg, SA) during incubation and storage. All experimental 96-well microtitre plates were sealed with parafilm and then placed in a plastic which was then sealed using PFS-300S Impulse Heat Sealer (China; supplied by takealot.com, SA) prior to incubation. It is vital to have a decontamination site within the laboratory when working with these organisms; as a result, in order to minimise unnecessary transmissions, contamination and infections, all used items were sterilised in a Sturdy Apex SA-300H benchtop autoclave (Sturdy, member of Apex Medical Group; supplied by United Scientific (Pty) Ltd., Cape Town, South Africa) prior to being discarded into a biological hazardous material waste box.

3.2.2. Sample collection and preparation

In instances where Biosafety Level 3 (BSL-3) laboratories are inaccessible or out of reach, clinical isolates can be substituted with other mycobacteria of choice. These mycobacteria include *M. smegmatis*, *M. bovis* BCG and MTB $H_{37}R_a$ (Nguta *et al.*, 2015). *Mycobacterium*

smegmatis has been reported to resemble identical susceptibility patterns against the two front-line TB treatment drugs being INH and RIF in comparison to that of MDR-TB clinical isolates (Mahairas *et al*., 1996). However, there are still variations between *M. smegmatis* and MTB where drug susceptibility is concerned. These are most likely attributed to genetic differences that are unique to the virulent MTB $H_{37}R_v$ of the *Mycobacterium tuberculosis* complex (MTBC) which are to a certain degree found to be similar to *M. bovis* (Mahairas *et al*., 1996; Nguta *et al*., 2015). In addition to the *M. smegmatis*, *M. bovis* BCG vaccine strain as well as MTB $H_{37}R_a$ can also be used as clinical isolate substitutes; the former two are non-pathogenic and slow-growing mycobacteria, but their drug susceptibility pattern is closely related to that of the rapidly growing MTB $H_{37}R_a$ (Nguta *et al*., 2015). Subtractive hybridisation between $H_{37}R_a$ and $H_{37}R_v$ suggests that there are undetectable point mutations or deletions which result in no obvious genetic differences between these two strains (Mahairas *et al*., 1996). However, there are clear and undeniable phenotypic differences between these isolates, which include but are not limited to virulence, bacterial proliferation and intracellular doubling time, among others (Kato-Maeda *et al*., 2001).

All acid-fast nontuberculous mycobacteria species cultured and used in subsequent experiments together with their respective information are listed in Table 3.2 below. Microbes that were received in a lyophilised state were cultured according to the manufacturer's guidelines on the Middlebrook 7H10 agar (Condalab, Madrid, Spain; supplied by Separation Scientific, South Africa). Once grown, a loop was used to collect the culture, then sub-cultured in the Middlebrook 7H9 broth (Sigma-Aldrich, India; supplied by Merck Scientific, South Africa) to be used in subsequent experiments. Microorganisms received in culture form on agar plates and/or as frozen glycerol stock were sub-cultured in broth. Once grown in broth, all cultures were stained for purity and acid-fast confirmed using a TB-colour staining kit based on the Kinyoun method (cold staining) which is the modified version of the Ziehl-Neelsen staining method (Kurup & Chester, 2014). For future use and easy access, cultures were maintained on agar, sealed and stored inverted in the fridge at $\pm$ 4 °C.

3.2.3. Agar and broth preparation

To make 1 L of the broth, 19 g of agar granules were suspended in 900 mL of ultrapure water, to which 5 mL of glycerol (VWR Chemicals, Frankenwald, Sandton, South Africa) was added and the mixture was shaken vigorously. In order to achieve a homogeneous mixture, magnetic stirring was used by adding a magnetic stir bar to the mixture contained in

the Schott bottle which was then placed on a magnetic stirrer hotplate. Once the broth granules had completely dissolved, the bottle was opened, the magnetic stirrer was retrieved, and the cap replaced and lightly sealed, and then covered with a foil before autoclaving at 121 °C for 10 min. The agar mixture was then enriched with 100 mL of oleic acid albumin dextrose catalase (OADC) enrichment growth supplement (Condalab, Madrid, Spain), mixed well while avoiding bubble formation, and then poured into agar plates. Plates not used where put back into a sterile plastic, sealed and stored inverted in the fridge until used.

Table 3.2. A representation of all microbes used in this study, their ATCC numbers as well as source and condition in which they were received.

Mycobacterium spp.	ATCC/NCTC Number	Source	State/Condition
M. avium	25291	KWIK-STIK™ (Microbiologics, Anatech, South Africa)	Lyophilised
***Mycolicibacterium aurum*	10437	University of Pretoria, Department of Phytomedicine	Culture plate
M. bovis BCG	27290	University of Pretoria, Department of Phytomedicine	Culture plate and frozen glycerol stock
M. fortuitum	6841	KWIK-STIK™ (Microbiologics, Anatech, South Africa)	Lyophilised
M. smegmatis	14468	KWIK-STIK™ (Microbiologics, Anatech, South Africa)	Lyophilised
***M. smegmatis*	1441	University of Pretoria, Department of Phytomedicine	Culture plate & Frozen glycerol stock
M. tuberculosis *($H_{37}R_a$)*	25177	KWIK-STIK™ (Microbiologics, Anatech, South Africa)	Lyophilised

* These strains were used as clinical isolates representative strains (Zhou *et al*., 2021).

** These strains were used as both study NTM of concern and MTB clinical isolate representative.

*** These strains were dropped from the study as they were contaminated. *Mycolicibacterium aurum* (NCTC 10437) is not part of the genus *Mycobacterium*. The commercial supplier did not have the strain in stock.

To make up a 400 mL of broth suspension, 1.88 g of Middlebrook 7H9 broth powder was added to 360 mL of ultrapure water in a 500 mL Schott bottle. Thereafter, 2 mL of glycerol was added and the mixture was shaken vigorously to mix. A homogeneous state was reached by applying the same heating block with stirring method as that used for the agar. The contents were then autoclaved at 121 °C for 10 min. Once cooled, 0.8 mL (800 µL) of 20% filter sterilised Tween® 80 (Sigma-Aldrich, France) was added to the broth, and thereafter finally enriched with 40 mL of albumin dextrose catalase (ADC) enrichment supplement (Condalab, Madrid, Spain) and stored in the fridge at 2 – 4 °C until further use.

3.2.4. Acid-fast characterisation and culture purity confirmation

Some mycobacteria bacilli were picked up with a sterile loop and transferred into a 50 mL T cell culture flask containing 25 mL of Middlebrook 7H9 broth. The broth was spiked with 125 µL of Tween® 80 which is a routinely used detergent in growth media for mycobacterial culturing. The detergent is used mainly to reduce aggregation, thus resulting in an increased growth rate as cells are allowed to grow in somewhat singular form (Pietersen *et al.*, 2020). Once grown to an optimum optical density, staining was done following the modified Kinyoun cold staining method as presented by Kurup and Chester (2014). The reagents that came with the staining kit (Merck, Germany) were ready to use and did not require any preparation or further dilution.

About two drops of broth microbe culture were harvested from the respective broth cultures using a sterile Pasteur pipette and dropped onto a clean labelled slide. These were then placed in the incubator set at 37 °C to allow the broth to evaporate before heat fixing over a burning Bunsen burner. In some instances, the slides were moved across a burning flame to evaporate the broth and heat-fix the microbes onto the slide. Once the cultures were heat fixed, they were covered completely with reagent 2 (carbolfuchsin solution) and allowed to stain for 5 min. The stain was rinsed under a running stream of ultrapure water until no further clouds of dye were visible. The slides were then flooded with reagent 3 (hydrochloric acid in ethanol) and allowed to react for 15 – 30 s. The acid was rinsed off immediately under a running stream of ultrapure water. The 3rd and final step required the slides to be flooded with reagent 4 (malachite green solution) for 1 min, and then rinsed under a running stream of ultrapure water. The slides were briefly placed in an incubator at 37 °C to dry before being visualised under a light microscope.

3.2.5. Minimum inhibitory concentration testing

The resazurin microtitre assay (REMA) plate method was followed according to Khan *et al.* (2011) and Palomino *et al.* (2002), with modifications. Optimal density (OD) of all broth cultures was measured using a SmartSpec™ Plus Spectrophotometer (Bio-Rad, USA). The final concentrations were calculated down to a desired colony-forming unit (CFU) concentration per millilitre (mL) (CFU/mL) per 50 mL to match the 0.5 McFarland standard, corresponding to 1.5 x 10^8 CFU/mL, and confirmed using a spectrophotometer. These 50 mL broths adjusted to the 0.5 McFarland standard were used as inoculum.

3.2.5.1. Minimum inhibitory concentration procedure for single compounds

The microtitre plates were positioned horizontally where A – H were used as rows and 1 – 12 were used as columns. Wells 1 – 9 of row A were filled with 160 µL of fresh broth topped up to 200 µL with the addition of 40 µL (250 µg/mL) of compound in triplicate. Wells 1 – 12 of rows B – H were filled with 100 µL of fresh broth. The 100 µL was aspirated from the contents of row A, wells 1 – 9 and serially diluted by an up and down pipette mixing motion down the plate to row H where the final 100 µL aspirated was discarded. Column 10 of rows A – H served as a blank control and was filled with 200 µL of fresh broth. The remaining two columns being column 11 and 12 served as negative control. In those, a 100 µL of fresh broth was added. A final addition of 100 µL of inoculum was added to all wells (except those of column 10 rows A – H) bringing the total volume of all wells to 200 µL. The plates were covered and sealed in a plastic bag, then incubated at 37 ℃ for 1 – 7 days depending on whether the sample is that of a slow growing NTM or rapidly growing NTM. After incubation, 30 µL of 0.02% resazurin solution was added to all 96 wells and thereafter incubated over 24 h for bacteriostatic results and over 48 h for bactericidal results. No change in colour observed represents bacterial growth inhibition. A change from blue to pink indicated resazurin reduction signifying bacterial growth. The schematic depiction of the above procedure is presented in Figure 3.1 below.
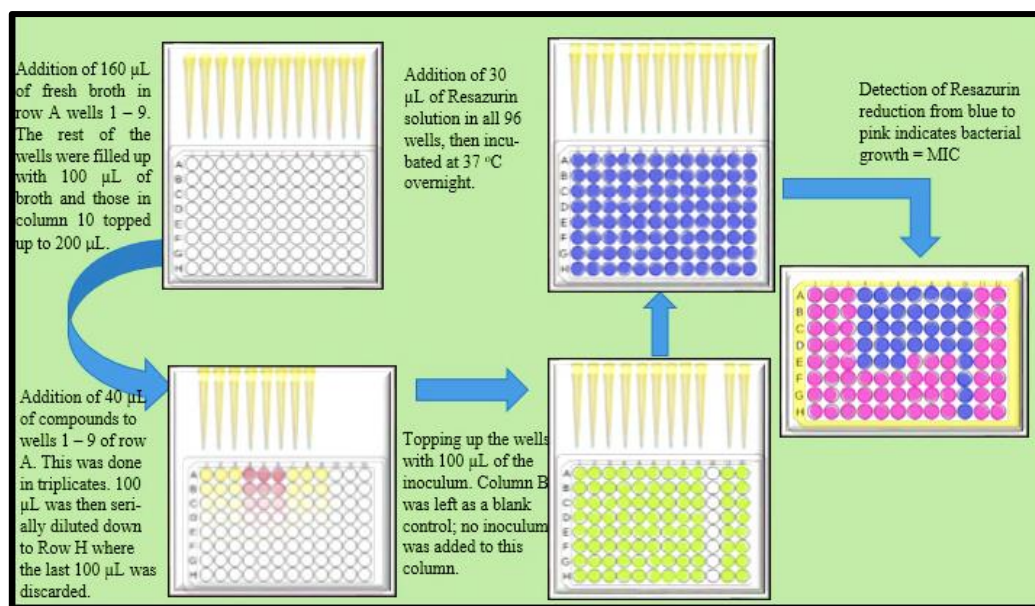
Figure 3.1. Schematic representation of the minimum inhibitory concentration procedure followed in **Section 3.2.5.1** above. This figure was compiled and edited by the author of this thesis for the purpose of this section using Microsoft paint 3D and Word tools.

3.2.5.2. Minimum inhibitory concentration method for combination compounds

Modification of this section is depicted in Figure 3.2 below and was carried out as follows: Microtitre plates were positioned in a vertical position where lanes A – H were used as column H – A and column 1 – 12 were used as raw 1 - 12. This was to allow for a longer serial dilution pattern to achieve the lowest MIC possible. About 100 µL of fresh non-inoculated broth prepared as mentioned in Section 3.2.2 was seeded into all 96 wells of the microtitre plate. The last two columns (B & A) were used as blank (B) and negative control (A). Column B was topped up with fresh broth to make up a total volume of 200 µL, whereas column A was topped up with 100 µL of the inoculum broth to a total volume of 200 µL.

The first test drugs (encore compounds) and/or positive control standards (clinical drug) were added according to the calculated volume per desired concentration (250 µg/mL) in the experimental wells (H-C) of row 1. These were then topped up with clean fresh media to make up a total of 200 µL. The total mixtures in the experimental wells were then mixed by pipetting up and down about 10 times, then serially diluted down from row 1 to row 12. The final 100 µL collected at row 12 was then discarded. The inoculum used to top up wells in column A, was used to top up all experimental wells with a 100 µL to make up a total volume of 200 µL. Where the compounds worked in synergy, the second test drug was laced over the inoculum at a volume (roughly 30 µL) of the desired concentration (about 150 µg/mL). The

57

plates were covered and sealed in a plastic bag, then incubated at 37 °C for 1 – 7 days depending on whether the sample is that of a slow growing NTM or rapidly growing NTM. After incubation, 30 µL of 0.02% of resazurin solution was added to all 96 wells and then incubated over 24 h to determine bacteriostatic effects and over 48 h for bactericidal effects. No change in colour observed represents bacterial growth inhibition. A change from blue to pink indicated resazurin reduction, therefore bacterial growth. Where there was very limited bacterial growth or where the bacteria seemed to be struggling to grow in larger quant ities, resazurin was replaced with 2-[4-iodophenyl]-3-[4-dinitrophenyl]-5-phenyltetrazoliumc hloride (INT) as INT reduction to formazan occurs more rapidly than that in other tetrazolium compounds. This is because INT has a strong electron affinity and is not dependent on cell quantity as compared to resazurin and other salts (von Mersi & Schinner, 1991) making it a more sensitive and reliable dye to use (Grare *et al*., 2008; Uzarski *et al*., 2017). A conversion of INT formazan from clear to a stable pink/red coloured complex indicates INT reduction by viable cells (von Mersi & Schinner, 1991). Minimum inhibitory concentration (MIC) is defined as the lowest concentration required to prevent this colour change (Uzarski *et al*., 2017).
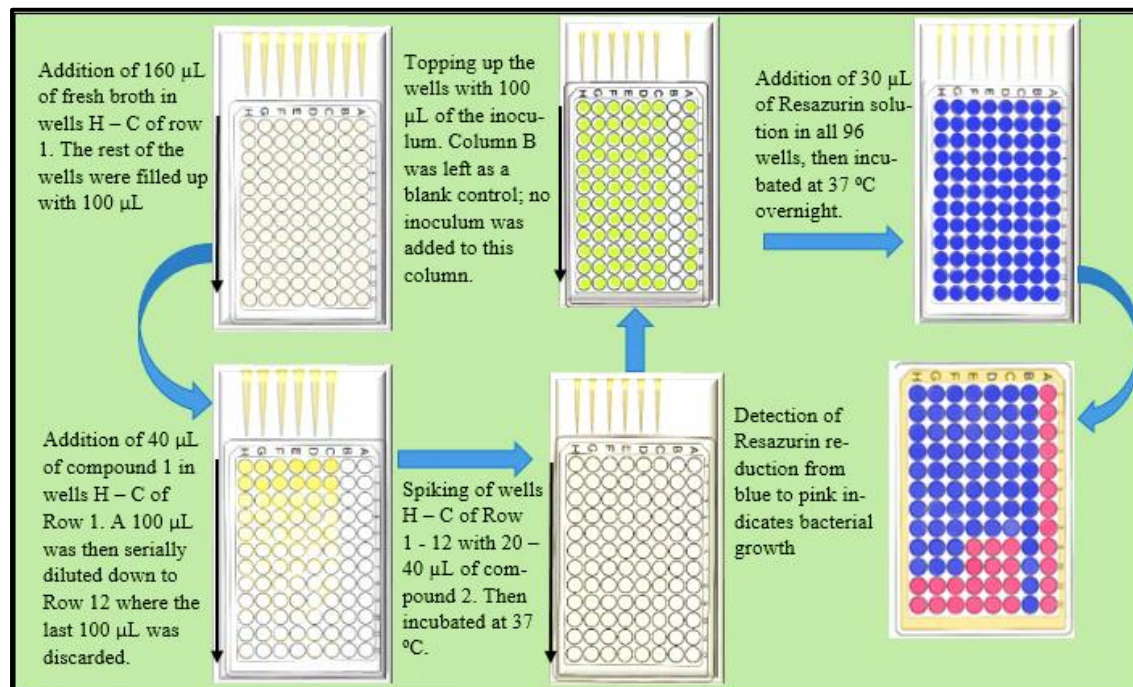
Figure 3.2. A schematic representation of the minimum inhibitory concentration procedure followed in **Section 3.2.5.2.** This figure was compiled and edited by the author of this thesis for the purpose of this section using Microsoft paint 3D and Word tools.

A formula for the calculation of the final MIC was generated and applied as described below:

$$C_a = \frac{V1}{1000} \; X \; C_{1a}$$

Where: C_a refers to compound A, V_1 is the initial volume in the well, and C_{1a} is the initial concentration of the compound added to the well.

To the above, 100 µL of the bacterial suspension was added, resulting in the weight and concentration of compound A being halved, thus resulting in a new concentration for compound A.

$$C_{2a} = \frac{W_a}{T_{Vm}} \; X \; 1000$$

Where: C_{2a} is the new concentration for compound A, W_a represents the weight of compound A, and T_{Vm} stands for the total volume in the well after the addition of the microbe.

Compound B was laced over the contents within the wells at a constant volume, meaning that the concentration was immediately diluted upon addition into the well.

$$C_{1b} = \frac{W_b}{T_v} \; X \; 1000$$

Where: C_{1b} stands for compound B, W is the weight of compound B, and T_V is the total volume in the wells after the microbe has been added.

The following formula represents the total concentration of both compound A and B in the wells:

$$TC = \frac{W_a + W_b}{T_v}$$

Where: TC is the total concentration, W_a is the weight of compound A, W_b represents the weight of compound B, and T_V is the total volume in the well.

3.2.6. Flow cytometry analysis – microbial cell viability assay

The aim of this experiment was to assess the type of cell death experienced by the aforementioned mycobacteria after treatment with combination drugs. The tested concentration used for each INH derivative was retrieved from MIC assay results where INH

and RIF were used as reference for each of the mycobacteria species. Acetone was a solvent in which INH derivatives were reconstituted. As a result, both untreated cells and those treated with 99.9% acetone were used as negative controls. Annexin V-FITC stain was used as a marker for apoptosis in cells where the cell membrane was still intact. This stain is used to quantify apoptosis and allows for distinguishing between apoptotic and necrotic cells by binding to phosphatidylserine (PS) found inside cells with a compromised plasma membrane. On the other end of the spectrum, propidium iodide (PI) was used for identifying dead cells in a mixed population of cells as it can penetrate the damaged cell membrane of dying or dead cells and stain their DNA content, excluding viable cells (Lakshmanan & Batra, 2013). Due to limited sample availability, only samples IBS008, IBS012, IBS013 and IBS017 were evaluated to assess their effects on the cells prior to being tested in combination for the assessment of their effects on the cells when applied synergistically. These compounds were screened against *M. smegmatis*, *M. fortuitum*, MTB H$_{37}$R$_a$ and *M. bovis* BCG. These were also tested synergistically where sample IBS008 was tested in combination with IBS013 and sample IBS012 was tested in combination with IBS017.

Cell apoptosis was determined by employing BD FACSAria^{TM} III Cell Sorter (BD Biosciences, San Jose, USA) following a method as described by (Barr *et al*., 2021). The inoculum mycobacteria were adjusted to 0.5 McFarland standard and treated with drugs at respective MIC obtained from the MIC assay. These were then incubated at 37 ℃ while agitated at 160 rpm for the respective number of days it took each organism to initially grow in broth. The cells were centrifuged at 3 000 rpm for 5 min and resuspended in 600 µL of PBS and stained in a dark room with 10 µL of fluorescein-5-isothiocyanate (FITC) and 10 µL of Alex Fluor 488, and then incubated for a further 30 min. A 70 µm nozzle, side-scatter height (SSC-H) filter was used for cell death determination, whereas phycoerythrin (PE-A) was used for fluorescence-based detection to measure stain excitation. The percentage of stained mycobacterial cells was obtained by using the BD FACSDiva™ Software v8.0.1.

3.3. Results and discussion

3.3.1. Agar and broth culture maintenance

Rapidly growing mycobacteria organisms take anything between one and three days to reach optimum growth, while slow growing mycobacteria take between four and seven days or longer. In most cases doubling time of mycobacteria highly depends on the type of medium and enrichments used, often selected in accordance with the subsequent experiments to be

carried out (Singh & Reyrat, 2009). Mycobacteria are generally creamy mat white in colour and finely wrinkled when growing on agar accessible nutrients as represented in Figure 3.3.1 below. However, when overgrown and stored for longer periods on agar, the colour changes to pale yellow due to carotenoid-like pigment production (Singh & Reyrat, 2009).
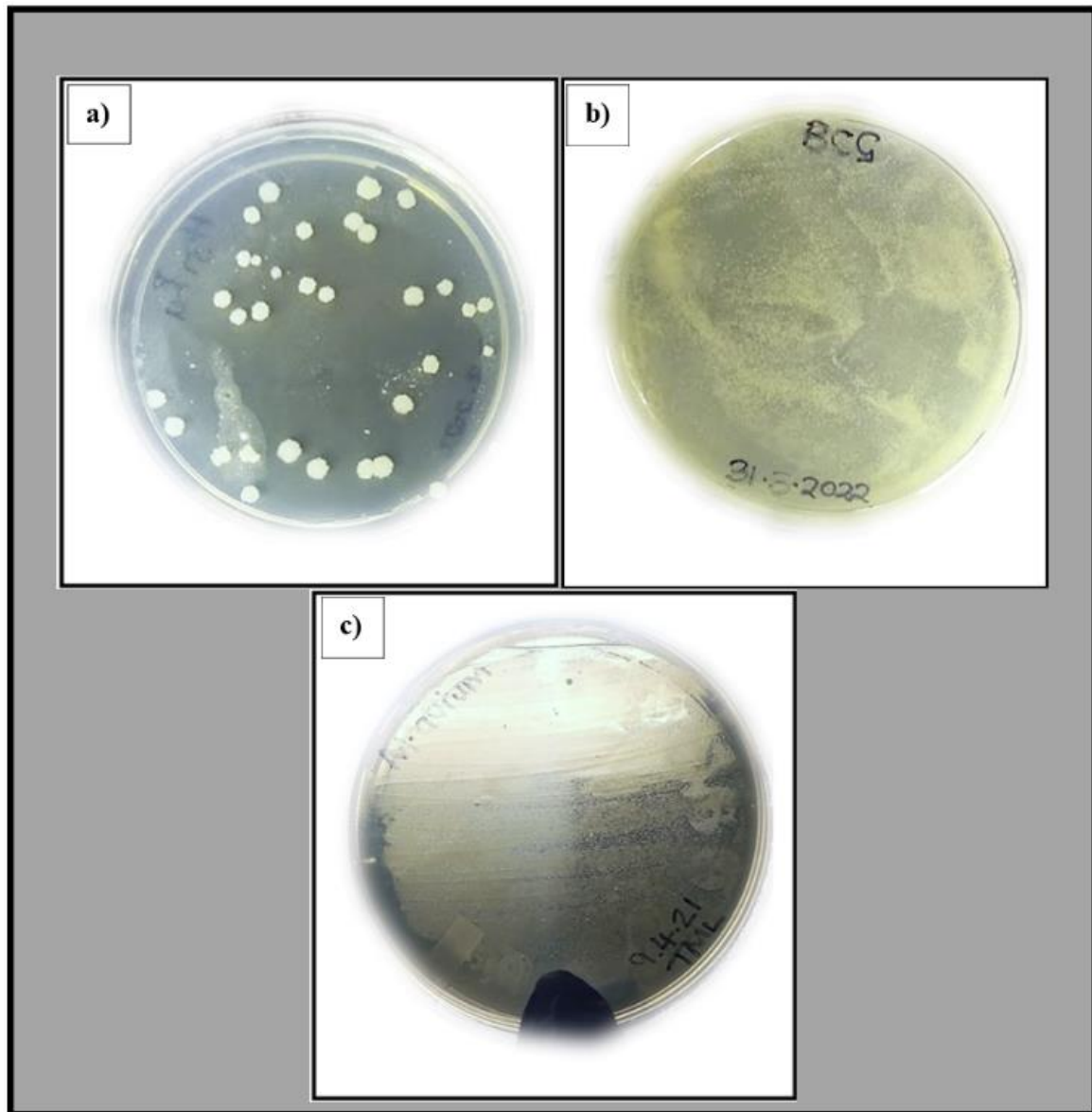
Figure 3.3.1. Image representation of cultured slow growing mycobacteria, where **(a)** represents colonies of the avirulent *M. tuberculosis* – H$_{37}$R$_a$ (ATCC 25177); **(b)** represents lawn culture of *M. bovis* BCG (ATCC 27290); and **(c)** represents lawn culture of *M. avium* (ATCC 25291).

3.3.2. Characterisation and purity confirmation

The resultant agar cultures were used in the microbial characterization step to confirm purity and that they are acid-fast tubercle bacilli/mycobacteria. The cultures were used as inoculum source plates for broth culture growth (as shown in Figure 3.3.3 below) to conduct subsequent experiments, i.e., MIC and flow cytometry. The Ziehl Neelsen (ZN) mycobacteria staining method continues to be the gold standard method employed across many diagnostic and research laboratories. However, this method is not ideal as heat application on carbol fuchsin results in phenol aerosolization which is most hazardous when inhaled in concentrations exceeding the permitted exposure limit (PEL) of roughly 19 mg/m^3.
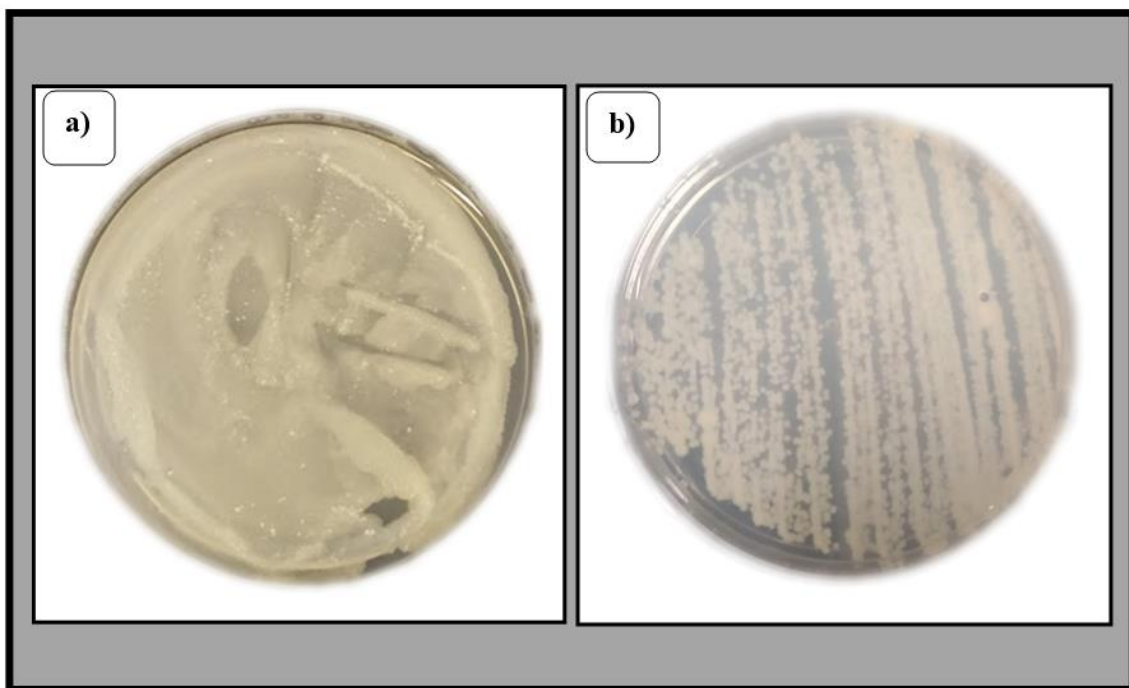
Figure *3.3.2.* Image representation of cultured *rapidly* growing mycobacteria organisms, where **a)** is a hockey stick lawn culture plate of *M. smegmatis* (ATCC 14468); and **(b)** represents loop lawn culture of *M. fortuitum* (ATCC 6841).

The allowed short-term exposure limit (STEL) is roughly 60 mg/m^3 which is impractical considering the number of samples analysed in diagnostic laboratories on a daily basis (Kurup & Chester, 2014). In the quest to prevent exposure to the mutagen phenol, a staining method called the "modified Kinyoun cold stain" (MKC) recommended and introduced by Kurup and Chester (2014) was employed. The MKC staining method can be used as a replacement for the ZN staining method and was employed in this regard as it is equally as effective as the ZN staining method in demonstrating the presence of tubercle

bacilli. The only difference is that MKC uses a highly concentrated phenol and fuchsin for the primary method of staining (Prakoeswa *et al*., 2022).

Figure 3.3.3. *Mycobacterium tuberculosis* $H_{37}R_a$ liquid culture in Middlebrook 7H9 broth enriched with OADC.

After staining, the slides were placed in a slanting position on a piece of paper and allowed to drain. Once the water had sufficiently drained, the slides where then placed in an incubator sets at 37 °C to dry. The slides were thereafter examined under a Zeiss Primo-Star light microscope. The bacilli appeared bright pink in some cases against a blue background as a result of the broth that was fixed during heat fixing and turned blue during staining. Under normal circumstances, mycobacteria bacilli appear as pink/red rods often when stained using sputum and/or blood samples (Holani *et al.*, 2014).

However, this is not always the case. Acid-fast mycobacteria bacilli can appear as red or bright pink odd-shaped lumps especially when stained using laboratory culture as those grow in lumps, hence the use of a detergent to reduce aggregation in broth cultures (Pietersen *et al*., 2020). All cultures gave a positive acid-fast stain result and did not present with any contamination when observed under a light microscope. The images thereof are presented in Appendix 1. Diverse morphology was observed in the bacteria, varying from rod bacilli (*M. smegmatis*) to flat square-like flakes (*M. fortuitum*), to a combination of both (*M. bovis* BCG), spiral-like rod bacilli *(M. tuberculosis* $H_{37}R_a$), and fine small rod bacilli. The slides were labelled inversely (on the flip side of the slide) to prevent the ink from washing off during staining.

3.3.3. Minimum inhibitory concentration

Minimum inhibitory concentration assays are methods that employ the dilution method of broth and/or agar to determine the lowest concentration of an antimicrobial agent required to visibly inhibit microbial growth carried out under a set of well-defined test conditions (Wiegand *et al.*, 2008). It is a technique that would be of great help if employed as a basic diagnostic laboratory assay in determining the MIC of drugs when tested against individual patient samples. Unfortunately, it is a tedious technique that can be an impractical method to adopt in clinical settings with limited resources (Kambli *et al*., 2015).

Minimum inhibitory concentration assay results can be quantified with the aid of digital scanners such as a spectrophotometer. This is mainly necessary when the sample contains an intense colour that needs to be subtracted from the total absorbance by reading absorbance minus the sample colour if necessary, or in instances where there is no colour change or possible visual detection (Gabrielson *et al*., 2002). This technique is also not as reliable as it is perceived to be as the resultant readings may be hindered by factors such as (i) bacterial aggregation, (ii) bacterial, media or treatment pigment, and/or (iii) changes in spectral characteristics of growth media (Grare *et al*., 2008).

In some cases, results can be read and recorded visually without the application of a spectrophotometer (Khalifa *et al*., 2013). However, this approach of bacterial growth assessment is sometimes perceived to lack objectivity and precision but can confidently be employed when applying colorimetric methods that use stains that have an intense and distinct colour. Those are stains such as resazurin and INT which result in clear transition

between bacterial growth and no growth colour change especially where there is no other colour influencing the results, i.e., sample colour (Grare *et al*., 2008).

Resazurin is a nonfluorescent royal blue stain (Alamar Blue) typically reduced to a fluorescent bright pink dye resorufin. The rate of reduction is directly proportional to metabolic activity of viable cells. Where there is no microbial activity, the stain remains royal blue, hence there is a clear distinction between viable and dead cells (Parandhaman *et al*., 2015). With INT, the colourless stain is converted to water-insoluble iodonitrotetrazolium formazan (INTF) which differs in intensity from light pink to dark red and used as an indicator of viability. The colour intensity is proportional to the number of viable cells; however, the rate at which the salt is reduced is not proportional to the number of viable cells as aforementioned (Von Mersi & Schinner, 1991). Where the sample has no colour, the results are easy to read. Therefore, for this purpose, MIC required to inhibit microbial growth was visually deducible (Figure 3.4 below) from experiments conducted with both stains and were not read using a spectrophotometer. The MIC concentrations were calculated manually and recorded in Table 3.3 below for single compounds and in Table 3.4 below for combined derivatives. A full list of concentrations can be found in the Appendix Section (Appendix 2).

3.3.3.1. Minimum inhibitory concentration – single compounds

Out of the 19 compounds synthesised, a few presented with some inhibitory activity against the experimental mycobacteria species. The results were read and deemed final and accurate after 48 h of incubation as some compounds were observed to have bacteriostatic effects on the microbes after 24 h of incubation (as presented by a green line in Figure 3.4 below) and only retained their bactericidal MIC effects after 48 h of incubation (as presented by a yellow line in Figure 3.4 below). The bacteriostatic wells would have a royal blue colour and would turn purple. However, in some instances, the wells would turn bright pink representing 100% bacterial activity. A bacteriostatic concentration is a concentration required to keep an organism in its stationary phase of growth. However, should the concentration not be increased or readded, the organism regains its viable state and continues to multiply. A bactericidal concentration is a concentration required to completely prevent the growth of bacteria (Pankey & Sabath, 2004).

The determining factor of which compounds were to be those of focus throughout the study was the compound's ability to inhibit a fast-growing NTM *M. smegmatis* (ATCC 14468) as it is a naturally INH resistant *M. smegmatis* mutant and was observed to be more resistant to INH and RIF than the ATCC 1441 mutant used in other research laboratories. The results of INH and RIF inhibition effects can be observed in Figure 3.5 (a) and (b) below where MICs for INH and RIF were 32.25 µg/mL (bactericidal) and 0.98 µg/mL (end of plate, the MIC is clearly lower than what was observed), respectively, against *M. smegmatis* (ATCC 1441). For *M. smegmatis* (ATCC 14468), RIF could not inhibit mycobacterial growth but presented with bacteriostatic effect with MIC at 32.25 µg/mL. The results show the strong resistance of this *M. smegmatis* mutant to both anti-mycobacterial inhibitors. The selection was also based on the hypothesis that if a compound modified and synthesised from INH could inhibit the growth of a naturally INH-resistant NTM mutant, then it might be effective against other MTB classified as INT (MDR and/or XDR) resistant.
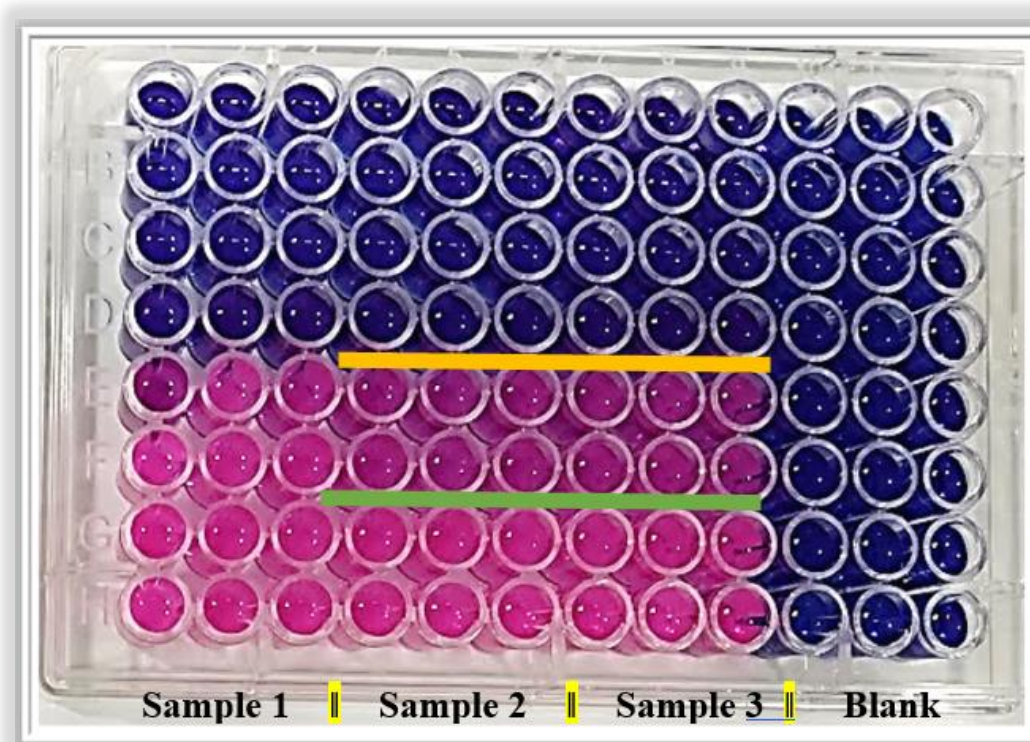
Figure 3.4. An image of MIC results conducted on *M. smegamatis* (ATCC 1441). The yellow line shows the bactericidal MIC, whereas the green line represents bacteriostatic MIC (was blue after 24 h of incubation but turned purple after 48 h of incubation). The image was captured by the author of this thesis.
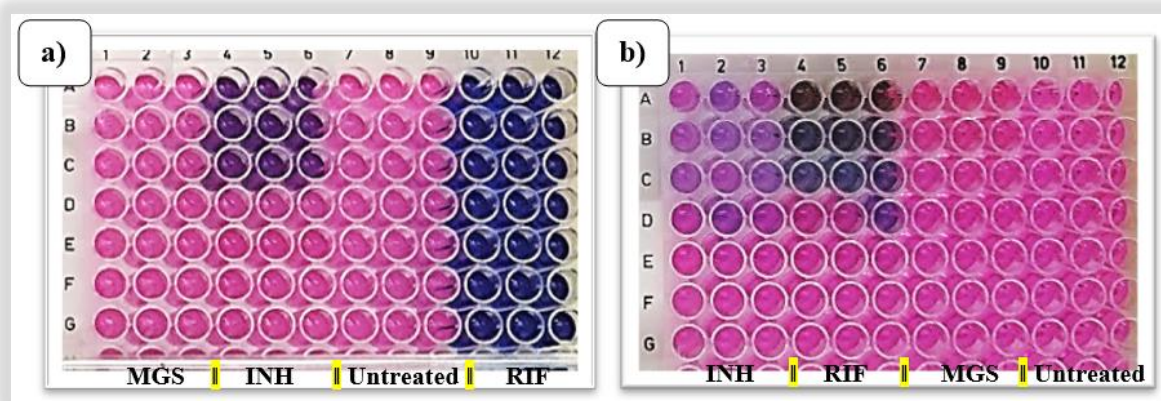
Figure 3.5. A representation of the difference in mycobacterial growth inhibition by both positive controls INH and RIF against **(a)** M. smegmatis ATCC 14411 and **(b)** M smegmatis ATCC 14468.

Samples IBS001 – IBS006 were unable to inhibit growth for all mycobacteria of interest, hence the results were not recorded in Table 3.3 below. None of the samples were able to show some inhibitory properties against *M. smegmatis* (ATCC 14468), whereas samples IBS011 – IBS018 were able to show some inhibition against *M. smegmatis* (ATCC 1441) at the lowest bacteriostatic concentrations of 3.9 µg/mL and bactericidal MIC of 15.6 µg/mL. Positive control INH presented the same bacteriostatic and bactericidal MIC similar to those above. This is somewhat justifiable as all the test compounds were derived from INH. However, a different outcome was expected which seemed to be the case with all other test mycobacteria organisms of interest as reflected in Table 3.3 below. Rifampicin presented with the lowest MIC of 0.25 µg/mL which could be lower than that as these were results recorded on a limited section of the 96 well plate as shown in Figure 3.5 (a) above. From the below results, it is clear that as successful as INH modification was, the derivatives did not have much significant effect as single compounds except against *M. bovis* BCG where seven of the derivatives presented with inhibitory concentrations below 1.0 µg/mL at concentrations of between 0.25 and 0.40 µg/mL, being lower than both INH at 3.9 µg/mL and relatively competitive to those of RIF.

From the results presented in Table 3.3 below, it is evident that the modified derivatives present with some inhibition against the microorganism of choice. However, the concentrations are not as competitive and of significant as compared to those of RIF. There were however, interesting results where some derivatives performed exceptionally well against certain mycobacteria better than the API they were derived from being INH. The

IBS013 derivative performed remarkably well at concentrations as low as 2.84 µg/mL against *M. fortuitum*. The MIC is similar to that of IBS017 and IBS018 against *M. avium*, with IBS010 following closely with an MIC of 3.9 µg/mL against MTB $H_{37}R_a$, performing exceptionally well against RIF whose MIC against MTB $H_{37}R_a$ was 15.56 µg/mL which is about four times weaker than that of IBS010. Interestingly enough, RIF performed slightly weaker against *M. smegmatis* (ATCC 14468) with an MIC of 31.3 µg/mL in comparison to the observed MIC of 0.25 µg/mL against *M. smegmatis* (ATCC 1441), thus confirming that *M. smegmatis* (ATCC 14468) is the most resistant strain of the two as none of the derivatives were able to inhibit its growth at concentrations of 250 µg/mL and below. After this revelation, *M. smegmatis* (ATCC 1441) was eliminated from further experiments and only *M. smegmatis* (ATCC 14468) was pursued. Understanding its mechanism of resistance and genomic differences could be the key in unlocking answers around some of the questions about TB resistance and treatment design.

Table 3.3. Minimum inhibitory concentrations of single drugs per organism

Sample number	Minimum concentration of drugs required to inhibit bacterial growth (µg/mL)					
	M. smegmatis (ATCC 1441)	*M. smegmatis* (ATCC 14468)	*M. fortuitum*	*M. avium*	MTB ($H_{37}R_a$)	*M. bovis* BCG
IBS007	-	-	-	90.90	90.90[*] 11.36[***]	0.40
IBS008	-	-	-	22.72	90.90[*] 11.36[***]	2.59
IBS009	-	-	22.72	90.90	5.68	1.34
IBS010	-	-	45.45	45.45	3.9	10.09
IBS011	45.45	-	-	90.90	-	5.09
IBS012	45.45	-	-	45.45	-	10.09
IBS013	-	-	2.84	11.36	11.36	0.25[*]
IBS014	11.36	-	5.68	11.36	22.72	0.25[*]
IBS015	11.36	-	-	22.72	-	0.40
IBS016		-	-	11.36	90.90	0.40
IBS017	11.36	-	45.45	2.84	11.36	0.25
IBS018	11.36[**] 2.84[***]	-	5.68	2.84	22.72	0.25
IBS019	-	-	-	-	-	-
INH	15.67	22.73[***]	3.9	-	15.65	3.9
RIF	0.25[*]	31.3	0.16[*]	0.98[*]	15.65[*]	0.78[*]

[*]   The concentration recorded was at the last row of the microplate. MIC could be lower than the recorded value.

[**]   The concentration was bacteriostatic due to the purple colour but remained constant days after incubation.

[***]   The concentration was bacteriostatic. All inhibited wells turned purple - pink after 48 h of incubation.

-        No mycobacteria inhibition was observed.

3.3.3.2. Minimum inhibitory concentration – combination drugs/synergy

3.3.4. Flow cytometry analysis

Cell death is an important and necessary process adopted by multicellular/complex animal cells as a way to eliminate invasive pathogens among other things. This process can occur in multiple forms which include necrosis, autophagy and apoptosis (Lakshmanan & Batra, 2013). Necrosis normally occurs as a result of cell trauma often induced by environmental or physical factor that leads to autolysis which results in unwanted toxins that leak during the loss of cell membrane integrity. Apoptosis is different from necrosis in that it follows signal transduction pathways that result in condensed nuclear structure that ultimately breaks down into membrane-enclosed apoptotic bodies which are removed from the system by phagocytosis before they can elicit any immune response such as inflammation and fever among others (Davidovich *et al.*, 2014). There are three different types of autophagy, namely microautophagy, macroautophagy, and chaperone-mediated autophagy. However, in general they are all responsible for self-degradation at lysosome level (Glick *et al*., 2010), thus making apoptosis the most desirable type of cell death among the three (Davidovich *et al*., 2014).

Mycobacterium-induced apoptotic cell responses have been reported. However, the components responsible in evoking such responses are unknown (Derrick & Morris, 2007).Similarly, factors involved in the *Mycobacterium* mechanism of evasion during drug-induced apoptosis within the macrophage cells are not entirely understood. Nonetheless, there is much more evidence in the literature on the possible involvement of the encoded Pro-Glu (PE) and the Pro-Pro-Glu (PPE) proteins in fostering MTB endurance and survival within the host's macrophages by directly increasing macrophage resistance against apoptosis (Xu *et al*., 2023).

Regardless of how little to no information is available around specific events that take place during the processes that lead to *Mycobacterium* host-immunity evasion, a scientific breakthrough has been made, where recent studies have shown that apoptosis can also occur in unicellular organisms in response to factors such as external stimuli which could in turn be beneficial to the host (Häcker, 2013). As rare and as questionable as it may be, the available literature indicates that bacteria can to a certain extent undergo "programmed cell death" where some level of cell signalling plays a role, thus justifying the use of apoptosis

experiments on unicellular organisms to investigate their response to direct stimuli, i.e., oxidative stress or effects of antibiotics, ultimately resulting in antibiotic-induced cell death (Dwyer *et al*., 2012). This type of cell death has been shown to be linked with fluorescently labelled caspase-substrate FITC binding as well as Annexin V cell binding stains (Häcker, 2013).

This evidence thus led to the purpose of this experiment which was to assess the type of cell death experienced by the aforementioned mycobacteria strains in response to the derivatives as single compounds and in synergy. Annexin V-FITC is a stain used to quantify apoptosis and allows for distinguishing between apoptotic and necrotic cells by binding to phosphatidylserine (PS) found inside cells with a compromised plasma membrane. Therefore, Annexin V-FITC was used as a marker of apoptosis in cells where the cell membrane was still intact. At the other end of the spectrum, propidium iodide (PI) was used for identifying dead cells in a mixed population of cells as it can penetrate the damaged cell membrane of dying or dead cells and stain their DNA content but is excluded by viable cells (Lakshmanan & Batra, 2013).

The tested concentration used for each INH derivative was retrieved from MIC assay results listed in Table 3.3 and Table 3.4 above where INH and RIF were used as reference for each *Mycobacterium* species. Acetone was a solvent in which INH derivatives were reconstituted. As a result, both untreated cells and those treated with 99.9% acetone were used as negative controls, and all the negative control results can be viewed in the Appendix Section (Appendix 3). The derivatives were evaluated individually against *M. smegmatis*, *M. fortuitum*, MTB H$_{37}$R$_a$ and *M. bovis* BCG to assess their effects on the cells prior to being tested in combination for the assessment of their effects on the cells when applied synergistically. Flow cytometry experiments were not conducted on *M. avium* due to the extremely low growth rate of the cells and producing very small cells at low concentrations thus not reaching the optimum OD, ultimately resulting in inconclusive results. For reporting and discussion purposes, combination IBS (008•017) was reported as Combination 1, and IBS (015•012) was reported as Combination 2, whereas Combination 3, IBS (009•013) was not tested due to sample quantity limitations. Although there were no MIC results for Combination 2 against *M. bovis* BCG, the concentrations were deduced by applying the calculations as stipulated in the MIC formulae provided in Section 3.2.5.2 above, and the

substitution values were sourced from individual compound MIC values provided in Table 3.3 above.

3.3.4.1. *Mycobacterium smegmatis*

Apoptotic efficacy of derivatives IBS008, IBS012, IBS015 and IBS017 was tested against *M. smegmatis,* all at an MIC of 22.72 µg/mL. As none of the derivatives were able to inhibit the growth of *M. smegmatis* ATCC 14468 after 24 h and were derived by modifying INH, they were tested at the same MIC exhibited by INH, with positive controls INH and RIF tested at 22.72 µg/mL and 3.31 µg/mL, respectively. Untreated cells had 99.9% parent percentage of viable cells benchmarked alongside the acetone sample with 100% of the cells being viable.

As single compounds, IBS008 presented with 40.9% apoptosis rate leaving about 49.5% of cells still viable after treatment; IBS012 presented with a later apoptosis rate of 41.2% resulting in 50% of cells still being viable after treatment; IBS015 presented with late apoptosis rate of 35.8% while leaving 61.6% of cells still viable after treatment; whereas IBS017 presented with only 21.5% of its mycobacterial cells experiencing late apoptosis, leaving a staggering 73.5% of cells still viable after treatment. The results thereof can be observed in Figure 3.6 below where the effect of IBS015 and IBS017 appeared to be slightly weaker when compared to IBS008 and IBS012.

The derivatives were also tested in combination to evaluate their synergistic effects where Combination 1 (0.10 µg/mL) presented with 25.8% of cells having undergone late apoptosis and a remainder of 66.7% of viable cells. Combination 2 (0.10 µg/mL) presented with 29.5% of cells experiencing late apoptosis, 3.2% of the cells experiencing early apoptosis, and 65.3% of the cells remaining viable. The results thereof are presented in the dot plot shown in Figure 3.7 below. The results do confirm that there is a slight improvement when the derivatives are combined, thus suggesting some level of synergism between the two.
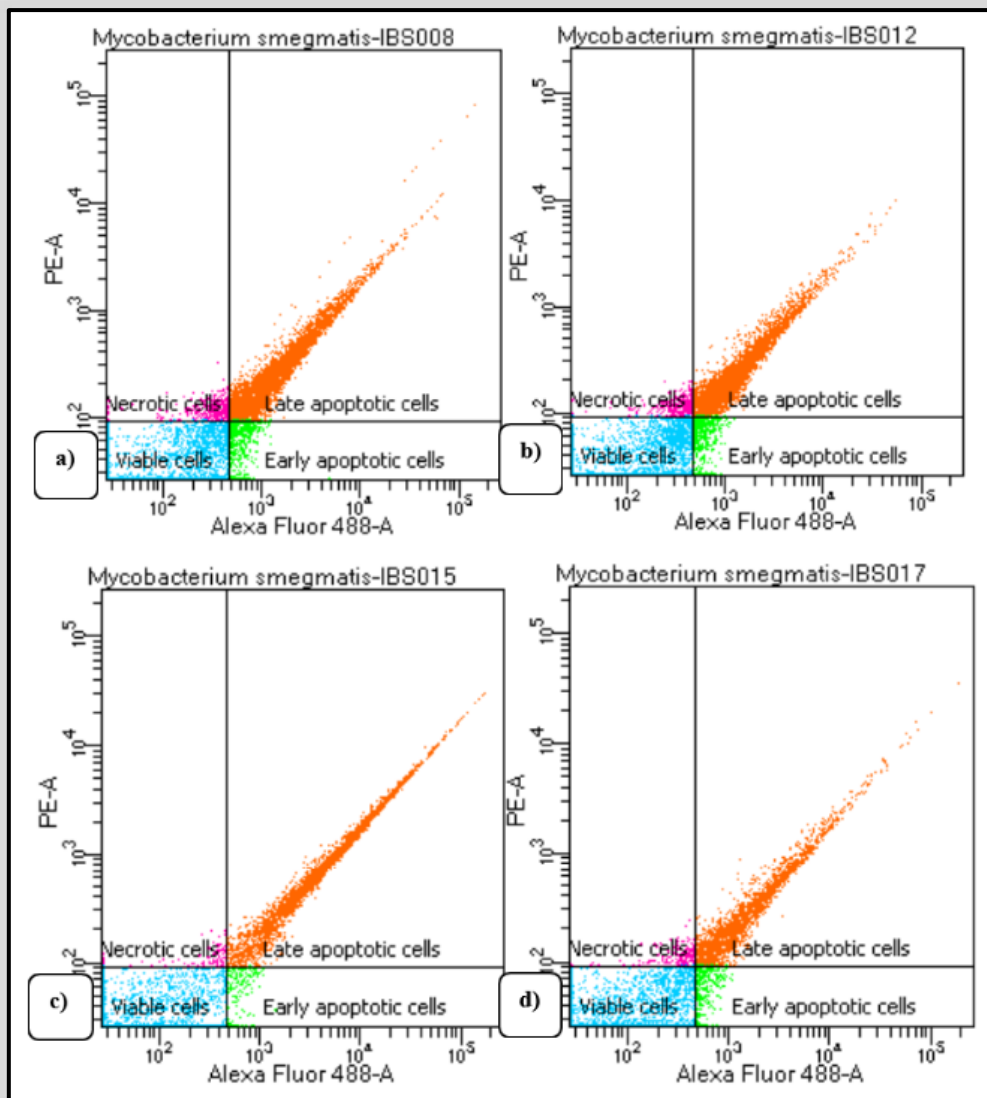
Figure 3.6. An Annexin V-FITC vs. PI dot plot showing the status of *M. smegmatis* cells in various quadrants after 24 h incubation treatment period with derivatives: IBS008, IBS012, IBS015 and IBS017.
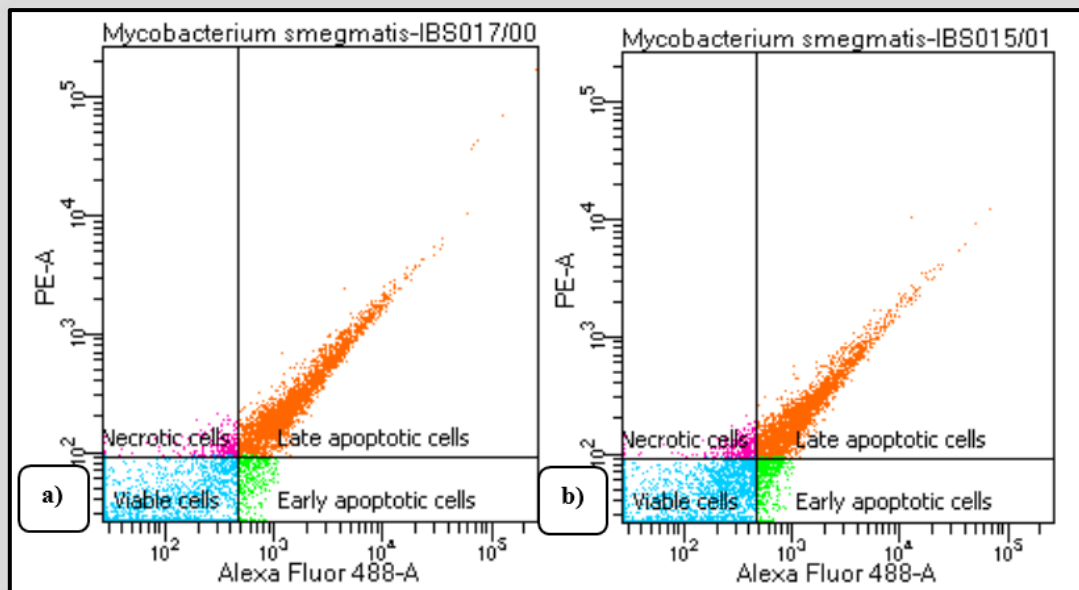
Figure 3.7. An Annexin V-FITC vs. PI dot plot showing the status of *M. smegmatis* cells in various quadrants after 24 h incubation treatment period with combination drugs, where **(a)** is the result of Combination 1, and **(b)** represents the result of Combination 2.
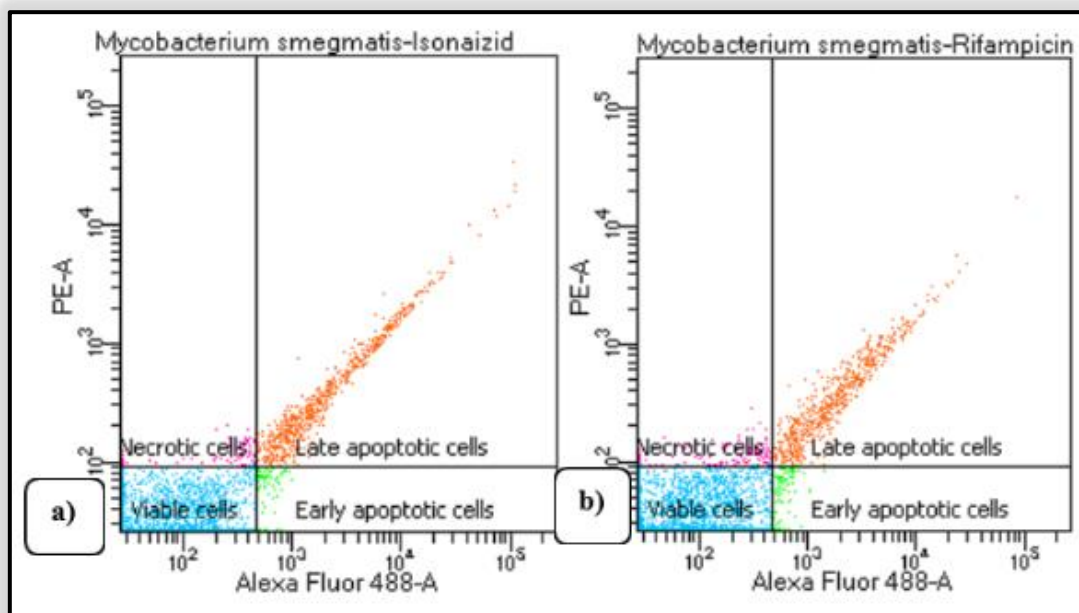
Figure 3.8. An Annexin V-FITC vs. PI dot plot showing the status of *M. smegmatis* cells in various quadrants after treatment with positive controls, where **(a)** is a representative of INH results, and **(b)** is a representative of RIF results.

Positive control INH presented with a 6.6% of *M. smegmatis* cells undergoing late apoptosis, while an astonishing 92.1% of the cells remained viable. For RIF, a 6.6% late apoptosis rate, with a staggering 91.7% of cells remaining viable as reflected in the dot plot presented in Figure 3.8 above. Overall, all test samples presented with less than 2% of early apoptosis, which could be cells that had morphological defects. It is clear that as much as the derivatives present with bacteriostatic results against this strain, the results are undeniably impressive. A large number of cells were found to undergo apoptosis when treated with the derivatives, whereas the leading drugs used as positive controls had close to no effect on the cells as they were both found to affect less than 10% of the mycobacterial cells.

3.3.4.2. *Mycobacterium fortuitum*

The apoptotic efficiency of IBS008 (22.72 µg/mL), IBS012 (0.71 µg/mL), IBS015 (11.36 µg/mL) and IBS017 (1.42 µg/mL) was tested against *M. fortuitum* with the two positive controls INH and RIF tested at 22.72 µg/mL and 2.95 µg/mL, respectively. Untreated cells had 100% parent percentage of viable cells benchmarked alongside the acetone sample which presented with 100% viable cell count and the results thereof can be viewed in Appendix 3.

As single compounds, drug efficiency of derivative IBS008 presented with a late apoptosis rate of 31.7%, with 65.7% of cells remaining viable after treatment; IBS012 presented with a late apoptosis rate of 28.1% while 70.3% of cells remained viable; and IBS015 presented with a late apoptosis rate of 30.8% while 67.31% of cells remained viable; while IBS017 presented with 49.1% of cells dying in the late stage of apoptosis and 48.5% of cells remained viable after treatment. The results thereof are presented by the dot plot of the supplementary data which shows the percentage of viable cells vs. percentage of dead cells after treatment as presented in Figure 3.9. below. Not much difference was observed among the four compounds with regards to their performance against *M. fortuitum*. However, IBS012 seemed to be the weakest performing INH derivative among the four, presenting with the lowest apoptosis rate.
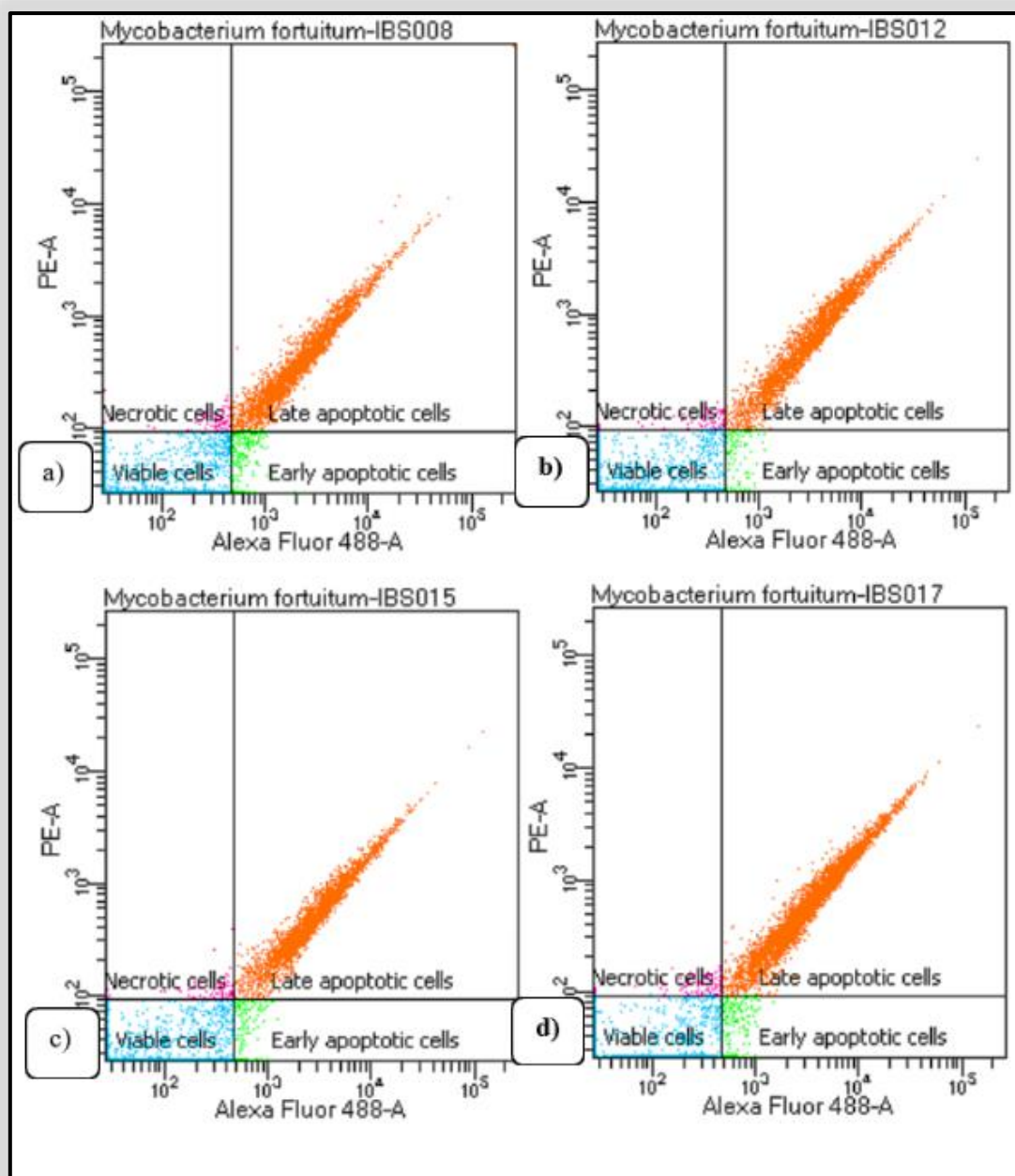
Figure 3.9. An Annexin V-FITC vs. PI dot plot showing the status of *M. fortuitum* cells in various quadrants after 24 h incubation treatment period with derivatives: IBS008, IBS012, IBS015 and IBS017.

As combination drugs, the derivatives were tested against *M. fortuitum* and their synergistic efficacy was evaluated, where Combination 1 was tested at 2.95 µg/mL MIC and Combination 2 was tested at 2.95 μg/mL MIC. Combination 1 presented with a late apoptosis rate of 38.1% while 60.9% of cells remained viable. Combination 2 presented with late apoptosis rate of 42.6% while 67.31% of cells remained viable after treatment; the results

thereof are presented by the dot plot depicted in Figure 3.10 below. While flow cytometry results show an average performance of apoptotic efficacy for Combination 1 against *M. fortuitum*, IBS017 stands a better chance as an individual drug candidate than in combination with IBS008. These findings do not in any way negate the observed improved synergistic MIC results obtained in Section 3.3.3.2 above (image results are presented in Appendix 3). The results are in agreement with the observed MIC results of individual derivative assessments as presented in Table 3.3 above. It seemed to be a different case with Combination 2 where there appears to be additivity and improved apoptotic efficacy in combination as compared to their individual performance for both experiments.
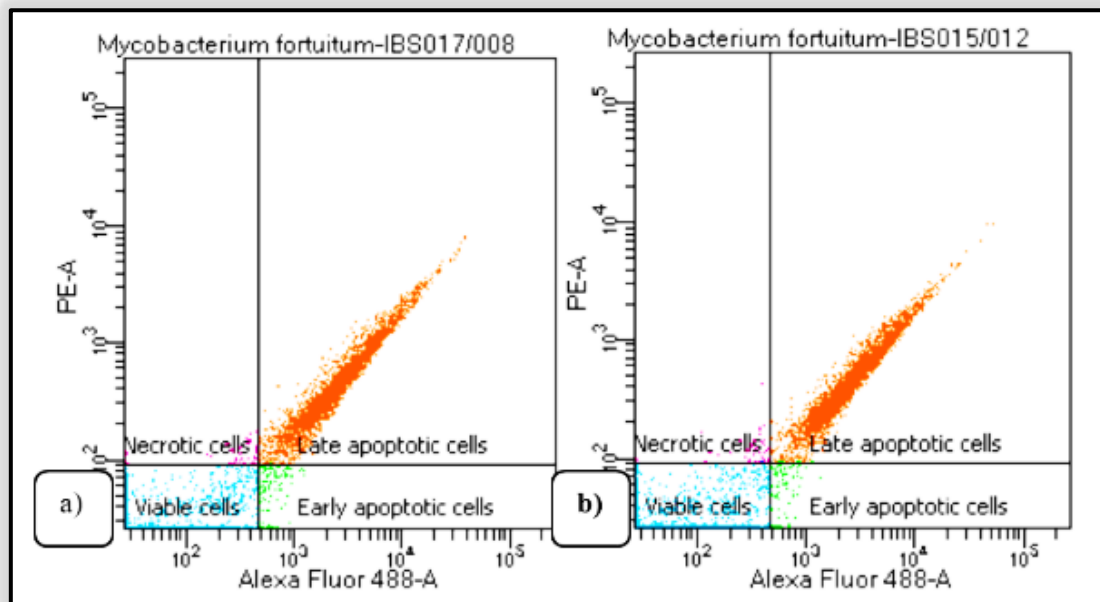
Figure 3.10. An Annexin V-FITC vs. PI dot plot showing the status of *M. fortuitum* cells in various quadrants after treatment with combination drugs: **(a)** represents Combination 1 results; and **(b)** represents Combination 2 results.

Positive controls INH and RIF presented with late apoptosis rate of 36.6% and 0.8%, while retaining viable cells at 60.9% and 98.7%, respectively. The results thereof are presented by the dot plot in Figure 3.11 below. These results are very interesting as they suggest that RIF is less effective against *M. fortuitum* as compared to INH and its derivatives, as shown in Figure 3.11 below. However, MIC results suggest otherwise. It is undisputable when observing MIC results that RIF inhibits *M. fortuitum* at a lower concentration than any of the derivatives with INH following closely behind, but not at equal concentrations. This suggests that RIF may be inhibiting *M. fortuitum* following a different pathway, thus killing the

organism with a cell death method not supported by the stains used in this experiment or a method that results in complete removal of the cell, i.e., autolysis. However, this is not the case, because if autolysis had taken place, then 98% of the cells would not have been detected in the viable cell quadrant.
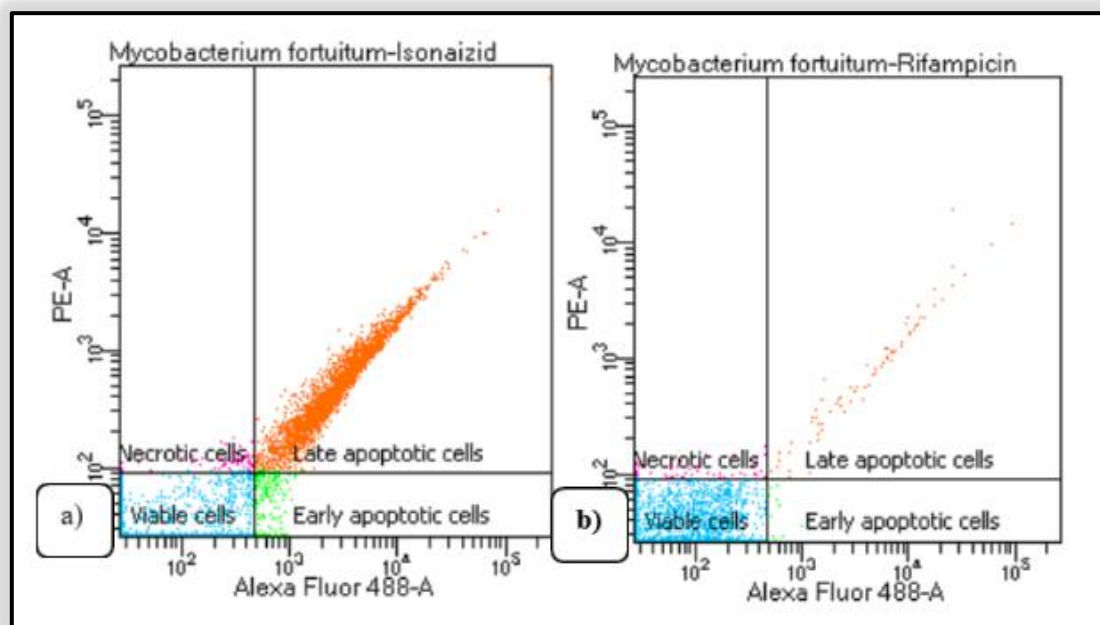
Figure 3.11. An Annexin V-FITC vs. PI dot plot of showing the status of *M. fortuitum* cells in various quadrants after treatment with positive controls, where **(a)** represents INH results, and **(b)** represents RIF results.

3.3.4.3. *Mycobacterium tuberculosis* (H$_{37}$R$_a$)

The apoptotic efficiency of IBS008 (22.72 µg/mL), IBS012 (22.72 µg/mL), IBS015 (2.84 µg/mL) and IBS017 (0.71 µg/mL) was tested against *M. tuberculosis* H$_{37}$R$_a$ with the two positive controls INH and RIF tested at 12.5 µg/mL and 0.19 µg/mL, respectively. Untreated cells had 98.2% parent percentage of viable cells benchmarked alongside the acetone sample which presented with 98.4% viable cell count and results thereof are presented in Appendix 3. Individually, IBS008 presented with 43.2% of cells in the quadrant representing late apoptosis, while 50.7% of the cells remained viable after treatment; IBS012 presented with a strong late apoptosis rate of 64.0% resulting in only 27.1% of cells remaining viable after a 24 h period of treatment; and IBS015 presented with a slightly lower late apoptosis rate of 38.0%, thus presenting with 53.2% of cells being viable after treatment. This also highlights a noteworthy significantly higher early apoptosis rate of 3.9% as compared to the performance

of other derivatives. Lastly, IBS017 also had a relatively strong late apoptosis rate of 50.8% with 49.2% of cells remaining viable after treatment. The results thereof are depicted by the dot plot in Figure 3.12 below.

Figure 3.12. An Annexin V-FITC vs. PI dot plot showing the status of *M. tuberculosis* (H$_{37}$R$_a$) cells in various quadrants after 24 h incubation treatment period with derivatives: IBS008, IBS012, IBS015 and IBS017.

When tested in combination for possible synergistic apoptotic effects, Combination 1 presented with a late apoptosis rate of 4.9% leaving a staggering 94.5% of cells still viable after treatment. The dot plot results can be viewed in Figure 3.13 below. This observation

suggests one of two things, the first being that the interaction between these two compounds is antagonistic, meaning that the derivatives directly influenced each other's performance resulting in an unexpected minimal effect (Tang & Zhang, 2009); and the second being that the mode of resistance against the complex only coded for by this organism in particular is at play. The latter explanation is the most likely favourable scenario considering that this strain is said to be the most resistant and closely related to the virulent strain among the selected group (Nguta *et al.*, 2015).

Even so, these results were shown not to correlate with the observed potency of the combination when tested for its MIC against MTB $H_{37}R_a$, as shown in Appendix 3. Combination 2 seemed to be presenting with slightly similar results as Combination 1, specifically around drug interaction. However, the results are not far off the expected outcome and are in agreement with the observed MIC results also presented in Appendix 3 and in Table 3.4 above.

Figure 3.13. An Annexin V-FITC vs. PI dot plot showing the status of *M. tuberculosis* ($H_{37}R_a$) cells in various quadrants after treatment with combination drugs, where **(a)** represents Combination 1, and **(b)** represents Combination 2.

Apoptotic efficacy of positive controls presented with an impressive apoptosis rate against MTB $H_{37}R_a$ where INH was observed to illicit a late apoptosis rate of 53.9% while 32.3% of the cells remained viable after treatment. Similarly, RIF presented with a solid late apoptosis

rate of 60.8%, thus leaving 31.5% of cells viable after treatment, as shown in the Annexin V-FITC vs. PI dot plot in Figure 3.14 below. Rifampicin seems to outperform most of the derivatives against MTB $H_{37}R_a$, but still lags behind IBS012 (64.0%), which as an individual drug candidate outperforms RIF and all the other derivatives.
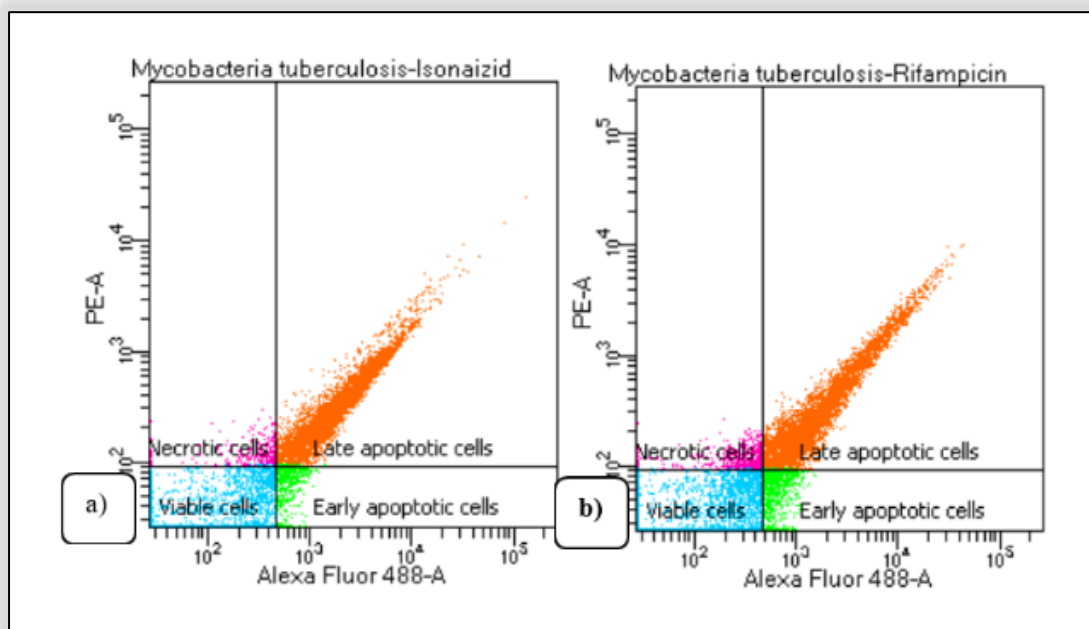
Figure 3.14. An Annexin V-FITC vs. PI dot plot of showing the status of *M. tuberculosis* ($H_{37}R_a$) cells in various quadrants after treatment with positive controls, where **(a)** represents INH results, and **(b)** represents RIF results.

3.3.4.4. *Mycobacterium bovis* BCG

Derivatives IBS008 (2.59 µg/mL), IBS012 (10.09 µg/mL) IBS015 (0.40 µg/mL) and IBS017 (0.25 µg/mL) were tested for their apoptotic efficacy against *M. bovis* BCG with the two positive controls INH and RIF tested at concentrations of 0.71 µg/mL and 0.78 µg/mL, respectively. Untreated cells had 100% parent percentage of viable cells benchmarked alongside the acetone sample which presented with 99.9% viable cell count and the results thereof can be viewed in the Appendix Section (Appendix 3). As single compounds, IBS008 presented with a low late apoptosis rate of 10.7%, leaving 84.5% of cells viable with a notable 4.95% of cell being necrotic. These results are in agreement with those observed in the MIC experiment as presented in Table 3.3 above. Treatment with IBS012 presented with an impressive late apoptosis rate of 62.8%, leaving a mere 24.9% of cells viable after treatment. On the other hand, treatment with IBS015 came close behind with a late apoptosis

rate of 50.8%, retaining 40.5% of cells viable after treatment. Cells treated with IBS017 presented with a late apoptosis rate of 61.0%, with 29.7% of the cells remaining viable. In general, the majority of these compounds were shown to have good inhibitory properties against *M. bovis* BCG and are in agreement with the inhibitory effects observed in MIC results. However, as indicated in MIC results, treatment with IBS008 inhibited *M. bovis* BCG growth at concentrations better than that of IBS012, as presented in Table 3.3 above. The results thereof are presented by the dot plot in Figure 3.15 below.

When tested for their possible synergistic efficacy against *M. bovis* BCG, derivative Combination 1 displayed a noteworthy late apoptosis rate of 52.6% while about 39.8% of the cells remained viable after treatment, as shown in the Annexin V-FITC vs. PI dot plot presented in Figure 3.15 below. Unfortunately, there are no MIC results for Combination 1 against *M. bovis* BCG as previously explained. However, if the MIC results for the individual compounds are to be considered, the concentrations displayed in Table 3.3 support the observed outcome. Combination 2 took the lead with a remarkable late apoptosis rate of 70.9%, while 19.4% of the cells remained viable. To an extent, the observed results support the observed MIC results obtained after 48 h of incubation. They also depict a clear example of synergy, where the combination was found to result in effects greater than the sum of the effects of the derivatives performing in their individual capacity (Tallarida, 2011).

Once again, INH remained consistent and performed slightly better than its commercial competitor presenting with a late apoptosis rate of 46%, while 50.2% of cells remained viable. Positive control RIF performed poorly, presenting with a lame late apoptosis rate of 4.5%, leaving almost all the cells (92.6%) viable after treatment, as shown in the Annexin V-FITC vs. PI dot plot in Figure 3.16 below. These results are similar to those of RIF against *M. fortuitum* presented in Figure 3.11 above. They are however, not in total agreement with MIC results stipulated in Table 3.3 above, it is nonetheless worth noting that the MIC experiments were conducted over a 48 h period of incubation, whereas flow cytometry assays were conducted after only 24 h of incubation. This was because most compounds presented with bacteriostatic results in the first 24 h of incubation where the mycobacteria were kept in their stationary phase and those were the concentrations used to run the flow cytometry experiments. However, the bacteria reverted to their growth state as the drugs became depleted within the experimental wells over the second 24 h incubation period leading to the 48 h incubation mark, thus corresponding to the results tabulated in Table 3.3 above.
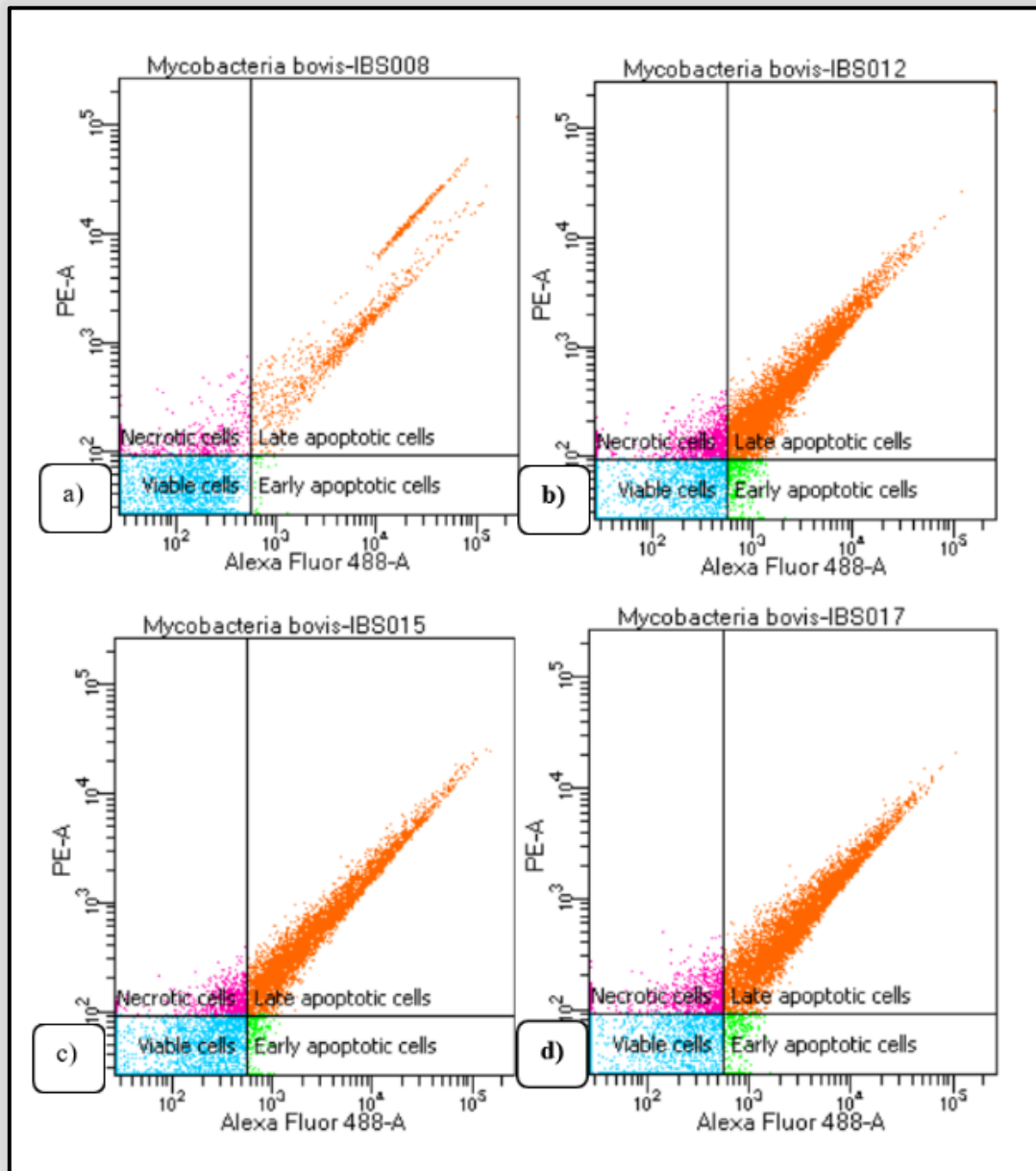
Figure 3.15. An Annexin V-FITC vs. PI dot plot showing the status of *Mycobacterium bovis* BCG cells in various quadrants after 24 h incubation treatment period with derivatives: IBS008, IBS012, IBS015 and IBS017.
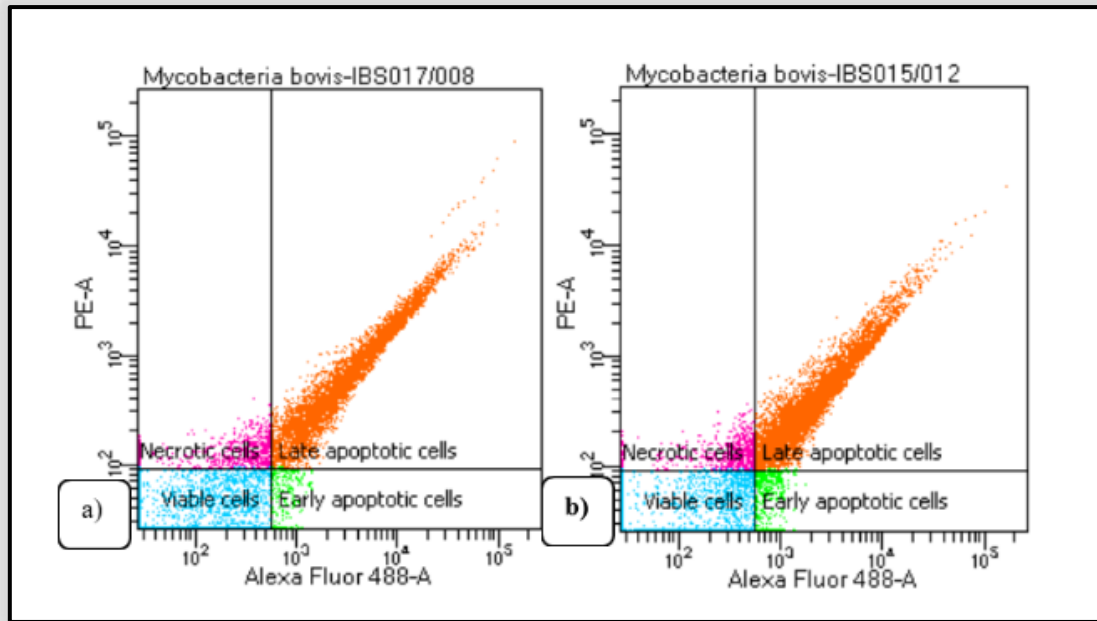
Figure 3.16. An Annexin V-FITC vs. PI dot plot showing the status of *M. bovis* BCG cells in various quadrants after treatment with combination drugs, where **(a)** represents Combination 1 results, and **(b)** Combination 2 results.
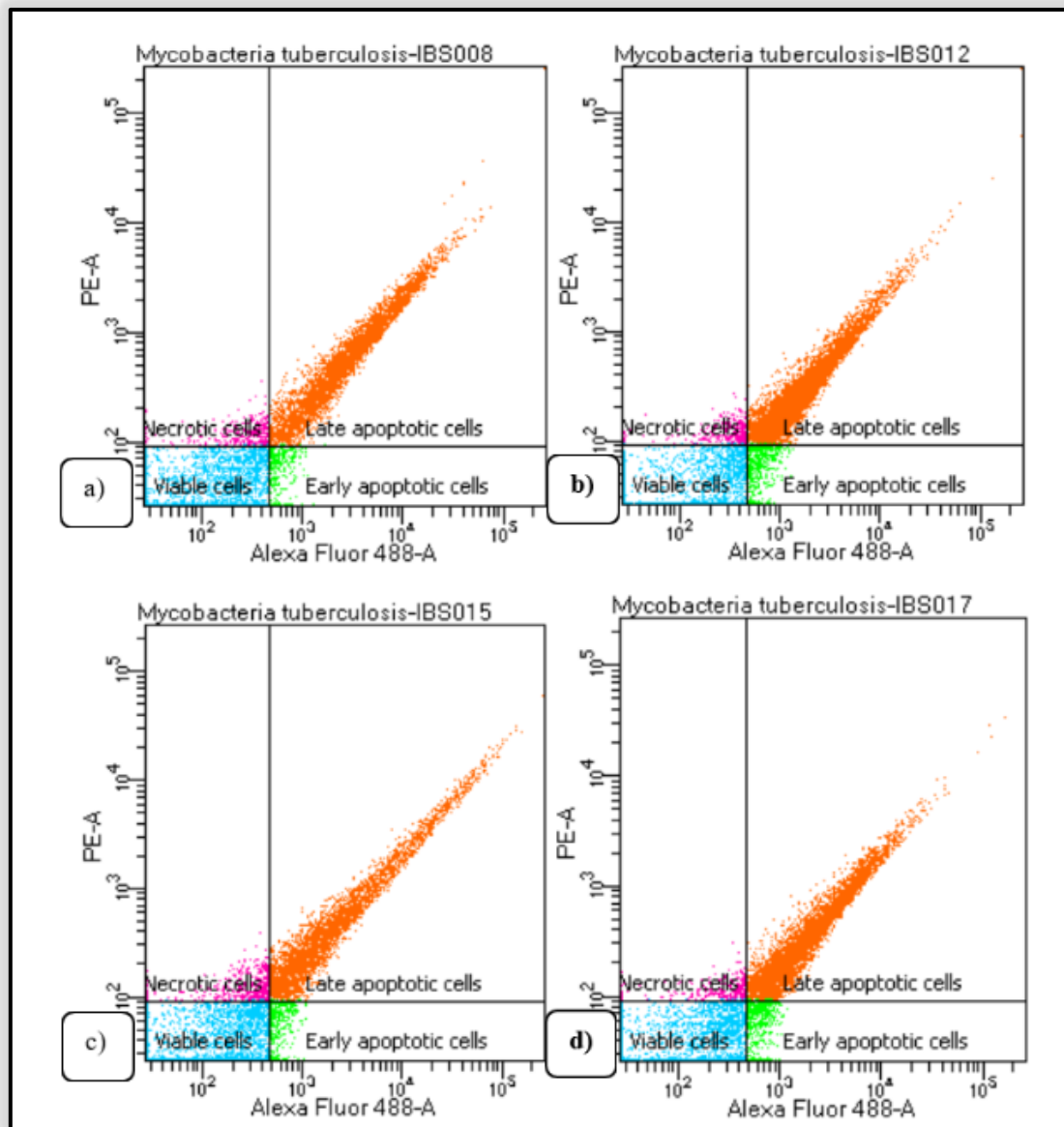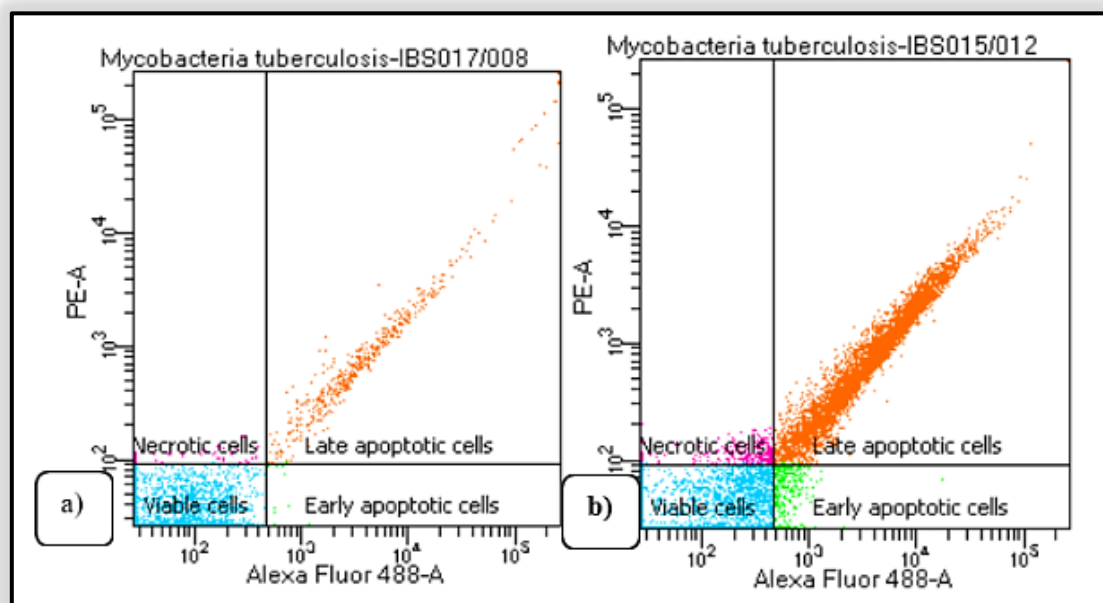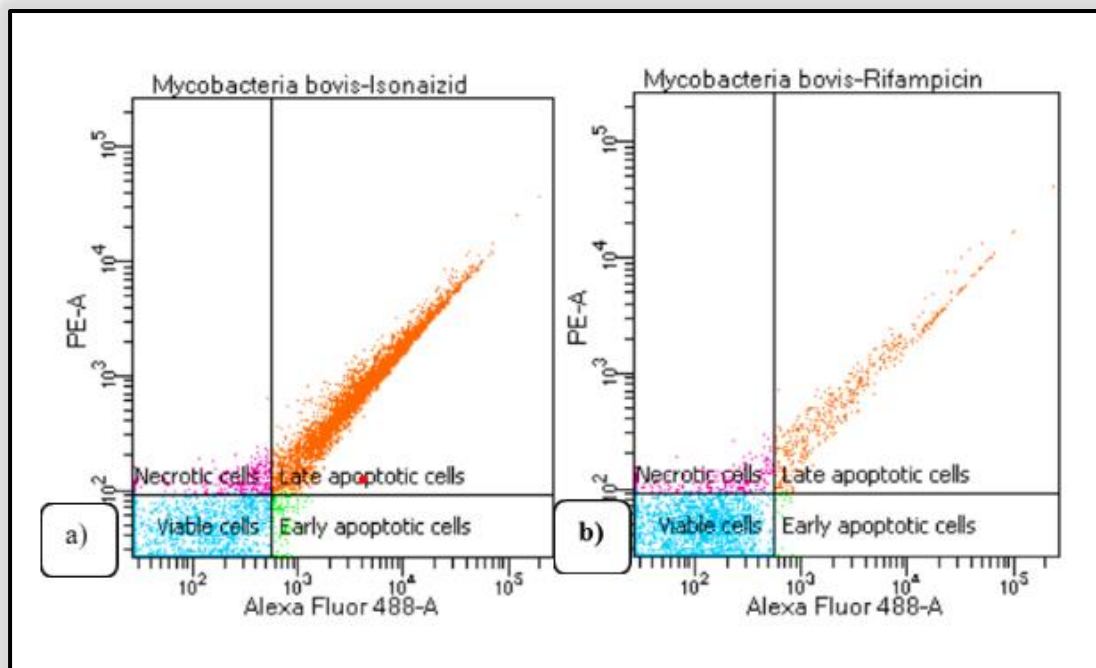

Figure 3.17. An Annexin V-FITC vs. PI dot plot of showing the status of *M. bovis* BCG cells in various quadrants after treatment with positive controls, where **(a)** represents INH results, and **(b)** represents RIF results.

In essence, this phenomenon justifies the observed MIC results versus the flow cytometry apoptosis results (Pankey & Sabath, 2004). Henceforth, the derivatives may seem to present with slightly undesirable MIC results after a 48 h incubation period when compared to the reality of the first 24 h of treatment as depicted in flow cytometry results above. The results confirm that the derivatives do possess potential apoptotic efficacy. The results also suggest that multiple doses as administered to a patient for treatment may prove beneficial and render the derivatives as good drug candidates effective when administered at the correct doses per half-life interval i.e., when administered two or three times a day (within 24 h) per treatment dose (Tallarida, 2011). The results also confirm some level of synergy between some derivatives but also highlight the individual strengths of some derivatives.

There were also some inexplicable discrepancies where RIF was shown to inhibit the growth of *M. bovis* BCG and *M. fortuitum*. There are no known obvious genomic similarities between these two bacteria to explain these results. However, it is an interesting observation worth investigating further, especially since RIF displayed strong inhibitory properties (recorded as MIC) against both bacteria. Overall, the experiment proved that unicellular organisms can undergo apoptosis and that transduction pathways are not limited to multicellular organisms.

3.4. Conclusion

The objective of this chapter was to conduct experiments that would allow the observation of the efficacy of the designed INH derivatives against NTM and clinical isolates in comparison to the main ingredients of the leading TB regimen being RIF and INH. The intention was also to confirm whether modification of INH would yield more effective results in inhibiting not only INH sensitive mycobacteria of interest, but also those that harbour natural resistance against INH. In addition, the objective was also to observe whether the hypothesis that supramolecular modification with salicylic acid would yield an improved efficacy compared to that of the modified INH or not. Lastly, the aim was to determine whether the derivatives displayed any level of synergism when combined in comparison to when performing independently.

The breakthrough was that the derivatives presented with a relatively good inhibition when tested in combination, indicating that they possess synergistic properties. However, it is clear that the concentrations resulting in such MIC results should undergo further flow cytometry

analysis to determine the direct impact on the organisms and the type of cell death elicited. The results also affirm that prokaryotes have the ability to undergo signal transduction induced apoptosis, and that cell death is not necessarily limited to drug-induced necrosis, thus providing further evidence in support of this subject, which is still argued by many as being controversial. Lastly, it might be beneficial to employ different methods of compound modification to produce derivatives with stronger bonds which might result in improved performance. Overall, the objectives of this chapter were successfully met where all questions posed by the intentions set above were answered.

In view of the fact that the results provide evidence that the derivatives can outperform INH and RIF at certain concentrations and that they elicit direct drug-induced apoptosis in the organisms, and also considering that the literature would have us believe that as effective as INH and RIF are, they have intolerable cytotoxic effects on the mycobacterium target host, the following question needs to be addressed: What are the effects of these derivatives in that regard? This issue is discussed in Chapter 4 below.

CHAPTER 4
Drug safety/cytotoxicity screening

4.1.   Drug toxicity, cytotoxicity and safety

The one major contribution of drug development failure in the pipeline stages is the toxicity caused by the drugs themselves (Riss *et al.*, 2013). Most drugs are generally toxic and are found to have toxic effects in varying degrees when consumed, thus making the assessment of the severity of drug-induced effects paramount in drug discovery. How toxic the substance is to an organism is generally referred to as "toxicity", whereas how toxic the substance is to a cell is referred to as "cytotoxicity". Toxicity can also be seen as the severity of the effects on the organism, while cytotoxicity can be seen as the dosage in which the severity is depended upon thus often resulting in cell death (Sun *et al.*, 2019).

Drug safety and toxicity assessment is a vital part of drug discovery as drug-induced toxicities such as kidney, heart, brain and liver have been reported to account for over 70% of drug withdrawals (Fang, 2016). The process of determining drug safety is known as pharmacovigilance. This is a scientific process that examines the activities involved in the detection, analysis, contextualization as well as prevention of adverse effects of complications caused by prospective vaccines or medicine (Setshedi *et al*., 2023). There are three very important phases of pharmacovigilance, and this includes the pre-clinical analysis, clinical trials and post-trial marketing. Information obtained from these phases is important in monitoring drug safety after the drug has been introduced commercially as there might be putative side effects that may still emerge over time (Biomapas, 2022). In most cases, compounds undergo metabolic activation through interaction with reactive intermediates that consequently bind to cell macromolecules resulting in cell-signalling disturbance or cause mutation in DNA adducts. Such toxicity is very difficult to identify or even predict more especially in the early stages of drug development and discovery (Liebler & Guengerich, 2005). When it comes to drug screening for toxic effects, cell-based assays are very useful in measuring cytotoxic and proliferation effects of drugs which may lead to cell death (Riss *et al*., 2013). These assays are used in vast processes mainly to monitor and record signal transduction events that are involved in organelle function, receptor binding expression and cell component trafficking, among other things (Nierode *et al*., 2016).

Often toxic effects caused by concentrations above the upper limit of the therapeutic range are easily predictable based on the drug's pharmacological effects. However, toxicity caused by lower concentrations at cellular level is not easily predictable (Silakari & Singh, 2021). The latter is the sole purpose of this chapter, where toxicity effects of the synthesised drugs are monitored at a cellular level by evaluating cell viability at different concentrations and combinations. There are a variety of these cell-based screening assays. However, this section will focus mainly on the methods employed using multi-well formats where a multi-plate reader, a real-time cell analyser, as well as the MUSE flow cytometry assay used to read the quantifiable results and measure cell viability, respectively.

4.1.1. MTT cell viability assay

The MTT (3-[4,5-dimethylthiazol-2-yl]-2,5 diphenyl tetrazolium bromide) assay is a test routinely used in drug discovery when screening for potential chemotherapeutic drugs (Marks *et al*., 1992). This assay is robust in that it allows for the detection of cell stress when subjected to a toxic substance in instances where there is no direct cell death (Kumar, Nagarajan & Uchil, 2018). It is because of its versatility in detecting the proportional relationship between the total number of cells and total mitochondrial activity that it is used primarily to determine mammalian cell sensitivity and/or viability (van Meerloo *et al*., 2011), thus rendering it an important part of measuring *in vitro* cytotoxicity effects of most drugs on desired cell lines (van Meerloo *et al*., 2011).

4.1.2. Real-time cell analysis assay

Real-time cell analysis (RTCA) is a technique that allows real-time uninterrupted experimental monitoring of cells over time (Yan *et al*., 2018). It is a technology designed to overcome the limitations of traditional drug-screening where markers are used for the quantification of the biological responses such as drug toxicity (Şener *et al*., 2017 and Yan *et al*., 2018). It monitors events such as cell attachment, rate of cell proliferation and morphology label free. Its impendency is highly reliant on the microelectrode biosensor array found on the bottom of the e-plates (Stefanowicz-Hajduk & Ochocka, 2020). These biosensors record alternating current caused during cell adhesion expressed as cell index (CI) value (Şener *et al*., 2017). The RTCA techniques are used in research to assess receptor-mediated signals, compound-mediated cytotoxicity as well as cell related experimental quality control in cell differentiation and proliferation studies (Stefanowicz-Hajduk &

Ochocka, 2020). Therefore, RTCA was employed to determine the concentration of the drugs required to produce negative cytotoxic effects on the cells.

4.1.3. Flow cytometry cell viability assay

Flow cytometry is a very powerful multidisciplinary tool used in molecular biology, virology and drug development among other biological fields of interest (McKinnon, 2018). It is an important multiparametric analytical assay used to assess cell viability, cell cycle, apoptosis and cell concentration, among other inquisitions (Luminex, 2020). There are a few flow cytometry instruments in the market providing a vast array of solutions. To corroborate MTT assay as well as the RTCA results, the Muse® Cell Analyser was employed. This miniature instrument uses fluorescence detection and microcapillary cytometry to provide highly quantitative single cell analytical results which are important in the characterisation of the overall cell health (Luminex, 2020; Lulijwa et al., 2019).

The aim of this chapter was to employ the above techniques in order to gain an understanding in the responsive behaviour of the murine cells to assist in drawing a picture of the effect of the synthesised isoniazid derivatives in comparison to those elicited by the positive controls.

4.2. Materials and methods

4.2.1. Cytotoxicity assays

Cell-based assays make an important part of drug discovery procedures contributing fundamental information around disease progression and biological processes. The majority of cell culture-based assays applied to date are two-dimensional monolayers of cells cultured on planar rigid synthetic surfaces optimised to allow cell attachment and growth. These assays are relatively easy to conduct, cost-effective and are easy to reproduce as compared to animal-based models (Langhans, 2018). For this purpose, RAW 264.7 murine macrophage cells were employed. They are Abelson leukaemia virus-transformed macrophage-like cells derived from the BALB/c mice, commonly used in cell-based studies as they maintain most macrophage properties and are thus ideal for application in immune response studies (Solhaug et al., 2013).

4.2.2. Cell culturing of RAW 264.7 murine macrophage cells

A 1 mL cryovial of frozen RAW 264.7 murine macrophage cells was removed from -80 ℃ storage and thawed at 37 ℃ for 1 – 2 min. The cell suspension was then mixed thoroughly

with a 200 µL pipette, and thereafter transferred to a 25 cm^2 (T25) tissue culture flask with 5 mL of Cellonex Recovery Media (Separation Scientific SA (Pty) Ltd) or maintenance Dulbecco's Modified Eagle Medium (DMEM, Gibco™, Thermo Fisher Scientific Inc. ZA) enriched with Fetal Bovine Serum (FBS, Gibco™, Thermo Fisher Scientific Inc. ZA) as well as 1% Penicillin-Streptomycin (10 000 U/mL of penicillin and 10 000 µg/mL of streptomycin) (Gibco™, Thermo Fisher Scientific Inc. ZA). The flask was then placed in a 5% carbon dioxide (CO_2) incubator set at 37 ℃ to incubate overnight or until cells had adhered to the flask and reached a minimum of 80% confluency, as shown in Figure 4.1 below.

4.2.3. MTT cell viability assay

The MTT assay was employed for its versatility in measuring cytotoxic effects of drugs on murine RAW 264.7 macrophage cells. Cells become stressed when exposed to multiple variants and this happens at different concentrations depending on the toxicity of the substrate. The MTT assay allows for the calculation of the lethal concentration required to kill at least 50% of cells, by measuring the production of a chromogenic by-product from a substrate within a living cell where the tetrazolium salt is converted from yellow to purple by metabolically active cells, as shown in Figure 4.2 below. In essence, the tetrazolium salt is reduced to water-insoluble formazan crystals, thus determining activities within the mitochondria of living cells which is information directly related to the number of viable cells (van Meerloo *et al*., 2011).

Figure 4.1. Image depiction of RAW 264.7 cells at 100% confluency (T-flask surface had 100% coverage). Image captured through a microscope 10X lens during an experiment.

Insoluble purple formazan salt

Yellow tetrazolium salt
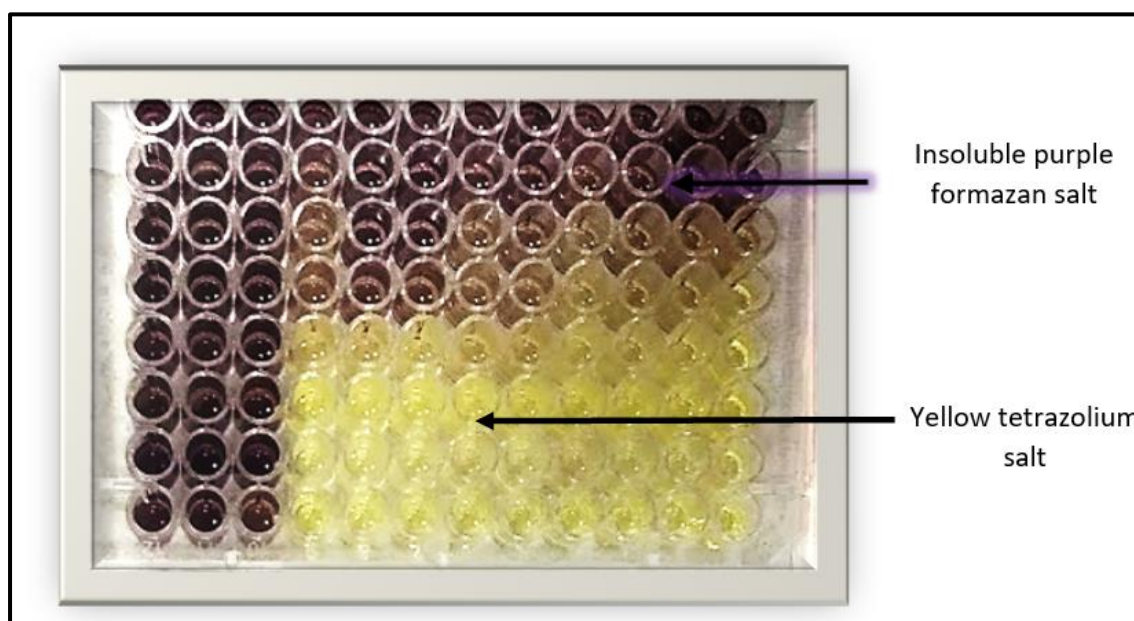
Figure 4.2. RAW 267.4 cytotoxicity assay showing the non-reduced tetrazolium salt and the resultant formazan salt after an experiment.

Previously cultured RAW 264.7 murine macrophage cells were detached using 1 mL of Accutase® (Biowest, USA, Separation Scientific RSA) and incubated at 37 ℃ for one minute or until completely detached. Ideally, to stop the effects of Accutase® and deactivate cell detatchment, ±1 mL of DMEM should be added into the flask. However, in this experiment, 100 mL of DMEM was added to stop the reaction and make up a sufficient volume for

seeding purposes. Approximately 100 µL of roughly 500 – 10 000 cells of the cell suspension were seeded into each well, and then incubated overnight at 37 ℃ in 5% CO_2. After 24 h, treatment drug concentrations were prepared in media using a separate 96 well microtitre plate. Once ready, the media in the experimental 96 well microtitre plate were discarded and replaced with 100 µL of fresh media per well excluding the first row. About 200 µL of experimental concentrations were then transferred from the preparatory 96 well plate into their respective wells of the first row of the experimental microtitre plate. These were then serially diluted down to 100 µL until the last row, where the final 100 µL was discarded. The experimental plates were then re-incubated overnight under previously described conditions. After 24 h, 10 mL of MTT was prepared per microtitre plate (at 5 mg/mL). From the prepared 10 mL of MTT, about 30 – 50 µL was added to each well and then incubated for a further 3 – 4 h. After the incubation period, 100 µL of DMSO was added to each well and incubated for a further 1 h before reading the results at a wavelength of 570 nm. The percentage of viable cells was calculated using the following formula:

$$\text{Cell viability (\%)} = {}^{AT}\!/_{AC} \text{ x } 100$$

Where: *AT* is absorbance of extract or derivative treated cells, and *AC* is the absorbance of untreated cells.

Raw data were used to generate bar graphs (supplementary data available in the Appendix Section (Appendix 5). However, some outlier values had to be omitted to generate a linear graph in order to calculate the R^2 value. This was achieved by employing the below linear regression equation.

$$y = mx + C$$

Where: *m* = slope of the graph, +*m* = positive linear regression, -*m* = negative linear regression. *c* = y-intercept (the point where the line crosses the y-axis) and *x* and *y* coordinates are independent and dependent variables, respectively.

The means ± SD (standard deviation) and the ρ-values (=T.Test) were calculated inbuilt excel formulas.

$$= T.Test(array1; array2; tail; type)$$

Where: array1 = avg, array2 = STDEV, tail = 1 and type = 1.

4.2.4. Real-time cell viability assay

Real-time cell analysis (RTCA) works together with MTT assay. To run the RTCA experiment, the lethal concentration values required to kill 50% of cells were deduced from

the MTT assay results, where 0.5 x LC_{50} and 2 x LC_{50} concentrations were calculated and used in testing samples to determine the effect of the drug at half the dosage as well as double the dosage of the LC_{50} in addition to the standard LC_{50} concentration tested. This means that the tests were run in triplicate. Due to the cost of running this experiment, only compounds that gave significantly good inhibitory results against mycobacteria species were screened for their toxicological effects on the RAW 264.7 murine macrophage cells as presented in Table 4.1. below.

Previously cultured RAW 264.7 murine macrophage cells were first rinsed with CELLOTION™ (Nippon Zenyaku Kogyo Co., Ltd., Japan, distributed by Separation Scientific RSA) and then detached with Accutase® and incubated at 37 ℃ for 1 min or until completely detached. The process was stopped by the addition of media equivalent to the volume required for the number of electronic cell plates (E-plates) analysed. The cells were then seeded at a concentration of 1.9 x 10^5 into the 16 wells of the E-plates, and then placed into the RTCA DP (dual purpose) system (xCELLigence RTCA DP System, Agilent Technologies, Santa Clara, California, USA) for monitoring. Once the cells had settled and stabilised in the wells, microelectrode biosensor stability and accuracy were assessed by running two sweeps over one minute before setting the experimental schedule. The instrument with the cells was then placed in a 5% CO_2 incubator and incubated for 24 h where cell adhesion, splitting and other activities were recorded using RTCA software (version 2.0.0.1301; Agilent, Santa Clara, CA, USA). After 24 h, the cell activity recording was stopped in order for the cells to be treated with the drugs. After addition of the drugs, the E-plates were placed back into the RTCA instrument and back into the incubator for a further 24 – 48 h.

Table 4.1. Samples tested for drug toxicology analysis using RTCA at 0.5 x LC_{50} and LC_{50} (µg/mL) obtained from MTT assay.

Sample number	Lethal concentration required to kill 50% of cells (LC_{50}) (µg/mL)	
	0.5 x LC_{50}	LC_{50}
IBS 008	60.23	120.47 $\pm$ 9.0[#]
IBS 009	41.71	83.42 $\pm$ 24.5[#]
IBS 012	40.91	81.18 $\pm$ 10.5[#]
IBS 013	80.02	164.04 $\pm$ 14.8[#]
IBS 015	75.84	151.58 $\pm$ 10.5[#]
IBS 017	93.11	186.21 $\pm$41.3[#]
INH	[*]-	186.97 $\pm$ 14.0[#]
RIF	[*]-	98.40 $\pm$ 15.4[#]

* - No concentration at 0.5 x LC50 was tested for these samples

Mean values reported as $\pm$ SD; # p < 0.001; ## p = 0.001

The samples worked very well in synergy and so they were tested as individual compounds as well as in synergy and in triplicate as represented in RTCA schedules given in Table 4.2. below.

Table 4.2. Samples tested in synergy (guided by minimum inhibitory concentration assay results) for drug toxicology analysis using RTCA at 0.5 x LC, LC_{50}, and 2 x LC_{50}.

Sample number	Lethal concentration required to kill 50% of cells, LC_{50} (µg/mL)		
	0.5 x LC_{50}	**LC_{50}**	**2 x LC_{50}**
IBS 008:017	155.41	$310.81 \pm 11.9^{\#}$	621.62
IBS 009:013	55.92	$111.84 \pm 22.3^{\#\#}$	223.68
IBS 015:012	184.87	$369.75 \pm 1.6^{\#}$	739.50
INH	93.48	$186.97 \pm 14.0^{\#}$	373.94
RIF	49.20	$98.40 \pm 15.4^{\#}$	196.80

* - No concentration at 0.5 x LC50 was tested for these samples

Mean values reported as $\pm$ SD; # $p < 0.001$; ## $p = 0.001$

4.2.5. Flow cytometry cell viability assay

Cells prepared for RTCA (outlined in Section 4.3.4. above) were split for two experiments, the second of which was flow cytometry analysis. The cells were cultured in 9 well plates to reach around 80 – 100% confluency. The cells were then treated with the respective concentration of combination drugs in triplicate, as outlined in Table 4.2 above, and then incubated at 37 ℃ in an incubator with 5% CO_2 saturation over 48 h. Wells of untreated cells were also cultured to run as blank controls in the experiment. After the 48 h incubation period had passed, the cells were gently rinsed with CELLOTION™, and then gently scraped off the bottom of the wells, transferred into 1.5 mL conical tubes, and vortexed gently at 1 500 rpm for 5 min to separate the cells into single cells in solution. The concentrations were adjusted to 1×10^6 cells/mL at a dilution factor of 20/20 µL. A volume of 380 µL of Muse$^{®}$ Count & Viability Reagent was added to 1.5 mL tubes and topped up to 400 µL by adding 20 µL of the cell suspension. The tubes were mixed by pulse-vortexing, and then incubated for 5 min at room temperature before being analysed with the Guava® Muse® Cell Analyzer (Luminex Corp., Austin, TX, USA) equipment with intuitive cell analysis software.

4.3. Results and discussion

4.3.1. MTT assay

In this study, 19 crystal and co-crystal compounds were designed and synthesised. Compound selection was determined by minimum inhibitory concentration assay results conducted on various mycobacteria species as detailed in Chapter 3 above. As a result, only six isoniazid derivatives (covalent and supramolecular modifications of isoniazid) were screened for their possible cytotoxic effect on RAW 264.7 murine macrophage cells as described by (More & Makola, 2020). The compounds were tested alongside positive controls isoniazid (INH) and rifampicin (RIF) (Hundie *et al.*, 2016), and evaluated at concentrations ranging between 3.0 and 200 µg/mL, respectively, in cells seeded at concentrations of 3.308 x 10^5 cells/mL. The compounds were also tested on cells such as Hek 293 and MCF cell lines, but the results reported in this section are those of the toxicological effects on macrophage cells as those are known to be mycobacteria target cells. Once analysed, the lethal concentration enough to kill 50% of the cells was recorded as LC_{50} (More & Makola, 2020).

The concentrations were calculated using trendline coefficient with a Goodness-of-Fit (R^2) ≥ 0.800. Upon evaluation of the results, it was observed that the majority of these compounds have a relatively low toxicity. For most samples, the concentrations required to kill 50% of the cells were higher than 100 µg/mL as shown in Table 4.3 below. Interestingly, IBS009, IBS012 and RIF presented with a relatively low LC_{50} (between 81.18 and 98.04 µg/mL) to kill 50% of the cells. However, these concentrations still do not reflect the actual behaviour of the cell in response to drug exposure. The plot diagrams/graphs of the concentrations can be viewed in Appendix 4. As previously mentioned, raw data were used to generate graphs. However, some outlier values had to be omitted to generate a linear graph in order to calculate the R^2 value using the linear regression equation. Henceforth, concentrations tabulated in the table below may differ slightly to those visually deduced from the graphs in the appendices. The actual behaviour and concentration effects of these compounds on RAW 264.7 are observed and discussed in RTCA and flow cytometry results in Sections 4.3.2 and 4.3.3 below.

Table 4.3. MTT assay lethal concentration of drugs required to kill 50% (LC_{50}) of RAW 264.7 cells.

Sample number	Lethal concentration required to kill 50% of cells (LC_{50} µg/mL)
IBS008	$120.47 \pm 9.0^{\#}$
IBS009	$83.42 \pm 24.5^{\#}$
IBS012	$81.18 \pm 10.5^{\#}$
IBS013	$164.04 \pm 14.8^{\#}$
IBS015	$151.58 \pm 10.5^{\#}$
IBS017	$186.21 \pm 41.3^{\#}$
INH	$186.97 \pm 14.0^{\#}$
RIF	$98.40 \pm 15.4^{\#}$

* - No concentration at 0.5 x LC50 was tested for these samples

Mean values reported as $\pm$ SD; # $p < 0.001$; ## $p = 0.001$

4.3.2. Real-time cell analysis

Real-time cell analysis (RTCA), a cellular biosensor platform that allows for an instantaneous, continuous, label free cell analysis in real-time over the duration of an experimental test (Yan *et al.*, 2018) was employed to provide a holistic understanding of the effects of the drugs on the cells. It is important to note that a higher or lower drug concentration required to induce its half-maximal effective concentration (EC_{50}) on the cells does not necessarily pose a reflection of its toxicity or toxic concentration required to negatively affect the mammalian cells.

The assay can be conducted in microplates ranging between 16-, 36-, and 96-well plates. Given the cost implications, it was not justifiable to perform such an expensive experiment to screen the performance of non-active compounds. It is therefore for this reason that only six samples (IBS008, IBS009, IBS012, IBS013, IBS015 and IBS017) were assessed for their toxicology effects on the RAW 264.7 murine cells using xCELLigence RTCA experiment. The compounds showed satisfactory inhibition against mycobacteria species of interest and were screened based on their MIC results as reported in Chapter 3 above.
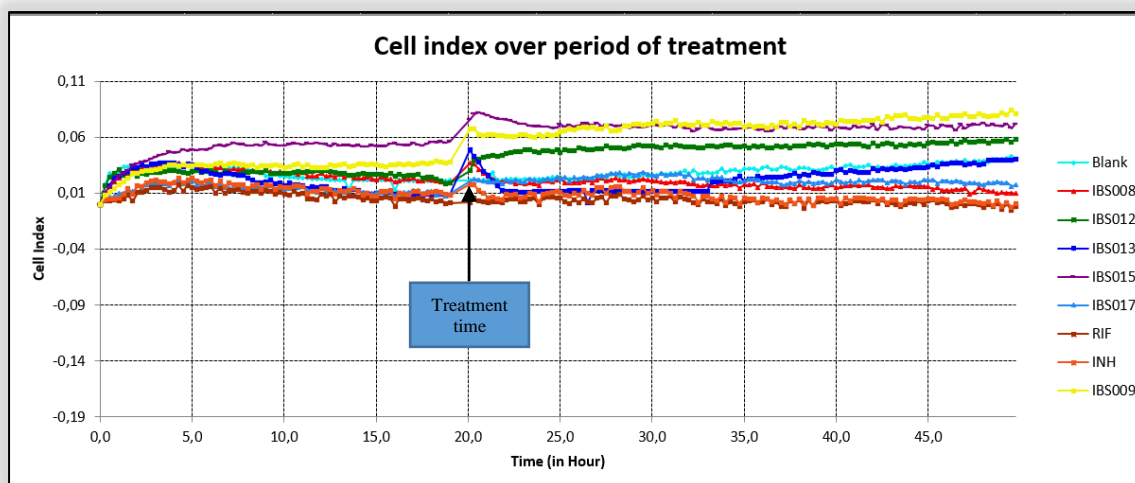
Figure 4.3. Cell index over period of treatment using the xCELLigence RTCA system

The six aforementioned compounds of interest were tested at LC$_{50}$ as reflected in Table 4.1 above. The experiments were conducted in triplicate where concentrations of 0.5 x LC, LC$_{50}$ and 2 x LC$_{50}$ were tested, respectively, and reported as an average (one line per triplicate). These were run against positive controls INH and rifampicin (RIF) that were only tested at one concentration of LC$_{50}$ in triplicate, also reflected in Table 4.1 above. The negative control was a blank batch of RAW 264.7 murine macrophage cells also run in triplicate and reported as an average like those of the test compounds.

In general, the cells did not seem to be performing well prior to treatment at 20 h after initial seeding as shown in the RTCA plot presented in Figure 4.3 above. However, after treatment, some cells in some wells seemed to recover and ultimately thrive and this could be attributed to by two factors, the first being the supplement of fresh nutrients while able to tolerate the presence of the treatment drugs; and the second being some possible growth enhancement attributed to the treatment drugs. Whichever the reason, it is safe to assume that the derivatives in the treatment wells are not toxic to the macrophage cells.

This also supports the hypothesis that a high concentration responsible for killing 50% of cells in MTT assay does not necessarily translate into a toxic compound. This was bluntly presented by the LC$_{50}$ values of samples IBS015 (151.58 µg/mL) and IBS013 (164.04 µg/mL) which were relatively higher than LC$_{50}$ of INH (186.97 µg/mL) and RIF (98.04 µg/mL). Samples IBS009 (83.42 µg/mL) and IBS012 (81.18 µg/mL) followed the same trend and seemed to be supporting cell growth and showed no signs of toxicity towards the cells

presenting with CI at ranges between 50% and > 60% after 45 h. In contrast, both negative controls together with IBS017 (186.21 µg/mL) and IBS008 (542.10 µg/mL) presented with a continuous downward trend where the cells seemed to die all together from the point of treatment throughout the duration of the treatment, mainly observed for both the negative controls, which is in agreement with a report by Zhang *et al*. (2012) which states that INH and RIF could increase liver toxicity thus resulting in decreased cell survival rate of liver cells.
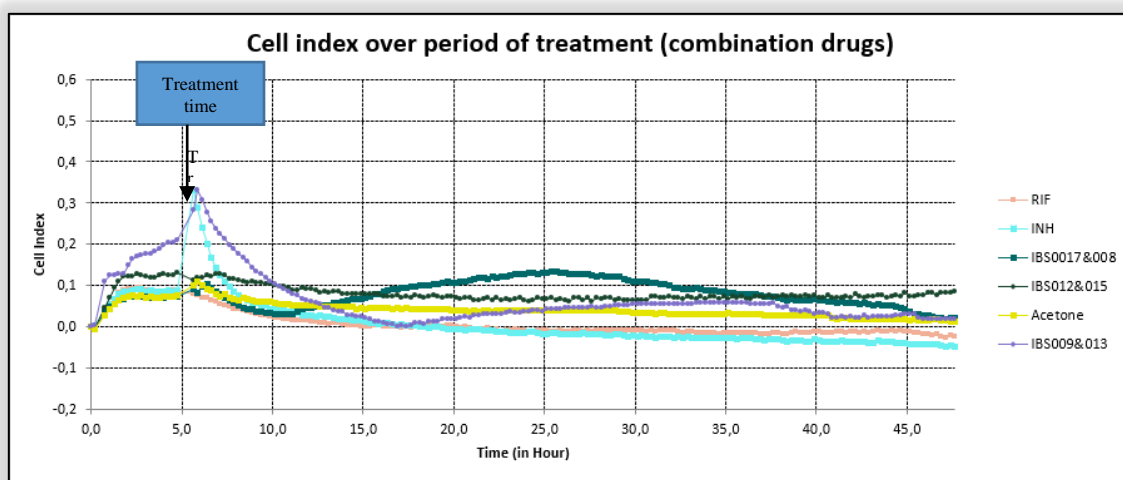
Figure 4.4. Cell index graph over period of treatment for combination drugs using the xCELLigence RTCA system.

Due to the synergistic inhibitory properties observed, cytotoxicity of combination drugs was also tested in amalgamation sequence, namely IBS008•IBS017, IBS009•IBS013 and IBS012:IBS015, respectively. The LC_{50} tests were run in triplicate, similar to those reported above for the toxicity monitoring of single compounds. In this section, due to the possible toxicity effects on the cells as a result of exposure to combined drugs, acetone was added and screened as a negative control in addition to RIF and INH to mitigate possible effects of the solvents on the cells.

The results seemed to be in agreement with those of single compounds, where INH and RIF presented with some toxic effects on the cells throughout the duration of the experiment. Combination IBS009•IBS013 as well as IBS008•IBS017seemed to affect the cells harshly after treatment of 5 h. However, the cells soon stabilised at very low concentrations of nearly 0%, and then recovered to a peak of 6% and 13% until they started dying shortly after

incubation times of 38 h and 30 h, respectively. Combination IBS012•IBS015 appeared not to have an adverse effect on the cells. No adverse effects were observed after treatment and the cells, although not actually thriving, remained constant, with a slight incline in the plot towards the end of the experiment and with an incline to 10% at nearly 45 h post exposure (± 50 h on plot in Figure 4.4 above). It is therefore presumed that acetone did not pose any contributory effects on the cells as although the cells did not thrive, they were consistently stable.

4.3.3. Flow cytometry cell viability

The aim of this experiment was to assess the effects of the derivatives on RAW 264.7 murine macrophage cells after treatment. The tested concentration used for each INH derivative were retrieved from MIC assay results where INH and RIF were used as reference drugs. Acetone was a solvent in which INH derivatives were reconstituted. Untreated cells were used as negative control and can be viewed in Appendix 6.

The flow cytometry cell viability assay results presented in Figure 4.5 and Figure 4.6 below show the concentration of viable cells versus concentration of dead cells after treatment with combination drugs. With reference to both the MTT assay and the RTCA analysis, the results for combination IBS008•IBS017 confirm that even though some cells died during this period of drug exposure, a substantial amount remained viable post 48 h of exposure to the drugs. However, this does not indicate how the cells died and does not confirm whether cell death was due to natural cell death at the end of a cell cycle or caused by exposure to the drugs. It does confirm that if the cells were indeed under severe stress as a result of drug presence, then most if not all of the cells would have died and not survived as depicted in Figure 4.6 presented below for combination IBS012•IBS015 which is very much in agreement with the constant cell performance level presented in the RTCA results shown in Figure 4.4 above.
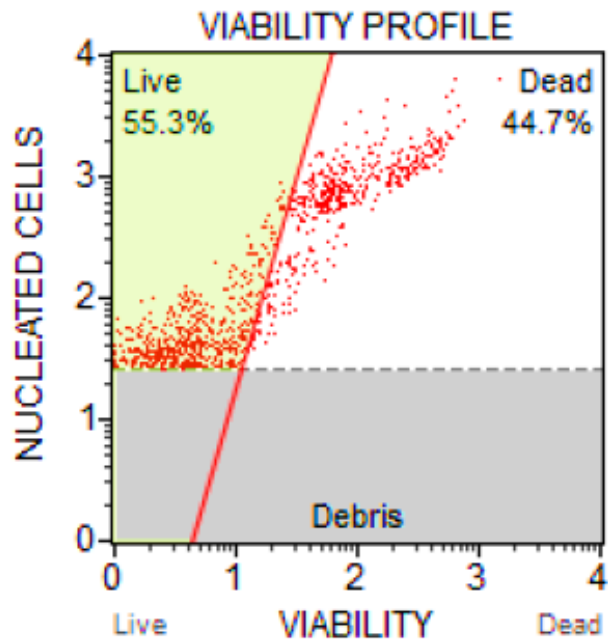
Figure 4.5. Cell viability results after 48 h treatment with combination drugs IBS008•IBS017**.** The dot plot highlights a clear division between living and dead cells.
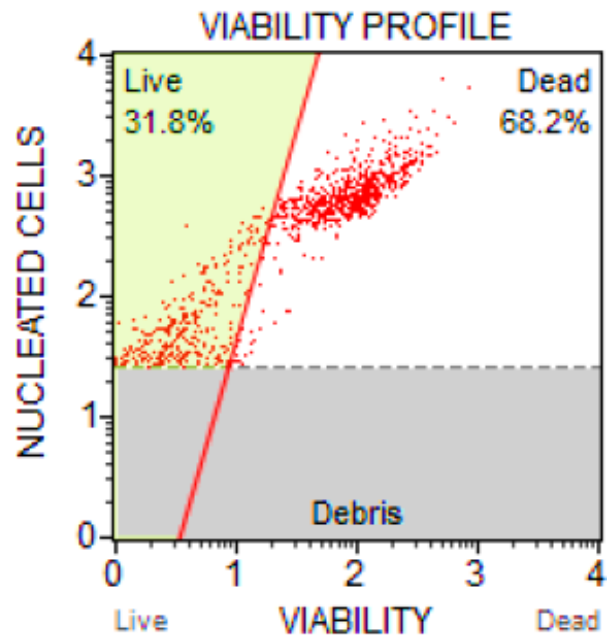
Figure 4.6. Cell viability results after 48 h treatment with combination drugs IBS012•IBS015. The dot plot highlights a clear division between living and dead cells.

These results do show that the cells exposed to this combination did not thrive and grow after stabilisation post drug exposure. Instead, they remained viable at the same concentration of 31% and did not peak significantly as compared to cells treated with other drug combinations. This performance could have been attributed to a number of factors including but not limited to poor cell health, cell stress during treatment, natural cell death at the end of a cell cycle, and lack of nutrients, among many other possible reasons which may require further experimental investigations to depict.
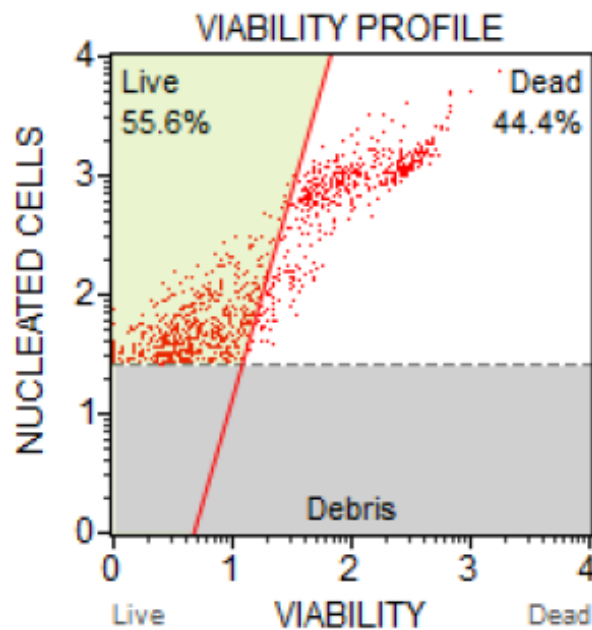
Figure 4.7. Murine macrophage cell viability results after 48 h treatment with combination drugs IBS009•IBS013. The dot plot highlights a clear division between living and dead cells.

Results of cells exposed to combination drugs IBS009•IBS013, shown in Figure 4.7 above, are in agreement with the RTCA cell performance as observed in Figure 4.4 above. In general, all these derivatives are modifications of INH whose cell viability results are presented in Figure 4.8 below which seem to have a similar pattern regarding cell survival where more than 50% of cells remained viable 48 h post exposure, and 44% of cells died possibly during initial exposure, and/or may be attributed to several other conditions as previously explained.
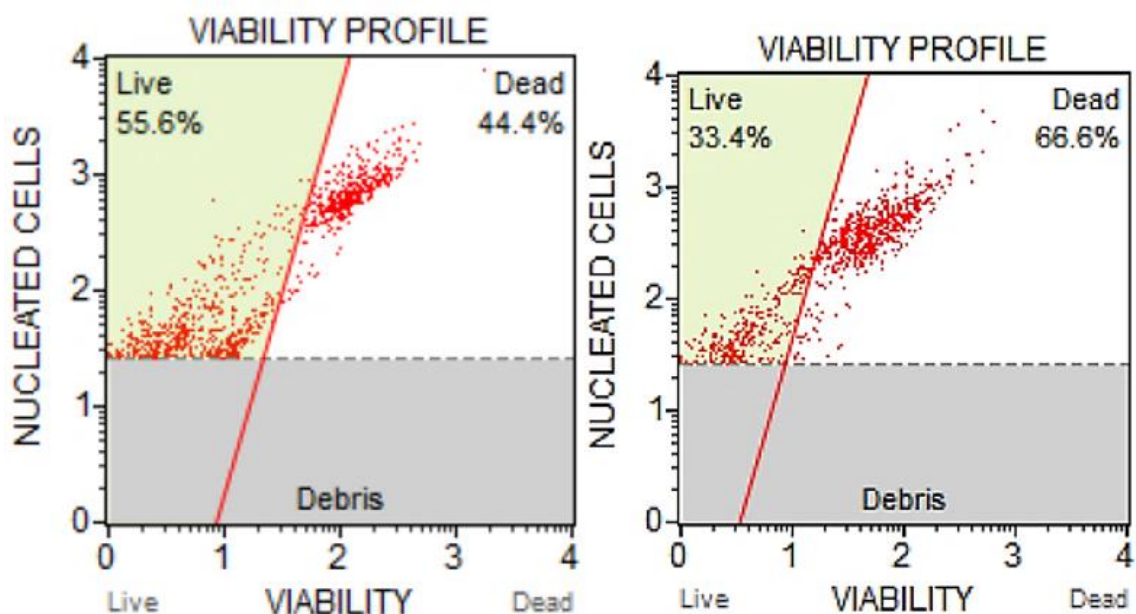
Figure 4.8. Cell viability results of murine macrophage cells treated with positive controls INH and RIF, respectively. The dot plots highlight a clear division between live (viable) and dead cells.

Comparing the concentration of viable cells vs. dead cells in flow cytometry cell viability results of cells exposed to INH (55.6% live cells and 44.4% dead cells) and RIF (33.4% live cells and 66.6% dead cells) (Figure 4.8 above), it can be seen that as much as both drugs were shown to have adverse effects on cells in terms of RTCA results, RIF is more toxic to the cells than INH. Given that cells exposed to drug combination IBS012:IBS015 had a similar cell viability pattern of 31.8% live cells and 68.2% dead cells when compared to RIF, the results provide compelling evidence that this drug combination might have adverse effects on the cells.

4.4. Conclusion

Cytotoxicity results showed that most of the compounds were non-toxic to– and are highly tolerated by– murine macrophage cells as compared to INH and RIF (backbone drugs of TB treatment). However, some flow cytometry cell viability results such as those of drug combination IBS012•IBS015 were of concern as they appeared to be in agreement with those of RIF observed to be more toxic to the cells than any other compound tested. It is decided that for a clearer understanding and to obtain a cohesive picture of the effects of the derivatives particularly that of drug combination IBS012•IBS015, further experiments need to be conducted in order to investigate the actual cause of cell death. It is therefore concluded

that the goals and objectives of this section were met yielding novel data and significant *in vitro* results, thus contributing a substantial new body of knowledge in multidisciplinary fields of research and may be of interest to researchers and pharmaceutical companies in pursuit of further drug development.

The main challenges contributing towards anti-TB drug discovery are vast yet limited to drug targets. This is attributed to the confusion around the mode of action of the currently active drugs against *M. tuberculosis*. In recent times, it has been encouraged that such challenges be tackled *in silico* to minimise animal brutality and cruelty. As such, only compounds that present with promising properties can be taken through to pre-clinical and clinical trials. Based on the observed results. The question remains, what are the probabilities that these drugs can indeed inhibit tuberculosis and what is the possible mode of action in that regard? Chapter 5 below is designed to address questions such as these.

CHAPTER 5

Molecular docking and dynamic studies

5.1. Molecular modelling

Drug design is almost always accompanied by *in vitro* studies which often yield positive and promising results. However, there are many limitations to *in vitro* investigations when it comes to the actual administration and efficacy thereof *in vivo*. It is for this reason that computational simulations (*in silico* models) have become paramount to the process as they assist with the confirmation of activity as well as with the identification of the most effective drug for treatment against a particular organism, consequently allowing for real application in drug discovery (Fatriansyah *et al*., 2022). Thus, molecular docking is a useful method employed in the drug discovery process as well as in medicinal chemistry, particularly to determine the positioning of a receptor structure in a number of conformations, positions and orientations within a computer-generated 3D structure of a small ligand (Jakhar *et al*., 2019).

It is speculated that INH targets a reduced nicotinamide adenine dinucleotide (NADH)-dependent enoyl reductase known as *InhA*, an enzyme essential in MTB cell wall synthesis (Vilchèze & Jacobs, 2019). By targeting this enzyme in particular there is a high probability of inhibiting mycobacterial growth as this enzyme is crucial for the production of molecules such as isoprenoids which are building blocks vital for the synthesis of an array of molecules responsible for virulence factors, respiratory pigment as well as cell wall components . However, for a while, there was no evidence to suggest that INH is active against this enzyme (Silverman & Holladay, 2014). Instead, the one accepted and understood mechanism of action of INH against MTB that stood true for some time was one that suggests that INH is oxidised into an acyl radical by the heme-containing peroxidase enzyme KatG, which then reacts with NAD^+ before undergoing one-electron reduction by a superoxide, subsequently producing a potent substrate analogue that inhibits *InhA* (Silverman & Holladay, 2014). There are two stipulated mechanisms in which this is possible. The first mechanism encompasses the 1-electron oxidation that is followed by the loss of diimide. The second mechanism involves the 1-electron oxidation that takes place in three sequential steps which then results in the loss of molecular nitrogen as shown in Scheme 5.1 below (Silverman & Holladay, 2014).

Since then, gene transfer technology has allowed for a successful elucidation of the INH mechanism of action which confirmed that INH is activated by cleaving of the hydrazide group by KatG to form an isonicotinoyl radical that goes on to react with NAD^+ to form an INH-NAD adduct. This then binds to *InhA* causing enzymatic inhibition that ultimately leads to cell death (Vilchèze & Jacobs, 2019).
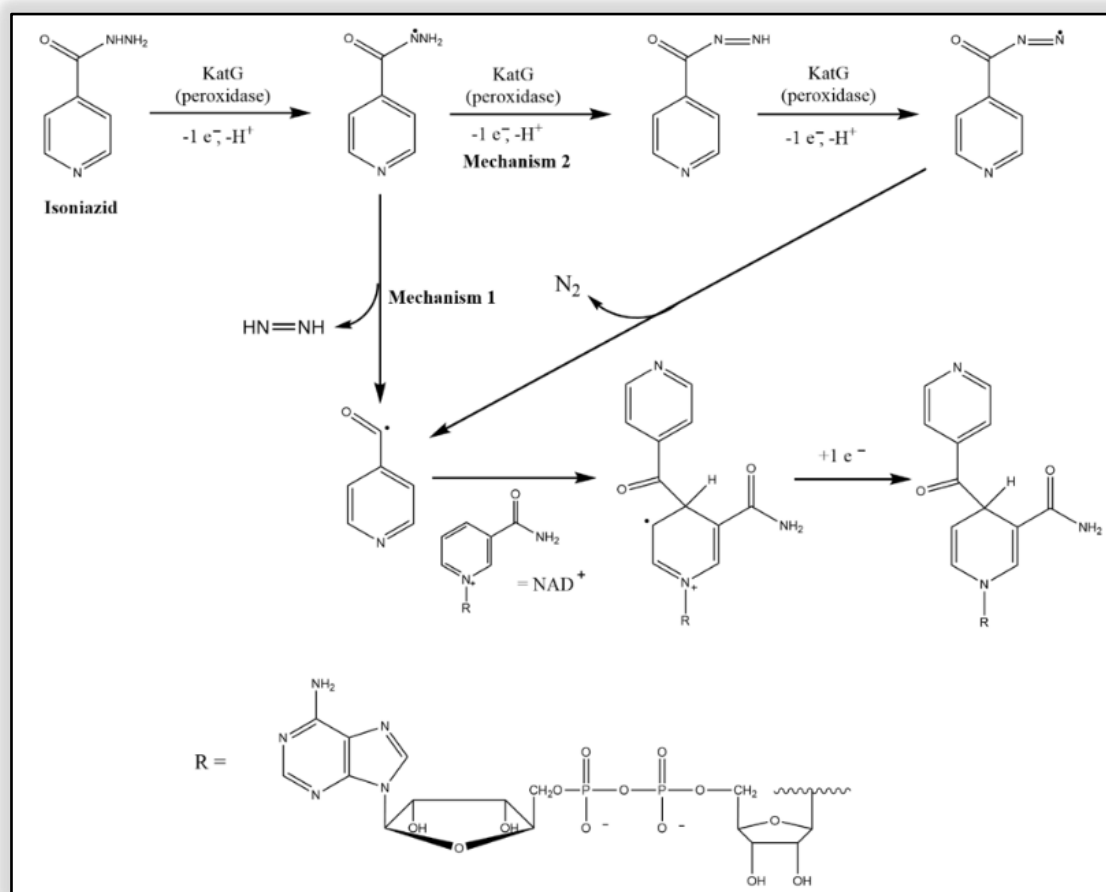
Scheme 5.1. Mechanism of action of isoniazid (Silverman & Holladay, 2014).

Even so, the main challenge around drug design remains an area of concern as it is not attributed to the mechanism of action but is rather attributed to the natural resistance and acquired genomic mutations of these target enzymes. Natural resistance includes the role played by the cell wall in interfering with drug uptake; biotransformation of anti-TB compounds within the intracellular environment; as well as inducible resistance which contributes to active efflux and disruption of target binding (Van Ingen *et al*., 2012b). With regards to acquired genomic mutations, drug treatment for NTM is identical to that used for *M. tuberculosis,* even though NTM are susceptible to an array of macrolide antibiotics, and

do not necessarily respond to the standard TB treatment regimen, neither are they susceptible to the same macrolide class (Van Ingen *et al*., 2012b).

This chapter focuses on the simulation of the compound activity against mycobacteria isolates based on the molecular data obtained mainly from the MIC results. Often, synergistic drug combinations are the result of two drugs that illicit distinct mechanisms of action (Lerche & Muir, 2009) which result in similar clinical effects (Tallarida, 2011). Accordingly, the objectives of this chapter were to determine whether KatG is the target enzyme of the synthesised INH derivatives during treatment as is the case with the API they were derivatised from; to determine and confirm synergistic binding of the derivatives, which would mean that the synergistically active derivatives would have to occupy different binding sites within the target enzyme; and ultimately, to confirm the potential inhibitory effects of the derivatives on the various mycobacteria species as observed in Chapter 3.

5.2.   Materials and methods

5.2.1. Molecular docking

Due to the unavailability of compound IBS008 and IBS009 crystallographic information files (.cif) at the time during which molecular docking studies were conducted, IBS012 was used as the first compound (drug 1) to be bound in the active site of the MTB catalase-peroxidase enzyme (KatG) protein replacing both IBS008 and IBS009. This was based on the prediction of the expected crystals for these compounds and the similarities they had with compound IBS012. Furthermore, the hypothesis was that either of the compounds used as compound one during serial dilution when conducting MIC can be used as a standard drug 1 (IBS012 in this case) during molecular docking and is expected to yield similar inhibitory effects when combined with any of the drug 2 candidates (those used as compound 2 in MIC experiments).

The MTB KatG protein crystal structure (PDB ID: 4c50) was retrieved from the protein data bank website (https://www.rcsb.org/). The protein was further used as a receptor prepared with a protein Maestro preparation wizard, v2021-2. The ligand crystal structures (test drugs) were obtained from their respective .cif format which were converted to suitable .pdb files using OPENBABEL (http://openbabel.org) and prepared using the Maestro ligand LigPrep wizard. To maintain the lowest possible energy, the compounds were ultimately converted to their 3D conformation state using the OPLS4 force field. The Maestro SiteMap tool was used to predict the binding site where site propensity was scored using the integrated SiteScore.

The grid generation panel in Maestro was used to compute receptor grids within the protein's active site, while SiteMap was used to generate the pharmaceutically active site 2. The test drugs were subjected to molecular docking employing the Glide module in Maestro v2021-2 (Schrödinger Inc.).

5.2.2. Dynamic studies

Protein-ligand complexes constituting of KatG and its potential inhibitors were exposed to the molecular docking simulation by employing the Desmond module in Schrödinger-Maestro v2021-2 with the OPLS4 force field. Nose–Hoover thermostat method was used to achieve a constant temperature (300 K) and Martyna–Tobias–Klein barostat method was used to keep a constant pressure (1.01325 kPA), both of which were achieved through the isobaric-isothermal ensemble (NPT) class (Jorgensen *et al.*, 1983). The relative stability of the ligand in the receptor binding site was determined using the root mean square deviation (RMSD) plot and root mean square fluctuation (RMSF) for the KatG as well as drug compounds using the following equations:

$$\text{RMSD}_X = \sqrt{\frac{1}{N}\sum_{i=1}^{N}(r'_i(t_x) - r_i(t_{ref}))^2}$$

Where: RMSR_x is the calculation for frame, N in the number of atoms, t_{ref} is the reference time, r' is thepositon of the selected atom in frame x and frame x is t_x.

$$\text{RMSF}_i = \sqrt{\frac{1}{T}\sum_{t=1}^{T}\langle(r'_i(t) - r_i(t_{ref}))^2\rangle}$$

Where: RMSF_i is a generic residue i, T is the trajectory time, t_{ref} is the reference time, r' is the position of residue i after superposition on the reference, and angle brackets indicate average of the square distance taken over the selection of atoms in the residue (Essmann *et al.*, 1995).

Simulations were monitored for 50 ns, and recorded at 50 ps intervals, resulting in 1 000 frames each. The results thereof were analysed by simulation interaction diagrams and MD trajectory analysis.

5.3. Results and discussion

5.3.1. Molecular docking analysis

The active site was targeted by compound IBS012 prior to the allosteric binding site prediction. This site is known to bind alpha-D-glucopyranose and constitutes a mixture of hydrophobic, polar and charged residues. As a result, compound IBS012 formed multiple polar, hydrophobic and ionic interactions within the active site thus facilitating binding coordination as shown in Figure 5.1(a) below. The image also shows hydrogen bonding between IBS012 and ASP573 as well as ARG498 which is critical in the facilitation of binding within the active site (Crennell *et al.*, 2000) as shown in Figure 5.1(b) below. (Author to check change, also in Ref List)
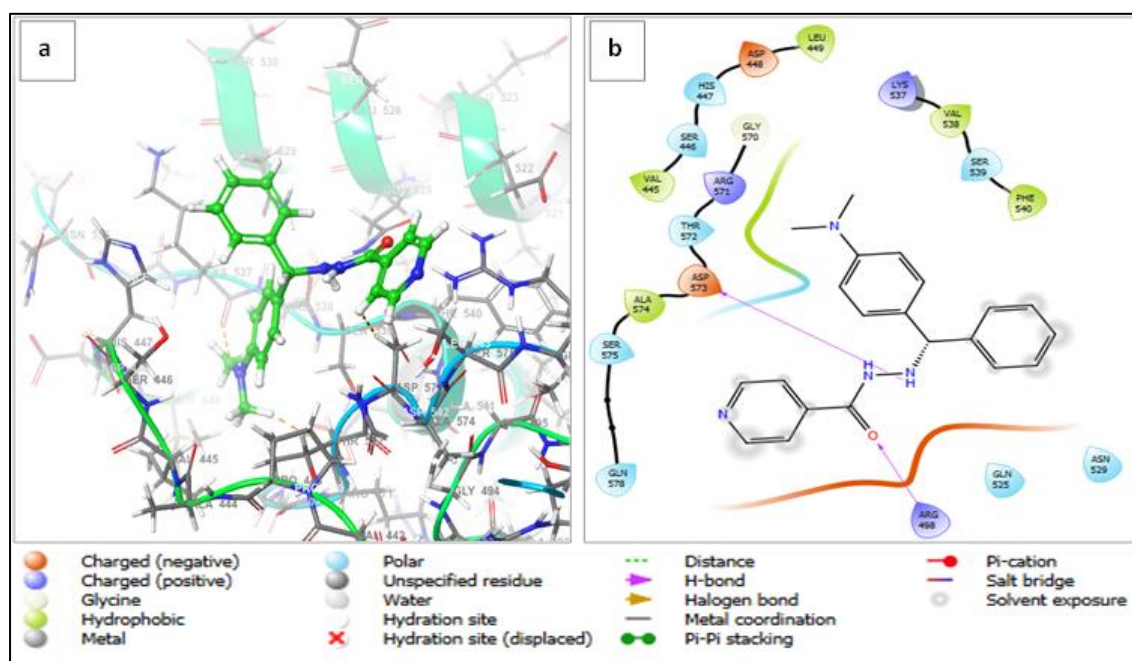
Figure 5.1. Molecular docking analysis of the *Mycobacterium tuberculosis* catalase-peroxidase enzyme (KatG) complexed with compound IBS012. **(a)** Shows compound IBS012 in green ball and stick model docked into the active site. The *M. tuberculosis* catalase-peroxidase enzyme is shown in ribbon graphic representation with alpha helices, loops and beta sheets as well as the grey stick model residues around the active site. **(b)** Depicts a 2d-ligand interaction diagram of compound 2b and the surrounding active site amino acid residues at 4Å axis. The purple arrows indicate two hydrogen bond interactions with ASP573 and ARG496.

A grey surface representation of KatG complexed with IBS012 together with the pharmaceutically active site 2 as described above is presented in the Appendix 7 below. The figure also shows computationally predicted allosteric sites presented in standard grid spheres – Site 2 (shown in white). The blue and red patches indicate hydrophobic and charged surfaces within the binding site. The depiction of a ball and stick model of compound IBS012 (shown in green) docked into the active site and sits ~180° relative to the predicted allosteric site is shown in Figure 5.2 below and Appendix 7.

The binding site prediction tool – SiteMap tool (Schrödinger software) was used for the prediction of the allosteric site on KatG. SiteScore analysis (Schrödinger software) revealed that site 2 was the best pharmaceutically relevant site especially for target binding of small-molecule inhibitors as in Figure 5.2 below. The figure shows compound IBS012 in green ball and stick model docked into the active site. The *M. tuberculosis* catalase peroxidase enzyme is shown in ribbon graphic representation with alpha helices, loops and beta sheets. The standard grid spheres (grey) are also depicted for sites 2, 3, 4 and 5.
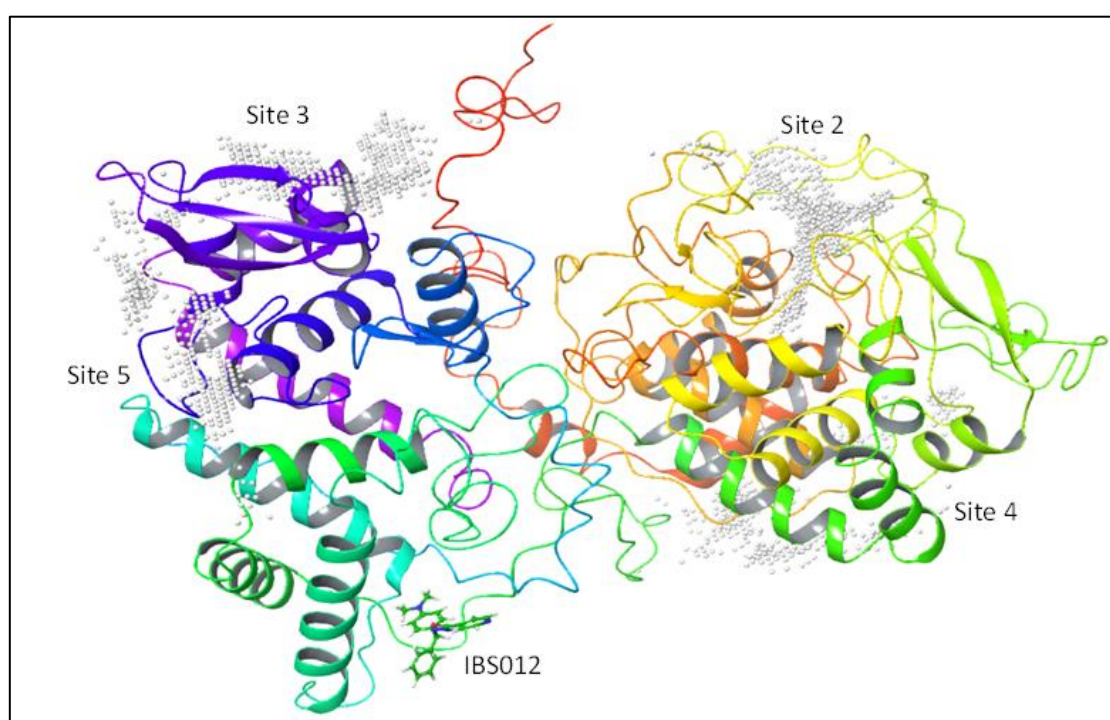
Figure 5.2. SiteMap analysis of the *Mycobacteria tuberculosis* catalase-peroxidase enzyme complex with compound IBS012.

Compounds IBS013, IBS015 and IBS017 also formed a mixture of multiple hydrogen bonds $\pi - \pi$ stacking, hydrophobic, polar and positive or negatively charged interactions amongst others with multiple residues within the predicted allosteric site appendaged in Appendix 7. The four hydrogen bonds formed by compound IBS012 contributed significantly to the conformational stability of the complex, thus resulting in a good binding affinity to MTB KatG compared to the other compounds appendaged in Appendix 7. The $\pi - \pi$ stacking interactions were observed in both compounds IBS015 and IBS017 with the HEM1741 (Protoporphyrin IX containing Fe) metal ion complex. These interactions are critical in providing further stability within the allosteric site and can greatly influence the activity of the potential drugs against KatG (Stornaiuolo *et al*., 2013).

5.3.2. Molecular docking analysis

To determine the thermodynamic stability of the complexes, four molecular dynamics (MD) simulation studies were conducted, with MD simulation trajectories examined for root mean square deviation (RMSD), protein-ligand interactions (PL-Contacts) and root mean square fluctuation (RMSF); trajectory forces indicated the ionic bonds, hydrogen bonds and water bridges as well as hydrophobic interactions, respectively. Solvated systems for molecular dynamics simulation of all four drug complexes were constructed using the Desmond system Builder Tool in Schrödinger-Maestro V2021-2. Notably, RMSD data for all four compounds depicted an excellent and consistent alignment with the Cα atoms of the MTB KatG, as shown in the PL-Contact plots in Figure 5.3 below.

The results of MD simulations showing RMSF values as a function of residue number of the four chemical compounds showed that all complexes were thermodynamically favourable, depicted by coordinating residues at their lowest energy state. All binding residues were less than 1.8 Å, thus confirming the thermodynamic stability of these complexes (Figure 5.4) (Sherman *et al*., 2004). However, on average, compound IBS017 was observed to form a more stable complex with KatG as compared to compound IBS012, IBS013 and IBS015, presenting with an RMSF value of less than 1 Å for all coordinating residues, shown in green vertical lines as depicted in Figure 5.4. below.
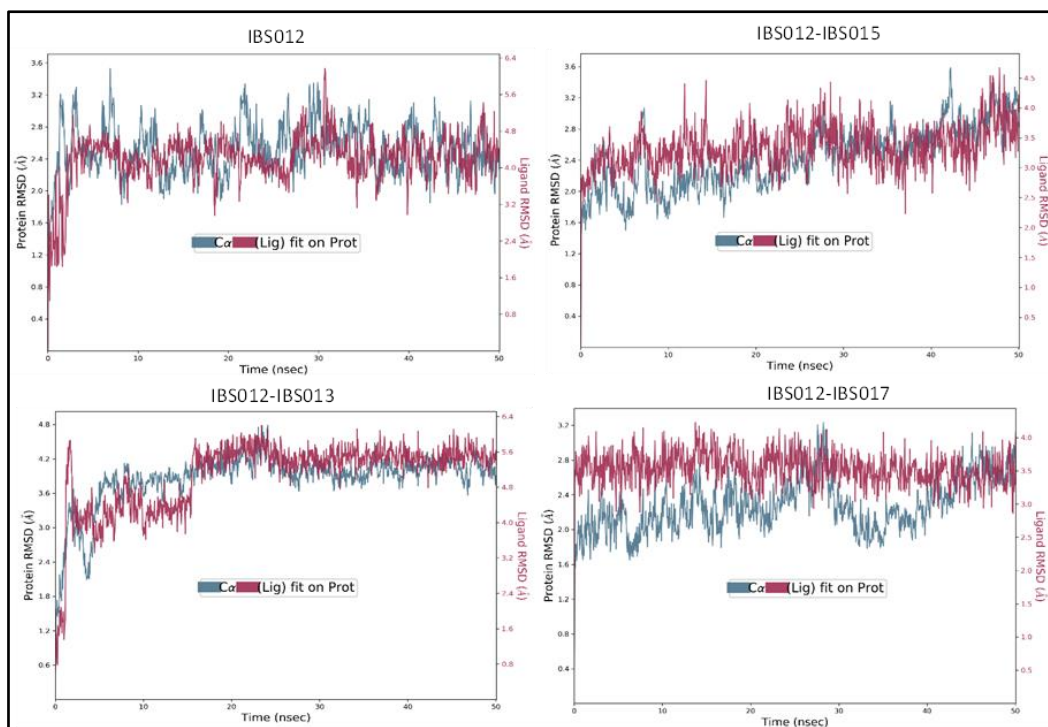
Figure 5.3. The PL-Contact plots obtained for compounds IBS012, IBS015, IBS013 and IBS017, respectively, indicating the scalar distance of the protein-ligand complexes over the 50 ns simulation period.
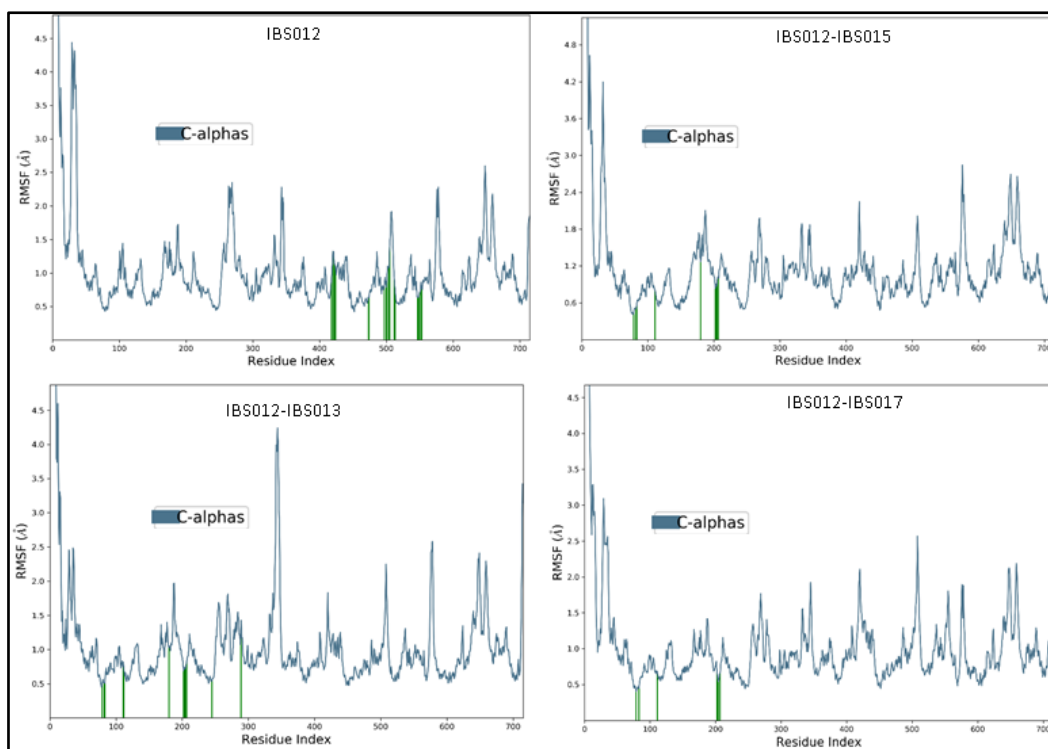
Figure 5.4. Results of MD simulations showing RMSF values with respect to Cα atoms of the KatG protein plotted as a function of residue number and with the protein-ligand contacts shown in green vertical lines for compounds IBS012, IBS013 and IBS015, respectively.

Analysis of the protein-ligand interactions (PL-Contacts) indicates two ionic bond interactions on compounds IBS012 and IBS013. These are coordinated by GLU522 and HIS270, respectively. More importantly, the binding coordination on these two compounds is largely dominated by hydrophobic interactions, water bridges and hydrogen bonding as shown in the histograms in Figure 5.5 below (Davis & Teague, 1999). In targeting the active site, compound IBS012 formed two stable hydrogen bond interactions (interaction fraction > 0.6) of three hydrogen bonds with ASN529 and ASP573 to facilitate the binding coordination. additional three hydrophobic interactions were formed between IBS012 with VAL445, HIS447 and ARG498, thus providing another stabilising force for the complex.

Upon targeting the allosteric site, site 2, compound IBS013 formed a strong water-bridge interaction with ILE228 and TYR229 in addition to the ionic bond interaction with HIS270 (Papageorgiou *et al*., 2019). There was also a significant hydrophobic interaction with ARG104 and IBS013. This confirms the observed high docking score and signifies that compound IBS013 is one of the most effective compounds in terms of targeting KatG. Notably, compounds IBS015 and IBS017 have a very strong hydrogen-bond interaction with ARG104 as well, which plays a critical role in stabilising both complexes (Dhingra *et al*., 2023).
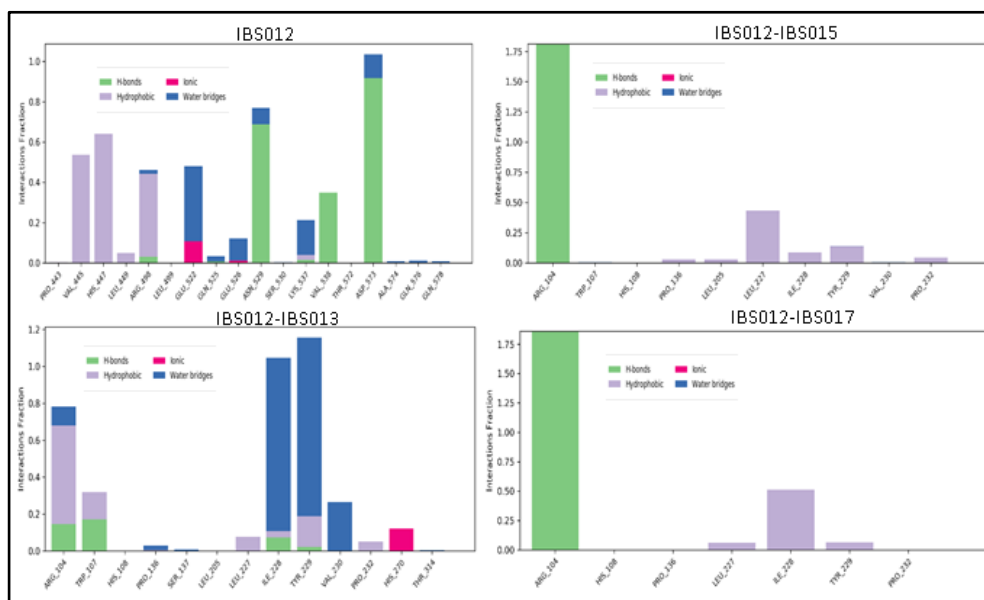
Figure 5.5. Protein-ligand interactions (PL-Contacts). The histograms indicate interactions of the docked ligands with *Mycobacterium tuberculosis* catalase-peroxidase enzyme (KatG), in which the hydrogen bonds, hydrophobic and water bridge interaction dominate the binding coordination sphere.

In addition, the PL-Contact timeline was computed to determine the duration and frequency by which these interactions occur (Figure 5.6 below). Notably, the number of interactions exhibited by some residues within the active site do not seem to last throughout the simulation, thus multiple white gaps are observed as presented in Figure 5.6 below. This finding suggests that these compounds are slow-tight-binding inhibitors (Silverman & Holladay, 2014), which means that it takes a while for both the target enzyme and the inhibitor to reach equilibrium making it a time-dependent inhibition (Silverman & Holladay, 2014). Compound IBS012 was observed to have consistent contacts with ANS529, ASP573, HIS447 and VAL445, whilst IBS013 has three consistent contacts with ARG104, ILE228 and TYR229 (Figure 5.6). It is also worth noting that compounds IBS015 and IBS017 have two critical contacts each with ARG104 as well as LEU227 and LEU228, respectively (Figure 5.6).
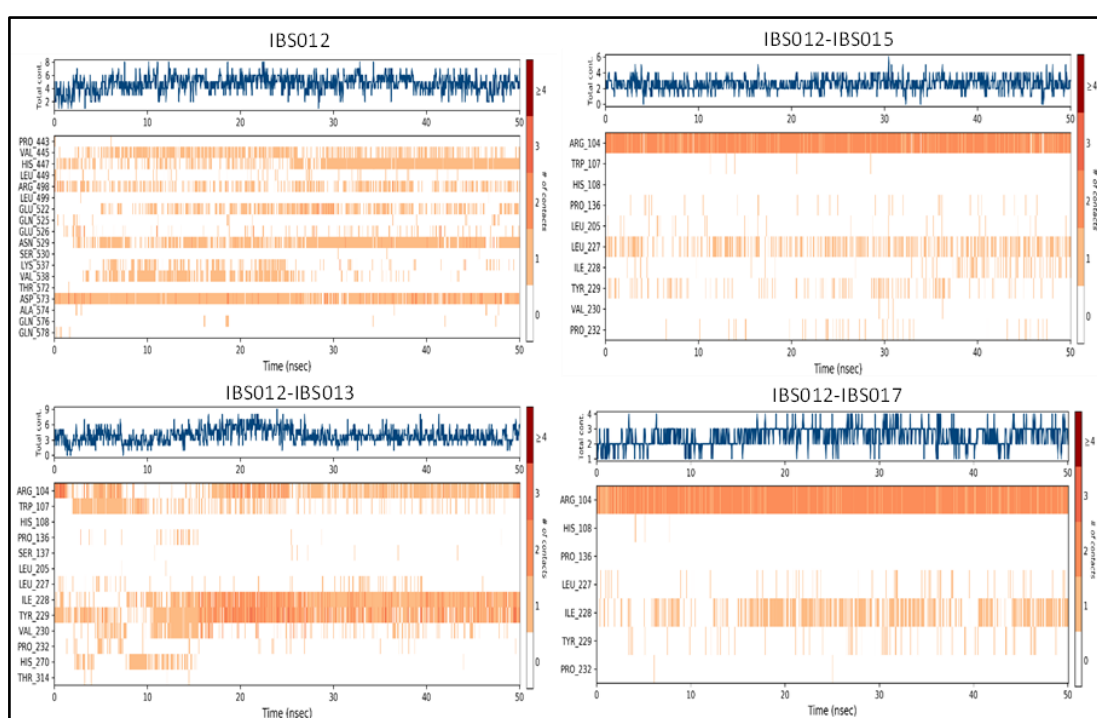
Figure 5.6. Graphs depicting PL-Contacts, showing the extent of binding as well as the number of contacts made throughout the 50 ns simulation time. The top panel shows the overall contact between protein and ligand.

5.4.   Conclusion

The compounds were shown to bind tightly to the *M. tuberculosis* catalase-peroxidase enzyme (KatG) with no degree or change of displacement, thus indicating a very good drug residence time. This observation further affirms the great potential effectiveness of these chemical compounds upon targeting KatG for the treatment of tuberculosis. The molecular docking studies revealed IBS012, in combination with the three synthetic drug molecules, IBS013, IBS015 and IBS017, as effective inhibitors targeting the KatG with docking scores of -5.390 kcal/mol, -6.065 kcal/mol, -5.395 kcal/mol and -4.879 kcal/mol, respectively. Even though sample IBS013 and IBS015 showed significant inhibitory effects in previous molecular experiments when paired with IB008 and IBS009, respectively, it can safely be seen that the same effects can be achieved when paired with sample IBS012. This is a huge breakthrough as it mitigates the challenge observed in Chapter 4 above, where drug combination IBS012•IBS015 was shown to possess some toxic effects in previous experiments. The ability to cross-combine these compounds might also resolve a problem such as this and is worth further investigation. This also suggests that either of the combinations can be effective for the treatment of tuberculosis. Another set of molecular dynamic studies will be conducted to observe the conformational stability of compounds IBS008 and IBS009 when substituting IBS012, especially when paired with IBS013, as it was observed to be the most effective compound when targeting KatG, even though IBS017 was observed to form a tighter-binding complex with KatG in comparison.

Chapter 6
General Discussion

Both *Mycobacterium tuberculosis* and nontuberculous mycobacteria cause chronic respiratory infections in humans. They both present with acid-fast bacilli in sputum and are therefore a cause of a serious public health concern. The only difference is that NTM do not spread from human to human through inhalation of airborne bacteria in expectorated sputum. Instead, they are contracted from the environment, i.e., dust, soil and different water sources (Kendall *et al*., 2011). It is concerning that no simple basic clinical diagnostic method is available for clinical officials to adopt in attempting to distinguish between infections caused by these nontuberculous mycobacteria (NTM) and *Mycobacterium tuberculosis* (MTB), thus resulting in incorrect diagnosis and treatment thereof. Existing methods are expensive and are generally available to research laboratories and hospitals and are inaccessible to the general population due to affordability. The other major concern is that NTM prevalence seems to be increasing, where in some countries like the United States, they are reported at a higher rate than the prevalence of TB (Ryu *et al*., 2016).

Considering that Africa and Asia have the highest TB prevalence in the world, it is impossible to believe that they are unique and immune to such an occurrence. It is a serious cause for concern there aren't sufficient reports on the increased prevalence of NTM from both these continents is available (Dahl *et al*., 2022), especially when Africa has vast stretches of land that support the growth and cultivation of NTM, i.e., rural areas, informal settlements and suburban areas as well as the dependence on public rivers and water systems in urbanised regions. It is also a mind-boggling and worrisome discovery that with all this available information in the literature regarding the increase in NTM prevalence, a global organisation such as the World Health Organization has not added this problem as one of the major gaps hindering diagnosis and drug development to their "Research gaps identified during tuberculosis policy guideline development" report (WHO, 2021c). To an extent, such findings justify the failure of the most affected developing countries to act with regards to diagnosis, treatment, reporting, as well as research focus. This also highlights a huge gap and distortion in global statistics, most especially when the global trend in NTM reporting has seen an increase of 82% infections and a 66.7% increase in disease burden (Dahl *et al*., 2022). Thus, the research gap was identified by and addressed in this study. If there are no

simpler ways of clinically distinguishing between infections caused by MTB and NTM species in humans, and their treatment is different, challenging and proven to be cumbersome, then perhaps designing drugs and developing a treatment regimen that can target all the species is what is needed. This would in turn eliminate incorrect treatment and incorrect classification of the causative agent.

Drug repurposing is one of the very promising approaches currently being employed in the investigation of anti-infective agents for the discovery of novel therapeutics against MDR-TB and XDR-TB strains (Mourenza *et al*., 2020). This project investigated the possibility of restoring the potency/efficacy of INH which is currently reported to be associated with resistance and reduced efficacy against tuberculosis-causing *Mycobacterium* strains (Fernandes *et al.*, 2017). This approach of repurposing former APIs has not yielded a significant number of novel and effective antimicrobials largely attributed to the challenges around the ineffectiveness *in vitro* testing as well as the low permeability of the TB cell wall which leads to the inability of the drugs to reach the targeted pathogen intracellularly (Mourenza *et al.*, 2020). Some other challenges are that drugs seem to fail mainly in clinical trials attributed to factors such as toxicity as well as the inability to reproduce efficacy in humans as displayed *in vitro* (Nierode *et al*., 2016). It is therefore recommended that compounds in the drug design and development phase be tested for efficacy and safety *in vitro* and *in silico* in order to predict human-compound interaction (Nierode *et al.*, 2016) as well ligand-protein interaction (for small molecules) (Stornaiuolo *et al*., 2013).

This study was designed to address the above gaps by employing the stipulated recommendations, where a set of known chemistry techniques was employed for the physical modification of INH as well as the safety and efficacy analysis *in vitro* and *in silico*. The approach was direct and depended on producing a product before performing molecular assays, drug docking and modelling studies. However, other methods are available that focus on the design and prediction of potential ligand-protein interactions prior to synthesising the drug candidates. Among these, a model referred to as quantitative structure-activity relationship (QSAR) methodology is often applied in medicinal chemistry. It is a method that identifies the relationship between chemical constituent molecular properties and measurable biological properties before synthesis (Martins *et al*., 2014). The selected study approach does not necessarily yield active antimycobacterial inhibitors, hence the application of methods such as the aforementioned QSAR modelling technique. However, this approach

guarantees *de novo* data not only limited to and controlled by expected outcome, thus contributing to the new body of knowledge. The design and synthesis part of this study yielded nineteen compounds whose structures were elucidated by employing a single crystal X-ray diffractometer instrument as described in Chapter 2 above, henceforth resulting in some known and some novel compounds. It is worth noting that there is no way of guaranteeing a novel product from every synthesis of a molecule even if the above QSAR method is observed. This is due to the ability of some molecules to possess diverse packing arrangements in a crystal structure, thus resulting in what is referred to as crystal polymorphism (Nogueira *et al*., 2020). This means that roughly three in five molecules are guaranteed to synthesise a known molecule different to the intended one based on their packing arrangement, thus resulting in polymorphism. Similarly, it can be as difficult to reproduce a particular molecule because of the same phenomenon (Grześkiewicz *et al*., 2023; Nogueira *et al*., 2020). However, polymorphic structures do result in the same vapour and liquid state (Grześkiewicz *et al*., 2023). Among those, some presented with significant activity while others displayed less activity, novel and known compounds alike.

When taking a closer look at the performance of the derivatives, it can be observed that as single derivatives, not much improvement or increased efficacy was detected between the derivatives and their parent API INH from which they were derived, except when screened against *M. bovis* BCG where the performance was comparable to that of RIF and INH. Interestingly, the derivatives presented with significant inhibitory effects against *Mycolicibacterium aurum* (NCTC 10437) with concentrations ranging between 11.36 and 2.80 µg/mL, where INH could not inhibit the growth of this organism at the starting concentration of 250 µg/mL (90.90 µg/mL after microbe addition). Unfortunately, the results could not be presented as the source plate was found to be contaminated. However, *Mycolicibacterium aurum* belongs to the genus *Mycolicibacterium* and not to the *Mycobacterium* genus, and therefore it was subsequently substituted with *M. avium*, a *Mycobacterium* known to cause chronic obstructive lung diseases in humans (Busatto *et al*., 2019). *Mycobacterium smegmatis* is known to harbour natural resistance against INH. However, there are multiple mutants presenting with different levels of resistance (Dussurget *et al*., 1998) as shown by the observed results discussed in Chapter 3 above. Some level of inhibition was observed against *M. smegmatis* ATCC 1441 at concentrations ranging between 2.84 and 45.45 µg/mL. Derivatives IBS014, IBS015, IBS017 and IBS018 seemed to have a slightly increased efficacy at an MIC of 11.36 µg/mL as compared to INH which presented

with an MIC of 15.67 µg/mL. However, this was not the case against *M. smegmatis* ATCC 14468. Based on these results it can be presumed that it is possible for the modification to be effective, but the results depend on the organism being targeted and cannot be of a general application.

With regards as to whether performance is enhanced when the derivatives are co-crystallised with salicylic acid, the observed results do confirm a difference in performance. The maximum observed difference between a derivative and its co-crystalised version or counterpart is at most two concentration bars, a finding which could be a significant breakthrough from a pharmacological point of view. However, in most instances, the results were comparable and slightly similar. Out of curiosity and not as part of the objectives set for the study, the compounds were spotted on a thin layer chromatography aluminium plate against INH as a reference compound, where acetone was used as a mobile phase to allow the compounds to migrate up along the plate in a closed system (result in Appendix 8). Some co-crystals were observed to decompose where it was assumed that the hydrogen bond holding the crystal and the salicylic acid together was weak and subsequently broke, thus resulting in the observation of two spots for each co-crystal, one of which correlated with INH and the other assumed to be that of salicylic acid. It is such an observation that leads to the conclusion that there was no improvement seen between the derivatives and their co-crystal counterpart due to the inability of the co-crystal to maintain its form. This does not negate the hypothesis applied in an instance where a stable co-crystal is concerned, as seen with IBS014 and IBS018 where they appeared to possess the strongest inhibition against more bacteria than other co-crystals.

In combination, the MIC synergistic effect was exceptional for all combinations when the second drug was added at a constant concentration of between 250 and 200 µg/mL thus resulting in the lowest observed MIC of between 0.18 and 014 µg/mL for both compounds in a well. However, because part of the study was to produce drugs that could have significant results when administered at the lowest concentration possible, the results reported in Chapter 3 above, were those where the second drug was added at constant concentrations of 150 µg/mL, which saw a variation of MIC for the different bacteria as presented in Table 3.4 of Chapter 3. Perhaps the flow cytometry assay would have yielded different results if the concentrations were increased as they were done with MIC experimental results. Flow cytometry assay results presented above were conducted with the second drug added at the

lowest concentration of 150 µg/mL which is in alignment with the differences observed, as lower concentrations seemed to show lower inhibitory properties and a decrease in synergistic effects, thus being in alignment with the statement made by Tallarida (2011), namely: "synergism is not only dependent on the drugs combined, or their individual performance, but is dependent mainly on the dose of the combined drugs."

It is recommended that compound safety be assessed in order to predict direct compound-human interactions and reactions. As a result, the derivatives were also tested for their safety on RAW 264.7 murine macrophage cells. This cell line is used in drug discovery experiments to determine human responses to the biological impacts of a product. The cell line is preferred in most studies for the cell's ability to engulf (ingest) fairly large particles such as viruses and bacteria by pinocytosis and phagocytosis processes, being an integral function of a macrophage cell in the human body, particularly with regards to tuberculosis infections (Merly & Smith, 2017). Cell death observed in the RAW 264.7 murine macrophage cells should be investigated further. It is obvious that the results thereof are in alignment with those presented by RTCA, confirming that any possible negative effect exerted on these cells by most derivatives are better and tolerable and not of toxic nature as observed in those treated with INH and RIF. In general, these derivatives, as individuals or in combination, proved to be less toxic to the cells when compared to RIF and INH.

There were some derivatives that presented with the potential to be toxic, but the positive outcome is that only one successful combination is essential as confirmed by the results presented in Chapter 5 above. Derivative combination results showed that derivatives can be swapped around and combined with other different derivatives to yield similar results. These results were presented well in Chapter 5 above. These results are very interesting and should be investigated further to determine molecular modelling and the relationship between the observed efficacy as well as compound pairing.

CHAPTER 7

General conclusion and future perspectives

7.1. General conclusion

7.1.1. Design and synthesis of isoniazid derivatives

The overall findings of this study as reported and discussed above provide insight into the challenges involved in drug discovery, particularly research conducted towards the long-standing problem that is *Mycobacterium tuberculosis*, and the challenges relating to treatment and diagnosis thereof. The study uncovered research gaps in the strategy to combat MTB infections. The study undertook to design and synthesise isoniazid derivatives with the goal to produce known and novel derivatives in crystal form as well as co-crystals with salicylic acid used as a co-former. The first two objectives were carried out successfully, where five of the ten novel compounds produced from this experiment were described and published in peer-reviewed journals. Thus, the first, second and third objectives of this study were accomplished in the "Design and synthesis" section. The published results make a significant contribution to the new body of knowledge especially in the chemistry field.

7.1.2. Antimycobacterial activity of isoniazid derivatives

The antimicrobial susceptibility assays and analysis conducted on the *Mycobacterium* pathogens provided great insight into the organism's ability to respond directly to antimicrobial stimuli and proved that prokaryotes could potentially possess certain pathways similar to those observed in unicellular organisms. This information directly imposes factual findings and probes controversial questions directly challenging existing information regarding the differences in physical and biological mechanisms between multicellular and unicellular organisms. The data also showed that the designed derivatives possessed considerable synergistic inhibition effects against *Mycobacterium* regardless of the strain and virulence. The data also confirmed that synergy is not as a result of two molecules interacting with one another, but rather because of a process which is dependent on the doses of the interacting molecules. The results showed that the derivatives could be applied in the treatment not only of a particular class of *Mycobacterium*, but across a broad array of both slow- and fast-growing mycobacteria, suggesting that the restoration of isoniazid's potency was successful to a certain extent and that the synergistic effects of these derivatives can be applied to inhibit most if not all *Mycobacterium* infections of clinical importance, including NTM. The results thereof are yet to be published; however, by virtue of making this thesis

available to the public, this part of the study contributes significantly to the body of knowledge in medicinal chemistry, biology and microbiology field of study as well as the pharmaceutical industry. These experiments made a significant contribution thus rendering objective four achieved.

7.1.3. Cytotoxicity assay

The aim of this study was not only to produce isoniazid derivatives that could inhibit *Mycobacterium* strains, but also those that were less toxic to humans and could result in efficacy with a longer half-life, thus reducing the dose and the number of times in which the drug would have to be administered in order to maintain their biological effectiveness on the organism. The results thereof proved that the majority of derivatives posed lower toxicity to the murine cells as compared to the leading drugs used in the treatment of tuberculosis being isoniazid and rifampicin. In addition, it is suggested that the stipulated inquisition was correct and that these derivatives tick all the boxes with regards to them being applied as prospective drug leads. A draft manuscript containing the data is yet to be published; however, by virtue of this thesis being made available to the public, this part of the study contributes a new body of knowledge in cell biology, medicinal chemistry and the pharmaceutical industry, and thus successfully concludes the fifth objective of this study.

7.1.4. *In silico* activity of isoniazid derivatives

Most drugs in the pipeline often fail in the early phase of clinical trials due to matters addressed by objective 4 and 5, as explained above. However, often the drugs would have had undergone numerous trials *in vivo* thus contributing to animal brutality; in most cases, promising *in vitro* test results are verified using *in vivo* studies to observe the overall effects on the whole organism; *in vitro* testing is useful for screening, but it cannot replace *in vivo* tests as the sole basis for screening drugs, which is very unfortunate. Moving away from the brutality associated with *in vivo* tests, and with irreproducible results *in vitro* due to different experimental conditions, *in silico* techniques have been developed and adopted to conduct such experiments, particularly for smaller molecules where their protein interaction is predicted. These techniques have been shown to achieve accurate protein-structure interactions useful in drug discovery.

Such an approach was to be addressed by the sixth and final objective set out for this study, where the ligand-protein interaction drug docking and modelling assay was conducted in order to confirm the target protein and the stability of the interaction of these compounds within the target protein. It can be concluded that KatG is still the correct protein to be targeted which makes sense since the intention of the study was to restore isoniazid activity. The results are promising and provide sufficient evidence to confidently conclude that the molecules are effective and that they are exceptional inhibitors and highly effective upon targeting KatG. Despite the positive and convincing evidence, it was also evident that the non-covalent residues are quite unstable, and thus will require more experiments to be conducted in the quest to improve compound stability. The objective was met successfully, and although further studies need to be conducted to investigate the binding of other combinations as concluded in Chapter 5 above, it cannot be disputed that the information is noteworthy and contributes significantly to the drug discovery and enzymology field of study, thus successfully concluding the investigation as set by objective six.

The overall aim of the study was to design isoniazid crystal and co-crystal derivatives and to assess their antimycobacterial activity and synergistic capabilities against mycobacteria species of choice. With all that has been reported, it can safely be concluded that the aim of the study was successfully met with every objective producing novel results. For every answer to a scientific question, one or more inquiries arise. In the scientific world, such is defined as a good project/scientific question. As a result, this project provided answers that gave rise to new questions, and hence the suggested future research perspectives outlined below.

7.2. Future research perspectives

7.2.1. Co-crystal stability

In some of the co-crystal derivatives, weak hydrogen bonds were observed that separated in solution. It is therefore recommended that further experiments be conducted to produce derivatives with stronger and more stable covalent bonds. Experiments to be considered are the employment of the click chemistry or microwave synthesis, especially for those compounds that work in synergy.

7.2.2. Test INH in combination with RIF

The derivatives were tested against INH and RIF as positive controls. However, INH is administered individually when targeting latent TB, but for active TB these two are administered together, among others. It would be interesting to observe the toxicity effect thereof as combination drugs. It is something that should have been done but was not and can still be investigated.

7.2.3. Screening of clinical isolates

Despite the solidity and justification behind the usage of the target isolates, objective four still needs to be repeated and conducted in an environment that would allow the testing of the derivatives on clinical isolates.

7.2.4. NTM or MTB

Clinical isolates from different provinces within the country need to be tested for antimicrobial resistance pattern and genome sequencing. The antimicrobial susceptibility patterns of NTM should be studied. Additionally, clinical isolates reported as MDR–TB, XDR–TB and totally resistant TB should be profiled against NTM to determine NTM incidence in South Africa and to allow correct and timeous treatment thereof.

7.2.5. Transfection studies

Host cell membrane permeability is pointed out to be one of the challenges in the early stages of drug development. Seeing that the pathogen can react to direct antimycobacterial stimuli, it would be interesting to see if the same effect can be observed when the organism is targeted within a macrophage cell, for example.

7.2.6. Molecular docking and modelling

Once the crystallographic information framework (.cif) files for IBS009 and IBS015 have been satisfactorily refined, molecular docking and modelling will be conducted based on the respective active combinations as well as tested with other derivatives to test different combinations that have not yet been assessed.

7.2.7. Ligand-protein interaction specificity

It was interesting to note that the order in which the drug was added in the microtitre wells as well as the concentrations thereof played a major role in the observed experimental results. Determining why a specific combination among the derivatives was more effective than others and why the order in which the derivatives were added is important could be a key to understand the organism's mode of resistance, the derivative's mode of inhibition and shed light on future drug development studies.

References

Aakeröy, C.B., Hussain, I., Forbes, S. & Desper, J. 2006. Exploring the hydrogen-bond preference of N–H moieties in co-crystals assembled via O–H(acid)⋯N(py) intermolecular interactions. *CrystEngComm*, 9(1):46–54.

Adjemian, J., Prevots, D.R., Gallagher, J., Heap, K., Gupta, R. & Griffith, D. 2014. Lack of adherence to evidence-based treatment guidelines for nontuberculous mycobacterial lung disease. *Annals of the American Thoracic Society*, 11(1):9–16.

Aitipamula, S., Banerjee, R., Bansal, A.K., Biradha, K., Cheney, M.L., … Zaworotko, M.J. 2012. Polymorphs, salts, and cocrystals: What's in a name? *Crystal Growth and Design*, 12(5):2147–2152.

Al-Ghafli, H. & Al-Hajoj, S. 2017. Nontuberculous mycobacteria in Saudi Arabia and Gulf Countries: A Review. *Canadian Respiratory Journal,* 2017:5035932.

Alqurashi, M.M., Alsaileek, A., Aljizeeri, A., Bamefleh, H.S. & Alenazi, T.H. 2019. *Mycobacterium smegmatis* causing a granulomatous cardiomediastinal mass. *IDCases*, 18.

African News Agency (ANA) Reporter. 2017. TB still top killer in SA – Stats SA / *Cape Times, 28 February 2017*. https://www.iol.co.za/capetimes/news/tb-still-top-killer-in-sa-stats-sa-7975577 (Date of access: 19 Feb. 2018).

BañUls, A.L., Sanou, A., Van Anh, N.T. & Godreuil, S. 2015. *Mycobacterium tuberculosis*: ecology and evolution of a human bacterium. *Journal of Medical Microbiology*, 64:1261–1269.

Barr, D.A., Omollo, C., Mason, M., Koch, A., Wilkinson, R.J., … Davies, G. 2021. Flow cytometry method for absolute counting and single-cell phenotyping of mycobacteria. *Scientific Reports*, 11(1):18661.

Bernstein, J., Davis, R.E., Shimoni, L. & Chang, N. -L. 1995. Patterns in hydrogen bonding: Functionality and graph set analysis in crystals. *Angewandte Chemie International Edition,* 34(15):1555–1573.

Biomapas, 2022. Setting Up a Pharmacovigilance System. Biomapas, Kaunas, Lithuania. https://www.biomapas.com/setting-up-a-pharmacovigilance-system/ (Date of access: 17 Sep. 2023).

Blumberg, H.M., Burman, W.J., Chaisson, R.E., Daley, C.L., Etkind, S.C., … American Thoracic Society, Centers for Disease Control and Prevention, and the Infectious Diseases Society. 2003. American Thoracic Society/Centers for Disease Control and Prevention/Infectious Diseases Society of America: treatment of tuberculosis. *American Journal of Respiratory and Critical Care Medicine*, 167(4):603–662.

Bos, K.I., Harkins, K.M., Herbig, A., Coscolla, M., Weber, N., … Krause, J. 2014. Pre-Columbian mycobacterial genomes reveal seals as a source of New World human tuberculosis. *Nature*, 514(7523):494–497.

Brosch, R., Philipp, W., Stavropoulos, E., Colston, M.J., Cole, S.T and Gordon, S.V. 2018. Genomic analysis reveals variation between *Mycobacterium tuberculosis* $H_{37}R_v$ and the attenuated M. tuberculosis $H_{37}R_a$ strain. Infection and Immunity, 67(11):5768 =–5774.

Burrows, A.D. 2004. Crystal engineering using multiple hydrogen bonds. In: David Michael P. Mingos (Editor), *Supramolecular Assembly via Hydrogen Bonds* I (*Structure and Bonding*, 108). Springer. pp. 55–96.

Busatto, C., Vianna, J.S., da Silva, L.V., Ramis, I.B. & da Silva, P.E.A. 2019. *Mycobacterium avium*: an overview. *Tuberculosis*, 114:127–134.

Butcher, C.E., Berg, L.E. & Kunkel, E. 2004. Systems biology in drug discovery. *Nature Biotechnology*, 22(10):1253–1259.

Caminero, J.A., Sotgiu, G., Zumla, A. & Migliori, G.B. 2010. Best drug treatment for multidrug-resistant and extensively drug-resistant tuberculosis. *The Lancet Infectious Diseases*, 10(9):621–629.

CDC. 2016. *Tuberculosis Fact Series | Exposure to TB | TB | CDC*. CDC - Division of Tuberculosis Elimination. https://www.cdc.gov/tb/publications/factseries/exposure_eng.htm (Date of access: 20 March 2018).

CDC. 2021. *Infographic: Biosafety Lab Levels | CDC*. Centers for Disease Control and Prevention. https://www.cdc.gov/cpr/infographics/biosafety.htm (Date of access: 28 Apr. 2022).

Churchyard, G.J., Mametja, L.D., Mvusi, L., Ndjeka, N., Hesseling, A.C., … Pillay, Y. 2014. Tuberculosis control in South Africa: Successes, challenges and recommendations. *South African Medical Journal*, 104(3):244.

Clarke, C., Van Helden, P., Miller, M. & Parsons, S. 2016. Animal-adapted members of the *Mycobacterium tuberculosis* complex endemic to the southern African subregion. *Journal of the South African Veterinary Association,* 87(1):1–7.

Cousins, D. V., Bastida, R., Cataldi, A., Quse, V., Redrobe, S., Dow, S., Duignan, P., Murray, A., Dupont, C., Bernardelli, A. 2003. Tuberculosis in seals caused by a novel member of the *Mycobacterium tuberculosis* complex: *Mycobacterium pinnipedii* sp. nov. *International Journal of Systematic and Evolutionary Microbiology*, 53(5):1305–1314.

Crennell, S., Takimoto, T., Portner, A. & Taylor, G. 2000. Crystal structure of the multifunctional paramyxovirus hemagglutinin-neuraminidase. *Nature Structural Biology*, 7:1068-1074.

Cully, M. 2014. Redesigned antibiotic combats drug-resistant tuberculosis. *Nature Reviews Drug Discovery*, 14(4). 256–257.

Dahl, V.N., Mølhave, M., Fløe, A., van Ingen, J., Schön, T., … Wejse, C. 2022. Global trends of pulmonary infections with nontuberculous mycobacteria: a systematic review. *International Journal of Infectious Diseases*. 125:120–131.

Daley, C.L., Iaccarino, J.M., Lange, C., Cambau, E., Wallace, R.J., … Winthrop, K.L. 2020. Treatment of nontuberculous mycobacterial pulmonary disease: An official ATS/ERS/ESCMID/IDSA clinical practice guideline. *Clinical Infectious Diseases*, (71):e1–e36.

Daniel, Thomas M. 2006. The history of tuberculosis. *Respiratory Medicine*, 100:1862–1870.

Davidovich, P., Kearney, C.J. & Martin, S.J. 2014. Inflammatory outcomes of apoptosis, necrosis and necroptosis. *Biological Chemistry*, 395(10):1163–1171.

Davis, A.M. & Teague, S.J. 1999. Hydrogen bonding, hydrophobic interactions, and failure of the rigid receptor hypothesis. *Angewandte Chemie International Edition,* 38(6):736-749. *https://onlinelibrary.wiley.com/doi/abs/10.1002/%28SICI%291521-3773%2819990315%2938%3A6%3C736%3A%3AAID-ANIE736%3E3.0.CO%3B2-R*

Derrick, S.C. & Morris, S.L. 2007. The ESAT6 protein of *Mycobacterium tuberculosis* induces apoptosis of macrophages by activating caspase expression. *Cellular Microbiology*, 9(6):1547–1555.

Dhingra, N., Kapoor, K., Sharma, S. & Saxena, A. 2023. Towards further understanding the structural insights of isoxazoles analogues against leishmaniasis using QSAR, molecular docking and molecular dynamics model. *Journal of the Indian Chemical Society*, 100(1).

Donohue, M.J. 2018. Increasing nontuberculous mycobacteria reporting rates and species diversity identified in clinical laboratory reports. *BMC Infectious Diseases*, 18(1):1–9.

Dussurget, O., Rodriguez, M. & Smith, I. 1998. Protective role of the *Mycobacterium smegmatis* IdeR against reactive oxygen species and isoniazid toxicity. *Tubercle and Lung Disease*, 79(2):99–106.

Dwyer, D.J., Camacho, D.M., Kohanski, M.A., Callura, J.M. & Collins, J.J. 2012. Antibiotic-induced bacterial cell death exhibits physiological and biochemical hallmarks of apoptosis. *Molecular Cell*, 46(5):561.

Essmann, U., Perera, L., Berkowitz, M.L., Darden, T., Lee, H. & Pedersen, L.G. 1995. A smooth particle mesh Ewald method. *The Journal of Chemical Physics*, 103(19):8577–8593.

Faksri, K., Prammananan, T., Leechawengwongs, M. & Chaiprasert, A. 2012. Molecular epidemiology and drug resistance of tuberculous meningitis. In: George Wireko-Brobby (Editor), *Meningitis*. InTech.

Falkinham, J.O. 2009. Surrounded by mycobacteria: Nontuberculous mycobacteria in the human environment. *Journal of Applied Microbiology*. 107(2):356–367.

Fang, Y. 2016. Label-Free Screening Technologies. *Comprehensive Medicinal Chemistry III*. 2–8:416–433.10.1016/B978-0-12-409547-2.12330-3.Farrugia, J.L. 1999. WinGX suite for small molecule single-crystal crystallography. *Journal of Applied Crystallography,* 32:837–838.

Farrugia, L.J. & IUCr. 1999. WinGX suite for small-molecule single-crystal crystallography. *urn:issn:0021-8898*. 32(4):837–838.

Fatriansyah, J.F., Rizqillah, R.K., Yandi, M.Y., Fadilah & Sahlan, M. 2022. Molecular docking and dynamics studies on propolis sulabiroin-A as a potential inhibitor of SARS-CoV-2. *Journal of King Saud University - Science*, 34(1):101707.

Fernandes, G.F. dos S., Salgado, H.R.N. & Santos, J.L. dos. 2017. Isoniazid: A review of characteristics, properties and analytical methods. *Critical Reviews in Analytical Chemistry*, 47(4):298–308.

Gabrielson, J., Hart, M., Jarelöv, A., Kühn, I., Mckenzie, D. & Möllby, R. 2002. Evaluation of redox indicators and the use of digital scanners and spectrophotometer for quantification of microbial growth in microplates. *Journal of Microbiological Methods*, 50:63–73. www.elsevier.com/locate/jmicmeth (Date of access: 04 June 2023).

Gagneux, S. 2012. Host–pathogen coevolution in human tuberculosis. *Philosophical Transactions of the Royal Society B: Biological Sciences*, 367(1590):850–859.

Gautam, S., Qureshi, K.A., Jameel Pasha, S.B., Dhanasekaran, S., Aspatwar, A., … Venugopal, D. 2023. Medicinal plants as therapeutic alternatives to combat *Mycobacterium tuberculosis*: A comprehensive review. *Antibiotics,* 12(3):541.

Glick, D., Barth, S. & Macleod, K.F. 2010. Autophagy: cellular and molecular mechanisms. *The Journal of Pathology*, 221(1):3–12.

Grare, M., Fontanay, S., Cornil, C., Finance, C. & Duval, R.E. 2008. Tetrazolium salts for MIC determination in microplates: Why? Which salt to select? How? *Journal of Microbiological Methods*, 75(1):156–159.

Grześkiewicz, A.M., Dutkiewicz, G., Aygun, O., Ozturk, I.I. & Kubicki, M. 2023. Solid-to-solid polymorphic phase transitions in two isostructural Bi(III) complexes with 1-phenylethyl-N-ethylthiosemicarbazide and halogens. *Scientific Reports,* 13(1):1–11.

Guirado, E., Schlesinger, L.S. & Kaplan, G. 2013. Macrophages in tuberculosis: friend or foe. *Seminars in Immunopathology*, 35(5):563–83.

Häcker, G. 2013. Is there, and should there be, apoptosis in bacteria? *Microbes and Infection*, 15(8–9):640–644.

Hearn, M.J. & Cynamon, M.H. 2004. Design and synthesis of antituberculars: preparation and evaluation against *Mycobacterium tuberculosis* of an isoniazid Schiff base. *Journal of Antimicrobial Chemotherapy*, 53(2):185–191.

Hesselberg, I. 1972. Drug resistance in the Swedish/Norwegian BCG strain. *Bulletin of the World Health Organization*, 46(4):503–507.

Holani, A.G., Ganvir, S.M., Shah, N.N., Bansode, S.C., Shende, V., … Bijjargi, S.C. 2014. Demonstration of *Mycobacterium tuberculosis* in sputum and saliva smears of tuberculosis patients using Ziehl Neelsen and fluorochrome staining - A comparative study. *Journal of Clinical and Diagnostic Research,* 8(7):ZC42.

Hu, C., Huang, L., Cai, M., Wang, W., Shi, X. & Chen, W. 2019. Characterization of non-tuberculous mycobacterial pulmonary disease in Nanjing district of China. *BMC Infectious Diseases*, 19(1).

Hu, Y.-Q., Zhang, S., Zhao, F., Gao, C., Feng, L.-S., … Wu, X. 2017. Isoniazid derivatives and their anti-tubercular activity. *European Journal of Medicinal Chemistry*, 133:255–267.

Hughes, J. & Osman, M. 2014. Diagnosis and management of drug-resistant tuberculosis in South African adults. *South African Medical Journal*, 104(12):894.

Hundie, G.B., Woldemeskel, D. & Gessesse, A. 2016. Evaluation of direct colorimetric MTT assay for rapid detection of rifampicin and isoniazid resistance in *Mycobacterium tuberculosis*. *PloS One*, 11(12):e0169188.

Isoniazid. 2008. *Tuberculosis (Edinburgh, Scotland)*, 88(2):112–116. DOI: 10.1016/S1472-9792(08)70011-8. PMID: 18486045.

Jakhar, R., Dangi, M., Khichi, A. & Chhillar, A.K. 2019. Relevance of molecular docking studies in drug designing. *Current Bioinformatics*, 15(4):270–278.

Jang, J.-C., Jung, Y.-G., Choi, J., Jung, H. & Ryoo, S. 2017. Bedaquiline susceptibility test for totally drug-resistant tuberculosis *Mycobacterium tuberculosis*. *Journal of Microbiology*, 55(6):483–487.

Janin, Y.L. 2007. Antituberculosis drugs: Ten years of research. *Bioorganic & Medicinal Chemistry*, 15(7):2479–2513.

Jeon, D. 2018. Infection source and epidemiology of nontuberculous mycobacterial lung disease. *Tuberculosis and Respiratory Diseases*, 82(2):94–101.

Jorgensen, W.L., Chandrasekhar, J., Madura, J.D., Impey, R.W. & Klein, M.L. 1983. Comparison of simple potential functions for simulating liquid water. *Journal of Chemical Physics*, 79:926–935.

Kambli, P., Ajbani, K., Sadani, M., Nikam, C., Shetty, A., … Rodrigues, C. 2015. Defining multidrug-resistant tuberculosis: correlating GenoType MTBDRplus assay results with minimum inhibitory concentrations. *Diagnostic Microbiology and Infectious Disease*, 82(1):49–53.

Kana, B.D., Karakousis, P.C., Parish, T. & Dick, T. 2014. Future target-based drug discovery for tuberculosis? *Tuberculosis (Edinburgh, Scotland)*, 94(6):551–6.

Kanabus, A. 2021. *TB Statistics for South Africa - including prevalence survey - TBFacts. Global Health Education (GHE)*. https://tbfacts.org/tb-statistics-south-africa/ (Date of access: 31 Dec. 2021).

Kato-Maeda, M., Bifani, P.J., Kreiswirth, B.N. & Small, P.M. 2001. The nature and consequence of genetic variability within *Mycobacterium tuberculosis*. *The Journal of Clinical Investigation*, 107(5):533–537.

Kendall, B.A., Varley, C.D., Choi, D., Maureen Cassidy, P., Hedberg, K., … Winthrop, K.L. 2011. Distinguishing tuberculosis from nontuberculous mycobacteria lung disease, Oregon, USA. *Emerging Infectious Diseases*, 17(3):506.

Khalifa, R.A., Nasser, M.S., Gomaa, A.A., Osman, N.M. & Salem, H.M. 2013. Resazurin Microtiter Assay Plate method for detection of susceptibility of multidrug resistant *Mycobacterium tuberculosis* to second-line anti-tuberculous drugs. *Egyptian Journal of Chest Diseases and Tuberculosis*, 62(2):241-247.

Khan, B., Abdukadir, A., Qureshi, R. & Mustafa, G. 2011. Medicinal uses of plants by the inhabitants of Khunjerab National Park, Gilgit, Pakistan. *Pakistan Journal of Botany*, 43(5):2301–2310.

Kock, R., Michel, A.L., Yeboah-Manu, D., Azhar, E.I., Torrelles, J.B., … Zumla, A. 2021. Zoonotic tuberculosis – the changing landscape. *International Journal of Infectious Diseases*, 113:S68–S72.

Koh, W.-J. 2017. Nontuberculous mycobacteria—Overview. *Microbiology Spectrum,* 5(1).

Kumar, P., Nagarajan, A. & Uchil, P.D. 2018. Analysis of cell viability by the MTT Assay. *Cold Spring Harbor Protocols*. 2018(6). DOI: 10.1101/pdb.prot095505

Kurup, R. & Chester, K. 2014. Comparative evaluation of Ziehl Neelsen staining and knowledge, attitudes and practices of laboratory personnel in relation to Ziehl Nielsen. *West Indian Medical Journal*, 63(1): 39-44.

Laifangbam, S. Singh, HL, Singh, NB, Devi, KM and Singh, N. 2009. A comparative study of fluorescent microscopy with Ziehl-Neelsen staining and culture for the diagnosis of pulmonary tuberculosis. *Kathmandu University Medical Journal*, 226–230.

Lakshmanan, I. & Batra, S. 2013. Protocol for apoptosis assay by flow cytometry using Annexin V staining method. *Bio-Protocol*, 3(6).

Langhans, S.A. 2018. Three-dimensional in vitro cell culture models in drug discovery and drug repositioning. *Frontiers in Pharmacology*, 9(JAN):6.

Lee, J.Y. 2015. Diagnosis and treatment of extrapulmonary tuberculosis. *Tuberculosis and Respiratory Diseases*. 78(2):47–55.

Lee, H.S., Park, K.U., Park, J.O., Chang, H.E., Song, J. & Choe, G. 2011. Rapid, sensitive, and specific detection of Mycobacterium tuberculosis complex by real-time PCR on paraffin-embedded human tissues. *The Journal of Molecular Diagnostics,* 13(4):390–394.

Lemmerer, A. 2012. Covalent assistance to supramolecular synthesis: modifying the drug functionality of the antituberculosis API isoniazid in situ during co-crystallization with GRAS and API compounds. *CrystEngComm*, 14(7):2465–2478.

Lerche, P. & Muir Iii, W.W. 2009. Pain management in horses and cattle. In: S.J. Gaynor & W.W. Muir (Eds.), *Handbook of Veterinary Pain Management*, 2nd edition. Mosby: Elsevier.

Liebler, D.C. & Guengerich, F.P. 2005. Elucidating mechanisms of drug-induced toxicity. *Nature Reviews Drug Discovery,* 4(5):410–420.

Loxton, A.G., Knaul, J.K., Grode, L., Gutschmidt, A., Meller, C., … Cotton, M.F. 2017. Safety and immunogenicity of the recombinant *Mycobacterium bovis* BCG vaccine VPM1002 in HIV-unexposed newborn infants in South Africa. *Clinical and Vaccine Immunology*, 24(2):1–16.

Lulijwa, R., Alfaro, A.C., Merien, F., burdass, M., Young, T., Meyer, J., Nguyen, T.V and Trembath. 2019. Characterisation of Chinook salmon (*Oncorhynchus tshawytscha*) blood and validation of flow cytometry cell count and viability assay kit. *Fish and Shellfish Immunology*, 88:179–188.

Luminex. 2020. Muse® Cell Analyzer. Luminex Corporation, Austin, Texas, United States. Pdf. www.luminexcorp.com

Madacki, J., Mas Fiol, G. & Brosch, R. 2019. Update on the virulence factors of the obligate pathogen *Mycobacterium tuberculosis* and related tuberculosis-causing mycobacteria. *Infection, Genetics and Evolution*, 72:67–77.

Mahairas, G.G., Sabo, P.J., Hickey, M.J., Singh, D.C. & Stover, C.K. 1996. Molecular analysis of genetic differences between *Mycobacterium bovis* BCG and virulent *M. bovis*. *Journal of Bacteriology*, 178(5):1274–1282.

Mahmoud, B.G., Khairy, M., Rashwan, F.A. & Banks, C.E. 2017. Simultaneous voltammetric determination of acetaminophen and isoniazid (hepatotoxicity-related drugs) utilizing bismuth oxide nanorod modified screen-printed electrochemical sensing platforms. *Analytical Chemistry*, 89:2170–2178.

Maitra, A., Bates, S., Kolvekar, T., Devarajan, P. v., Guzman, J.D. & Bhakta, S. 2015. Repurposing—a ray of hope in tackling extensively drug resistance in tuberculosis. *International Journal of Infectious Diseases*, 32:50–55.

Motherwell, W.D.S. & Clegg, W. 1978. PLUTO. Program for plotting molecular and crystal structures. University of Cambridge, UK.

Marks, D.C., Belov, L., Davey, M.W., Davey, R.A. & Kidman, A.D. 1992. The MTT cell viability assay for cytotoxicity testing in multidrug-resistant human leukemic cells. *Leukemia Research*, 16(12):1165–1173.

Martins, F., Santos, S., Ventura, C., Elvas-Leitão, R., Santos, L., … Viveiros, M. 2014. Design, synthesis and biological evaluation of novel isoniazid derivatives with potent antitubercular activity. *European Journal of Medicinal Chemistry*, 81:119–138.

McKinnon, K.M. (2018). Flow cytometry: An overview. *Current Protocols in Immunology*, 120:5.1.1-5.1.11.

Meena, L.S. & Rajni, T. 2010. Survival mechanisms of pathogenic *Mycobacterium tuberculosis* H 37Rv. *FEBS Journal*, (277):2416–2427.

Merly, L. & Smith, S.L. 2017. Murine RAW 264.7 cell line as an immune target: are we missing something? *Immunopharmacology and Immunotoxicology*, 39(2):55–58.

Microbiology Society, 2003. *What is Microbiology?* | Microbiology Society, London, UK. https://microbiologysociety.org/why-microbiology-matters/what-is-microbiology.html (Date of access: 29 March 2022).

More, G.K. & Makola, R.T. 2020. In-vitro analysis of free radical scavenging activities and suppression of LPS-induced ROS production in macrophage cells by *Solanum sisymbriifolium* extracts. *Scientific Reports,* 10(1):1–9.

Mourenza, Á., Gil, J.A., Mateos, L.M. & Letek, M. 2020. Novel treatments against *Mycobacterium tuberculosis* based on drug repurposing. *Antibiotics*, 9(9):1–12.

Mukherjee, J.S., Rich, M.L., Socci, A.R., Joseph, J.K., Virú, F.A., … Seung, K.J. 2004. Programmes and principles in treatment of multidrug-resistant tuberculosis. *The Lancet*, 363(9407):474–481.

Narasimham, M. V., Sahu, S.K., Mohanty, I., Dash, M., Panda, P. & Parida, B. 2013. Pyopericardium due to infection with *Mycobacterium tuberculosis* - A rare case report. *Indian Journal of Tuberculosis*, 60(2):118–120.

Nascimento, I.P. & Leite, L.C.C. 2005. The effect of passaging in liquid media and storage on *Mycobacterium bovis*– BCG growth capacity and infectivity. *FEMS Microbiology Letters*, 243(1):81–86.

National Department of Health, South Africa. 2016. *South Africa's National Strategic Plan for HIV, TB and STIs. 2017-2022*. https://www.gov.za/sites/default/files/gcis_document/201705/nsp-hiv-tb-stia.pdf

Nguta, J.M., Appiah-Opong, R., Nyarko, A.K., Yeboah-Manu, D. & Addo, P.G.A. 2015. Current perspectives in drug discovery against tuberculosis from natural products. *International Journal of Mycobacteriology*, 4(3):165–183.

Nierode, G., Kwon, P.S., Dordick, J.S. & Kwon, S.J. 2016. Cell-based assay design for high-content screening of drug candidates. *Journal of Microbiology and Biotechnology,* 26(2): 213-225.

Nogueira, B.A., Castiglioni, C. & Fausto, R. 2020. Color polymorphism in organic crystals. *Communications Chemistry,* 3(1):1–12.

Orgeur, M. & Brosch, R. 2018. Evolution of virulence in the *Mycobacterium tuberculosis* complex. *Current Opinion in Microbiology.* https://www.sciencedirect.com/science/article/pii/S1369527417300796?casa_token=fuo7l2llxooaaaaa:hskz9exdgofpbkqpnbmvlvqovz5_oeiktsegfqs0el7h00spviw6fwotwxur2oftbcldofzhpa (Date of access: 04 Feb. 2021).

Palomino, J., Martin, A., Camacho, M., Guerra, H., Swings, J. & Portaels, F. 2002. Resazurin microtiter assay plate: Simple and inexpensive method for detection of drug resistance in *Mycobacterium tuberculosis*. *Antimicrobial Agents and Chemotherapy*, 46(8):2720–2722.

Pandey, A. s.a. Overview of all phases in drug development and discovery process. Pandey, Abhay, NorthEast BioAnalytical Laboratories, Hamden, Connecticut, USA. https://www.nebiolab.com/drug-discovery-and-development-process/ (Date of access: 17 Sept. 2023).

Pankey, G.A. & Sabath, L.D. 2004. Clinical relevance of bacteriostatic versus bactericidal mechanisms of action in the treatment of Gram-positive bacterial infections. *Clinical Infectious Diseases*, 38:864–70. https://academic.oup.com/cid/article/38/6/864/320723 Date of access: 21 Jul. 2023.

Papageorgiou, A., Foscolos, A.-S., Papanastasiou, I.P., Vlachou, M., Siamidi, A., … Tsotinis, A. 2019. Synthesis, biology, computational studies and in vitro controlled release of new isoniazid-based adamantane derivatives. *Future Medicinal Chemistry,* 11(4).

Parandhaman, T., Das, A., Ramalingam, B., Samanta, D., Sastry, T.P., … Das, S.K. 2015. Antimicrobial behavior of biosynthesized silica-silver nanocomposite for water disinfection: A mechanistic perspective. *Journal of Hazardous Materials*, 290:117–126.

Pietersen, R.-D., du Preez, I., Loots, D.T., van Reenen, M., Beukes, D., … Baker, B. 2020. Tween 80 induces a carbon flux rerouting in Mycobacterium tuberculosis. *Journal of Microbiological Methods*, 170:105795.

Prakoeswa, F.R.S., Rumondor, B.B. & Prakoeswa, C.R.S. 2022. Acid-fast staining revisited, a dated but versatile means of diagnosis. *The Open Microbiology Journal*, 16(1).

PubChem. 2018. *Isoniazid. Open Chemistry Database*. https://pubchem.ncbi.nml.nih.gov/compound/isoniazid#section=Top

Ratnatunga, C.N., Lutzky, V.P., Kupz, A., Doolan, D.L., Reid, D.W., … Miles, J.J. 2020. The rise of non-tuberculosis mycobacterial lung disease. *Frontiers in Immunology*, 11(March):1–12.

Riss, T.L., Moravec, R.A., Nile, A.L., Duellman, S., Benink, H.A., … Minor, L. 2013. Cell viability assays. In: S. Markossian *et al*. (Eds.), *The Assay Guidance Manual*. Eli Lilly & Company and National Center for Advancing Translational Sciences, Bethesda, MD, USA. https://www.ncbi.nlm.nih.gov/books/.

Rogall, T., Flohr, T. & Böttger, E.C. 1990. Differentiation of *Mycobacterium* species by direct sequencing amplified DNA. *Journal of General Microbiology*, 136:1915–1920.

Ryu, Y.J., Koh, W.J. & Daley, C.L. 2016. Diagnosis and treatment of nontuberculous mycobacterial lung disease: Clinicians' perspectives. *Tuberculosis and Respiratory Diseases*, 79(2):74–84.

Saboe, A., Sari, M.T. & Febrianora, M. 2020. A rare manifestation of Takotsubo Cardiomyopathy associated with non-tuberculous mycobacterium. *Journal of Clinical Tuberculosis and Other Mycobacterial Diseases*, 21:100191.

Sankar, M., Nowicka, E., Carter, E., Murphy, D.M., Knight, D.W., … Hutchings, G.J. 2014. The benzaldehyde oxidation paradox explained by the interception of peroxy radical by benzyl alcohol. *Nature Communications,* 5(1):1–6.

Schmid, K.B., Scherer, L., Barcellos, R.B., Kuhleis, D., Prestes, I.V., … Rossetti, M.L.R. 2014. Smear plus Detect-TB for a sensitive diagnosis of pulmonary tuberculosis: A cost-effectiveness analysis in an incarcerated population. *BMC Infectious Diseases*, 14(1):1–10.

Scholar, E. 2007. Isoniazid. In: S.J. Enna and David B. Bylund (Editors-in-Chief), *xPharm: The Comprehensive Pharmacology Reference*. Elsevier. pp. 1–7.

Şener, L.T., Albeniz, G., Dinç, B. & Albeniz, I. 2017. iCELLigence real-time cell analysis system for examining the cytotoxicity of drugs to cancer cell lines. *Experimental and Therapeutic Medicine*, 14(3):1866–1870.

Setshedi, I.B. & Smith, M.G. 2021. The crystal structure of the co-crystal: 2-hydroxybenzoic acid-N′-(butan-2-ylidene)pyridine-4-carbohydrazide, C10H13N3O·C7H6O3. *Zeitschrift für Kristallographie - New Crystal Structures*. 236(5):1093–1095.

Setshedi, I.B. & Smith, M.G. 2022. The crystal structure of 4-phenyl-4-[2-(pyridine-4-carbonyl)hydrazinylidene]butanoic acid, C16H15N3O3. *Zeitschrift für Kristallographie - New Crystal Structures*. 237(1):133–134.

Setshedi, I.B., Lemmerer, A. & Smith, M.G. 2021. The crystal structure of (E)-N′-(butan-2-ylidene)isonicotinohydrazide 0.5 hydrate C10H13N3O·0.5H2O. *Zeitschrift für Kristallographie - New Crystal Structures*, 236(6):1295–1296.

Setshedi, I.B., Lemmerer, A. & Smith, M.G. 2022. The crystal structure of N′-[bis(2-hydroxyphenyl)methylidene]pyridine-4-carbohydrazide, C19H15N3O3. *Zeitschrift für Kristallographie - New Crystal Structures*. 237(6):1105-1107.

Setshedi, I.B., Lemmerer, A. & Smith, M.G. 2023. Co-crystallization of N′-benzyl-idene-pyridine-4-carbohydrazide and benzoic acid via autoxidation of benzaldehyde. *Acta Crystallographica* Section E: *Crystallographic Communications*, 79(8):682–685.

Shehzad, A., Rehman, G., Ul-Islam, M., Khattak, W.A. & Lee, Y.S. 2013. Challenges in the development of drugs for the treatment of tuberculosis. *The Brazilian Journal of Infectious Diseases*, 17(1):74–81.

Sheldrick, G.M. 2007. A short history of SHELX. *Acta Crystallographica A,* 64(1):112–122.

Sherman, D.B., Zhang, S., Pitner, J.B. & Tropsha, A. 2004. Evaluation of the relative stability of liganded vs. ligand-free protein conformations using Simplicial Neighborhood Analysis of Protein Packing (SNAPP) Method. *Proteins*, 56(4):828.

Silakari, O. & Singh, P.K. 2021. ADMET tools: Prediction and assessment of chemical ADMET properties of NCEs. *Concepts and Experimental Protocols of Modelling and Informatics in Drug Design*, 299–320.

Silverman, R.B. & Holladay, M.W. 2014. *The Organic Chemistry of Drug Design and Drug Action*. Elsevier.

Singh, A.K. & Reyrat, J.-M. 2009. Laboratory maintenance of *Mycobacterium smegmatis*. *Current Protocols in Microbiology*, 14.

Sinha, S. & Vohora, D. 2018. Drug discovery and development: An overview. *Pharmaceutical Medicine and Translational Clinical Research*, (1):19–32.

Small, P.M., McClenny, N.B., Singh, S.P., Schoolnik, G.K., Tompkins, L.S. & Mickelsen, P.A. 1993. Molecular strain typing of *Mycobacterium tuberculosis* to confirm cross-contamination in the mycobacteriology laboratory and modification of procedures to minimize occurrence of false-positive cultures. *Journal of Clinical Microbiology*, 31(7):1677–1682.

Smith, M.G. & Lemmerer, A. 2018. Covalent assisted supramolecular synthesis: The influence of crystallization conditions on co-crystals of "masked" isoniazid derivatives. *Crystal Growth and Design*, 18(8):4777–4789.

Smith, M.G., Forbes, R.P. & Lemmerer, A. 2015. Covalent-assisted supramolecular synthesis: Masking of amides in co-crystal synthesis using benzophenone derivatives. *Crystal Growth and Design*, 15(8):3813–3821.

Solhaug, A., Holme, J.A., Haglund, K., Dendele, B., Sergent, O., … Alternar, al. 2013. iol induces abnormal nuclear morphology and cell cycle arrest in murine RAW 264.7 macrophages. *Toxicology Letters*, 219(1):8–17.

Spek, A.L. 2009. Structure validation in chemical crystallography. *Acta Crystallographica* Section D: *Biological Crystallography*, 65(2):148–155.

Stefanowicz-Hajduk, J. & Ochocka, J.R. 2020. Real-time cell analysis system in cytotoxicity applications: Usefulness and comparison with tetrazolium salt assays. *Toxicology Reports,* 7:335–344.

Stornaiuolo, M., De Kloe, G.E., Rucktooa, P., Fish, A., Van Elk, R., … Sixma, T.K. 2013. Assembly of a π–π stack of ligands in the binding site of an acetylcholine-binding protein. *Nature Communications,* 4(1):1–11.

Suarez, J., Ranguelova, K., Jarzecki, A.A., Manzerova, J., Krymov, V., … Magliozzo, R.S. 2009. An oxyferrous heme/protein-based radical intermediate is catalytically competent in the catalase reaction of *Mycobacterium tuberculosis* catalase-peroxidase (KatG). *The Journal of Biological Chemistry*, 284(11):7017–29.

Sun, H., Jiang, C., Wu, L., Bai, X. & Zhai, S. 2019. Cytotoxicity-related bioeffects induced by nanoparticles: The role of surface chemistry. *Frontiers in Bioengineering and Biotechnology*, 7.

Sun, J.R., Lee, S.Y., Perng, C.L. & Lu, J.J. 2009. Detecting *Mycobacterium tuberculosis* in BACTEC MGIT 960 cultures by inhouse IS6110-based PCR assay in routine clinical practice. *Journal of the Formosan Medical Association*, 108(2):119–125.

Tallarida, R.J. 2001. Drug synergism: Its detection and applications. *Journal of Pharmacology and Experimental Therapeutics*, 298(3).

Tallarida, R.J. 2011. Quantitative methods for assessing drug synergism. *Genes and Cancer*, 2(11):1003–1008.

Tamai, I. & Tsuji, A. 1996. Carrier-mediated approaches for oral drug delivery. *Advanced Drug Delivery Reviews*, 20(1):5–32.

Tang, M. & Zhang, W. 2009. [Pharmacodynamic interaction model and its clinical application]. *Sheng wu yi xue Gong Cheng xue za zhi = Journal of Biomedical Engineering = Shengwu Yixue Gongchengxue Zazhi*. 26(3):692–696. https://europepmc.org/article/med/19634700 (Date of access: 29 July 2023).

TBFacts.org. 2010. *TB Statistics for South Africa | National & Provincial*. https://www.tbfacts.org/tb-statistics-south-africa/ (Date of access: 12 Feb. 2018).

Thapa, J., Nakajima, C., Gairhe, K.P., Maharjan, B., Paudel, S., … Suzuki, Y. 2017. Wildlife tuberculosis: An emerging threat for conservation in South Asia. In: Lameed, G.S.A. (Ed.), *Global Exposition of Wildlife Management.* IntechOpen.

Tortoli, E., Cichero, P., Piersimoni, C., Simonetti, M.T., Gesu, G. & Nista, D. 1999. Use of BACTEC MGIT 960 for recovery of mycobacteria from clinical specimens: Multicenter study. *Journal of Clinical Microbiology*, 37(11):3578–82.

UNAIDS. 2011. *South Africa launches its new National Strategic Plan on HIV, STIs and TB, 2012-2016 UNAIDS*. https://www.unaids.org/en/resources/presscentre/featurestories/2011/december/20111220sansp (Date of access: 20 Feb. 2023).

Uzarski, J.S., DiVito, M.D., Wertheim, J.A. & Miller, W.M. 2017. Essential design considerations for the resazurin reduction assay to noninvasively quantify cell expansion within perfused extracellular matrix scaffolds. *Biomaterials*, 129:163.

Van Cleeff, M., Kivihya-Ndugga, L., Githui, W., Ng'ang'a, L., Kibuga, D., … Klatser, P.R. 2005. Cost-effectiveness of polymerase chain reaction versus Ziehl-Neelsen smear microscopy for diagnosis of tuberculosis in Kenya. *International Journal of Tuberculosis and Lung Disease*, 9(8):877–883.

Van Ingen, J., Boeree, M.J., Van Soolingen, D. & Mouton, J.W. 2012a. Resistance mechanisms and drug susceptibility testing of nontuberculous mycobacteria. *Drug Resistance Updates*, 15(3):149–161.

Van Ingen, J., Rahim, Z., Mulder, A., Boeree, M.J., Simeone, R., … van Soolingen, D. 2012b. Characterization of *Mycobacterium orygis* as *M. tuberculosis* complex subspecies. *Emerging Infectious Diseases*, 18(4):653–655.

Van Meerloo, J., Kaspers, G.J.L. & Cloos, J. 2011. Cell sensitivity assays: The MTT Assay. *Methods in Molecular Biology*, 731:237–245.

Varghese, B., Memish, Z., Abuljadayel, N., Al-Hakeem, R., Alrabiah, F. & Al-Hajoj, S.A. 2013. Emergence of clinically relevant non-tuberculous mycobacterial infections in Saudi Arabia. *PLOS Neglected Tropical Diseases*, 7(5):e2234.

Vergne, I., Gilleron, M. & Nigou, J. 2015. Manipulation of the endocytic pathway and phagocyte functions by *Mycobacterium tuberculosis* lipoarabinomannan. *Frontiers in Cellular and Infection Microbiology*, 4:187.

Vilchèze, C. & Jacobs, W.R. 2019. The isoniazid paradigm of killing, resistance, and persistence in *Mycobacterium tuberculosis*. *Journal of Molecular Biology*, 431(18):3450.

Vishweshwar, P., McMahon, J.A., Bis, J.A. & Zaworotko, M.J. 2006. Pharmaceutical co-crystals. Journal of Pharmaceutical Sciences, 95(3):499–516.

Von Mersi, W. & Schinner, F. 1991. An improved and accurate method for determining the dehydrogenase activity of soils with iodonitrotetrazolium chloride. *Biology and Fertility of Soils,* 11(3):216–220.

Vorster, M.J., Allwood, B.W., Diacon, A.H. & Koegelenberg, C.F.N. 2015. Tuberculous pleural effusions: Advances and controversies. *Journal of Thoracic Disease*, 7(6):981–991.

WHO (World Health Organization). 2012. Global tuberculosis report 2012. *WHO Library cataloguing-in-publication data*. ISBN:9789241564502.

WHO (World Health Organization). 2016. *Global* Tuberculosis Report 2016. *WHO Library cataloguing-in-publication data*. ISBN: 9789241656394.

WHO (World Health Organization). 2017. *Global Tuberculosis Report 2017*. http://www.who.int/mediacentre/factsheets/fs104/en/ (Date of access: 19 Feb. 2018).

WHO (World Health Organization). 2018. Let us END Tuberculosis. WHO Fact Sheet. https://www.afro.who.int/news/let-us-end-tuberculosis (Date of access: 19 Feb. 2018).

WHO. 2021a. WHO global lists of high burden countries for tuberculosis (TB), TB/HIV and multidrug/rifampicin-resistant TB (MDR/RR-TB), 2021-2025 Background document. http://apps.who.int/bookorders (Date of access: 06 May 2023).

WHO. 2021b. *Global Tuberculosis Report 2021*.

WHO. 2021c. Evidence and research gaps identified during development of policy guidelines for tuberculosis. World Health Organization. 1–26.

Wiegand, I., Hilpert, K. & Hancock, R.E.W. 2008. Agar and broth dilution methods to determine the minimal inhibitory concentration (MIC) of antimicrobial substances. *Nature Protocols,* 3(2):163–175.

Wilson, K. & Walker, J. (Eds). 2010. *Principles and Techniques of Biochemistry and Molecular Biology*, 7th edition. Cambridge University Press, New York. pp. 1–2.

World Health Organization (WHO), Food and Agriculture Organization of the United Nations (FAO), World Organisation for Animal Health (WOAH). 2017. Roadmap for zoonotic tuberculosis. World Health Organization. 24 pp. https://www.who.int/publications/i/item/9789241513043

Xu, T., Wang, C., Li, M., Yuan, M., Wei, J., … Wang, H. 2023. *Mycobacterium tuberculosis* PE8 (Rv1040c) promotes the intracellular survival of recombinant *Mycobacterium* by regulating host inflammatory cytokines and inhibiting cell late apoptosis. *DNA and Cell Biology*, 42(5):254–264.

Yan, G., Du, Q., Wei, X., Miozzi, J., Kang, C., … Zhang, W. 2018. Application of real-time cell electronic analysis system in modern pharmaceutical evaluation and analysis. *Molecules,* 23(12):3280.

Yogan Pillay. 2017. We can achieve a TB-free South Africa, but it's time to pick up the pace. *Bhekisisa Centre for Health Journalism.* http://bhekisisa.org/article/2017-03-23-00-we-can-achieve-a-tb-free-south-africa-but-its-time-to-pick-up-the-pace (Date of access: 27 March 2018).

Zhang, R.Y., Qin, Y., Lv, X.Q., Wang, P., Xu, T.Y., … Miao, C.Y. 2011. A fluorometric assay for high-throughput screening targeting nicotinamide phosphoribosyltransferase. *Analytical Biochemistry*, 412(1):18–25.

Zhang, T., Zhang, J., Wei, L., Liang, H., Zhang, J., … Wang, Z. 2023. The global, regional, and national burden of tuberculosis in 204 countries and territories, 1990–2019. *Journal of Infection and Public Health*, 16(3):368–375.

Zhang, Z.H., Tang, J.H., Zhan, Z.L., Zhang, X.L., Wu, H.H. & Hou, Y.N. 2012. Cellular toxicity of isoniazid together with rifampicin and the metabolites of isoniazid on QSG-7701 hepatocytes. *Asian Pacific Journal of Tropical Medicine*, 5(4):306–309.

Zhao, L.L., Sun, Q., Liu, H.C., Wu, X.C., Xiao, T.Y., … Wan, K.L. 2015. Analysis of embCAB mutations associated with ethambutol resistance in multidrug-resistant *Mycobacterium tuberculosis* isolates from China. *Antimicrobial Agents and Chemotherapy*, 59(4):2045–2050.

Zhou, W., Yang, B., Zou, Y., Rahman, K., Cao, X., … Cao, G. 2021. Screening of compounds for anti-tuberculosis activity, and *in vitro* and *in vivo* evaluation of potential candidates. *Frontiers in Microbiology*, 12:658637.
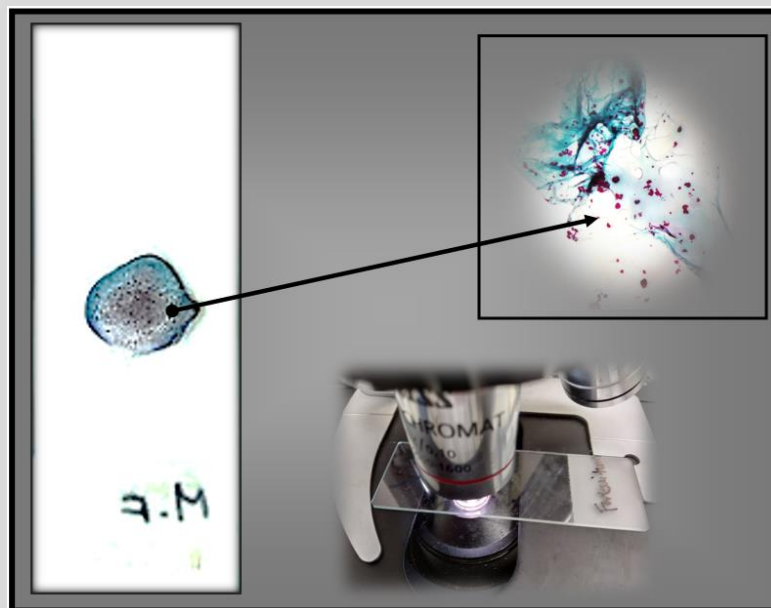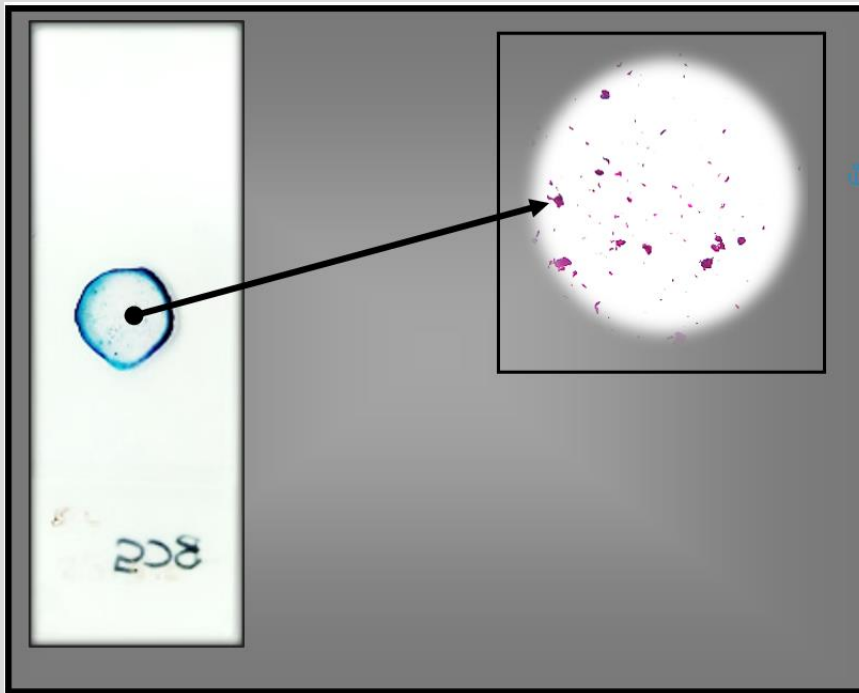
Appendix 1

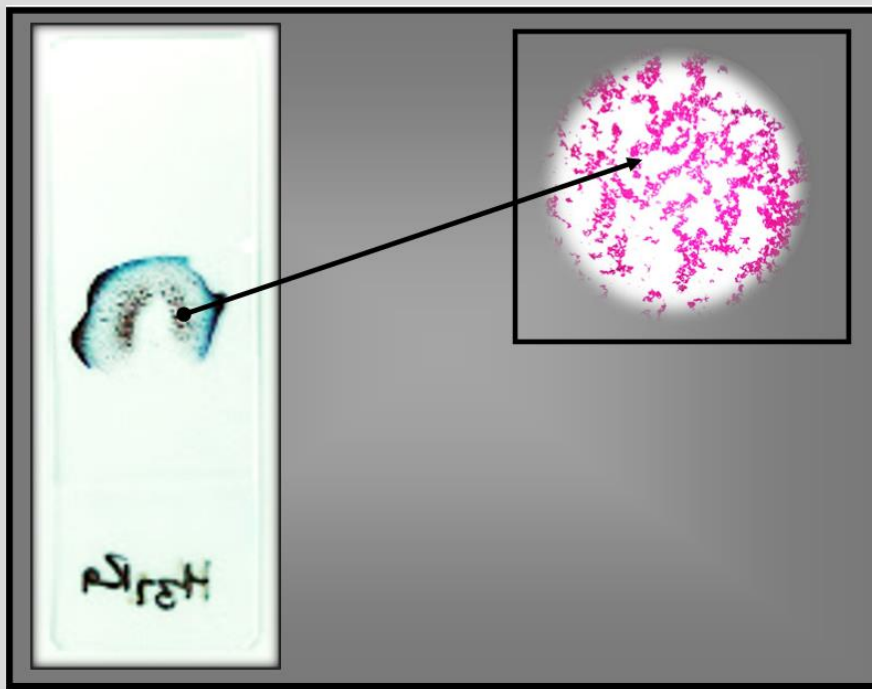*Mycobacterium* acid-fast results and purity confirmation
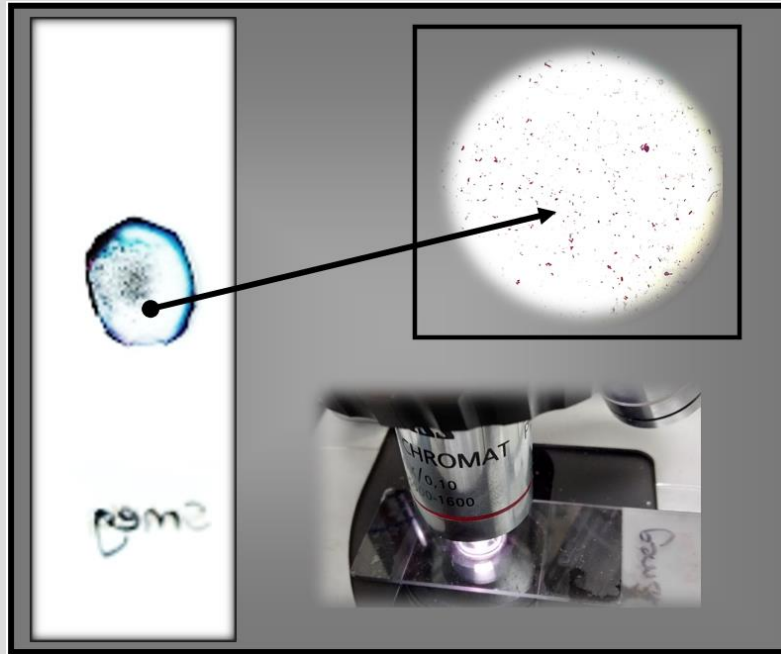
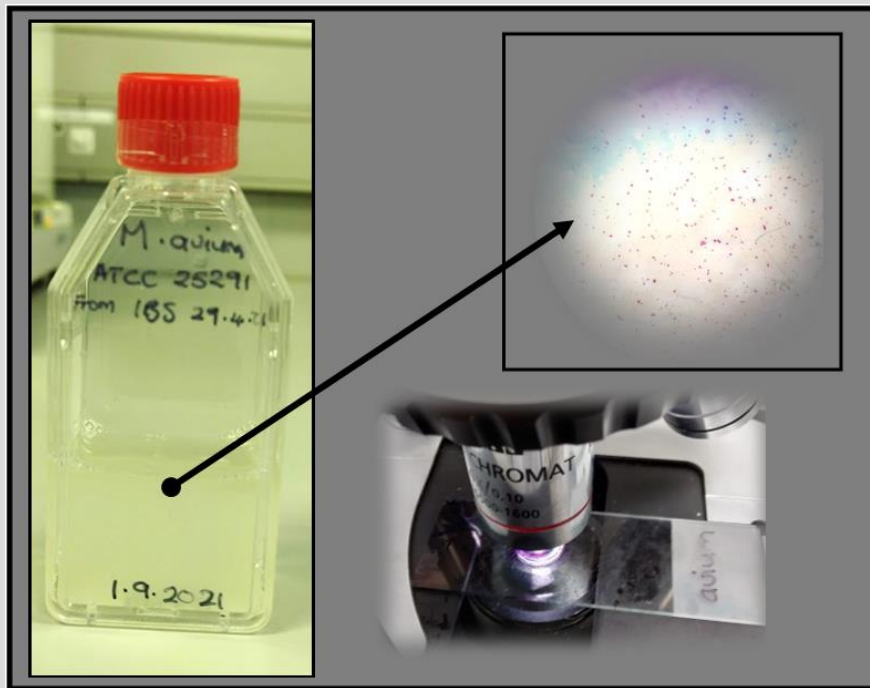**Appendix 1.1.** An image representation of the stained *M. smegmatis* cultured in broth.

Appendix 1.2. An image representation of the stained *M. fortuitum* cultured in broth.

Appendix 1.3. An image representation of the stained *M. bovis* (BCG).

Appendix 1.4. An image representation of the stained *M. tuberculosis* ($H_{37}R_a$).

**Appendix 1.5.** An image representative of the stained *M. avium*.

Appendix 2

Single compound and synergy compound serial dilution calculations
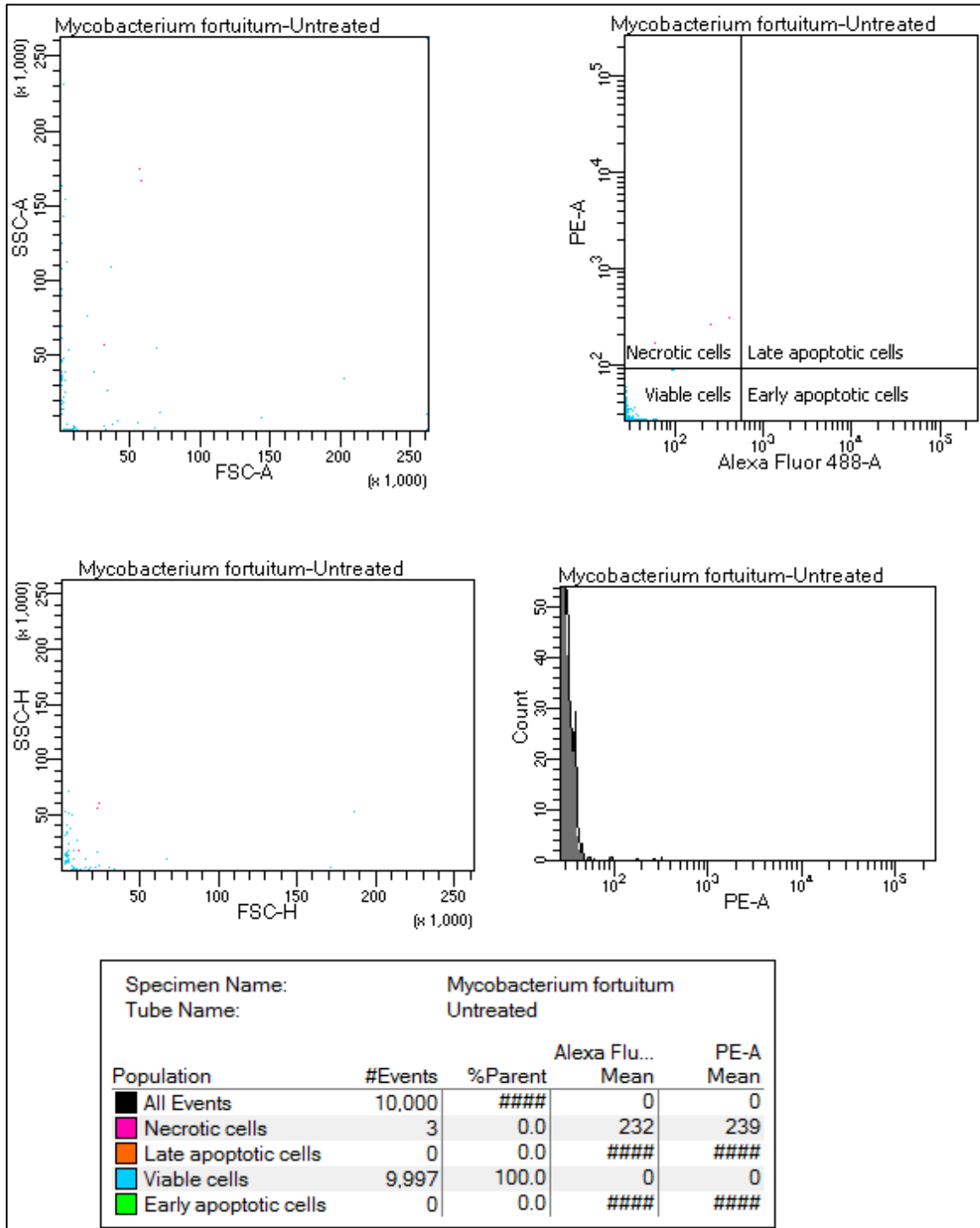
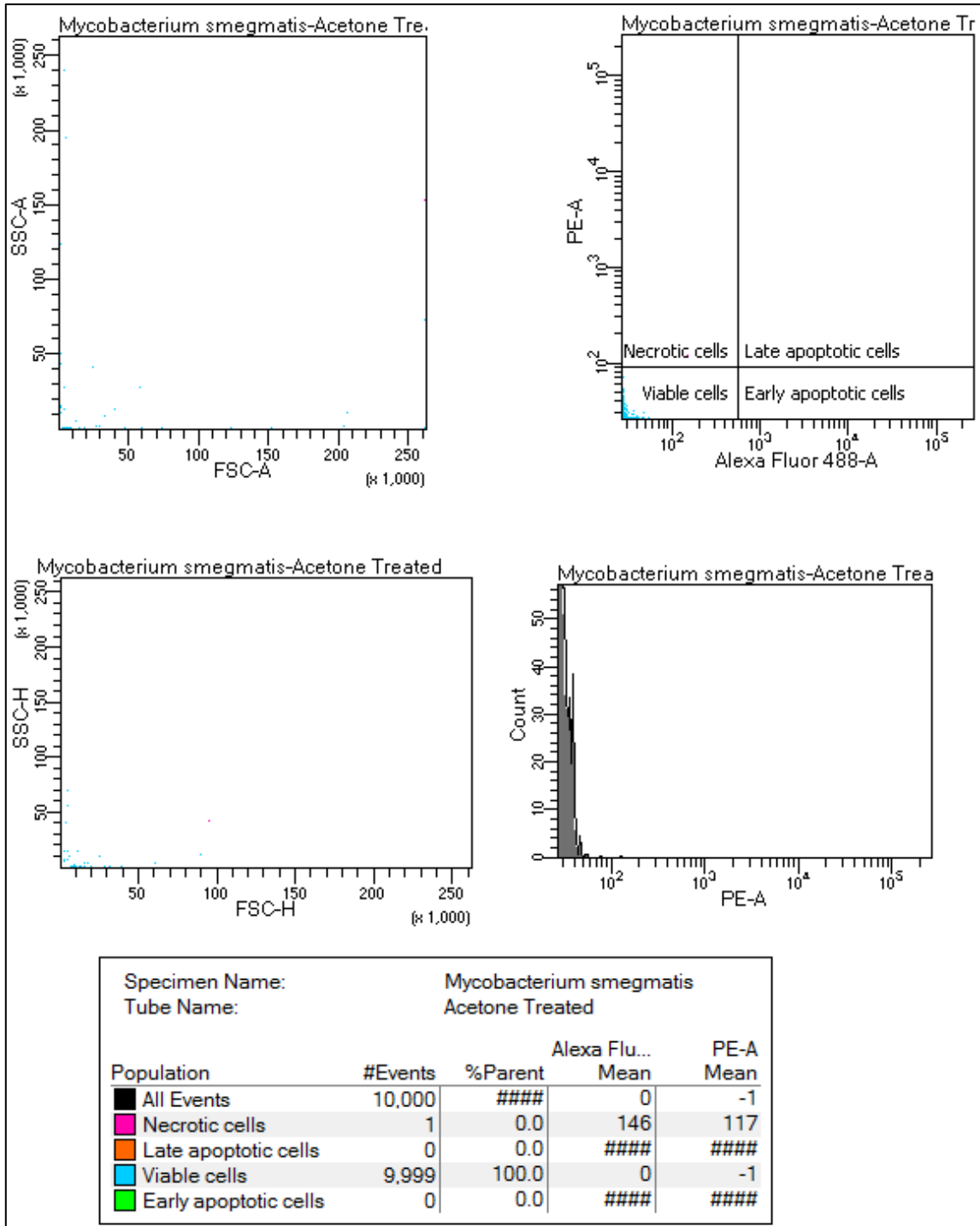| Dilutions - Synergy compound dilution calculations									
	Step 1				Step 2				
	After adding A				Remove 100uL A and add B				
									Conc of A + B after microbe
	A		B		A		B		
	ug/mL	ug A	ug/mL	Vol	ug/mL	ug A	ug/mL	ugB	Vol	ug/mL
Row 1	200	40	0	200	90,90909	20	90,90909	20	220	20,09091
Row 2	100	20	0	200	45,45455	10	90,90909	20	220	10,09091
Row 3	50	10	0	200	22,72727	5	90,90909	20	220	5,090909
Row 4	25	5	0	200	11,36364	2,5	90,90909	20	220	2,590909
Row 5	12,5	2,5	0	200	5,681818	1,25	90,90909	20	220	1,340909
Row 6	6,25	1,25	0	200	2,840909	0,625	90,90909	20	220	0,715909
Row 7	3,125	0,625	0	200	1,420455	0,3125	90,90909	20	220	0,403409
Row 8	1,5625	0,3125	0	200	0,710227	0,15625	90,90909	20	220	0,247159
Row 9	0,78125	0,15625	0	200	0,355114	0,078125	90,90909	20	220	0,169034
Row 10	0,390625	0,078125	0	200	0,177557	0,039063	90,90909	20	220	0,129972
Row 11	0,195313	0,039063	0	200	0,088778	0,019531	90,90909	20	220	0,11044
Row 12	0,097656	0,019531	0	200	0,044389	0,009766	90,90909	20	220	0,100675
Row 13	0,048828	0,009766	0	200	0,022195	0,004883	90,90909	20	220	0,095792
Row 14	0,024414	0,004883	0	200	0,011097	0,002441	90,90909	20	220	0,09335
Row 15	0,012207	0,002441	0	200	0,005549	0,001221	90,90909	20	220	0,09213
Row 16	0,006104	0,001221	0	200	0,002774	0,00061	90,90909	20	220	0,091519
Row 17	0,003052	0,00061	0	200	0,001387	0,000305	90,90909	20	220	0,091214
Row 18	0,001526	0,000305	0	200	0,000694	0,000153	90,90909	20	220	0,091062
Row 19	0,000763	0,000153	0	200	0,000347	7,63E-05	90,90909	20	220	0,090985
Row 20	0,000381	7,63E-05	0	200	0,000173	3,81E-05	90,90909	20	220	0,090947
Row 21	0,000191	3,81E-05	0	200	8,67E-05	1,91E-05	90,90909	20	220	0,090928
Row 22	9,54E-05	1,91E-05	0	200	4,33E-05	9,54E-06	90,90909	20	220	0,090919
Row 23	4,77E-05	9,54E-06	0	200	2,17E-05	4,77E-06	90,90909	20	220	0,090914
Row 24	2,38E-05	4,77E-06	0	200	1,08E-05	2,38E-06	90,90909	20	220	0,090911
Row 25	1,19E-05	2,38E-06	0	200	5,42E-06	1,19E-06	90,90909	20	220	0,09091
Row 26	5,96E-06	1,19E-06	0	200	2,71E-06	5,96E-07	90,90909	20	220	0,09091
Row 27	2,98E-06	5,96E-07	0	200	1,35E-06	2,98E-07	90,90909	20	220	0,090909
Row 28	1,49E-06	2,98E-07	0	200	6,77E-07	1,49E-07	90,90909	20	220	0,090909
Row 29	7,45E-07	1,49E-07	0	200	3,39E-07	7,45E-08	90,90909	20	220	0,090909
Row 30	3,73E-07	7,45E-08	0	200	1,69E-07	3,73E-08	90,90909	20	220	0,090909
Row 31	1,86E-07	3,73E-08	0	200	8,47E-08	1,86E-08	90,90909	20	220	0,090909
Row 32	9,31E-08	1,86E-08	0	200	4,23E-08	9,31E-09	90,90909	20	220	0,090909
Row 33	4,66E-08	9,31E-09	0	200	2,12E-08	4,66E-09	90,90909	20	220	0,090909
Row 34	2,33E-08	4,66E-09	0	200	1,06E-08	2,33E-09	90,90909	20	220	0,090909
Row 35	1,16E-08	2,33E-09	0	200	5,29E-09	1,16E-09	90,90909	20	220	0,090909
Row 36	5,82E-09	1,16E-09	0	200	2,65E-09	5,82E-10	90,90909	20	220	0,090909
Row 37	2,91E-09	5,82E-10	0	200	1,32E-09	2,91E-10	90,90909	20	220	0,090909
Row 38	1,46E-09	2,91E-10	0	200	6,61E-10	1,46E-10	90,90909	20	220	0,090909
Row 39	7,28E-10	1,46E-10	0	200	3,31E-10	7,28E-11	90,90909	20	220	0,090909
Row 40	3,64E-10	7,28E-11	0	200	1,65E-10	3,64E-11	90,90909	20	220	0,090909
Row 41	1,82E-10	3,64E-11	0	200	8,27E-11	1,82E-11	90,90909	20	220	0,090909
Row 42	9,09E-11	1,82E-11	0	200	4,13E-11	9,09E-12	90,90909	20	220	0,090909
Row 43	4,55E-11	9,09E-12	0	200	2,07E-11	4,55E-12	90,90909	20	220	0,090909
Row 44	2,27E-11	4,55E-12	0	200	1,03E-11	2,27E-12	90,90909	20	220	0,090909
Row 45	1,14E-11	2,27E-12	0	200	5,17E-12	1,14E-12	90,90909	20	220	0,090909
Row 46	5,68E-12	1,14E-12	0	200	2,58E-12	5,68E-13	90,90909	20	220	0,090909
Row 47	2,84E-12	5,68E-13	0	200	1,29E-12	2,84E-13	90,90909	20	220	0,090909
Row 48	1,42E-12	2,84E-13	0	200	6,46E-13	1,42E-13	90,90909	20	220	0,090909
Row 49	7,11E-13	1,42E-13	0	200	3,23E-13	7,11E-14	90,90909	20	220	0,090909
Row 50	3,55E-13	7,11E-14	0	200	1,61E-13	3,55E-14	90,90909	20	220	0,090909
Row 51	1,78E-13	3,55E-14	0	200	8,07E-14	1,78E-14	90,90909	20	220	0,090909
Row 52	8,88E-14	1,78E-14	0	200	4,04E-14	8,88E-15	90,90909	20	220	0,090909
Row 53	4,44E-14	8,88E-15	0	200	2,02E-14	4,44E-15	90,90909	20	220	0,090909
Row 54	2,22E-14	4,44E-15	0	200	1,01E-14	2,22E-15	90,90909	20	220	0,090909
Row 55	1,11E-14	2,22E-15	0	200	5,05E-15	1,11E-15	90,90909	20	220	0,090909
Row 56	5,55E-15	1,11E-15	0	200	2,52E-15	5,55E-16	90,90909	20	220	0,090909
Row 57	2,78E-15	5,55E-16	0	200	1,26E-15	2,78E-16	90,90909	20	220	0,090909
Row 58	1,39E-15	2,78E-16	0	200	6,31E-16	1,39E-16	90,90909	20	220	0,090909
Row 59	6,94E-16	1,39E-16	0	200	3,15E-16	6,94E-17	90,90909	20	220	0,090909
Row 60	3,47E-16	6,94E-17	0	200	1,58E-16	3,47E-17	90,90909	20	220	0,090909
Row 61	1,73E-16	3,47E-17	0	200	7,89E-17	1,73E-17	90,90909	20	220	0,090909
Row 62	8,67E-17	1,73E-17	0	200	3,94E-17	8,67E-18	90,90909	20	220	0,090909
Row 63	4,34E-17	8,67E-18	0	200	1,97E-17	4,34E-18	90,90909	20	220	0,090909
Row 64	2,17E-17	4,34E-18	0	200	9,86E-18	2,17E-18	90,90909	20	220	0,090909
Row 65	1,08E-17	2,17E-18	0	200	4,93E-18	1,08E-18	90,90909	20	220	0,090909
Row 66	5,42E-18	1,08E-18	0	200	2,46E-18	5,42E-19	90,90909	20	220	0,090909
Row 67	2,71E-18	5,42E-19	0	200	1,23E-18	2,71E-19	90,90909	20	220	0,090909
Row 68	1,36E-18	2,71E-19	0	200	6,16E-19	1,36E-19	90,90909	20	220	0,090909
Row 69	6,78E-19	1,36E-19	0	200	3,08E-19	6,78E-20	90,90909	20	220	0,090909
Row 70	3,39E-19	6,78E-20	0	200	1,54E-19	3,39E-20	90,90909	20	220	0,090909
Row 71	1,69E-19	3,39E-20	0	200	7,7E-20	1,69E-20	90,90909	20	220	0,090909
Row 72	8,47E-20	1,69E-20	0	200	3,85E-20	8,47E-21	90,90909	20	220	0,090909

Appendix 3

Flow cytometry results.
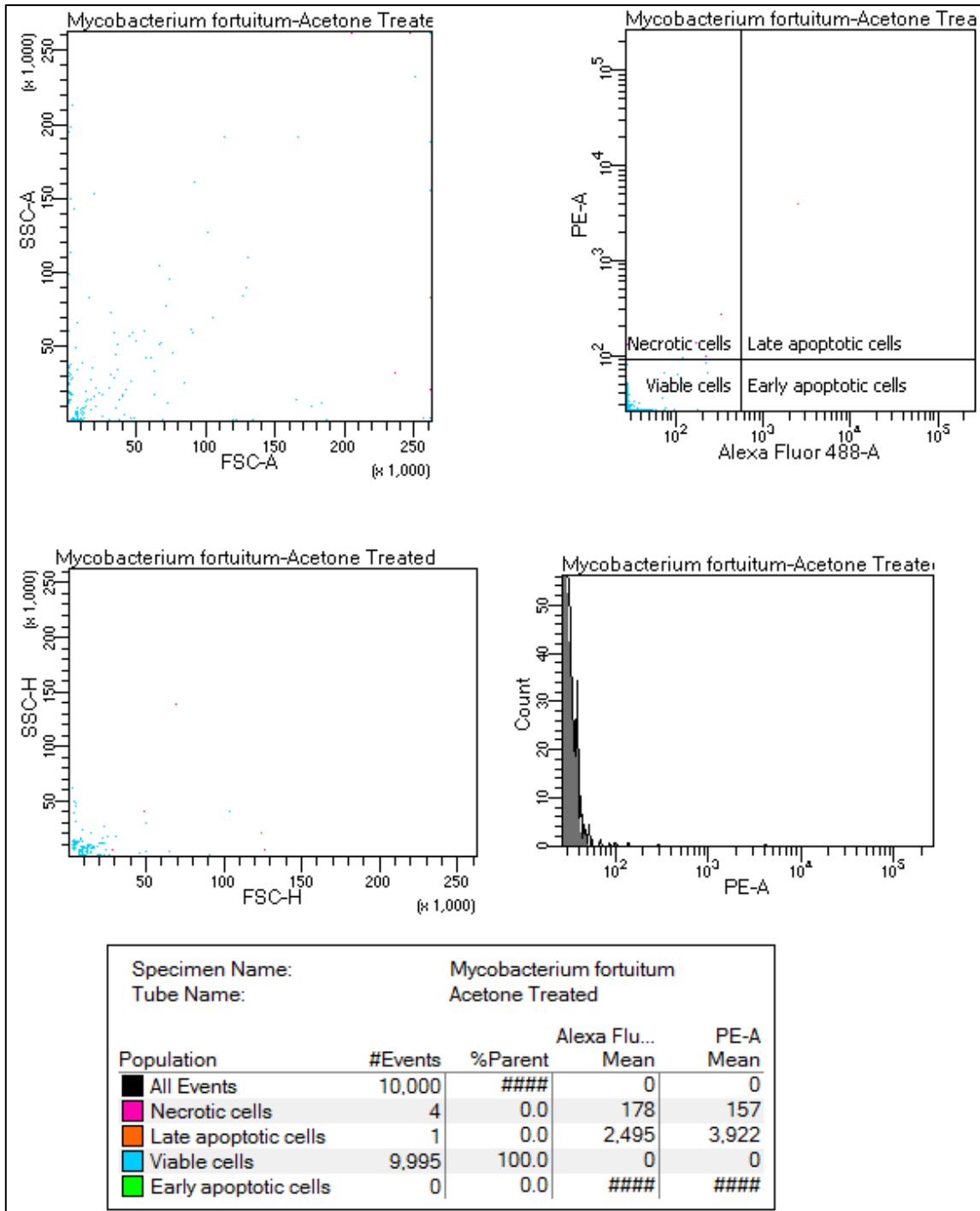
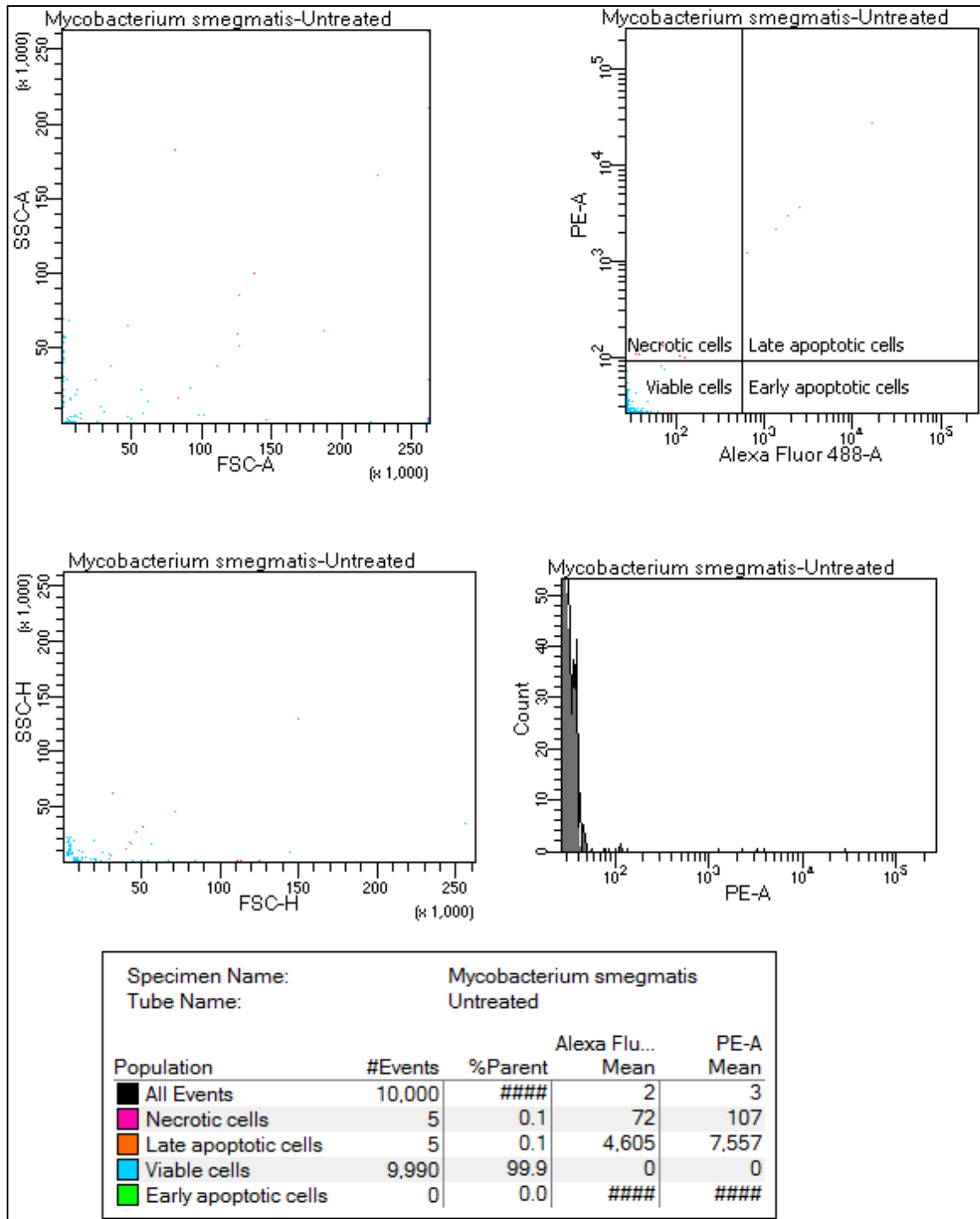**Appendix 3.1.** Acetone treated *M. fortuitum* control cells.

**Appendix 3.2.** Untreated (blank) *M. fortuitum* control cells.
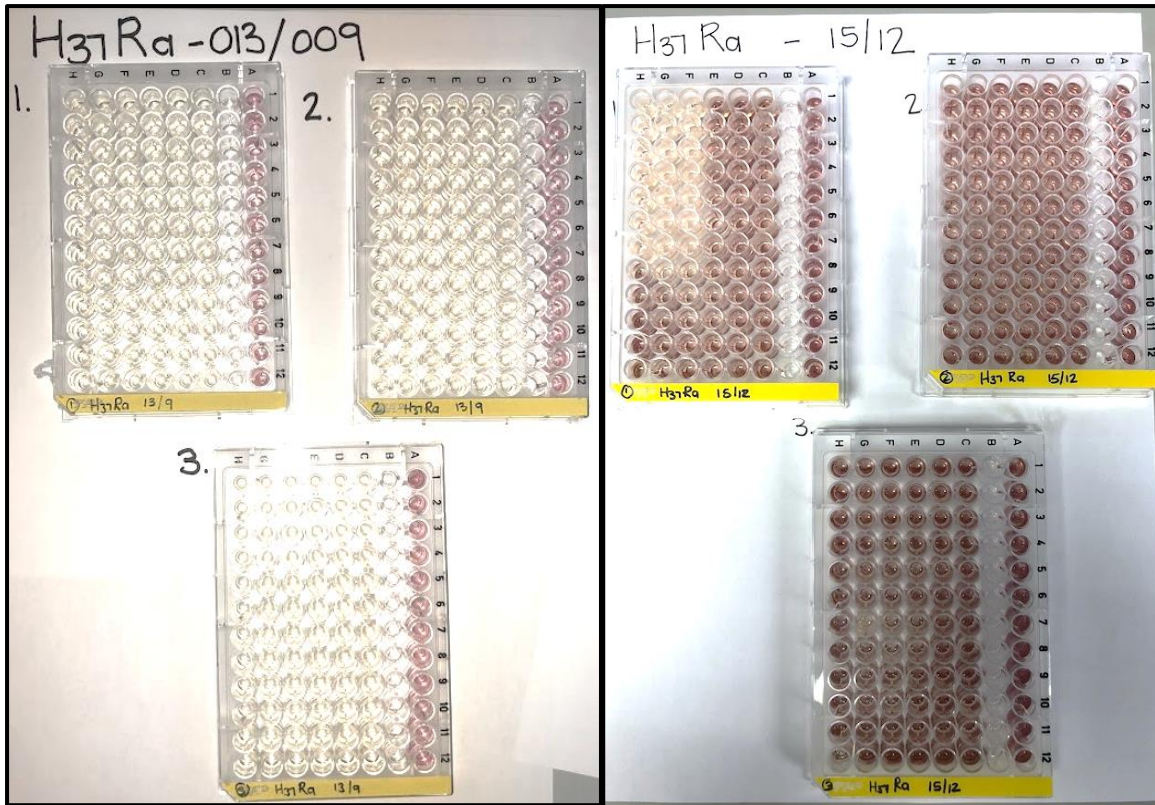
Mycobacterium smegmatis-Acetone Tre.

Mycobacterium smegmatis-Acetone Tr

| Necrotic cells | Late apoptotic cells |
| Viable cells | Early apoptotic cells |

Mycobacterium smegmatis-Acetone Treated

Mycobacterium smegmatis-Acetone Trea

| Specimen Name: | Mycobacterium smegmatis |
| Tube Name: | Acetone Treated |

Population	#Events	%Parent	Alexa Flu... Mean	PE-A Mean
All Events	10,000	####	0	-1
Necrotic cells	1	0.0	146	117
Late apoptotic cells	0	0.0	####	####
Viable cells	9,999	100.0	0	-1
Early apoptotic cells	0	0.0	####	####

Appendix 3.3. Acetone treated *M. smegmatis* control cells.

Appendix 3.4. Untreated (blank) *M. smegmatis* control cells.
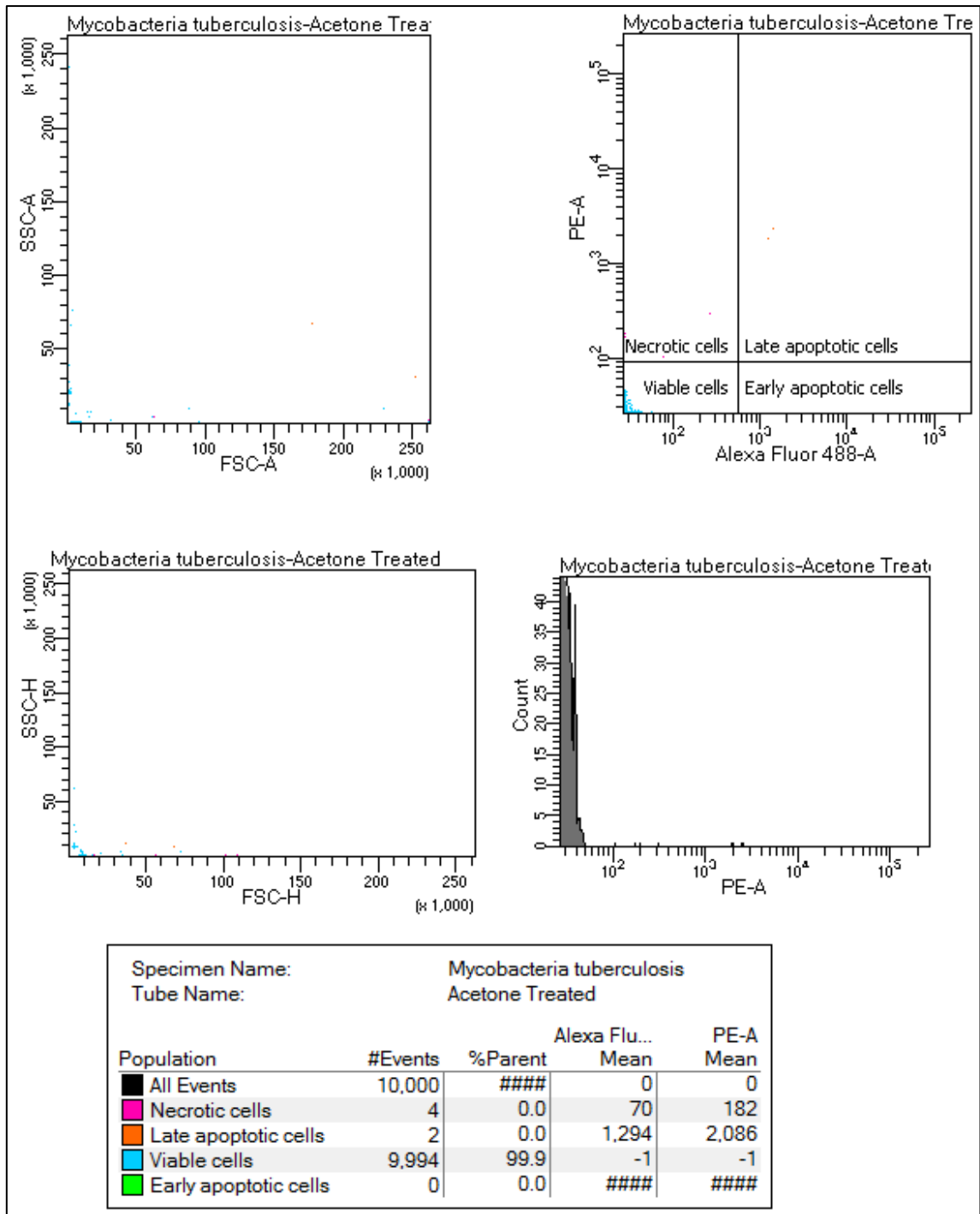
Appendix 3.5. Acetone treated MTB ($H_{37}R_a$) control cells.
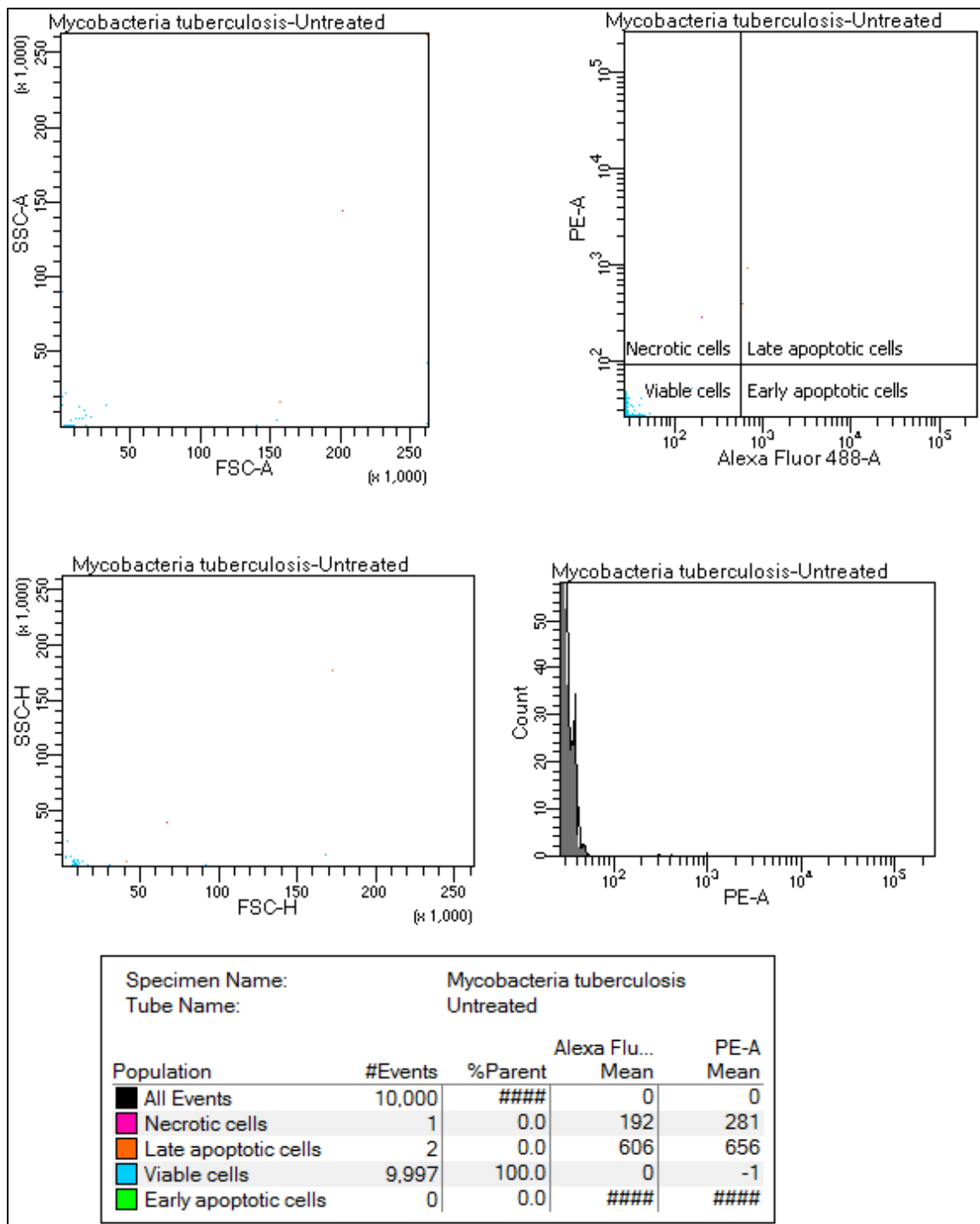
Appendix 3.6. Untreated MTB ($H_{37}R_a$) control cells.
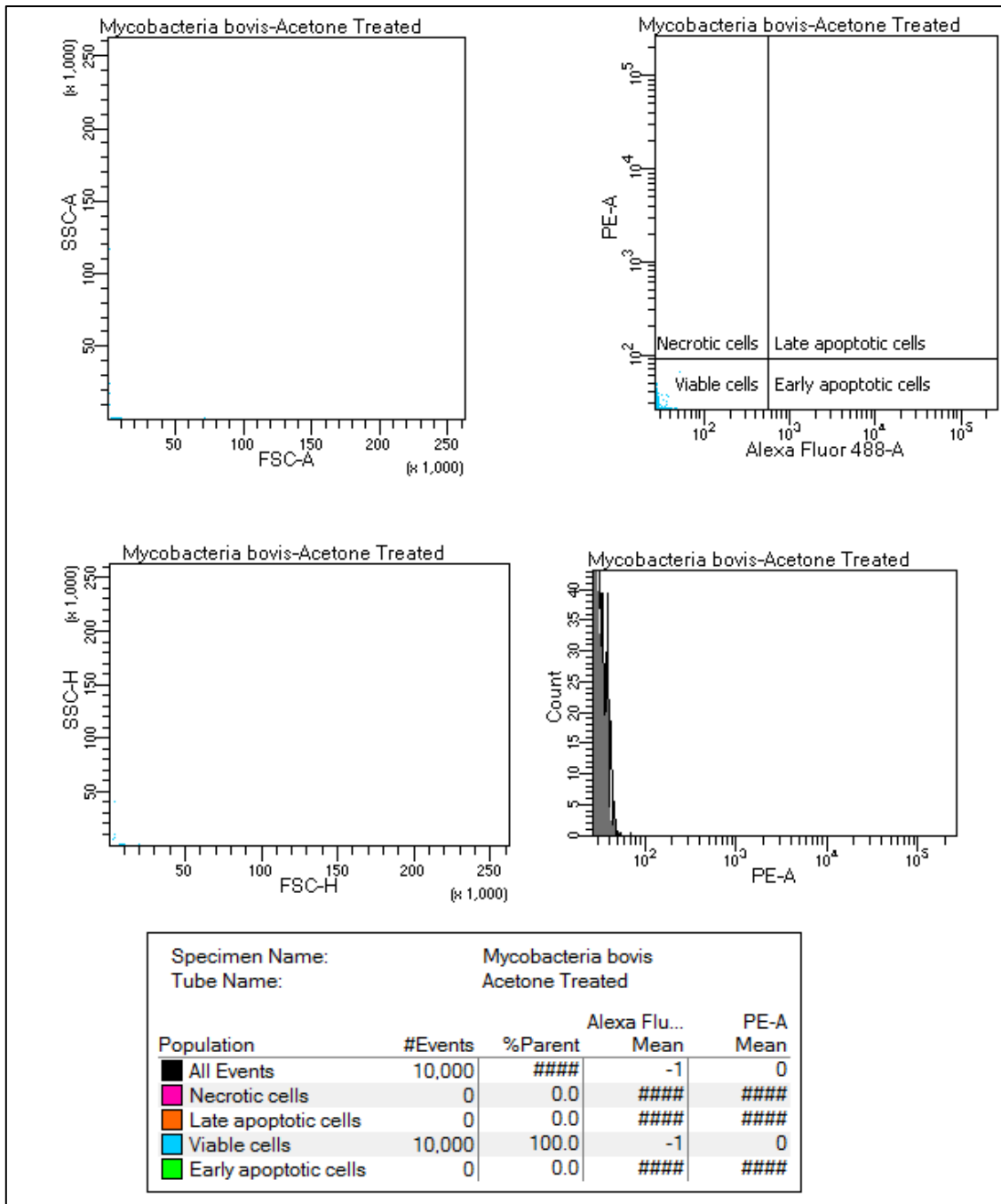
Appendix 3.7. Acetone treated *M. bovis* BCG control cells.
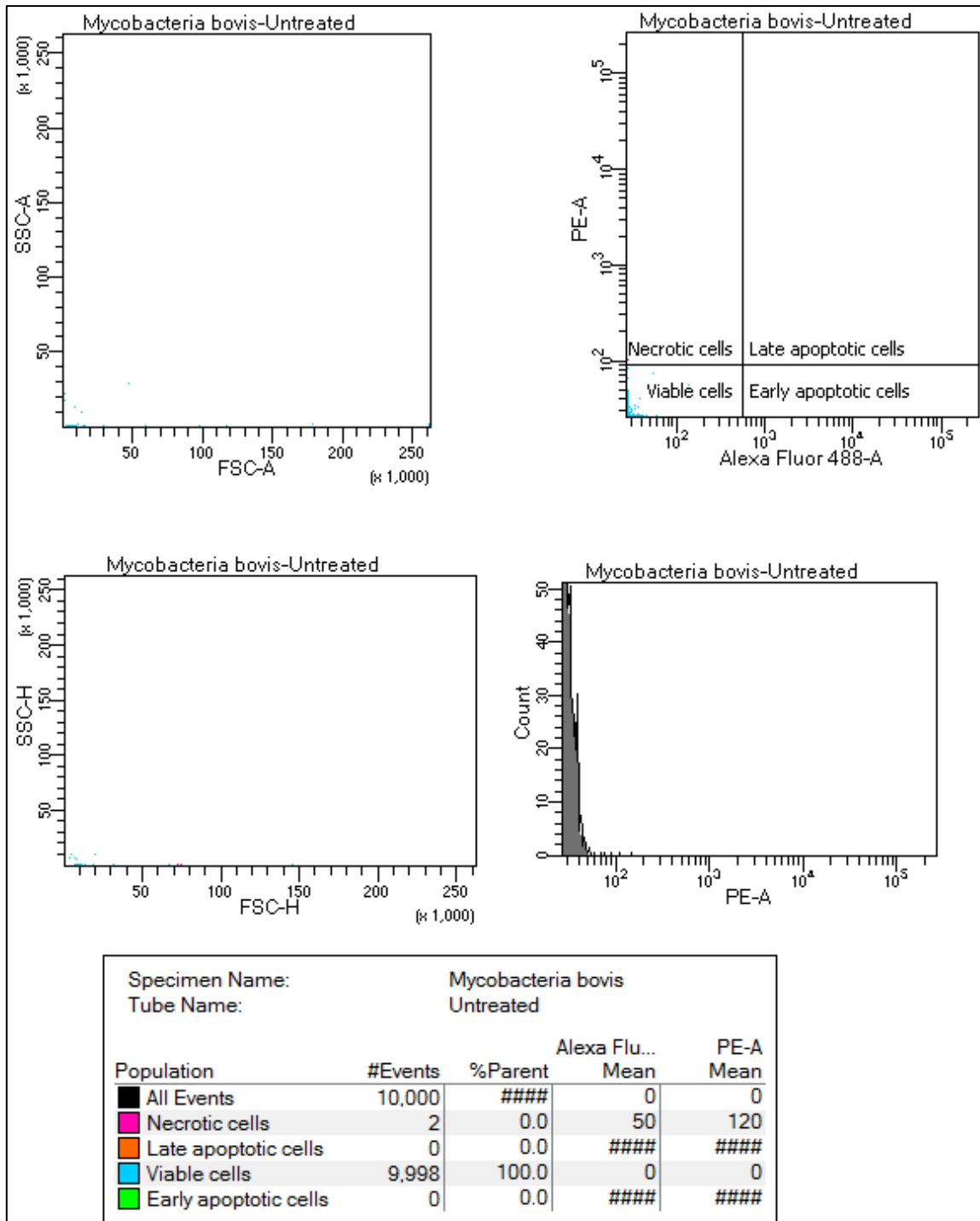
Appendix 3.8. Untreated *M. bovis* BCG control cells.

Appendix 4

Minimum inhibitory concentration results

Appendix 4.1. *Mycobacterium tuberculosis* ($H_{37}R_a$) MIC result images
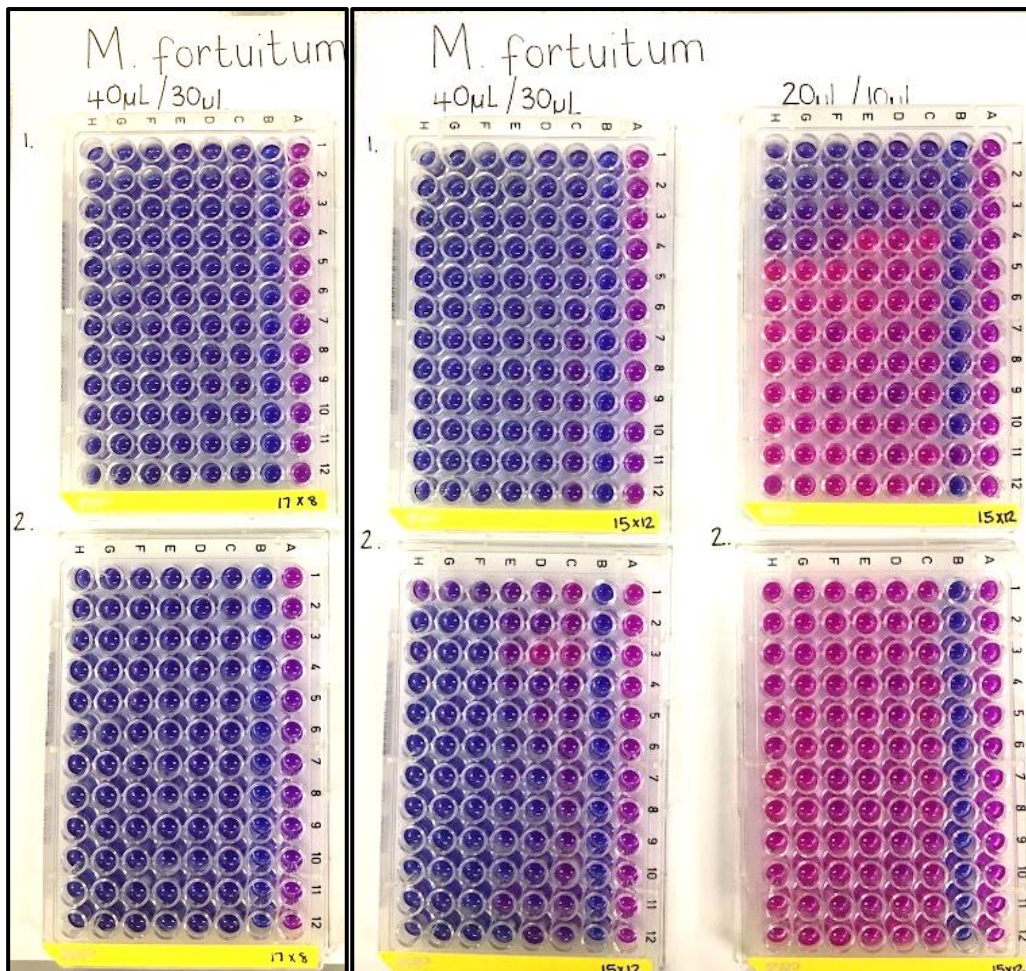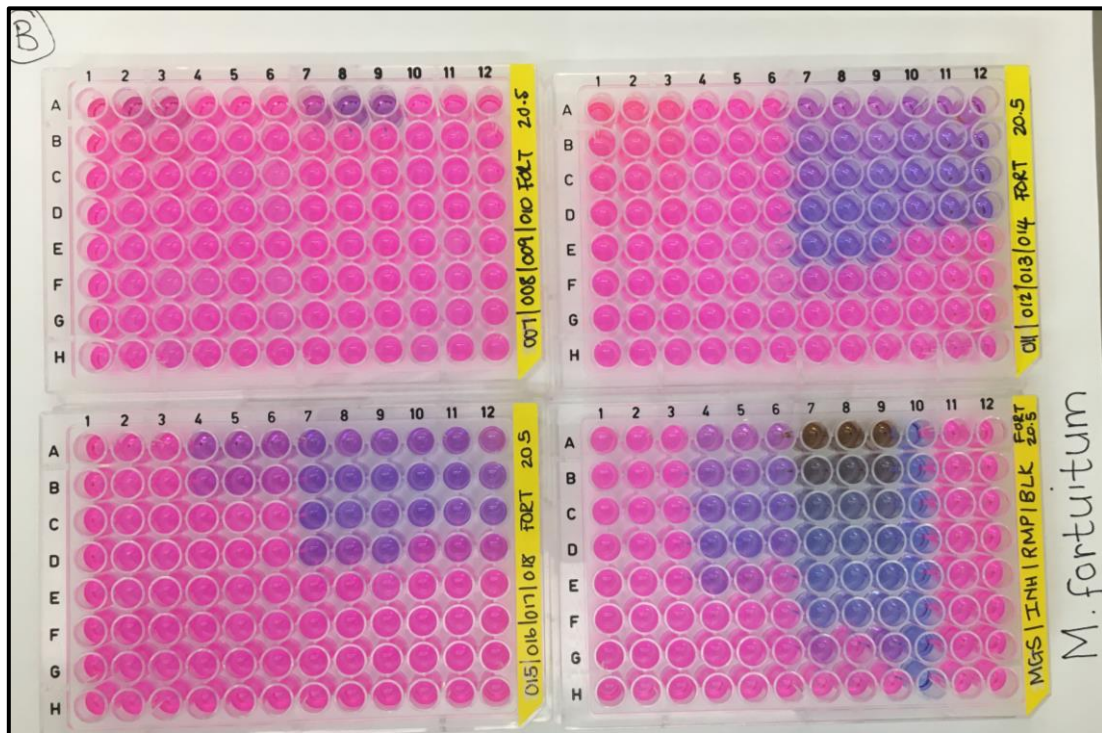

154
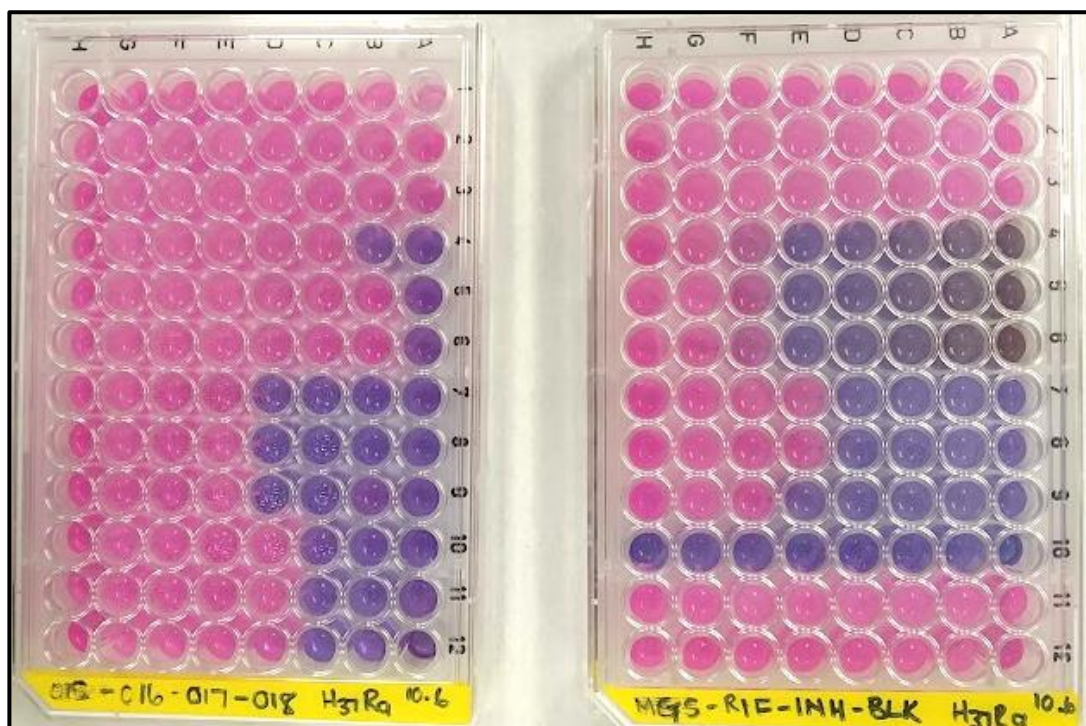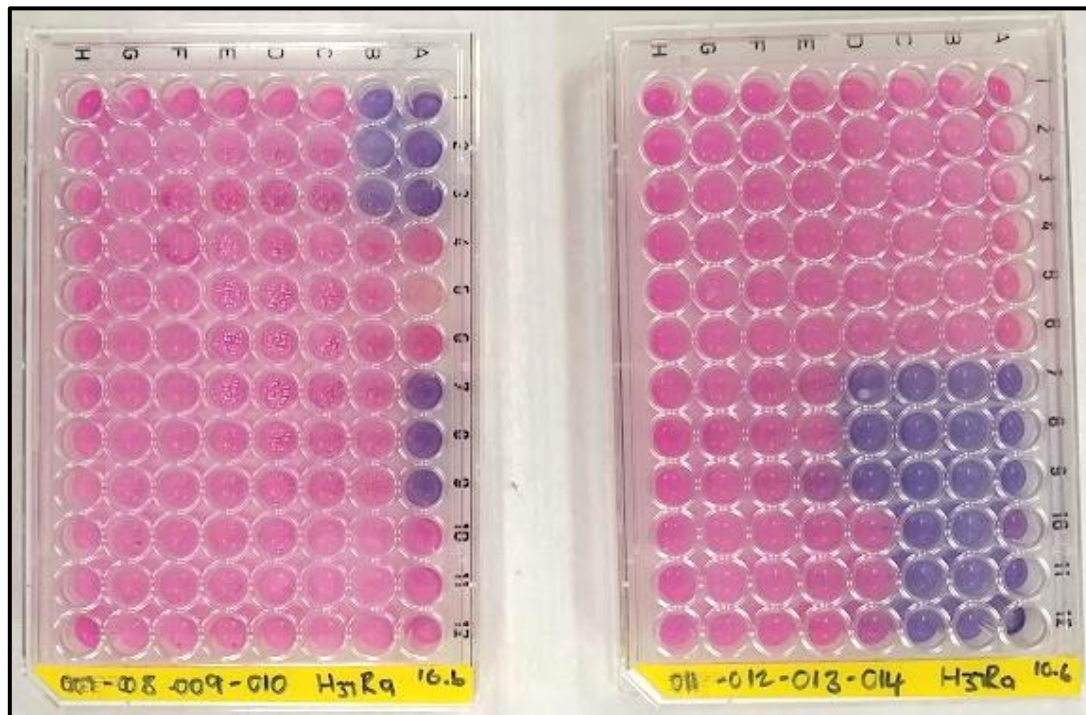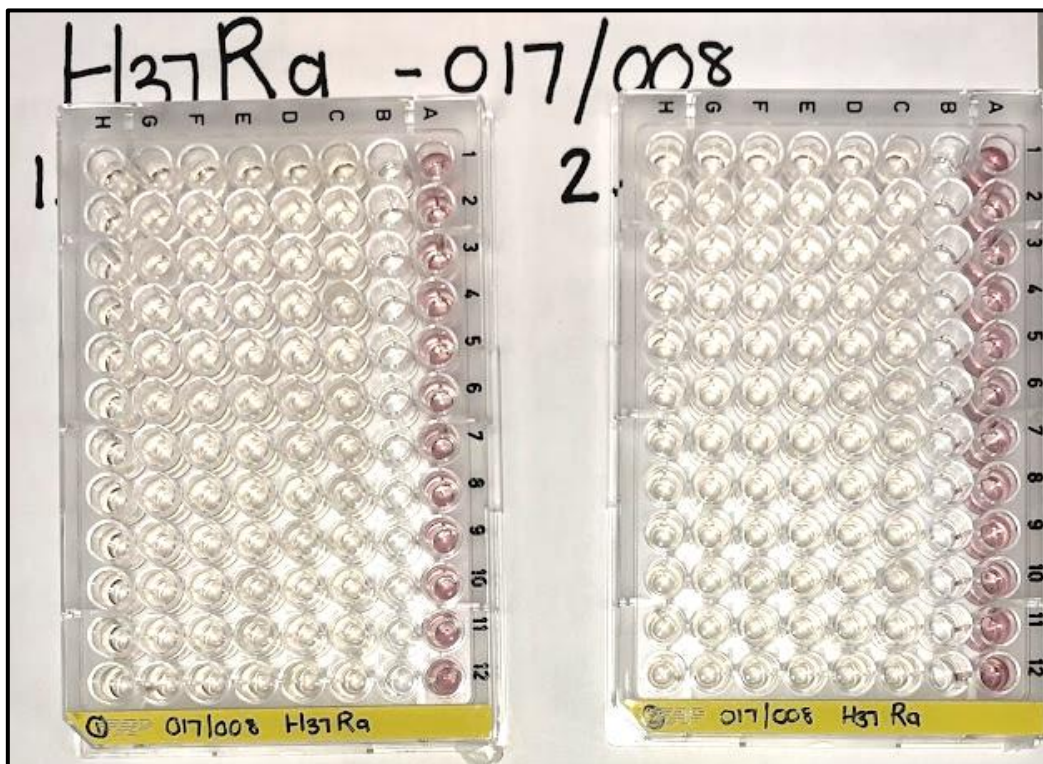
Appendix 4.2. *Mycobacterium bovis* (BCG) MIC.

157
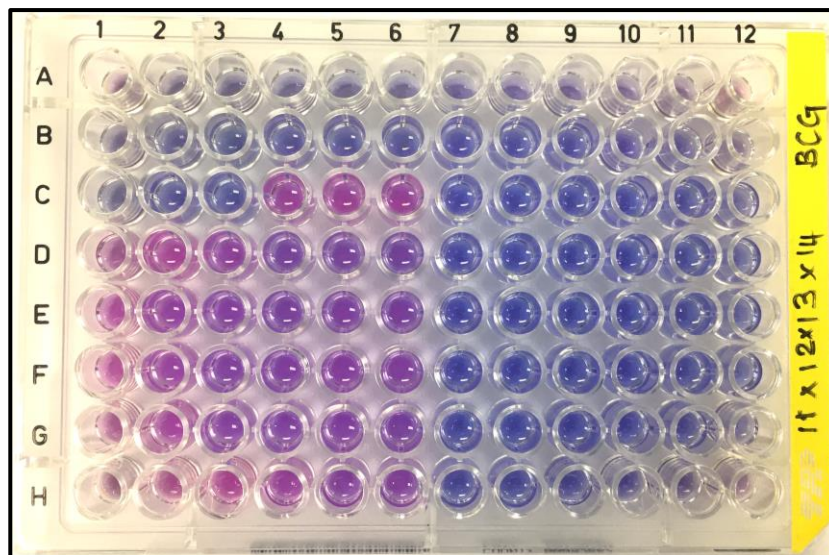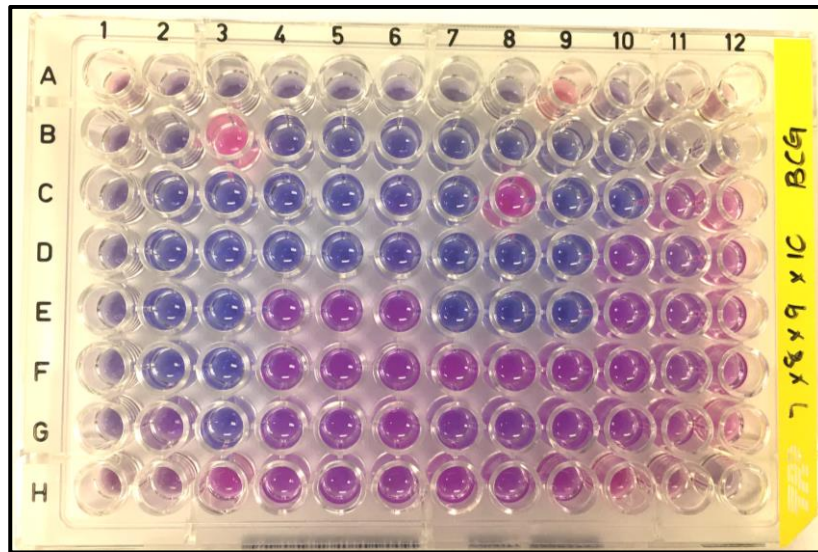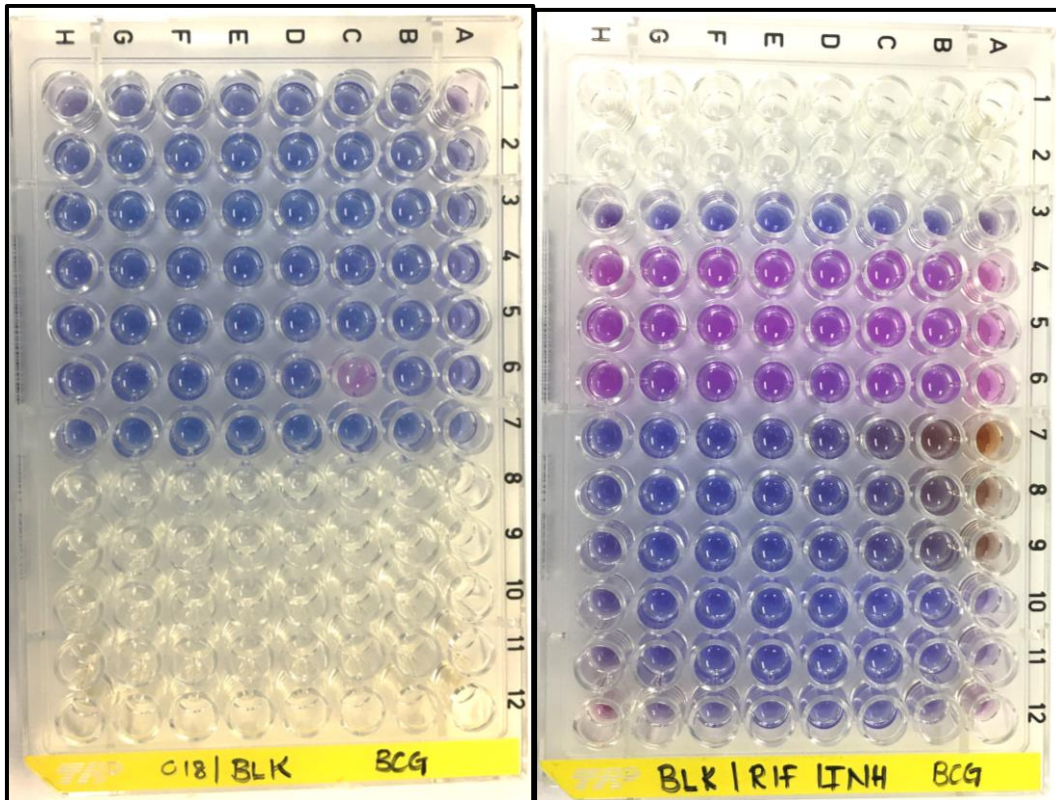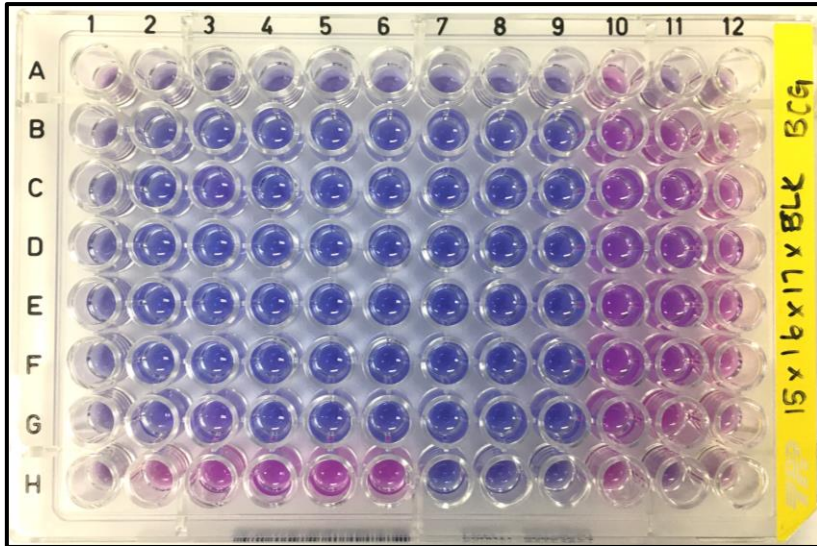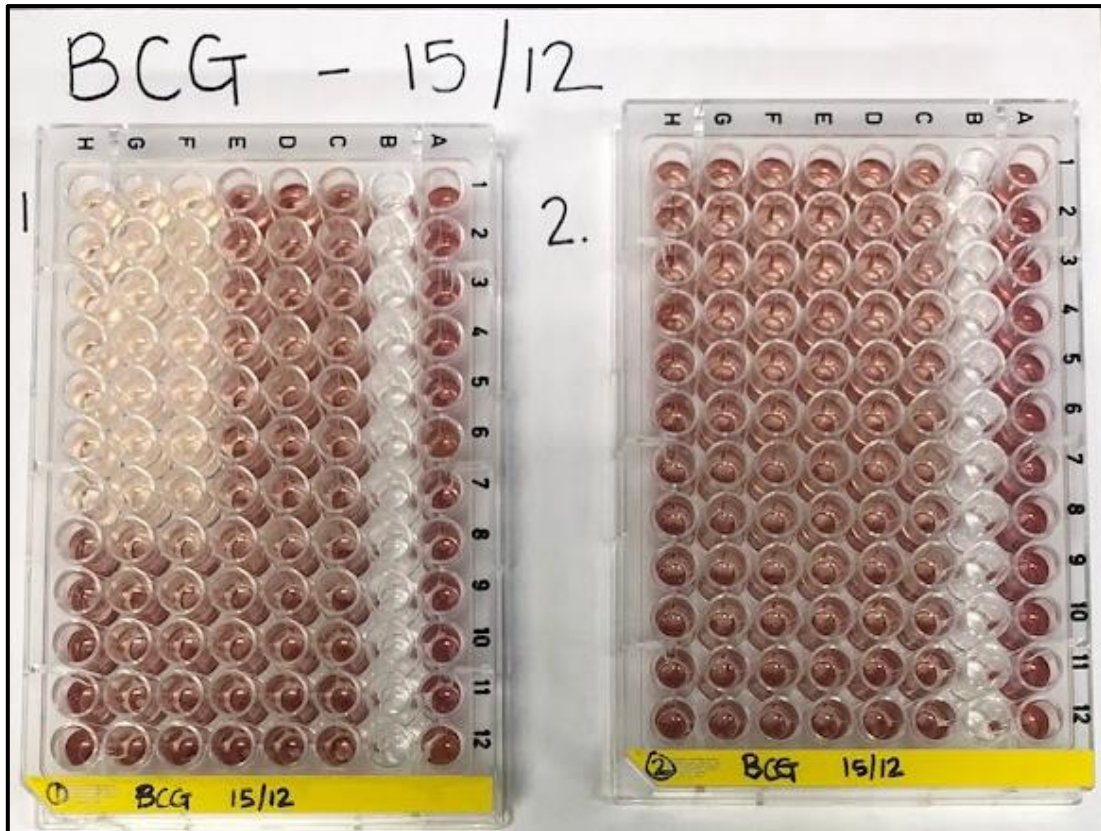
Appendix 4.3. *Mycobacterium smegmatis* (ATCC 14468) MIC results.
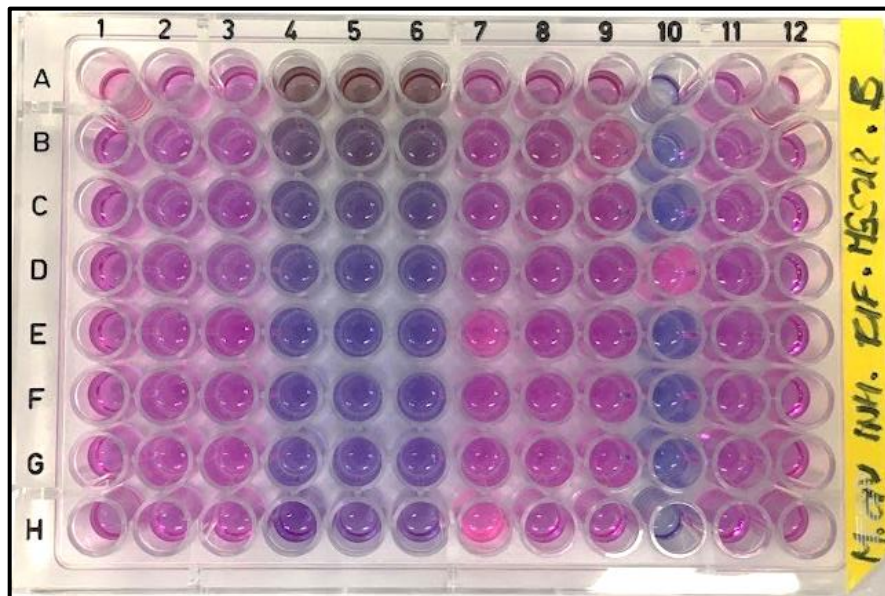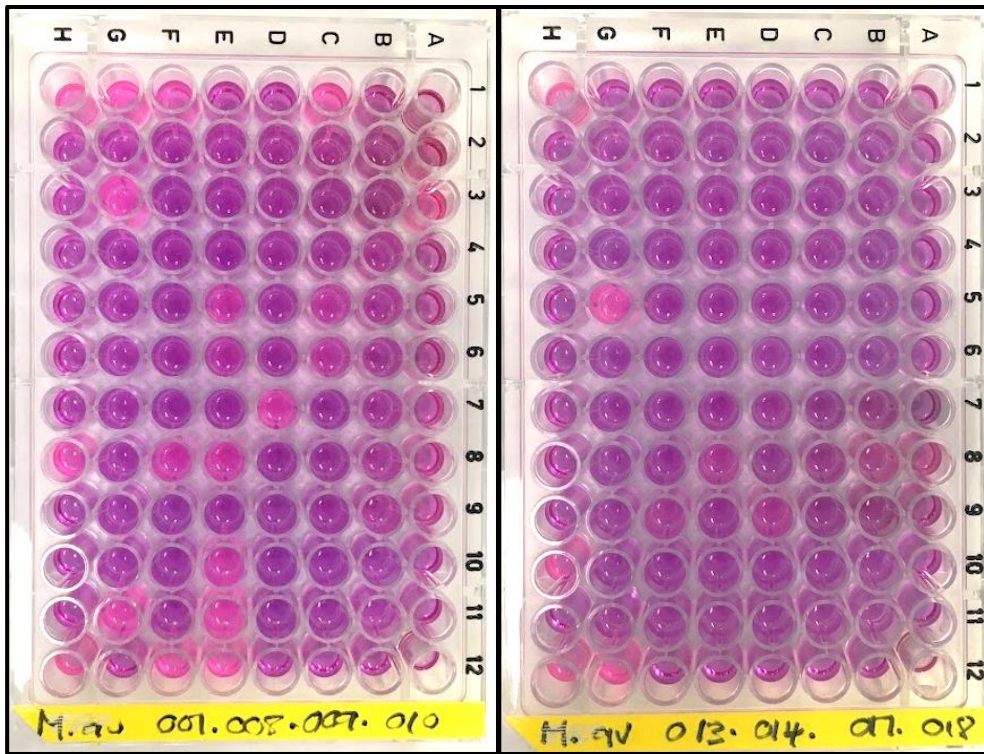
IBS 012/015

IBS 008/017

IBS 009/013
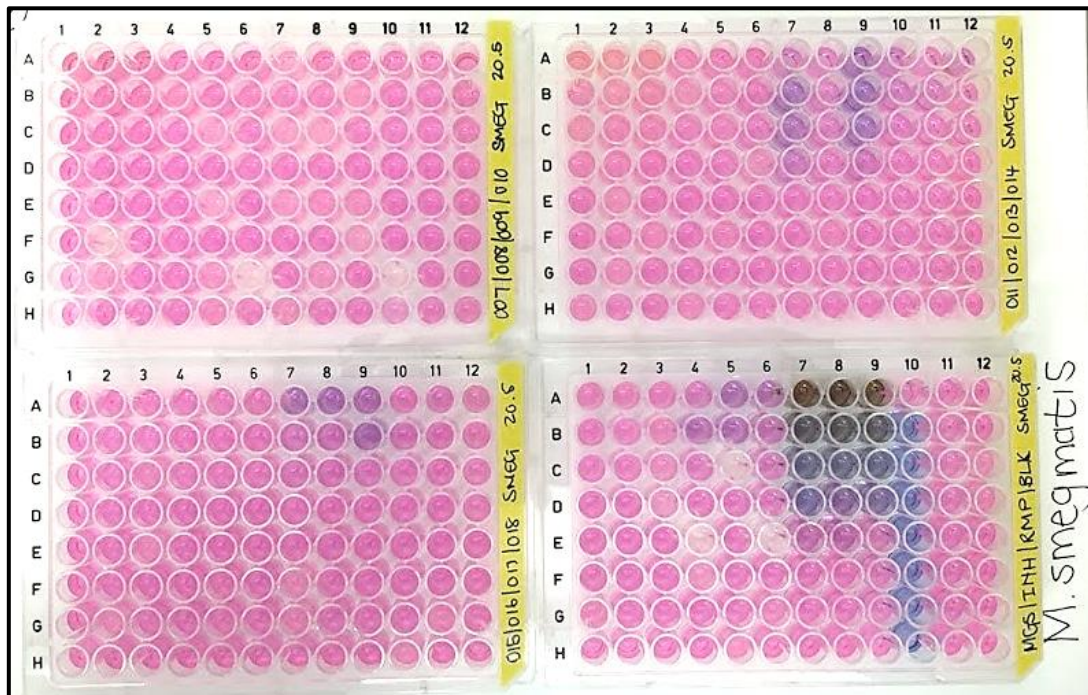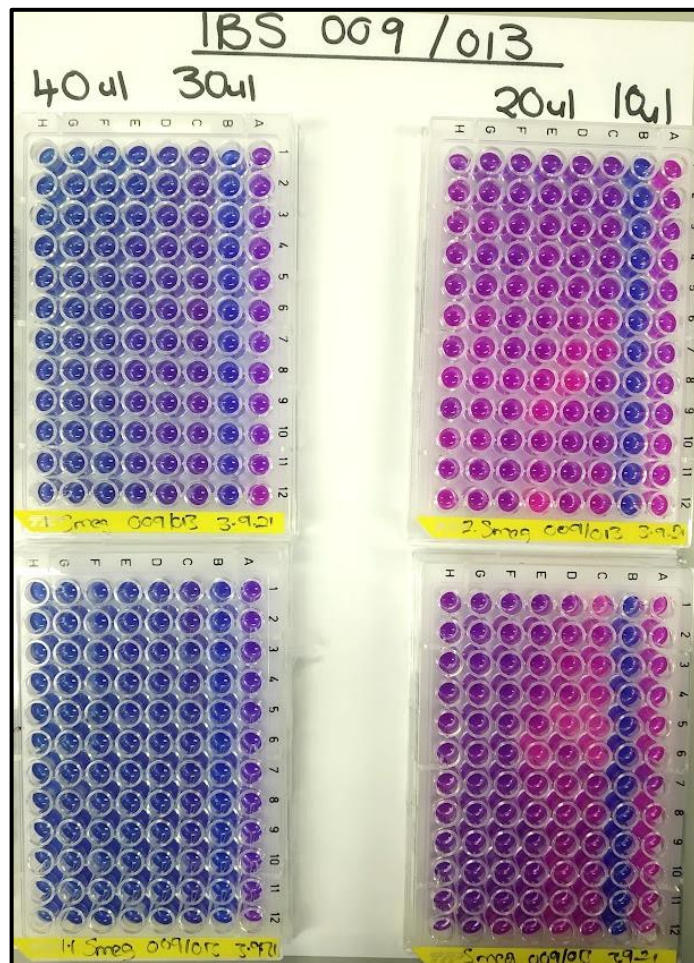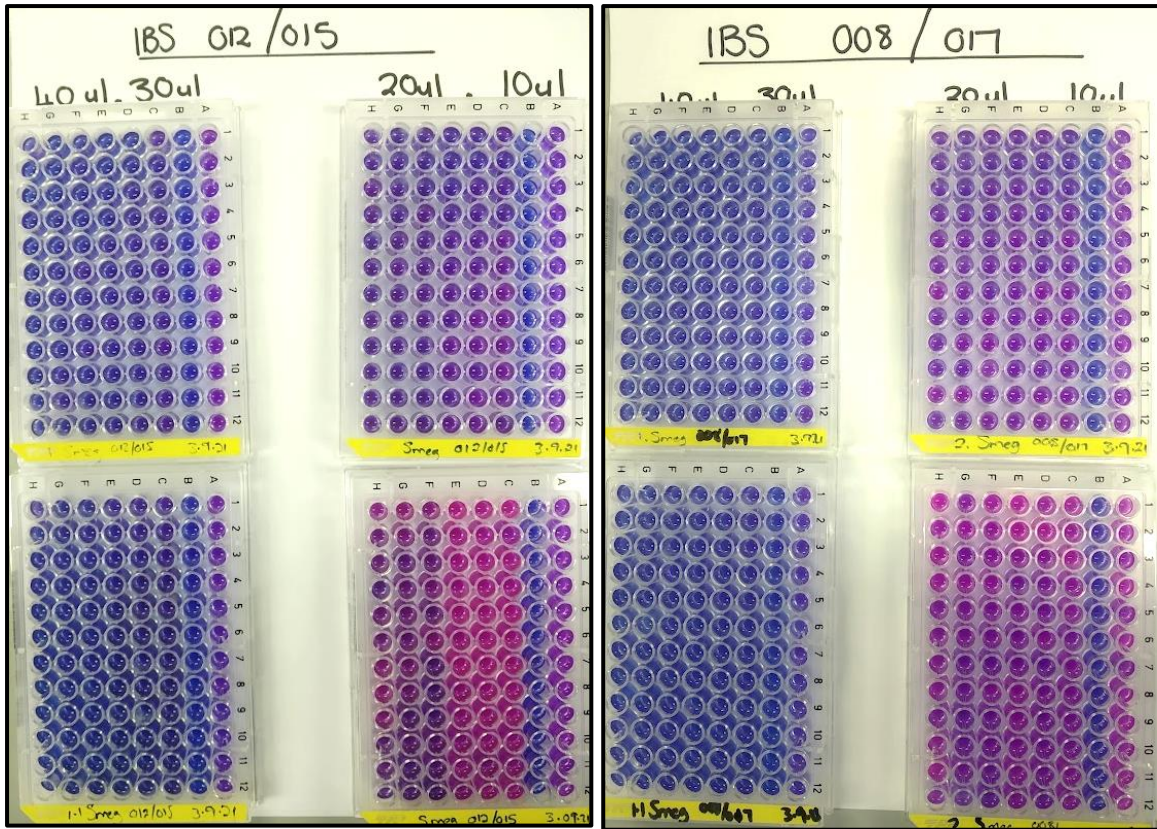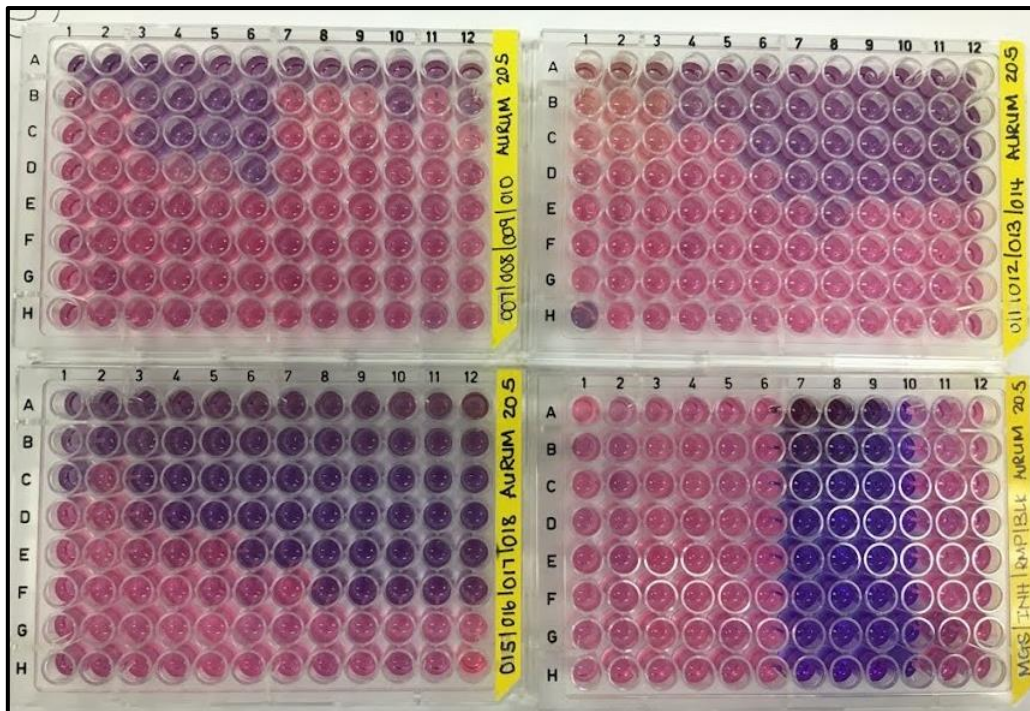
Appendix 4.4. *Mycobacterium fortuitum* MIC results.

Appendix 4.5. *Mycobacterium avium* MIC results.

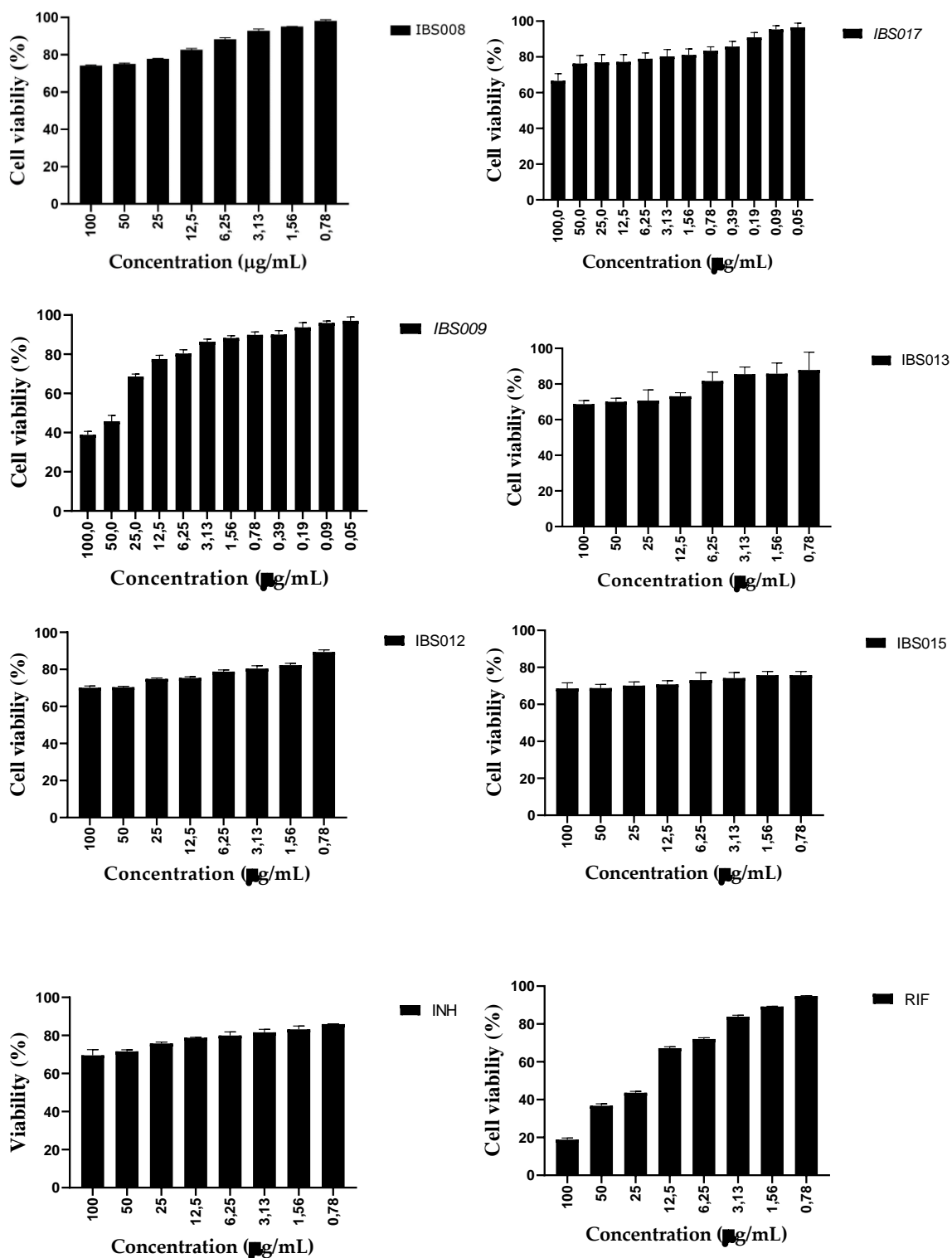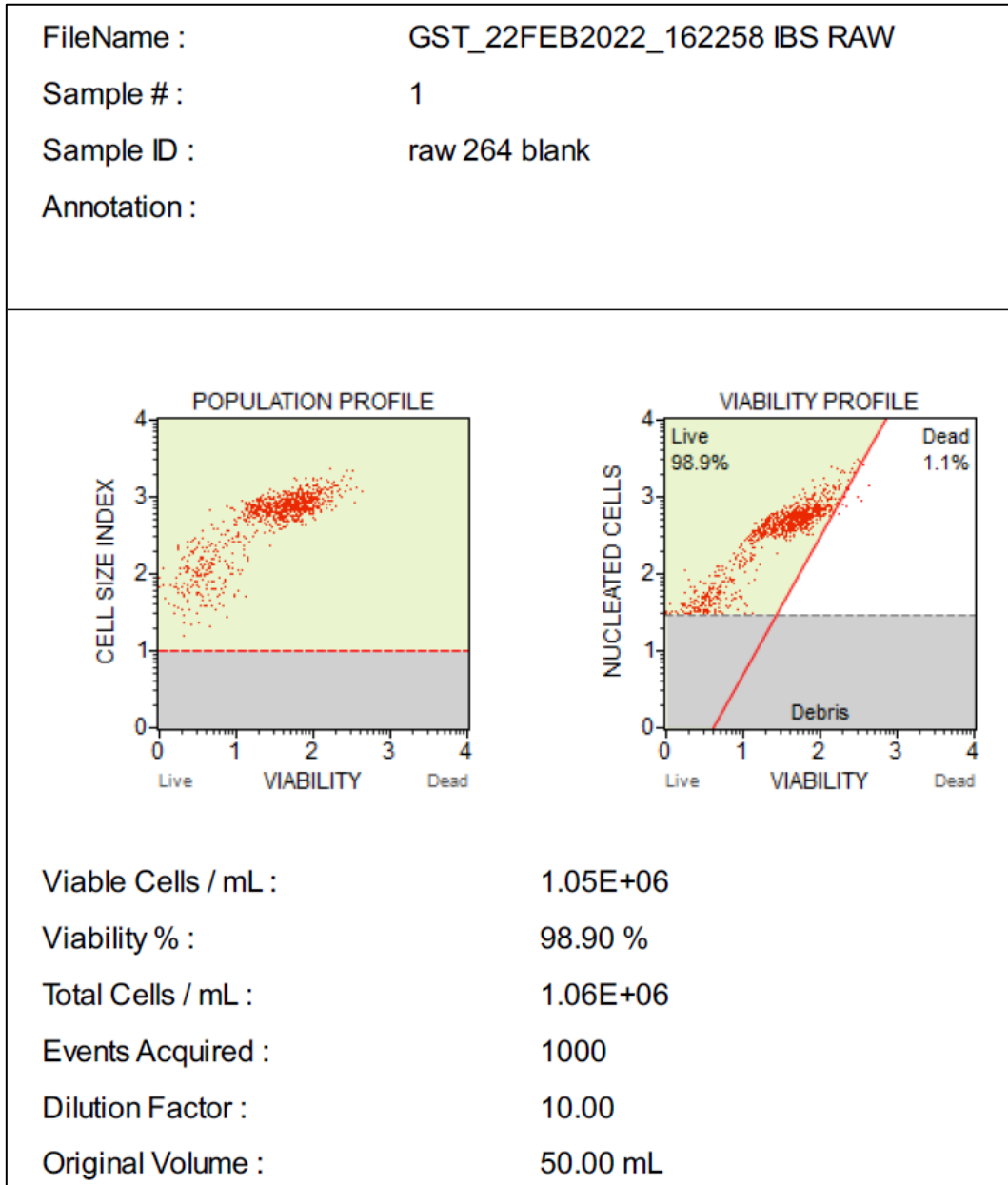**Appendix 4.6.** *Mycolicibacterium aurum* MIC results.

Plot diagram/graph of MTT concentration results: trendline coefficient calculated with goodness-of-fit (R^2) of ≥ 0.800.

Appendix 6

Negative control in flow cytometry mycobacteria RAW 464.7 cell benchmark experimental
results – Untreated

FileName :	GST_22FEB2022_162258 IBS RAW
Sample # :	1
Sample ID :	raw 264 blank
Annotation :	

Viable Cells / mL :	1.05E+06
Viability % :	98.90 %
Total Cells / mL :	1.06E+06
Events Acquired :	1000
Dilution Factor :	10.00
Original Volume :	50.00 mL

Appendix 7

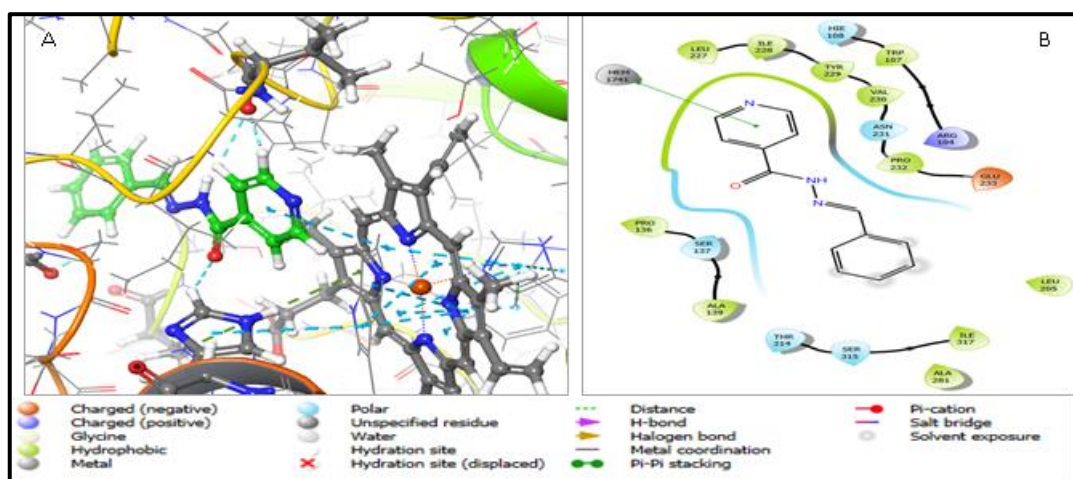Molecular docking analysis of KatG complexed with derivatives at site 2.
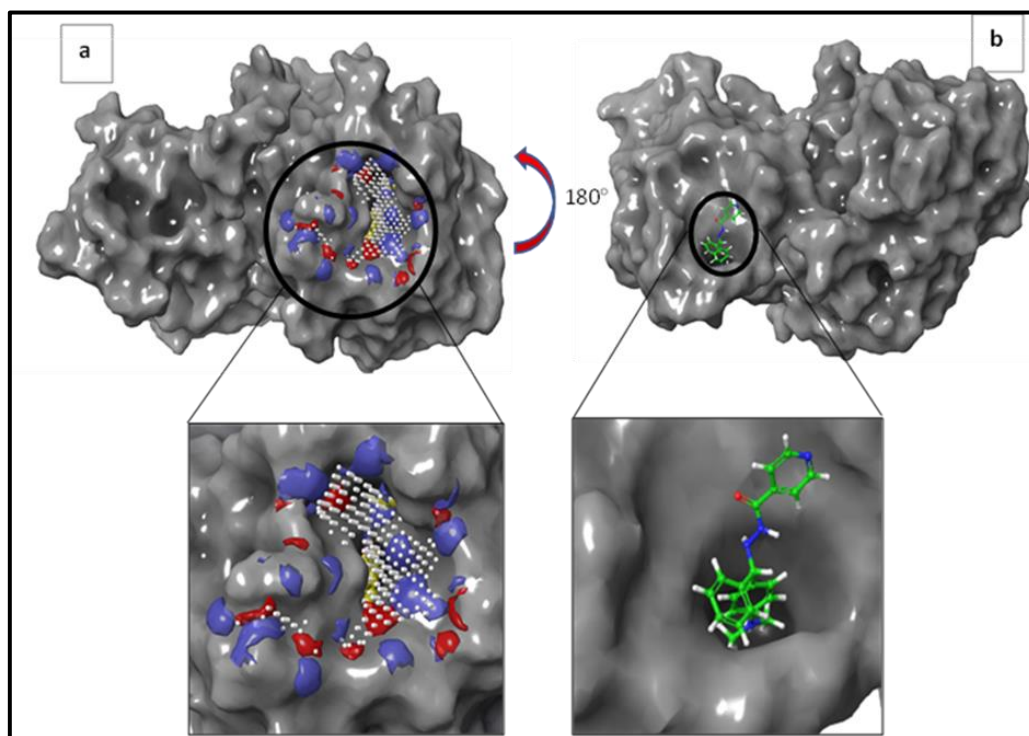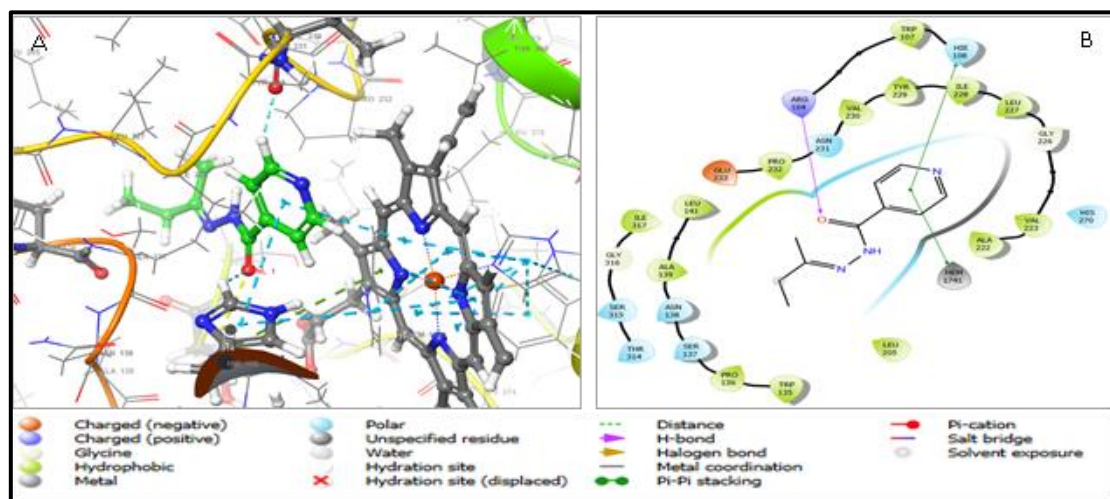

Appendix 7.1. A Grey surface representation of the *Mycobacterium tuberculosis* catalase-peroxidase enzyme (KatG) complexed with compound IBS012 (green) and the highly pharmaceutically active site 2 generated through SiteMap.

Appendix 7.2. Molecular docking analysis of IBS012 bound-KatG complexed with compound IBS015 on site 2. (A) shows compound IBS015 (green) in ball and stick model docked into site 2 of the IBS012 bound-KatG. The *Mycobacterium tuberculosis* catalase-peroxidase enzyme is shown in a ligand zoomed ribbon graphic representation with alpha helices, loops, and beta sheets. (B) Depicts a

2d-ligand interaction diagram of compound IBS015 and the surrounding active site amino acid residues at 4Å axis. The green line shows a single $\pi - \pi$ stacking interaction with the HEM1741 (Protoporphyrin IX Containing Fe) metal ion.

Appendix 7.3. Molecular docking analysis of IBS012 bound-KatG complexed with compound IBS017 on site 2. (A) shows compound IBS017 (green) in ball and stick model docked into site 2 of the IBS012 bound-KatG. The *Mycobacterium tuberculosis* catalase-peroxidase enzyme is shown in a ligand zoomed ribbon graphic representation with alpha helices, loops, and beta sheets. (B) Depicts a 2d-ligand interaction diagram of compound IBS015 and the surrounding active site amino acid residues at 4Å axis. The green and purple lines show two $\pi - \pi$ stacking interactions with the HEM1741 (Protoporphyrin IX Containing Fe) metal ion and HIS108 together with a hydrogen bond to ARG104, respectively.

Appendix 8

Thin layer chromatography aluminium plate showing compound migration of samples
IBS011 – IBS018 against isoniazid (INH)
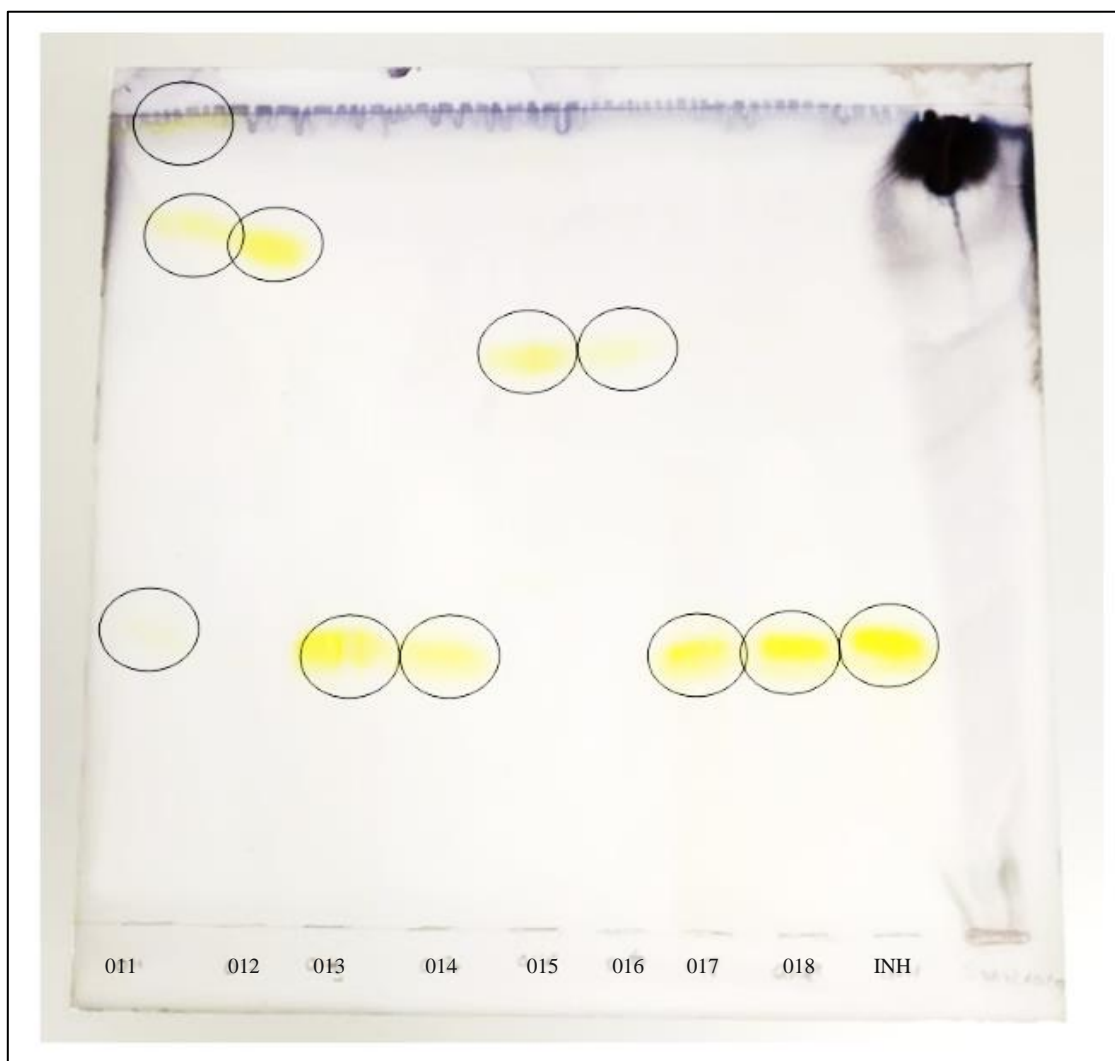
Annexure 1

The asymmetric unit of the co-crystal *N'*-benzylidenepyridine-4 carbohydrazide and benzoic acid – IBS015.

Co-crystallization of *N'*-benzylidenepyridine-4-carbohydrazide and benzoic acid *via* autoxidation of benzaldehyde

Itumeleng B. Setshedi,[a] Andreas Lemmerer[b] and Mark G. Smith[c]*

[a]University of South Africa, Department of Life Science, Unisa Science Campus, 28 Pioneer Avenue, Florida, Roodepoort, Gauteng, South Africa, [b]Molecular Sciences Institute, School of Chemistry, University of the Witwatersrand, Johannesburg, Gauteng, South Africa, and [c]University of South Africa, Chemistry Department, Unisa Science Campus, 28 Pioneer Avenue, Florida, Roodepoort, Gauteng, South Africa. *Correspondence e-mail: smithm2@unisa.ac.za

The 1:1 co-crystal *N'*-[(2-methylphenyl)methylidene]pyridine-4-carbohydrazide–benzoic acid (1/1), $C_{13}H_{11}N_3O \cdot C_7H_6O_2$, formed unexpectedly after autoxidation of benzaldehyde during the slow evaporation process of a solution of isoniazid in benzaldehyde. The original intent of the synthesis was to modify isoniazid with benzaldehyde and crystallize the product in order to improve efficacy against *Mycobacteria* species, but benzoic acid formed spontaneously and co-crystallized with the intended product, *N'*-benzylidenepyridine-4-carbohydrazide.

1. Chemical context

Mycobacterial infections are a historic tribulation to mankind, and are managed with an array of drugs ranging from natural to synthetic derivatives that possess antimicrobial properties. However, these strategies have failed over time due to the emergence of resistant *mycobacteria* (Cully, 2014). A number of constituents such as isoniazid (INH) have been modified to try and curb the scourge of tuberculosis (Cully, 2014). Some of the resulting modified INH derivatives have been shown to render the active pharmaceutical ingredients (API) a lot more active to the circulating resistant strains of TB (Hearn & Cynamon, 2004; Suarez *et al.*, 2009). It was for this reason that the covalent modification of API's was adopted to synthesize new analogues by modifying the NH_2 group of the hydrazide moiety of INH (Smith *et al.*, 2015), believed to assist in the evasion of the N-arylaminoacetyl transferases, an enzyme capable of reducing the efficacy of INH in particular, by acetylating the NH_2 position, thus ultimately preventing its reaction with nicotinamide adenine dinucleotide (NADH) (Vishweshwar *et al.*, 2006; Smith *et al.*, 2015).

Benzaldehyde is known to undergo autoxidation resulting in the formation of benzoic acid. The formation of benzoic acid occurs when benzaldehyde is exposed to air at room temperature (293 K) where the rate of the reaction is increased by the presence of a catalyst. However, this phenomenon can occur spontaneously without a catalyst over a prolonged period (Sankar *et al.*, 2014). The synthesis of this co-crystal was interesting as there were three separate processes that took place within the reaction mixture to create the final product. Firstly, benzaldehyde reacted with isoniazid to form *N'*-benzylidenepyridine-4-carbohydrazide. Secondly, excess benzaldehyde spontaneously autoxidized to form
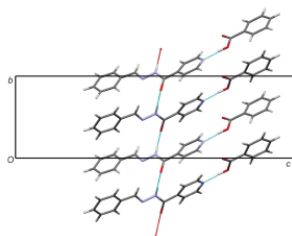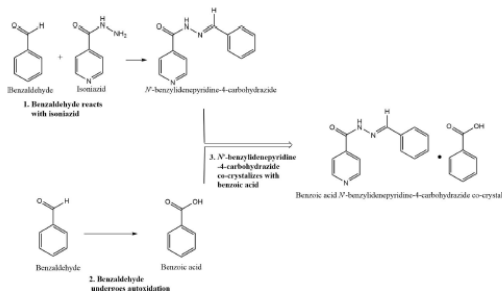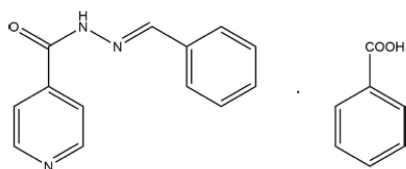
Figure 1
Modification and autoxidative co-crystallization.

benzoic acid as described above (no benzoic acid was added to the reaction mixture). Lastly, the carbohydrazide moiety co-crystallized with the benzoic acid (as shown in Fig. 1) to form the product, N'-[(2-methylphenyl)methylidene]pyridine-4-carbohydrazide–benzoic acid (1/1).

2. Structural commentary

The asymmetric unit contains one molecule of N'-benzylidenepyridine-4-carbohydrazide ($C_{13}H_{11}N_3O_1 \cdot C_7H_6O_2$) and one molecule of benzoic acid (as shown in Fig. 2). This co-crystal crystallizes in the $Pbca$ space group. The benzoic acid molecule lies in the plane of the pyridine ring of the benzylidene derivative. All bond lengths and angles are normal.

3. Supramolecular features

Each carbohydrazide moiety is hydrogen bonded by a strong O2—H2···N2 hydrogen bond (Table 1) to a benzoic acid molecule to form a co-crystal. This interaction is supported by
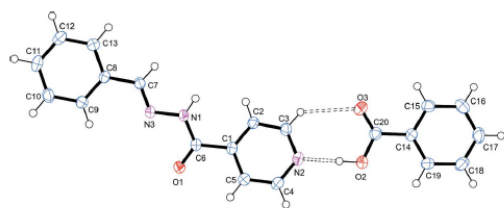

Figure 2
Asymmetric unit of N'-[(2-methylphenyl)methylidene]pyridine-4-carbohydrazide–benzoic acid (1/1).

Table 1
Hydrogen-bond geometry (Å, °).

D—H···A	D—H	H···A	D···A	D—H···A
N1—H1···O1^i	0.89 (2)	2.02 (2)	2.8981 (17)	171 (2)
O2—H2···N2	0.95 (2)	1.72 (3)	2.6693 (17)	176 (2)
C3—H3···O3	0.95	2.53	3.236 (2)	131

Symmetry code: (i) $-x + \frac{3}{2}, y + \frac{1}{2}, z$.

a weaker C—H···O hydrogen bond that stabilizes the co-planar arrangement of the carboxylic acid moiety and the pyridine ring. The graph-set notation for this would be $R_2^2(7)$ (Bernstein et al., 1995), and is observed in other isoniazid co-crystals (Lemmerer et al., 2010) (Fig. 2). This co-crystal is another example of the robust carboxylic acid···pyridine heterosynthon (Shattock et al., 2008; Aakeröy et al., 2007). Each carbohydrazide moiety is also hydrogen bonded via its N1—H1 donor to the carbonyl oxygen (O1) acceptor of an adjacent carbohydrazide moiety. This results in a mono-periodic hydrogen-bonded chain along the b-axis direction, with graph-set notation $C(4)$. Overall, the combined carbohydrazide moiety with the benzoic acid forms a ribbon motif (as shown in Fig. 3a). Viewed along the b-axis, the ribbons forms a X-shaped motif seen in other carbohydrazide moieties (Hean et al. 2018) (Fig. 3b).

4. Database survey

ConQuest (Bruno et al., 2002), Version 2022.1.0 of the CSD (Groom et al., 2016) was used for the database survey, where
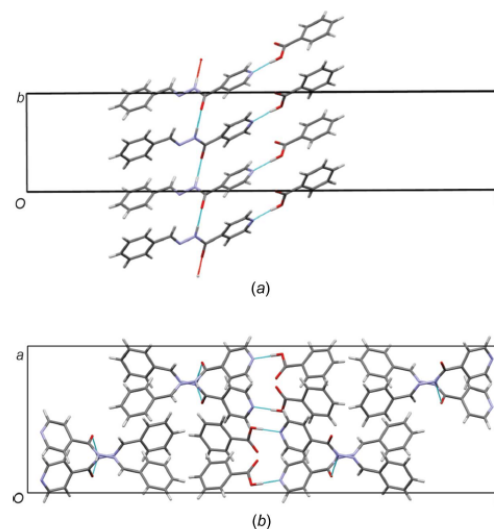

Figure 3
(a) View of the strong hydrogen bonds that link the carbohydrazide molecules in a chain, and the benzoic acid molecules to the carbohydrazide forming a ribbon. (b) Packing diagram along the b axis.
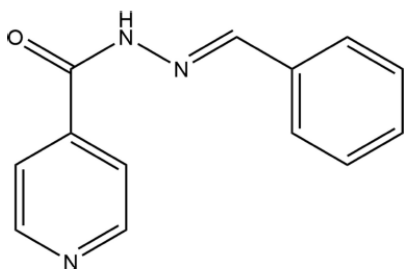
169

Figure 4
Benzylidene derivative of isoniazid.

only one similar structure was found. The survey consisted of structures consisting of isoniazid that had been modified with benzaldehyde and may have either a co-former or solvent molecule in the crystal structure. The structure of the anhydrous benzylidene derivative, N'-[(2-methylphenyl)methylidene]pyridine-4-carbohydrazide (as shown in Fig. 4), formed from the reaction of isoniazid and benzaldehyde, was reported by Wardell *et al.*, (2007) (YIQDEI). Several structures have been reported where substituted benzaldehyde reacted with isoniazid, for example, three polymorphs of the 4-methylbenzylidene derivative (WOGGOR, WOGGOR01 and WOGGUX) were reported by Purushothaman *et al.* (2019) and in 2016, Almeida and colleagues published the structure of a hydrate of the same 4-methylbenzylidene derivative (OLECOZ; Pereira Almeida *et al.*, 2016). However, there has not been any co-crystal of the benzylidene derivative (Fig. 4) reported in the literature to date.

5. Synthesis and crystallization

All reagents were commercially sourced and used without further purification. 1.00 g of isonicotinic acid hydrazide (isoniazid) (7.29 mmol) were dissolved in 15 ml of benzaldehyde in a 50 ml amber Schott bottle. The mixture was placed on a stirring heating block and heated to 333 K while stirring with a magnetic stirrer bar. Once the isoniazid had completely dissolved, the lid was tightly sealed. The solution was then allowed to react for 24 h. To maintain the temperature throughout the duration of the experiment, the amber Schott bottle was covered with an inverted round glass evaporation dish. After 24 h, the solution was allowed to cool to ambient temperature. The stirrer bar was retrieved and the sample was left to evaporate slowly for 6 weeks at ambient temperature without a lid. Over the 6 weeks, the temperature in the laboratory fluctuated between 298 and 300 K. Due to the fact that benzaldehyde evaporates extremely slowly, the Schott bottle was placed in the laminar flow biohazard safety level 2 cabinet to facilitate evaporation. Crystals (colourless blocks) started forming on the rim on the outside of the bottle as the benzaldehyde evaporated. One of these crystals was sampled for XRD analysis.

Table 2
Experimental details.

Crystal data	
Chemical formula	$C_{13}H_{11}N_3O \cdot C_7H_6O_2$
M_r	347.36
Crystal system, space group	Orthorhombic, $Pbca$
Temperature (K)	173
a, b, c (Å)	11.7044 (17), 7.8531 (10), 38.253 (5)
V (Å^3)	3516.1 (8)
Z	8
Radiation type	Mo $K\alpha$
μ (mm^{-1})	0.09
Crystal size (mm)	$0.30 \times 0.22 \times 0.16$
Data collection	
Diffractometer	Bruker D8 Venture Microfocus with Photon III CCD area-detector
Absorption correction	Multi-scan (*SADABS*; Krause *et al.*, 2015)
T_{min}, T_{max}	0.709, 0.746
No. of measured, independent and observed [$I > 2\sigma(I)$] reflections	73794, 4239, 3902
R_{int}	0.036
$(\sin\theta/\lambda)_{max}$ (Å^{-1})	0.660
Refinement	
$R[F^2 > 2\sigma(F^2)]$, $wR(F^2)$, S	0.054, 0.112, 1.18
No. of reflections	4239
No. of parameters	243
H-atom treatment	H atoms treated by a mixture of independent and constrained refinement
$\Delta\rho_{max}, \Delta\rho_{min}$ (e Å^{-3})	0.33, −0.21

Computer programs: *APEX3, SAINT-Plus* and *XPREP* (Bruker 2016), *SHELXT2014* (Sheldrick, 2015a), *SHELXL2019/2* (Sheldrick, 2015b) and *ORTEP-3 for Windows* and *WinGX* (Farrugia, 2012).

6. Refinement

Crystal data, data collection and structure refinement details are summarized in Table 2. C-bound H atoms were first located in the difference map, then positioned geometrically and allowed to ride on their respective parent atoms, with thermal displacement parameters 1.2 times of the parent C atom. The coordinates and isotropic displacement parameters of the O and N-bound H atoms involved in hydrogen-bonding interactions (H1 and H2) were allowed to refine freely.

References

Aakeröy, C. B., Hussain, I., Forbes, S. & Desper, J. (2007). *CrystEngComm*, **9**, 46–54.
Bernstein, J., Davis, R. E., Shimoni, L. & Chang, N.-L. (1995). *Angew. Chem. Int. Ed. Engl.* **34**, 1555–1573.

170

Bruker (2016). *APEX3*, *SAINT-Plus* and *XPREP*. Bruker AXS Inc., Madison, Wisconsin, USA.

Bruno, I. J., Cole, J. C., Edgington, P. R., Kessler, M., Macrae, C. F., McCabe, P., Pearson, J. & Taylor, R. (2002). *Acta Cryst.* B**58**, 389–397.

Cully, M. (2014). *Nat. Rev. Drug Discov.* **13**, 257. https://doi.org/10.1038/nrd4287

Farrugia, L. J. (2012). *J. Appl. Cryst.* **45**, 849–854.

Groom, C. R., Bruno, I. J., Lightfoot, M. P. & Ward, S. C. (2016). *Acta Cryst.* B**72**, 171–179.

Hean, D., Michael, J. P. & Lemmerer, A. (2018). *J. Mol. Struct.* **1157**, 693–707.

Hearn, M. J. & Cynamon, M. H. (2004). *J. Antimicrob. Chemother.* **53**, 185–191.

Krause, L., Herbst-Irmer, R., Sheldrick, G. M. & Stalke, D. (2015). *J. Appl. Cryst.* **48**, 3–10.

Lemmerer, A., Bernstein, J. & Kahlenberg, V. (2010). *CrystEng-Comm*, **12**, 2856–2864.

Pereira Almeida, W., Paes Koury, I. & Simoni, D. de A. (2016). *IUCrData*, **1**, x160752.

Purushothaman, G., Angira, D. & Thiruvenkatam, V. (2019). *J. Mol. Struct.* **1197**, 34–44.

Sankar, M., Nowicka, E., Carter, E., Murphy, D., Knight, D., Bethell, D. & Hutchings, G. (2014). *Nat. Commun.* **5**, 3332. https://doi.org/10.1038/ncomms4332

Shattock, T. R., Arora, K. K., Vishweshwar, P. & Zaworotko, M. J. (2008). *Cryst. Growth Des.* **8**, 4533–4545.

Sheldrick, G. M. (2015a). *Acta Cryst.* A**71**, 3–8.

Sheldrick, G. M. (2015b). *Acta Cryst.* C**71**, 3–8.

Smith, M. G., Forbes, R. P. & Lemmerer, A. (2015). *Cryst. Growth Des.* **15**, 3813–3821.

Suarez, J., Ranguelova, K., Jarzecki, A. A., Manzerova, J., Krymov, V., Zhao, X., Yu, S., Metlitsky, L., Gerfen, G. J. & Magliozzo, R. S. (2009). *J. Biol. Chem.* **284**, 7017–7029.

Vishweshwar, P., McMahon, J. A., Bis, J. A. & Zaworotko, M. J. (2006). *J. Pharm. Sci.* **95**, 499–516.

Wardell, S. M. S. V., de Souza, M. V. N., Wardell, J. L., Low, J. N. & Glidewell, C. (2007). *Acta Cryst.* B**63**, 879–895.

171

Annexure 2

The asymmetric unit of the crystal: N′-[bis(2-hydroxyphenyl)methylidene]pyridine-4-carbohydrazide, $C_{19}H_{15}N_3O_3$ – IBS007

Itumeleng B. Setshedi, Andreas Lemmerer and Mark G. Smith*

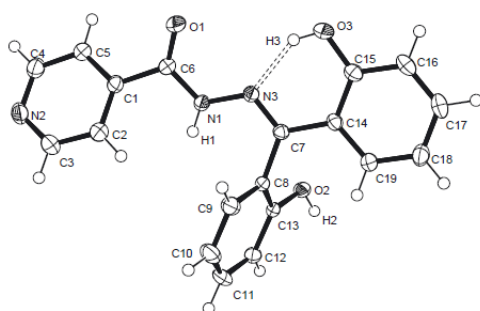# The crystal structure of *N′*-[bis(2-hydroxyphenyl) methylidene]pyridine-4-carbohydrazide, $C_{19}H_{15}N_3O_3$

Abstract

$C_{19}H_{15}N_3O_3$, monoclinic, $C2/c$ (no. 15), $a = 20.6917(6)$ Å, $b = 10.1392(3)$ Å, $c = 16.9544(5)$ Å, $\beta = 115.739(1)°$, $V = 3204.07(17)$ Å^3, $Z = 8$, $R_{gt}(F) = 0.0364$, $wR_{ref}(F^2) = 0.1009$, $T = 173$ K.

CCDC no.: 2167402

The molecular structure is shown in the figure. Table 1 contains crystallographic data and Table 2 contains the list of the atoms including atomic coordinates and displacement parameters.

*Corresponding author: Mark G. Smith, Department of Chemistry, University of South Africa, Unisa Science Campus, 28 Pioneer Avenue, Florida, Roodepoort, Gauteng, South Africa,
E-mail: smithm2@unisa.ac.za. https://orcid.org/0000-0003-2553-2540
Itumeleng B. Setshedi, Department of Life Science, University of South Africa, Unisa Science Campus, 28 Pioneer Avenue, Florida, Roodepoort, Gauteng, South Africa. https://orcid.org/0000-0001-8865-4735
Andreas Lemmerer, Molecular Sciences Institute, School of Chemistry, University of the Witwatersrand, Johannesburg, Gauteng, South Africa. https://orcid.org/0000-0003-1569-2831

Table 1: Data collection and handling.

Crystal:	Colourless block
Size:	$0.36 \times 0.25 \times 0.20$ mm
Wavelength:	Mo $K\alpha$ radiation (0.71073 Å)
μ:	0.10 mm^{-1}
Diffractometer, scan mode:	Bruker D8 Venture Photon, ω
θ_{max}, completeness:	28.0°, >99%
$N(hkl)_{measured}$, $N(hkl)_{unique}$, R_{int}:	23,999, 3872, 0.037
Criterion for I_{obs}, $N(hkl)_{gt}$:	$I_{obs} > 2\,\sigma(I_{obs})$, 3340
$N(param)_{refined}$:	238
Programs:	Bruker [1], SHELX [2, 3], ORTEP-3 [4], WinGX [5], PLATON [6]

Source of material

All reagents used were used without further purification. An amount of 0.0857 g of isonicotinic acid hydrazide (isoniazid) (0.6249 mmol) and 0.1340 g of 2,2′-dihydroxybenzophenone (0.6255 mmol) were added into a vial. *p*-Hydroxybenzoic acid 0.086 g (0.6255 mmol) was added to catalyze the reaction. The solids were dissolved in 3 mL of AP-grade methanol and refluxed in a closed screw-top vial for 24 h at 67 °C, and were left to stand at room temperature slightly open to the atmosphere. Yellow plates were afforded after 3 days.

Experimental details

C-bound hydrogen atoms were located in the difference map then positioned geometrically and were allowed to ride on their respective parent atoms with thermal displacement parameters 1.2 times of the parent C atom. The coordinates and isotropic displacement parameters of the N-bound and O-bound H atoms involved in hydrogen bonding interactions were allowed to refine freely.

Comment

Isoniazid has been modified to enhance activity against multidrug resistant mycobacteria [7]. Several modified

Table 2: Fractional atomic coordinates and isotropic or equivalent isotropic displacement parameters ($Å^2$).

Atom	x	y	z	$U_{iso}*/U_{eq}$
C1	−0.18530 (6)	0.48217 (11)	0.00875 (7)	0.0229 (2)
C2	−0.18090 (7)	0.59801 (12)	−0.03244 (8)	0.0313 (3)
H2A	−0.135895	0.629967	−0.02665	0.038*
C3	−0.24367 (7)	0.66582 (13)	−0.08216 (8)	0.0357 (3)
H3A	−0.240643	0.744564	−0.110745	0.043*
C4	−0.31206 (6)	0.51342 (12)	−0.05324 (8)	0.0309 (3)
H4	−0.357842	0.483541	−0.060549	0.037*
C5	−0.25246 (6)	0.43823 (11)	−0.00302 (8)	0.0266 (2)
H5	−0.257386	0.358104	0.022907	0.032*
C6	−0.12008 (6)	0.39996 (11)	0.06116 (7)	0.0222 (2)
C7	0.06093 (5)	0.48892 (10)	0.18322 (7)	0.0188 (2)
C8	0.05681 (5)	0.63347 (10)	0.16316 (7)	0.0192 (2)
C9	0.03440 (6)	0.67069 (11)	0.07594 (8)	0.0273 (2)
H9	0.023726	0.604289	0.032532	0.033*
C10	0.02733 (7)	0.80184 (12)	0.05115 (8)	0.0352 (3)
H10	0.012886	0.825523	−0.008337	0.042*
C11	0.04170 (7)	0.89814 (12)	0.11462 (9)	0.0341 (3)
H11	0.036033	0.988493	0.09816	0.041*
C12	0.06415 (6)	0.86438 (10)	0.20145 (8)	0.0261 (2)
H12	0.0739	0.931475	0.244231	0.031*
C13	0.07259 (5)	0.73183 (10)	0.22665 (7)	0.0195 (2)
C14	0.13043 (6)	0.42320 (10)	0.23167 (7)	0.0203 (2)
C15	0.13587 (6)	0.28567 (11)	0.24744 (7)	0.0244 (2)
C16	0.20348 (7)	0.22849 (12)	0.29311 (8)	0.0302 (3)
H16	0.207129	0.136371	0.30448	0.036*
C17	0.26498 (7)	0.30374 (13)	0.32192 (8)	0.0321 (3)
H17	0.310523	0.263249	0.35287	0.038*
C18	0.26061 (6)	0.43870 (13)	0.30584 (8)	0.0301 (3)
H18	0.302982	0.490499	0.325066	0.036*
C19	0.19407 (6)	0.49667 (11)	0.26166 (7)	0.0246 (2)
H19	0.191331	0.589034	0.25127	0.03*
N1	−0.06094 (5)	0.47504 (9)	0.10727 (6)	0.0233 (2)
N2	−0.30829 (6)	0.62593 (10)	−0.09190 (7)	0.0324 (2)
N3	0.00444 (5)	0.41459 (9)	0.15336 (6)	0.02117 (19)
O1	−0.12054 (4)	0.28042 (8)	0.05804 (6)	0.0318 (2)
O2	0.09561 (4)	0.69679 (8)	0.31188 (5)	0.02388 (18)
O3	0.07849 (5)	0.20449 (8)	0.21997 (6)	0.0337 (2)
H1	−0.0664 (8)	0.5585 (16)	0.1199 (10)	0.037 (4)*
H2	0.1230 (10)	0.768 (2)	0.3467 (12)	0.062 (5)*
H3	0.0405 (11)	0.2535 (19)	0.1922 (12)	0.058 (5)*

isoniazid derivative have been synthesized [8–12]. In this paper we present the crystal structure of isoniazid modified with 2,2′-dihydroxybenzophenone. The compound crystallizes in the monoclinic $C2/c$ space group and the asymmetric unit contains one molecule. There is one hydroxyl group on each of the benzophenone rings. As expected from Etter's rules of hydrogen bonding [13], one of the hydroxyl groups forms a six-membered intramolecular hydrogen bonded ring with the hydrazide nitrogen atom (N3) and is not

involved in anyntermolecular interactions. The other hydroxyl group is hydrogen bonded to the pyridyl nitrogen atom of an adjacent molecule *via* the robust O−H··· $N_{pyridine}$ heterosynthon. Its oxygen atom acts as an acceptor to the amide hydrogen atom donor (H1). The packing of the crystal forms one-dimensional ribbons with a two-one screw axis. These hydrogen bonding patterns form two rings, namely an R_4^4 (18) ring involving four molecules, and an R_4^4 (14) ring involving three molecules.

References

1. Bruker. APEX2 (Version 2012.10-0), SAINT (Version 8.27B), SADABS (Version 2012/1); Bruker AXS Inc: Madison, Wisconsin, USA, 2012.
2. Sheldrick G. M. *SHELXTL* – Integrated space-group and crystal-structure determination. *Acta Crystallogr.* 2015, *A71*, 3–8.
3. Sheldrick G. M. Crystal structure refinement with SHELXL. *Acta Crystallogr.* 2015, *C71*, 3–8.
4. Farrugia L. J. WinGX and ORTEP for Windows: an update. *J. Appl. Crystallogr.* 2012, *45*, 849–854.
5. Farrugia L. J. WinGX suite for small-molecule single-crystal crystallography. *J. Appl. Crystallogr.* 1999, *32*, 837–838.
6. Spek A. L Structure validation in chemical crystallography. *Acta Crystallogr.* 2009, *D65*, 148–155.
7. Coelho T. S., Cantos J. B., Bispo M. L. F., Gonçalves R. S. B., Lima C. H. S., da Silva P. E. A., De Souza M. Vitro anti-mycobacterial activity of (E)-N′-(monosubstituted-benzylidene) isonicotinohydrazide derivatives against isoniazid-resistant strains. *Infect. Dis. Rep.* 2012, 4, e13.
8. Smith M. G., Lemmerer A. Covalent assisted supramolecular synthesis: the influence of crystallization conditions on co-crystals of "masked" isoniazid derivatives. *Cryst. Growth Des.* 2018, *18*, 4777–4789.
9. Setshedi I. B., Smith M. G. The crystal structure of 4-phenyl-4-[2-(pyridine-4-carbonyl)hydrazinylidene] butanoic acid, $C_{16}H_{15}N_3O_3$. *Z. Kristallogr. N. Cryst. Struct.* 2022, *237*, 133–134.
10. Meenatchi V., Meenakshisundaram S. P. Synthesis, growth, spectral studies, first-order molecular hyperpolarizability and Hirshfeld surface analysis of isonicotinohydrazide single crystals. *RSC Adv.* 2015, *5*, 64180–64191.
11. Madeley L. G., Levendis D. C., Lemmerer A. Covalent-assisted supramolecular synthesis: the effect of hydrogen

The asymmetric unit of the crystal: 4-phenyl-4-[2-(pyridine-4-carbonyl)hydrazinylidene]buta

noic acid, C16H15N3O3 – IBS019.

Itumeleng B. Setshedi and Mark G. Smith*

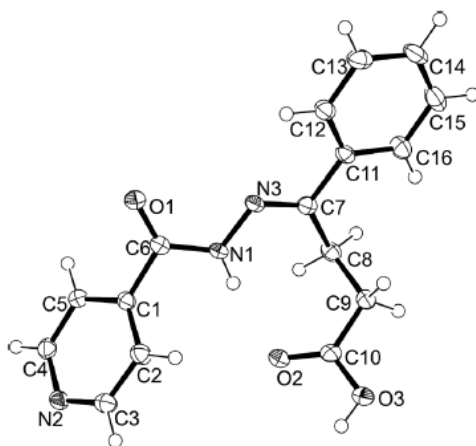# The crystal structure of 4-phenyl-4-[2-(pyridine-4-carbonyl)hydrazinylidene]butanoic acid, $C_{16}H_{15}N_3O_3$

Abstract

$C_{16}H_{15}N_3O_3$, monoclinic, $P2_1/c$ (no. 14), $a = 9.4957(3)$ Å, $b = 18.2275(5)$ Å, $c = 9.0896(3)$ Å, $\beta = 114.372(1)°$, $V = 1433.05(15)$ Å³, $Z = 4$, $R_{gt}(F) = 0.0380$, $wR_{ref}(F^2) = 0.1011$, $T = 173$ K.

CCDC no.: 2120068

The molecular structure is shown in the figure. Table 1 contains crystallographic data and Table 2 contains the list of the atoms including atomic coordinates and displacement parameters.

*Corresponding author: Mark G. Smith, Chemistry Department, University of South Africa, Unisa Science Campus, 28 Pioneer Avenue, Florida, Roodepoort, Gauteng, South Africa, E-mail: Smithm2@unisa.ac.za. https://orcid.org/0000-0003-2553-2540
Itumeleng B. Setshedi, Department of Life Science, University of South Africa, Unisa Science Campus, 28 Pioneer Avenue, Florida, Roodepoort, Gauteng, South Africa, E-mail: Setshib@unisa.ac.za. https://orcid.org/0000-0001-8865-4735

Table 1: Data collection and handling.

Crystal:	Colourless cuboid
Size:	$0.62 \times 0.25 \times 0.23$ mm
Wavelength:	Mo $K\alpha$ radiation (0.71073 Å)
μ:	0.10 mm⁻¹
Diffractometer, scan mode:	Bruker D8 Venture, ω
θ_{max}, completeness:	28.0°, >99%
$N(hkl)_{measured}$, $N(hkl)_{unique}$, R_{int}:	20,811, 3446, 0.072
Criterion for I_{obs}, $N(hkl)_{gt}$:	$I_{obs} > 2\sigma(I_{obs})$, 3009
$N(param)_{refined}$:	199
Programs:	Bruker [1], SHELX [2], WinGX [3], PLATON [4], ORTEP-III [5, 6]

Source of material

All reagents were commercially sourced and used without further purification. 1.035 g of isonicotinic acid hydrazide (7.55 mmol) and 1.359 g of 3-benzoylpropionic acid (7.63 mmol) were added into a screw-cap dram vial (with rubber septum). 5 mL of methanol was added and stirred at 70 °C for 24 h. The solution was then left slightly open to allow slow evaporation at room temperature. Colourless block crystals were observed after three days.

Experimental details

The collection method involved ω-scans of width 0.5°. Data reduction was carried out using SAINT-Plus version 6.02.6 software, and SADABS was used to process empirical absorption corrections [1]. The crystal structure was solved through direct methods using SHELXS [2]. Hydrogen atoms were positioned geometrically and $U_{iso}(H) = 1.2U_{eq}(C)$. Diagrams and publication material were generated using WinGX [3], PLATON [4] and Ortep [5, 6].

Comment

Isonicotinic acid hydrazide (isoniazid) is primarily used as a treatment for Tuberculosis (TB). It is effective against both latent and active *Mycobacteria tuberculosis* [7]. However, improper and long term use of the drug has resulted in the

Table 2: Fractional atomic coordinates and isotropic or equivalent isotropic displacement parameters (Å²).

Atom	X	y	z	$U_{iso}*/U_{eq}$
C1	0.61662 (13)	0.15765 (6)	−0.15151 (13)	0.0196 (2)
C2	0.53059 (14)	0.11646 (7)	−0.08990 (15)	0.0252 (3)
H2	0.539844	0.124459	0.016986	0.03*
C3	0.43079 (14)	0.06337 (7)	−0.18705 (15)	0.0260 (3)
H3	0.370744	0.035936	−0.144879	0.031*
C4	0.50060 (14)	0.08846 (7)	−0.39467 (14)	0.0237 (2)
H4	0.491771	0.07815	−0.500585	0.028*
C5	0.60104 (14)	0.14341 (7)	−0.30792 (14)	0.0229 (2)
H5	0.657964	0.170748	−0.353972	0.028*
C6	0.71859 (13)	0.21952 (6)	−0.05705 (13)	0.0199 (2)
C7	1.02496 (13)	0.23387 (6)	0.32495 (14)	0.0193 (2)
C8	1.07640 (13)	0.15568 (6)	0.37160 (14)	0.0220 (2)
H8A	1.190778	0.154373	0.424005	0.026*
H8B	1.042697	0.125597	0.272244	0.026*
C9	1.01330 (13)	0.12102 (6)	0.48624 (14)	0.0212 (2)
H9A	1.093684	0.088636	0.563263	0.025*
H9B	0.992392	0.160471	0.549382	0.025*
C10	0.86795 (14)	0.07715 (6)	0.40142 (14)	0.0217 (2)
C11	1.11203 (13)	0.29500 (6)	0.43327 (13)	0.0206 (2)
C12	1.06091 (14)	0.36753 (7)	0.39634 (14)	0.0245 (3)
H12	0.967967	0.377376	0.304194	0.029*
C13	1.14419 (17)	0.42516 (7)	0.49252 (16)	0.0301 (3)
H13	1.108799	0.474128	0.465188	0.036*
C14	1.27918 (16)	0.41148 (8)	0.62870 (16)	0.0330 (3)
H14	1.336257	0.451024	0.694349	0.04*
C15	1.33022 (16)	0.34035 (8)	0.66842 (16)	0.0341 (3)
H15	1.422212	0.330898	0.761944	0.041*
C16	1.24725 (15)	0.28234 (7)	0.57182 (15)	0.0283 (3)
H16	1.283044	0.233508	0.600454	0.034*
N1	0.82074 (11)	0.19997 (5)	0.09310 (11)	0.0210 (2)
H1	0.829793	0.15393	0.124855	0.025*
N2	0.41509 (11)	0.04898 (5)	−0.33750 (12)	0.0225 (2)
N3	0.91012 (11)	0.25417 (5)	0.19479 (11)	0.0203 (2)
O1	0.70748 (10)	0.28075 (5)	−0.11510 (10)	0.0275 (2)
O2	0.80366 (11)	0.06912 (5)	0.25575 (10)	0.0284 (2)
O3	0.81920 (10)	0.04563 (5)	0.50306 (10)	0.0271 (2)
H3A	0.738051	0.021825	0.450823	0.041*

resistance of the microorganism [8]. This in turn has led to research focused on the modification of isoniazid to develop derivatives that may be effective against drug resistant mycobacteria strains [9, 10]. The crystal structure being reported in this article represents one such covalently modified isoniazid derivative.

The asymetric unit shown in the figure contains one molecule of 4-phenyl-4-[2-(pyridine-4-carbonyl)hydrazinylidene]butanoic acid. There is an intramolecular hydrogen bond between the O2 oxygen and the H1 donor atom, forming an $S_1^1(8)$ ring in graph set notation [11]. Every molecule is bonded to an adjacent molecule which is flipped over, thus forming a symmetrical dimer with an inversion center

between the two molecules. This results in each molecule being hydrogen bonded to its neighbour twice *via* COOH⋯N heterosynthons, namely O3–H3A⋯N2. The COOH⋯N heterosynthons are as expected in literature [12]. The bonding between the two adjacent molecules is further stabilized by a weak C–H⋯O interaction between H3 and O2.

References

1. Bruker. *SAINT-Plus and* SADABS; Bruker AXS Inc.: Wisconsin, Madison, USA, 2004.
2. Sheldrick G. M. A short history of *SHELX. Acta Crystallogr.* 2008, *A64*, 112–122.
3. Farrugia L. J. WinGX suite for small-molecule single-crystal crystallography. *J. Appl. Crystallogr.* 1999, *32*, 837–838.
4. Spek A. L. Structure validation in chemical crystallography. *Acta Crystallogr.* 2009, *D65*, 148–155.
5. Burnett M. N., Johnson C. K. *ORTEPIII. Report ORNL-6895*; Oak Ridge National Laboratory: Tennessee, USA, 1996.
6. Farrugia L. J. ORTEP-3 for Windows – a version of ORTEP-III with a graphical user interface (GUI). *J. Appl. Crystallogr.* 1997, *30*, 565.
7. Torres E., Moreno E., Ancizu S., Barea C., Galiano S., Aldana I., Monge A., Silanes S. P. New 1,4-di-*N*-oxide-quinoxaline-2-ylmethylene isonicotinic acid hydrazide derivatives as anti-mycobacterium tuberculosis agents. *Bioorg. Med. Chem. Lett.* 2011, *21*, 3699–3703.
8. Setshedi I. B., Smith M. G. The crystal structure of the co-crystal: 2-hydroxybenzoic acid *N*-(butan-2-ylidene)pyridine-4-carbohydrazide, $C_{10}H_{13}N_3O·C_7H_6O_3$. *Z. Kristallogr. N. Cryst. Struct.* 2021, *236*, 1093–1095.
9. Hu Y.-Q., Zhang S., Zhao F., Gao C., Feng L.-S., Lv Z.-S. Isoniazid derivatives and their anti-tubercular activity. *Eur. J. Med. Chem.* 2017, *133*, 255–267.
10. Lemmerer A., Bernstein J., Kahlenberg V. Covalent assistance in supramolecular synthesis: in situ modification and masking of the hydrogen bonding functionality of the supramolecular reagent isoniazid in co-crystals. *CrystEngComm* 2011, *13*, 5692–5708.
11. Bernstein J., Davis R. E., Shimoni L., Chang N.-L. Patterns in hydrogen bonding: functionality and graph set analysis in crystals. *Angew. Chem. Int. Ed. Engl.* 1995, *34*, 1555–1573.
12. Aakeröy C. B., Hussain I., Forbes S., Desper J. Exploring the hydrogen-bond preference of N–H moieties in co-crystals assembled via O–H(acid)⋯N(py) intermolecular interactions. *CrystEngComm* 2007, *9*, 46–54.

Annexure 4

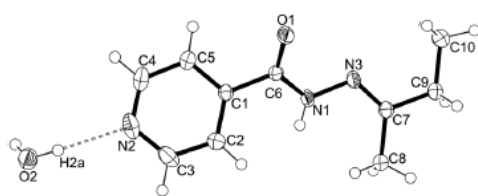The asymmetric unit of the crystal: (E)-N′-(butan-2-ylidene)isonicotinohydrazide 0.5 hydrate

$C_{10}H_{13}N_3O \cdot 0.5H_2O$ – IBS017

Itumeleng B. Setshedi, Andreas Lemmerer and Mark G. Smith*

The crystal structure of (E)-N'-(butan-2-ylidene) isonicotinohydrazide 0.5 hydrate C₁₀H₁₃N₃O· 0.5H₂O

Abstract

$C_{10}H_{13}N_3O \cdot 0.5H_2O$, orthorhombic, $Aba2$ (no. 41), $a = 19.9676(19)$ Å, $b = 8.4674(7)$ Å, $c = 12.4082(10)$ Å, $V = 2097.9(3)$ Å³, $Z = 8$, $R_{gt}(F) = 0.0299$, $wR_{ref}(F^2) = 0.0849$, $T = 173$ K.

CCDC no.: 2086756

The asymmetric unit of the title structure is shown in the figure. Table 1 contains crystallographic data and Table 2 contains the list of the atoms including atomic coordinates and displacement parameters.

Source of material

All reagents used were purchased and used without further purification. Isonicotinic acid hydrazide (isoniazid) (1.0 g; 7.29 mmol) and 15.0 mL of 2-butanone were added to a

Table 1: Data collection and handling.

Crystal:	Colourless block
Size:	$0.91 \times 0.79 \times 0.14$ mm
Wavelength:	Mo $K\alpha$ radiation (0.71073 Å)
μ:	0.09 mm⁻¹
Diffractometer, scan mode:	Bruker D8 Venture Photon, ω
θ_{max}, completeness:	28.0°, >99%
$N(hkl)_{measured}$, $N(hkl)_{unique}$, R_{int}:	58009, 2526, 0.040
Criterion for I_{obs}, $N(hkl)_{gt}$:	$I_{obs} > 2\ \sigma(I_{obs})$, 2474
$N(param)_{refined}$:	138
Programs:	Bruker [1], SHELX [2], WinGX [3], PLATON [4], ORTEP-III [5]

25 mL stainless steel jar containing 2×7 mm stainless steel balls. The jar was tightly sealed and the contents were shaken for 30 min at 25 Hz using the Retsch Mixer Mill MM 200. The mixture was then transferred into a 50 ml amber Schott bottle and left slightly open to allow slow evaporation at room temperature. Colourless block crystals were observed after three days.

Experimental details

The collection method involved ω-scans of width 0.5°. Data reduction was carried out using SAINT–Plus version 6.02.6 software, and SADABS was used to process empirical absorption corrections [1]. Hydrogen atoms were allowed to ride on their respective parent atoms with d(C–H) = 0.95 [2]. Hydrogen atoms were positioned geometrically Å and $U_{iso}(H) = 1.2U_{eq}(C)$. Diagrams and publication material were generated using WinGX [3], PLATON [4] and Ortep [5, 6].

Comment

Isoniazid, a synthetic derivative of nicotinic acid [7] has been used as a frontline drug for the treatment of Tuberculosis (TB) for decades [8]. Tuberculosis-causing mycobacteria have developed resistance against this drug, thus there is an urgent need for novel and effective drug design and

*Corresponding author: Mark G. Smith, Chemistry Department, University of South Africa, Unisa Science Campus, 28 Pioneer Avenue, Florida, Roodepoort, Gauteng, South Africa,
E-mail: smithm2@unisa.ac.za. https://orcid.org/0000-0003-2553-2540
Itumeleng B. Setshedi, Department of Life Science, University of South Africa, Unisa Science Campus, 28 Pioneer Avenue, Florida, Roodepoort, Gauteng, South Africa. https://orcid.org/0000-0001-8865-4735
Andreas Lemmerer, School of Chemistry, Molecular Sciences Institute, University of the Witwatersrand, Johannesburg, Gauteng, South Africa. https://orcid.org/0000-0003-1569-2831

Table 2: Fractional atomic coordinates and isotropic or equivalent isotropic displacement parameters ($Å^2$).

Atom	x	y	z	$U_{iso}*/U_{eq}$
C1	0.33289 (7)	0.36429 (17)	0.48805 (12)	0.0191 (3)
C2	0.30391 (9)	0.2671 (2)	0.41159 (14)	0.0277 (3)
H2	0.2566	0.2608	0.4052	0.033*
C3	0.34505 (11)	0.1786 (2)	0.34421 (16)	0.0359 (4)
H3	0.3247	0.1136	0.2911	0.043*
C4	0.43912 (9)	0.2735 (2)	0.42588 (16)	0.0329 (4)
H4	0.4865	0.2746	0.4321	0.039*
C5	0.40252 (8)	0.3686 (2)	0.49557 (14)	0.0247 (3)
H5	0.4243	0.4344	0.5468	0.03*
C6	0.29301 (7)	0.47594 (17)	0.55704 (12)	0.0196 (3)
C7	0.13160 (8)	0.50920 (19)	0.65346 (13)	0.0211 (3)
C8	0.09319 (8)	0.3983 (2)	0.58217 (16)	0.0295 (4)
H8A	0.118	0.3815	0.515	0.044*
H8B	0.0872	0.297	0.6192	0.044*
H8C	0.0493	0.4439	0.5657	0.044*
C9	0.09022 (8)	0.6141 (2)	0.72541 (13)	0.0235 (3)
H9A	0.0624	0.5461	0.7725	0.028*
H9B	0.0593	0.6761	0.6795	0.028*
C10	0.12885 (9)	0.7277 (2)	0.79610 (16)	0.0309 (4)
H10A	0.1608	0.7871	0.7519	0.046*
H10B	0.1532	0.6684	0.8515	0.046*
H10C	0.0976	0.8011	0.8307	0.046*
N1	0.23250 (6)	0.42502 (15)	0.58957 (12)	0.0237 (3)
H1A	0.2167	0.3325	0.5695	0.028*
N2	0.41190 (9)	0.1807 (2)	0.35055 (14)	0.0373 (4)
N3	0.19548 (7)	0.52638 (16)	0.65723 (12)	0.0238 (3)
O1	0.31550 (6)	0.60805 (13)	0.57675 (11)	0.0276 (3)
O2	0.5	0	0.20287 (16)	0.0330 (4)
H2A	0.4739 (15)	0.050 (3)	0.244 (3)	0.059 (9)*

development. Modifying existing drugs to target resistant organisms intend to mitigate the deactivation process by the mycobacteria [9]. The crystal structure being reported in this article represents a covalent modification of isoniazid. The compound crystallizes in the orthorhombic *Aba2* space group. The asymmetric unit shown in the figure is a hemihydrate, containing one organic target molecule and half a water molecule. The water sits in a special position in the unit cell, with a twofold rotation axis passing through the oxygen atom of the water molecule. Bond lengths and angles are all in the expected ranges [10, 11]. The crystal packing contains bilayers of (*E*)-*N′*-(butan-2-ylidene)iso-nicotinohydrazide alternating with layers of water molecules. Each carbohydrazide moiety is hydrogen bonded by a O2–H2a⋯N2 hydrogen bond to a water molecule to

form the hemihydrate. Each carbohydrazide moiety is also hydrogen bonded via its N1–H donor to the carbonyl oxygen (O1) acceptor of an adjacent carbohydrazide moiety. The water present in the crystal is generated as a byproduct of the Schiff base reaction between isoniazid and butanone and is not added to the reaction mixture.

References

1. Bruker. SAINT–Plus and SADABS; Bruker AXS Inc.: Madison, Wisconsin. USA, 2004.
2. Sheldrick G. M. A short history of *SHELX. Acta Crystallogr.* 2008, *A64*, 112–122.
3. Farrugia L. J. WinGX suite for small-molecule single-crystal crystallography. *J. Appl. Crystallogr.* 1999, *32*, 837–838.
4. Spek A. L. Structure validation in chemical crystallography. *Acta Crystallogr.* 2009, *D65*, 148–155.
5. Burnett M. N., Johnson C. K. *ORTEPIII* Report ORNL-6895; Oak Ridge National Laboratory: Tennessee, USA, 1996.
6. Farrugia L. J. WinGX and ORTEP for Windows: an update. *J. Appl. Crystallogr.* 2012, *45*, 849–854.
7. Pubchem. Isoniazid. Open chemistry database, 2018, 1–75. Available from https://pubchem.ncbi.nml.nih.gov/compound/isoniazid#section=Top.
8. Setshedi I. B., Smith M. G. The crystal structure of the co-crystal: 2-hydroxybenzoic acid *N′*-(butan-2-ylidene)pyridine-4-carbohydrazide, $C_{10}H_{13}N_3O \cdot C_7H_6O_3$. *Z. Kristallogr. N. Cryst. Struct.* 2021, *236*, 1093–1095.
9. Hu Y.-Q., Zhang S., Zhao F., Gao C., Feng L.-S., Lv Z.-S. Isoniazid derivatives and their anti-tubercular activity. *Eur. J. Med. Chem.* 2017, *133*, 255–267.
10. Madeley L. G., Levendis D. C., Lemmerer A. Covalent-assisted supra molecular synthesis: the effect of hydrogen bonding in cocrystals of 4-*tert*-butyl benzoic acid with isoniazid and its derivatized forms. *Acta Crystallogr.* 2019, *C75*, 200–207.
11. Lemmerer A., Bernstein J., Kahlenberg V. Covalent assistance in supramolecular synthesis: in situ modification and masking of the hydrogen bonding functionality of the supramolecular reagent isoniazid in co-crystals. *CrystEngComm* 2011, *13*, 5692–5708.

Annexure 5

The asymmetric unit of the co-crystal: 2-hydroxybenzoic acid – N′-(butan-2 ylidene)

pyridine-4-carbohydrazide, C₁₀H₁₃N₃O·C₇H₆O₃ – IBS018

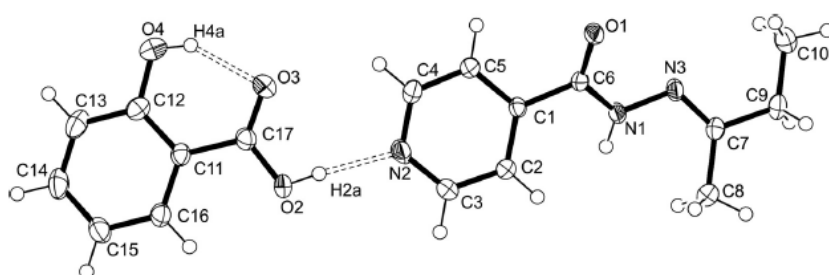Itumeleng B. Setshedi and Mark G. Smith*

The crystal structure of the co-crystal: 2-hydroxybenzoic acid – *N′*-(butan-2-ylidene) pyridine-4-carbohydrazide, C₁₀H₁₃N₃O·C₇H₆O₃

Abstract

$C_{10}H_{13}N_3O\cdot C_7H_6O_3$, monoclinic, $P2_1/n$ (no. 14), a = 7.4038(9) Å, b = 30.448(3) Å, c = 7.6744(8) Å, β = 112.013(3)°, V = 1603.9(3) Å³, Z = 4, $R_{gt}(F)$ = 0.0492, $wR_{ref}(F^2)$ = 0.1384, T = 173 K.

CCDC no.: 2081948

The asymmetric unit of the title crystal structure is shown in the figure. Table 1 contains crystallographic data and Table 2 contains the list of the atoms including atomic coordinates and displacement parameters.

Source of material

All reagents used were commercially available and used without further purification. An amount of 0.220 g of isonicotinic acid hydrazide (1.60 mmol), 0.220 g of 2-hydroxy-

Table 1: Data collection and handling.

Crystal:	Colourless block
Size:	0.43 × 0.34 × 0.31 mm
Wavelength:	Mo Kα radiation (0.71073 Å)
μ:	0.10 mm⁻¹
Diffractometer, scan mode:	Bruker D8 Venture Photon, ω
θ_{max}, completeness:	28.0°, >99%
$N(hkl)_{measured}$, $N(hkl)_{unique}$, R_{int}:	77005, 3868, 0.034
Criterion for I_{obs}, $N(hkl)_{gt}$:	I_{obs} > 2 σ(I_{obs}), 3459
$N(param)_{refined}$:	217
Programs:	Bruker [1], SHELX [2], WinGX [3], PLATON [4]

benzoic acid (1.59 mmol) and 3.0 mL of 2-butanone were added into a screw-top dram vial (with rubber septum) and stirred at 300 rpm at 60 °C for 10 min. The vial was closed, and the solution was allowed to reflux in the vial at 60 °C for 24 h. The solution was then left slightly open to allow slow evaporation at room temperature. Colourless block crystals were observed after three days.

Experimental details

The collection method involved ω-scans of width 0.5°. Data reduction was carried out using SAINT–Plus version 6.02.6 software, and SADABS was used to process empirical absorption corrections [1]. The crystal structure was solved through direct methods using SHELXS-97 [2]. Hydrogen atoms were positioned geometrically and allowed to ride on their respective parent atoms with d(C—H) = 0.95 Å and

*Corresponding author: Mark G. Smith, Chemistry Department, University of South Africa, Unisa Science Campus, 28 Pioneer Avenue Florida, Roodepoort, Gauteng, South Africa, E-mail: smithm2@unisa.ac.za. https://orcid.org/0000-0003-2553-2540
Itumeleng B. Setshedi, Department of Life Science, University of South Africa, Unisa Science Campus, 28 Pioneer Avenue Florida, Roodepoort, Gauteng, South Africa, E-mail: setshib@unisa.ac.za. https://orcid.org/0000-0001-8865-4735

Table 2: Fractional atomic coordinates and isotropic or equivalent isotropic displacement parameters ($Å^2$).

Atom	x	y	z	$U_{iso}*/U_{eq}$
C1	0.47422 (19)	0.69710 (4)	0.79314 (18)	0.0183 (3)
C2	0.4466 (2)	0.71769 (5)	0.6233 (2)	0.0232 (3)
H2	0.4381	0.7488	0.6132	0.028*
C3	0.4316 (2)	0.69213 (5)	0.4685 (2)	0.0262 (3)
H3	0.4147	0.7064	0.3534	0.031*
C4	0.4657 (2)	0.62846 (5)	0.6387 (2)	0.0267 (3)
H4	0.4704	0.5973	0.644	0.032*
C5	0.4857 (2)	0.65154 (5)	0.8007 (2)	0.0228 (3)
H5	0.5069	0.6364	0.915	0.027*
C6	0.5103 (2)	0.72181 (4)	0.97278 (18)	0.0188 (3)
C7	0.4555 (2)	0.82709 (5)	1.1042 (2)	0.0218 (3)
C8	0.4302 (3)	0.85230 (5)	0.9284 (2)	0.0322 (4)
H8A	0.4336	0.8839	0.9544	0.048*
H8B	0.5358	0.8448	0.886	0.048*
H8C	0.3048	0.8447	0.8302	0.048*
C9	0.4893 (2)	0.85415 (5)	1.2773 (2)	0.0267 (3)
H9A	0.3772	0.8743	1.2516	0.032*
H9B	0.6064	0.8725	1.3007	0.032*
C10	0.5164 (3)	0.82882 (6)	1.4547 (2)	0.0327 (4)
H10A	0.5372	0.8494	1.5586	0.049*
H10B	0.3998	0.8112	1.4357	0.049*
H10C	0.6297	0.8094	1.4849	0.049*
C11	0.2919 (2)	0.52453 (5)	0.0505 (2)	0.0222 (3)
C12	0.2453 (2)	0.48062 (5)	0.0713 (2)	0.0272 (3)
C13	0.1844 (2)	0.45300 (5)	−0.0850 (3)	0.0344 (4)
H13	0.1503	0.4234	−0.0727	0.041*
C14	0.1737 (3)	0.46848 (6)	−0.2571 (2)	0.0362 (4)
H14	0.1321	0.4493	−0.3625	0.043*
C15	0.2225 (2)	0.51151 (5)	−0.2795 (2)	0.0313 (3)
H15	0.2161	0.5218	−0.3986	0.038*
C16	0.2807 (2)	0.53909 (5)	−0.1255 (2)	0.0250 (3)
H16	0.3138	0.5687	−0.1398	0.03*
C17	0.3518 (2)	0.55441 (5)	0.2134 (2)	0.0248 (3)
N1	0.42658 (18)	0.76138 (4)	0.95584 (16)	0.0222 (3)
H1A	0.3544	0.7721	0.8451	0.027*
N2	0.43990 (19)	0.64817 (4)	0.47484 (18)	0.0267 (3)
N3	0.45845 (18)	0.78518 (4)	1.12194 (17)	0.0226 (3)
O1	0.61992 (16)	0.70594 (3)	1.12281 (14)	0.0255 (2)
O2	0.38141 (18)	0.59551 (3)	0.17611 (15)	0.0307 (3)
H2A	0.415	0.6104	0.2753	0.046*
O3	0.3705 (2)	0.54221 (4)	0.37140 (16)	0.0391 (3)
O4	0.2580 (2)	0.46347 (4)	0.23750 (18)	0.0404 (3)
H4A	0.2961	0.4829	0.321	0.061*

$U_{iso}(H) = 1.2U_{eq}(C)$. Diagrams and publication material were generated using WinGX [3] and PLATON [4].

Comment

Isoniazid, a synthetic derivative of nicotinic acid [5] is a drug that has been used for many years as a first-line anti–tuberculosis (TB) drug. However, bacterial strains targeted by isoniazid have developed resistance over the years, thus leading to the urgent need to develop novel drugs. There are several ways in which novel anti–TB drugs can be derived. However, one method that stands out is by making modifications to existing drugs so that they can no longer be deactivated by mycobacteria [6]. Therefore, the compound being reported in this article is a modification of isoniazid.

As shown in the figure, the asymmetric unit contains one molecule of N′-(butan-2-ylidene)pyridine-4-carbohydrazide and one molecule of 2-hydroxybenzoic acid (salicylic acid). All bond lengths and angles are as expected [7]. Each carbohydrazide moiety is hydrogen bonded by a O2—H2a···N2 hydrogen bond to a salicylic acid molecule to form a co-crystal. As is expected from similar co-crystals reported in the literature [8], this co-crystal is formed through a robust carboxylic acid ··· pyridine heterosynthon. The phenol group on the salicylic acid molecule forms an expected intramolecular S(6) hydrogen bond [9], between the H4a donor and the O3 acceptor. Each carbohydrazide moiety is also hydrogen bonded via its N1–H donor to the carbonyl oxygen (O1) acceptor of an adjacent carbohydrazide moiety (not shown in the figure). These hydrogen bonding interactions within the packing form a one dimensional (1D) ribbon along the a-axis. The plane of the salicylic acid is slightly offset from the plane of the pyridine ring by an acute angle of 22°. However, the pyridine rings of the carbohydrazide moiety as well as the benzene rings of salicylic acid lie parallel to each other respectively, and the packing is thus stabilized by π-stacking of these rings along the a-axis.

References

1. Bruker. SAINT–Plus and SADABS; Bruker AXS Inc.: Madison, WI, USA, 2004.
2. Sheldrick G. M. A short history of SHELX. Acta Crystallogr. 2008, A64, 112–122.
3. Farrugia L. J. WinGX suite for small-molecule single-crystal crystallography. J. Appl. Crystallogr. 1999, 32, 837–838.

4. Spek A. L. Structure validation in chemical crystallography. *Acta Crystallogr.* 2009, *D65*, 148–155.

5. Pubchem. Isoniazid open chemistry database. 2018, 1–75. https://pubchem.ncbi.nml.nih.gov/compound/isoniazid#section=Top.

6. Hu Y.-Q., Zhang S., Zhao F., Gao C., Feng L.-S., Lv Z.-S. Isoniazid derivatives and their anti-tubercular activity. *Eur. J. Med. Chem.* 2017, *133*, 255–267.

7. Lemmerer A., Bernstein J., Kahlenberg V. One-pot covalent and supramolecular synthesis of pharmaceutical co-crystals using the API isoniazid: a potential supramolecular reagent. *CrystEngComm* 2010, *12*, 2856–2864.

8. Aakoroy C. B., Hussain I., Forbes S., Desper J. Exploring the hydrogen-bond preference of N–H moieties in co-crystals assembled via O–H(acid)···N(py) intermolecular intereactions. *CrystEngComm* 2007, *9*, 46–54.

9. Bernstein J., Davis R. E., Shimoni L., Chang N. L. Patterns in hydrogen bonding: functionality and graph set analysis in crystals. *Angew. Chem. Int. Ed.* 1995, *34*, 1555–1573.